



KATHOLIEKE UNIVERSITEIT LEUVEN  
FACULTEIT WETENSCHAPPEN  
DEPARTEMENT GEOLOGIE-GEOGRAFIE  
AFDELING HISTORISCHE GEOLOGIE

FACULTEIT TOEGEPASTE WETENSCHAPPEN  
DEPARTEMENT BURGERLIJKE BOUWKUNDE  
LABORATORIUM voor HYDRAULICA

# **MODELLING CURRENTS AND SEDIMENT TRANSPORT PHENOMENA IN SHELF SEAS AND ESTUARIES**

Promotoren:  
Prof. dr. ir. J. Berlamont  
Prof. dr. N. Vandenberghe

Proefschrift voorgedragen  
tot het behalen van het  
Doctoraat in de  
Wetenschappen

door  
**Michael FETTWEIS**

November 1995

**VLIZ (vzw)**

**VLAAMS INSTITUUT VOOR DE ZEE**

**FLANDERS MARINE INSTITUTE**

**Oostende - Belgium**





KATHOLIEKE UNIVERSITEIT LEUVEN  
FACULTEIT WETENSCHAPPEN  
DEPARTEMENT GEOLOGIE-GEOGRAFIE  
AFDELING HISTORISCHE GEOLOGIE  
Redingenstraat 16bis, B-3000 Leuven

FACULTEIT TOEGEPASTE WETENSCHAPPEN  
DEPARTEMENT BURGERLIJKE BOUWKUNDE  
LABORATORIUM voor HYDRAULICA  
de Croylaan 2, B-3001 Leuven

## MODELLING CURRENTS AND SEDIMENT TRANSPORT PHENOMENA IN SHELF SEAS AND ESTUARIES

66350

Jury :

Prof. W. Viaene, Voorzitter  
Prof. J. Berlamont, Promotor  
Prof. N. Vandenberghe, Promotor  
Prof. R. Swennen  
Prof. E. Smets  
Prof. F. Runday (Université de Liège)  
Prof. M. Garcia (Universitat Politècnica de Catalunya)

Proefschrift voorgedragen  
tot het behalen van het  
Doctoraat in de  
Wetenschappen

door  
Michael FETTWEIS

November 1995

## ACKNOWLEDGEMENT

*This thesis summarizes the work on numerical modelling of the marine and estuarine environment I carried out throughout the last years. From 1986 till 1991 I stayed at the Hydraulics Laboratory of the KULeuven. The research focused on the development of numerical models for the simulation of wind induced currents at high latitudes and has been carried out in the framework of the ANTAR project (Belgian Scientific Programme on Antarctica), financed by the Services of the Prime Minister, Science Policy Office. In 1991 I started to work for IMDC (International Marine and Dredging Consultants). The thesis has been written in 1994-1995. The special doctoral grant of the Belgian National Fund for Scientific Research (NFWO), which I received during this year, is gratefully acknowledged.*

*Throughout these years, many research projects have been carried out in collaboration with several institutes and companies, and by the joint effort of many people. It is a pleasure for me to express several grateful words to them.*

*First of all, I want to express my deep gratitude to my promoters, Professor Jean Berlamont and Professor Noël Vandenberghe. Professor Jean Berlamont offered me the opportunity to work at the Hydraulics Laboratory and supervised this study. Professor Noël Vandenberghe accepted to be the promoter of the thesis for the Science Faculty. He gave comments and suggestions which improved the structure of the thesis as a whole.*

*The study leave during the period September 1994 - September 1995 given by ir. Christian Claeys, director of IMDC, is sincerely acknowledged. He gave me the possibility to use the infrastructure of IMDC during this period.*

*I want to thank especially dr. Chia-Shun Yu (KUL) and ir. Marc Sas (IMDC). They played a key role during my research. Their many discussions, comments and suggestions have substantially improved the thesis.*

*Professor Jaak Monbaliu (KUL and IMDC) played an important role during the writing period. His corrections and critical comments have much improved the work.*

*The collaboration with dr. Jozé Ozer and his group (MUMM) and with dr. Hubert Gallée (UCL) in the framework of the ANTAR project resulted in an intercomparison exercise of two 2.5D models forced by a katabatic wind. The interesting discussions we had together are much appreciated.*

*The stay of ir. Maurizio Rosso (Politecnico di Torino) in Leuven and the many discussions and talks we had together have much stimulated my research work.*

*Dr. K.P.P. Pathirana and dr. Erik Toorman (KUL) helped me a lot during the numerical simulation in the framework of the EC MAST G8 Coastal Morphodynamics project. The experimental data which have been used for the mud transport model verification, were made available by SOGREAH. This support is sincerely acknowledged.*

*Thanks are due to dr. K.P.P. Pathirana and to dr. Ebrahim Jabbari (KUL) for their collaboration in this study by providing me with two other transport models which were used for a model intercomparison.*

*I thank dr. Rob Wild and other scientists of HR Wallingford for their hospitality and for introducing me to the Tideway modelling system.*

*I am grateful to Professor Eddy Smets (Waterbouwkundig Laboratorium) and to Professor François Ronday (ULg) for their comments and suggestions on the manuscript. Also many thanks to the other members of the jury: Professor Willy Viaene (KUL), Professor Rudy Swennen (KUL) and Professor Marc Garcia (Univ. Catalunya).*

*I wish to thank the engineers of the Ministerie van de Vlaamse Gemeenschap, afdeling Maritieme Schelde (former Antwerpse Zeehavendienst) and of the Waterbouwkundig Laboratorium for the fruitful discussions and collaborations during the study of the Northern Container Terminal. The support of the survey crews of the vessels of the afdeling Maritieme Schelde and the Meetdienst Zeeland (Rijkswaterstaat) are gratefully acknowledged.*

*I extend my thanks to all the members of the Hydraulics Laboratory (KUL) and of IMDC for creating such a nice working environment. Thanks also to my friends and family for their moral supports throughout the years.*

*Mr. Antùn Pinterovič played, although not directly perceptible, a fundamental role. He knows why.*

*Finally, I would like to express my deep appreciation to my parents for their continuous support throughout the years.*

*To Patty and our child(ren), for their love, patience and tolerance.*

*Antwerp, November 1995*

*Michael Fettweis*



## ABSTRACT

Numerical models are an important tool for describing and understanding hydrodynamic and transport processes in the marine and estuarine environment. The success of these models is due to the fact that they are based on physical laws which describe in detail the processes involved. Two aspects of modelling, which are closely related, are highlighted. The first one focusses on the numerical aspects, while the second deals with validating the models through intercomparison with other models or analytical solutions and through field measurements.

A 2.5D vertical plane ice-ocean model and a 3D barotropic ocean model has been developed which simulates the wind induced currents in high latitude seas. The models solve the hydrodynamic and ice dynamic equations using finite different techniques. Because the domain of integration is very often smaller than the ocean basin non physical boundaries have to be introduced. Numerically this means that an open boundary condition has to be implemented. The Orlanski and the Camerlengo-O'Brien open boundary conditions have been introduced in an existing 2D depth averaged hydrodynamic model and have been validated by applying the model to some well defined test cases. It was found that the Camerlengo and O'Brien condition gave the best results. The Camerlengo-O'Brien open boundary condition has been used to simulate the flow behind a backward facing step in a long channel with the downstream boundaries open in order to investigate the quality of the results as a function of the advection scheme (1<sup>st</sup> order upstream and 3<sup>rd</sup> order QUICK).

The 2.5D ocean model was validated by comparing the results to those of an other model and to an analytical solution. The 2.5D ice-ocean model was forced by a katabatic wind. It is shown that coastal polynyas can be formed by these strong off coastal winds. The differences found between both model results have been summarized and explained.

The 2.5D model has been applied to an (idealized) ocean covered by an ice layer and deal with the behaviour of an ocean in the vicinity of an ice edge and a continental slope.

The second part is devoted to the study of mud transport in a part of the Scheldt estuary using field measurements and numerical models. The observations show the great variations in mud concentration found in the Scheldt estuary. The mud transport is simulated using a 2D and a 3D model. The 2D transport model is a Lagrangian model. The model has been validated by comparing the model results to the data obtained from a laboratory model. This experiment has shown that the model is able to reproduce qualitatively and quantitatively well the observations,

but that the predictive capability of the model suffers from a good description and integration of the various physical processes which governs the mud transport. The 2D mud transport model has then been applied to a part of the Scheldt estuary. The results of the model have been compared to the results of two other mud transport models.

The 3D mud transport model and several observations have been used to study the mud transport in an access channel. It is shown that the high mud deposition in the access channels is mainly due to the density gradients existing between the river and the access channel and in the vertical plane.

# TABLE OF CONTENTS

Acknowledgement	i
Abstract	iii
Table of contents	v
List of figures	ix
List of tables	xiii
List of symbols	xiv
List of abbreviations	xvii
Samenvatting	xix
1. Objectives and scope of the study	1
1.1. Introduction	1
1.2. Objectives	2
1.3. Structure of the text	5
2. Formulation of the Ice-Ocean Numerical Models	9
2.1. Introduction	9
2.2. The 2.5D hydrodynamic model	12
2.2.1. The governing equations	12
2.2.2. Finite difference equations	15
2.2.3. Computational scheme	17
2.3. The 1.5D ice dynamic model	18
2.3.2. Introduction	18
2.3.2. The governing equations of ice dynamics	19
2.3.3. Numerical scheme of the ice model	22
2.4. Coupling of the 2.5D ocean and the 1.5D ice model	22
2.5. Open boundary condition	23
2.5.1. Introduction	23
2.5.2. Numerical experiments of open boundary conditions	25
2.5.2.1. Barotropic relaxation	26
2.5.2.2. Alongshelf wind stress	27
2.5.2.3. Forcing at the open boundary	27
2.5.3. Conclusions	33
2.6. Numerical experiments of convection-diffusion dominated flow problems and open boundary conditions	33
2.6.1. Governing equations and numerical procedure	34
2.6.2. Approximation of the advection and diffusion terms	34
2.6.3. Discussion of the backward facing step results	36
2.7. Conclusion and summary	40
3. Hydrodynamic Response to Katabatic Wind Forcing	41
3.1. Introduction	41
3.2. Katabatic wind simulation	43
3.3. Description of the two 2.5D models	43
3.4. Differences between the models	45

3.5.	Comparison of the model results	46
3.5.1.	Description of the Test Cases	46
3.5.2.	Case 1: Flat Bottom	48
3.5.2.1.	Ekman's Solution	48
3.5.2.2.	Results of the Simulations	49
3.5.3.	Case 2: Shelf/Ocean	52
3.6.	Discussion	59
3.6.1.	Advection-diffusion	63
3.6.2.	Timestep-size	63
3.6.3.	Ekman's solution	63
3.6.4.	Vertical resolution	64
3.7.	3D model of the Terra Nova coastal area	67
3.7.1.	Description of the 3D model	67
2.7.1.1.	Finite difference equations	68
2.7.1.2.	Computational scheme	70
3.7.2.	Description of the model area	72
3.7.3.	Result of the simulation	72
3.8.	Conclusion	74
4.	<b>Wind-Driven Circulation Along an Ice Edge</b>	77
4.1.	Introduction	77
4.2.	Model results	79
4.2.1.	Case 1 (shelf - flat bottom)	81
4.2.2.	Case 2 (shelf - ocean)	82
4.3.	Discussion and conclusion	90
5.	<b>Cohesive Sediment Transport in the Scheldt Estuary</b>	95
5.1.	Introduction	95
5.2.	The Scheldt estuary	97
5.2.1.	Hydrodynamic aspects	98
5.2.2.	Lithology and morphology	101
5.2.3.	Cohesive sediments	102
5.2.3.1.	Origin of mud in the estuary	102
5.2.3.2.	Suspended mud distribution	104
5.3.	Through tide measurements at 'Drempel van Zandvliet'	108
5.3.1.	Tides, currents and discharges	110
5.3.2.	Salinity	115
5.3.3.	Cohesive suspended sediments	120
5.3.4.	Effective fall velocity	125
5.3.5.	Erosion and sedimentation of mud	125
5.3.6.	Velocity-, sediment and transport profiles	127
5.3.7.	Transport of suspended sediments	128
5.3.8.	Conclusions	129
5.4.	Through tide measurements at 'Plaat van Lillo' and 'Vaarwater boven Bath'	132
5.5.	Measurements in the access channel to the Zandvliet and Berendrecht locks	133
5.5.1.	Currents	135



5.5.2.	Salinity	139
5.6.	Long term measurements at Prosperpolder	139
5.6.1.	Introduction	139
5.6.2.	Salinity	139
5.6.2.1.	Seasonal variations	142
5.6.2.2.	Variations with tidal range	145
5.6.2.3.	Variations with tide	145
5.6.3.	Temperature	145
5.6.4.	Suspended mud concentration	149
5.6.4.1.	Variation of averaged quantities	149
5.6.4.2.	Seasonal variations	154
5.6.4.3.	Tidal variations	158
5.6.4.4.	Conclusions	159
5.7.	Summary	162
6.	<b>2D Modelling of Cohesive Sediment Transport</b>	165
6.1.	Cohesive sediment processes	165
6.1.1.	Bottom stress	166
6.1.2.	Settling of mud particles	166
6.1.3.	Deposition	168
6.1.4.	Erosion	169
6.1.5.	Consolidation and bed structure	170
6.1.6.	Numerical modelling of cohesive sediment transport	171
6.2.	The 2D particle tracking model TRASIL	172
6.3.	Validation of the model using laboratory data	174
6.3.1.	Introduction	174
6.3.2.	Numerical model setup	175
6.3.3.	Erosion tests under uniform currents	177
6.3.4.	Erosion and deposition tests under alternating currents	178
6.3.5.	Conclusions	178
6.4.	2D mud transport model of a part of the Scheldt estuary	184
6.4.1.	The Scheldt model	184
6.4.1.1.	The 2D hydrodynamic model FINEL	184
6.4.1.2.	The mud transport model	188
6.4.2.	Model intercomparison	189
6.4.3.	Diffusion sensitivity studies	195
6.5.	Conclusions	198
7.	<b>Sedimentation of Mud in an Access Channel</b>	201
7.1.	Introduction	201
7.2.	Flow in the access channel	202
7.2.1.	The 3D hydrodynamic model	202
7.2.2.	Flow field in the river	204
7.2.3.	Flow field in the access channel	206
7.3.	Salinity in the access channel	211
7.3.1.	Salinity in the river	211
7.3.2.	Salinity in the access channel	214
7.4.	Water exchange between the river and the access channel	216

7.5.	Sedimentation in the access channel . . . . .	218
7.4.1.	The 3D mud transport model . . . . .	219
7.4.2.	Observations of sedimentation in the access channel . . . . .	219
7.4.3.	Model results . . . . .	220
7.6.	Conclusions . . . . .	223
8.	<b>Conclusions and Recommendations</b> . . . . .	225
8.1.	General conclusions . . . . .	225
8.2.	Recommendation for further research . . . . .	231
	References . . . . .	235
	Appendix 1: Position of some locations in the Scheldt estuary . . . . .	249
	List of Publications . . . . .	251
	Curriculum Vitae . . . . .	253

## LIST OF FIGURES

2.1	Numerical grid used by the 2.5D model . . . . .	16
2.2	Processes near the ice margin . . . . .	18
2.3	Geometry of the three open boundary test basins . . . . .	26
2.4	Barotropic relaxation, Camerlengo & O'Brien open boundary condition . . . . .	28
2.5	Alongshelf wind, Orlanski open boundary condition . . . . .	29
2.6	Alongshelf wind, Camerlengo & O'Brien open boundary condition . . . . .	30
2.7	Forced wave, Orlanski open boundary condition . . . . .	31
2.8	Forced wave, Camerlengo & O'Brien open boundary condition . . . . .	32
2.9	Geometry of the basin for the backward facing step problem . . . . .	36
2.10	Backward facing step, long mesh calculations . . . . .	38
2.11	Backward facing step, shear stress along walls . . . . .	39
2.12	Backward facing step, short mesh calculations . . . . .	39
3.1	x dependence of the horizontal wind component . . . . .	44
3.2	x dependence of the friction velocity and the horizontal wind norm . . . . .	44
3.3	Dimensions of the basins . . . . .	47
3.4	Pressure gradient with distance, case 1, vertical grid size 10m . . . . .	50
3.5	Flow field in the vertical plane, case 1, vertical grid size 10m . . . . .	53
3.6	Enlargement of Figure 3.5 . . . . .	54
3.7	Northward velocity component, case 1, vertical grid size 10m . . . . .	56
3.8	Eastward velocity component, case 1, vertical grid size 10m . . . . .	58
3.9	Vertical velocity component, case 1, vertical grid size 10m . . . . .	59
3.10	Flow field in the vertical plane, case 2s . . . . .	60
3.11	Flow field in the vertical plane, case 2o . . . . .	61
3.12	Flow field in the vertical plane, case 2l . . . . .	62
3.13	Pressure gradient with distance, case 1, vertical grid size 5m . . . . .	64
3.14	Northward velocity component, case 1, vertical grid size 5m . . . . .	65
3.15	Eastward velocity component, case 1, vertical grid size 5m . . . . .	66
3.16	Numerical grid used by the 3D model . . . . .	69
3.17	Katabatic wind over Terra Nova coastal area . . . . .	73
3.18	3D model, flow field in the surface layer . . . . .	73
3.19	3D model, flow field at 20m depth . . . . .	74
4.1	Dimension of the basin for case 1 and 2 . . . . .	80
4.2	Initial density stratification for case 1 and 2 . . . . .	80
4.3	Flow field in vertical plane, ice free shelf case . . . . .	83
4.4	Flow field in vertical plane, shelf case with a non moving ice cover . . . . .	84
4.5	Flow field in vertical plane, shelf case with a moving ice cover . . . . .	85
4.6	Flow field in vertical plane, non stratified ice free shelf-ocean case . . . . .	86
4.7	Flow field in vertical plane, stratified ice free shelf-ocean case . . . . .	87
4.8	Flow field in vertical plane, stratified shelf-ocean case with a non moving ice cover . . . . .	88
4.9	Flow field in vertical plane, stratified shelf-ocean case with a moving ice cover . . . . .	89
4.10	Flow field perpendicular to vertical plane showing the occurrence of	



an alongshore & along ice jet . . . . .	93
5.1 The Scheldt estuary . . . . .	99
5.2 Longitudinal salinity distribution in the Scheldt estuary . . . . .	100
5.3 Longitudinal mud concentration in the Scheldt estuary . . . . .	106
5.4 Location of the measurement points . . . . .	109
5.5 Neap tide, vertical averaged velocities, Drempel van Zandvliet . . . . .	112
5.6 Spring tide, vertical averaged velocities, Drempel van Zandvliet . . . . .	112
5.7 Spring tide, maximum flood velocity over the cross section, Drempel van Zandvliet . . . . .	113
5.8 Spring tide, maximum ebb velocity over the cross section, Drempel van Zandvliet . . . . .	113
5.9 Spring tide, velocity profile at point 2, Drempel van Zandvliet . . . . .	114
5.10 Neap tide, vertical averaged salinity, Drempel van Zandvliet . . . . .	116
5.11 Spring tide, vertical averaged salinity, Drempel van Zandvliet . . . . .	116
5.12 Spring tide, salinity in point 2, Drempel van Zandvliet . . . . .	117
5.13 Spring tide, salinity distribution at about LW over the cross section, Drempel van Zandvliet . . . . .	119
5.14 Spring tide, salinity distribution at about HW over the cross section, Drempel van Zandvliet . . . . .	119
5.15 Neap tide, depth averaged mud concentration, Drempel van Zandvliet . . . . .	122
5.16 Spring tide, depth averaged mud concentration, Drempel van Zand- vliet . . . . .	122
5.17 Neap tide, mud concentration at bottom, Drempel van Zandvliet . . . . .	123
5.18 Spring tide, mud concentration at bottom, Drempel van Zandvliet . . . . .	123
5.19 Neap tide, erosion/sedimentation cycle of mud, Drempel van Zand- vliet . . . . .	126
5.20 Spring tide, erosion/sedimentation cycle of mud, Drempel van Zand- vliet . . . . .	126
5.21 Spring tide, profiles of velocity, mud concentration and transport in point 2, Drempel van Zandvliet . . . . .	128
5.22 Spring tide, contourlines of velocity as a function of time and water depth, Drempel van Zandvliet . . . . .	130
5.23 Spring tide, contourlines of salinity as a function of time and water depth, Drempel van Zandvliet . . . . .	131
5.24 Spring tide, contourlines of mud concentration as a function of time and water depth, Drempel van Zandvliet . . . . .	131
5.25 Mud concentration at Drempel van Zandvliet, Plaat van Lillo and Vaar- water boven Bath . . . . .	133
5.26 Zandvliet-Berendrecht access channel, velocity 5h31 before HW . . . . .	136
5.27 Zandvliet-Berendrecht access channel, velocity 1h06 before HW . . . . .	136
5.28 Zandvliet-Berendrecht access channel, velocity 1h21 after HW . . . . .	137
5.29 Zandvliet-Berendrecht access channel, velocity 2h04 after HW . . . . .	137
5.30 Zandvliet-Berendrecht access channel, velocity 5h05 after HW . . . . .	138
5.31 Zandvliet-Berendrecht access channel, velocity 0h38 after LW . . . . .	138
5.32 Zandvliet-Berendrecht access channel, salinity during flood . . . . .	140
5.33 Zandvliet-Berendrecht access channel, salinity during ebb . . . . .	140
5.34 Tidal averaged salinity and fresh water discharge, Sep'92 - Dec'93,	

Prosperpolder	143
5.35 Salinity as a function of fresh water discharge, Sep'92 - Dec'93, Prosperpolder	144
5.36 Hysteresis of fresh water discharge vs. salinity, Sep'92 - Dec'93, Prosperpolder	144
5.37 Salinity and tidal elevation, Oct'92, Prosperpolder	146
5.38 Salinity and tidal elevation, Dec'92, Prosperpolder	146
5.39 Relative salinity as a function of time related to HW, Prosperpolder	147
5.40 Tidal averaged temperature, Sep'92 - Dec'93, Prosperpolder	148
5.41 Relative temperature as a function of time related to HW, Prosperpolder	148
5.42 Flood-averaged mud concentration 0.5m from bottom and tidal range, Sep'92 - Dec '93, Prosperpolder	150
5.43 Ebb-averaged mud concentration 0.5m from bottom and tidal range, Sep'92-Dec '93, Prosperpolder	150
5.44 Flood-averaged mud concentration 1.5m from bottom and fresh water discharge, Sep'92 - Dec'93, Prosperpolder	151
5.45 Ebb-averaged mud concentration 1.5m from bottom and fresh water discharge, Sep'92 -Dec'93 Prosperpolder	151
5.46 Mud concentration 0.5m from bottom and tidal elevation, Jan'93, Prosperpolder	160
5.47 Mud concentration 0.5m from bottom and tidal elevation, May'93, Prosperpolder	160
5.48 Mud concentration 1.5m from bottom and tidal elevation, Jan'93, Prosperpolder	161
5.49 Mud concentration 1.5m from bottom and tidal elevation, May'93, Prosperpolder	161
6.1 Uniform flow test 2, different erosion models	179
6.2 Uniform flow test 2, different erosion rates M	180
6.3 Uniform flow test 2, different erosion rates M'	180
6.4 Uniform flow test 6, different erosion models	181
6.5 Uniform flow test 7, different erosion models	181
6.6 Uniform flow test A1, different erosion models	182
6.7 Alternating flow test 1	182
6.8 Alternating flow test 3	183
6.9 Alternating flow test 4	183
6.10 2D and 3D hydrodynamic and mud transport model boundaries	185
6.11 Bathymetry of the model area	186
6.12 Concentration field 1 hour before LW	192
6.13 Concentration field 1 hour before HW	193
6.14 Deposition of mud after one tidal cycle	194
6.15 Mud concentration in function of time (point 2)	195
6.16 TRASIL, deposition of mud per tide ( $D = 10\text{m}^2/\text{s}$ )	196
6.17 TRASIL, deposition of mud per tide ( $D = 100\text{m}^2/\text{s}$ )	196
6.18 TRASIL, particle tracking during one tidal cycle ( $D = 10\text{m}^2/\text{s}$ )	197
6.19 TRASIL, particle tracking during one tidal cycle ( $D = 100\text{m}^2/\text{s}$ )	197

7.1 Spring tide high salinity gradient, maximum flood and ebb velocities in surface layer . . . . . 206

7.2 Spring tide high salinity gradient, velocity profiles . . . . . 205

7.3 Comparison between 3D model results and ADCP, 5.5h before HW . 208

7.4 Comparison between 3D model results and ADCP, 1h after HW . . . 208

7.5 Spring tide without salinity gradient, maximum flood flow . . . . . 209

7.6 Spring tide without salinity gradient, maximum ebb flow . . . . . 210

7.7 Spring tide high salinity gradient, flow field 2h before HW . . . . . 211

7.8 Spring tide high salinity gradient, flow field 4h after HW . . . . . 212

7.9 Spring tide high salinity gradient, salinity compared to observations . 213

7.10 Spring tide high salinity gradient, salinity at maximum salinity . . . . 214

7.11 Spring tide high salinity gradient, salinity at minimum salinity . . . . 215

7.12 Spring tide high salinity gradient, salinity in the access channel . . . . 217

7.13 Mud deposition per spring tide with high and without salinity gradient 221



## LIST OF TABLES

2.1	Scaling of the different terms in the vertical equation of motion . . . .	13
3.1	Difference between both models and the Ekman solution . . . . .	45
4.1	Overview of the different simulations . . . . .	81
5.1	Measured tidal variations, 27/09/90 and 04/10/90 at Prosperpolder .	110
5.2	Mean ratio $v_{\text{surface}}/v_{\text{average}}$ for ebb and flood, Drempel van Zandvliet . .	111
5.3	Neap tide, discharges at Drempel van Zandvliet . . . . .	114
5.4	Spring tide, discharges at Drempel van Zandvliet . . . . .	114
5.5	Extreme salinity values at Drempel van Zandvliet . . . . .	118
5.6	Vertical salinity stratification at Drempel van Zandvliet . . . . .	118
5.7	Mean ratio $C_{\text{bottom}}/C_{\text{average}}$ during ebb and flood, Drempel van Zandvliet	124
5.8	Neap tide, depth averaged mud concentration, Drempel van Zandvliet	124
5.9	Spring tide, depth averaged mud concentration, Drempel van Zand- vliet . . . . .	124
5.10	Effective fall velocity at decreasing velocity, Drempel van Zandvliet .	125
5.11	Neap and spring tide, total mud transport, Drempel van Zandvliet . .	129
5.12	Measured tidal variations at Zandvliet, 19 & 29/04/93 . . . . .	134
5.13	Tidal salinity range, averaged data, Prosperpolder . . . . .	145
5.14	Tidal temperature range, averaged data, Prosperpolder . . . . .	147
5.15	Mud concentration 0.5m from bottom, averaged data, Prosperpolder	152
5.16	Mud concentration 1.5m from bottom, averaged data, Prosperpolder	152
6.1	Uniform flow tests, initial properties of the mud layer . . . . .	175
6.2	Alternating flow tests, initial properties of the mud layer . . . . .	175
6.3	Uniform flow test, density profile of the mud bed . . . . .	176
6.4	Standard model parameter values, uniform floe tests . . . . .	177
6.5	Standard model parameters, alternating flow tests . . . . .	178
7.1	Water exchange between the access channel and the river . . . . .	218
7.2	Sedimentation of mud per tide and per year in the access channel . .	222



## LIST OF SYMBOLS

$adu/adv$	advective terms in the 2.5D $u/v$ -momentum equation
$c$	propagation speed of disturbance [m/s]
$c_0$	typical value of $c$ for 100% ice cover [m/s]
$c_\phi$	phase speed [m/s]
$d$	ice thickness [m]
$d_0$	typical ice thickness [m]
$diffu/diffv$	diffusion terms in the 2.5D $u/v$ -momentum equation
$f$	Coriolis parameter [1/s]
$f$	friction factor of Darcy-Weissbach []
$g$	acceleration due to gravity [ $9.81\text{m}^2/\text{s}$ ]
$h$	water depth [m]
$i$	complex number ( $i^2 = -1$ )
$i$	subscript, indicating the $x$ coordinate in the finite difference equations
$j$	subscript, indicating the $y$ coordinate in the finite difference equations
$k$	dispersivity coefficient for sea ice
$k$	bed roughness [m]
$k$	subscript, indicating the $z$ coordinate in the finite difference equations
$k_n$	bed roughness following Nikuradse [m]
$m$	mass of suspended sediments per unit area [ $\text{kg}/\text{m}^2$ ]
$n$	Manning resistance coefficient
$n$	superscript, indicating the current time level in the finite difference equations.
$n-1$	superscript, indicating the previous time level in the finite difference equations.
$n+1$	superscript, indicating the future time level in the finite difference equations.
$p$	pressure [Pa]
$p_s$	pressure at the sea surface [Pa]
$p_l$	pressure on the rigid lid due to the flow [Pa]
$p^*$	typical value of the plastic strength of sea ice (N/m)
$s$	salinity [g/l]
$t$	time [s]
$u$	water velocity in $x$ -direction [m/s]
$u$	vertical averaged velocity [m/s]
$u'$	explicit part of the $u$ -velocity [m/s]
$u''$	implicit part of the $u$ -velocity [m/s]
$u_i$	ice velocity in $x$ -direction [m/s]
$u_*$	friction velocity
$v$	water velocity in $y$ -direction [m/s]
$v_i$	ice velocity in $y$ -direction [m/s]
$w$	water velocity in $z$ -direction, positive upward [m/s]
$w$	fall velocity of mud 'particles' [m/s]
$w_{s\text{ eff}}$	effective fall velocity of mud 'particles' [m/s]
$x$	horizontal direction [m], perpendicular to $y$ , $z$

$x_i$	random displacement of a particle due to diffusion
$y$	horizontal direction [m], perpendicular to $x$ , $z$
$z$	vertical direction [m], perpendicular to $x$ , $y$
$A$	part of unit area covered by ice [%]
$A_h$	horizontal kinematic eddy viscosity coefficient [ $\text{m}^2/\text{s}$ ]
$A_i$	surface of the elementary area covered by ice [ $\text{m}^2$ ]
$A_t$	total surface of the elementary area [ $\text{m}^2$ ]
$A_v$	vertical kinematic eddy viscosity coefficient [ $\text{m}^2/\text{s}$ ]
$C$	(depth averaged) mud concentration [ $\text{kg}/\text{m}^3$ ]
$C_{ai}$	air/ice drag coefficient ( $2 \times C_{aw}$ )
$C_{aw}$	air/water drag coefficient
$C_{\text{bottom}}$	mud concentration in the bottom layer of the water column [ $\text{kg}/\text{m}^3$ ]
$C_h$	Chézy coefficient [ $1/\text{s}$ ]
$C_l$	layer averaged mud concentration times layer thickness [ $\text{mkg}/\text{m}^3$ ]
$C_{\text{max}}$	maximum vertical averaged mud concentration [ $\text{kg}/\text{m}^3$ ]
$C_{\text{mean}}$	vertical averaged mud concentration [ $\text{kg}/\text{m}^3$ ]
$C_{\text{min}}$	minimum vertical averaged mud concentration [ $\text{kg}/\text{m}^3$ ]
$C_{wi}$	water/ice drag coefficient
$D$	source term for deposition [ $\text{kg}/\text{m}^2\text{s}$ ]
$D$	effective diffusivity [ $\text{m}^2/\text{s}$ ]
$D_i$	diffusive coefficient
$D_l$	horizontal dispersion coefficient [ $\text{m}^2/\text{s}$ ]
$D_v$	vertical diffusion coefficient [ $\text{m}^2/\text{s}$ ]
$E$	source term for erosion [ $\text{kg}/\text{m}^2\text{s}$ ]
$E_a$	variation of ice mass due to melting or freezing [kg]
$G$	root mean square velocity gradient
$H$	eroded bed thickness [m]
$H_0$	initial bed thickness [m]
$K_x$	horizontal eddy diffusivity coefficient [ $\text{m}^2/\text{s}$ ]
$K_v$	vertical eddy diffusivity coefficient [ $\text{m}^2/\text{s}$ ]
$M$	erosion constant [ $\text{kg}/\text{m}^2\text{s}$ ]
$M'$	erosion constant [ $\text{kg}/\text{Ns}$ ]
$R_a$	variation of ice mass due to mechanical redistribution [kg]
$Re$	Reynolds number
$R[0;1]$	random number between 0 and 1
$S$	salinity [g/l]
$V$	horizontal water velocity vector [ $\text{m}/\text{s}$ ]
$V_d$	horizontal water velocity vector caused by density gradients [ $\text{m}/\text{s}$ ]
$V_i$	ice velocity vector [ $\text{m}/\text{s}$ ]
$W$	wind velocity vector [ $\text{m}/\text{s}$ ]
$\alpha$	erosion constant [ $\text{mN}^{-0.5}$ ]
$\Delta t$	time step [s]
$\Delta s$	random step size [m]
$\Delta x$	grid size of a numerical grid in $x$ -direction [m]
$\Delta y$	grid size of a numerical grid in $y$ -direction [m]
$\Delta z$	grid size of a numerical grid in $z$ -direction [m]
$\epsilon_0$	erosion constant [ $\text{kg}/\text{m}^2\text{s}$ ]

$\phi$	a variable
$\phi_k$	known value of $\phi$ at boundary
$K$	von Karman constant
$\nu$	kinematic viscosity [ $\text{m}^2/\text{s}$ ]
$\rho$	density ( $\text{kg}/\text{m}^3$ )
$\rho$	dry density of deposit ( $\text{kg}/\text{m}^3$ )
$\rho$	vertical averaged density ( $\text{kg}/\text{m}^3$ )
$\rho_a$	air density ( $\text{kg}/\text{m}^3$ )
$\rho_{\text{mean}}$	mean dry density of deposit ( $\text{kg}/\text{m}^3$ )
$\rho_i$	sea ice density ( $\text{kg}/\text{m}^3$ )
$\sigma$	internal ice stress tensor [...]
$T_{ai}$	wind stress at the air/ice interface [Pa]
$T_{ai,x}$	wind stress at the air/ice interface in x-direction [Pa]
$T_{ai,y}$	wind stress at the air/ice interface in y-direction [Pa]
$T_{aw}$	wind stress at the air/water interface [Pa]
$T_{aw,x}$	wind stress at the air/water interface in x-direction [Pa]
$T_{aw,y}$	wind stress at the air/water interface in y-direction [Pa]
$T_b$	bottom stress [Pa]
$T_{cd}$	critical shear stress for deposition [Pa]
$T_{ce}$	critical shear stress for erosion [Pa]
$T_{s,x}$	wind and ice stress in x-direction on the surface of the ocean [Pa]
$T_{s,y}$	wind and ice stress in y-direction on the surface of the ocean [Pa]
$T_{wi}$	stress at the water/ice interface [Pa]
$T_{wi,x}$	stress at the water/ice interface in x-direction [Pa]
$T_{wi,y}$	stress at the water/ice interface in y-direction [Pa]
$T_y$	yield stress [Pa]
$\omega_k$	weighting factor depending on the vertical grid size

## LIST OF ABBREVIATIONS

<i>A.G.U.</i>	American Geophysical Union.
<i>A.Z.</i>	Antwerpse Zeehavendienst (now afdeling Maritieme Schelde), Ministerie van de Vlaamse Gemeenschap.
<i>BBADCP</i>	Broad Band Acoustic Doppler Current Profiler.
<i>BMM</i>	Beheerseenheid van het Mathematisch Model, Ministerie van Volksgezondheid.
<i>B.G.</i>	Bestuur Geotechniek, Ministerie van de Vlaamse Gemeenschap.
<i>D.D.K.</i>	Dienst Der Kusthavens, Ministerie van de Vlaamse Gemeenschap.
<i>HR</i>	Hydraulics Research Wallingford Ltd.
<i>I.M.D.C.</i>	International Marine and Dredging Consultants N.V.
<i>KUL</i>	Katholieke Universiteit Leuven.
<i>MP</i>	Measurement Point
<i>MUMM</i>	Management Unit of the Mathematical Models, Ministry of Public Health.
<i>N.F.W.O.</i>	Nationaal Fonds voor Wetenschappelijk Onderzoek.
<i>OBC</i>	Open boundary condition.
<i>R.W.S.</i>	Rijkswaterstaat.
<i>UCL</i>	Université Catholique de Louvain.
<i>ULg</i>	Université de Liège.
<i>W.L.</i>	Waterloopkundig Laboratorium Delft (Delft Hydraulics).
<i>W.L.B.</i>	Waterbouwkundig Laboratorium Borgerhout, Ministerie van de Vlaamse Gemeenschap.





# SAMENVATTING

## 1. Inleiding

Een groot deel van onze planeet is bedekt met water. Het water is nooit zuiver omdat er op verschillende wijze een wisselwerking optreedt tussen het water en de vaste materie. Stoffen kunnen ofwel opgelost zijn (b.v. zout) of kunnen als zwevende deeltjes in het water opgenomen worden (b.v. sedimenten). Het water op de aarde is in beweging. De stromingen in oceanen, kustzeeën en estuaria worden veroorzaakt door enerzijds de energie toevoer van de zon (direct als warmte en indirect als wind of atmosferische drukverschillen) en anderzijds door de relatieve bewegingen van de aarde, de maan en de zon ten opzichte van elkaar.

Numerieke modellen zijn een belangrijk instrument om hydrodynamische en transportprocessen in oceanen, kustzeeën en estuaria te beschrijven en te bestuderen. Het succes van numerieke modellen is voornamelijk het gevolg van de sterke ontwikkeling van computers, maar kan ook verklaard worden door het feit dat zij gebaseerd zijn op fysische wetten, die de betrokken processen in detail beschrijven. Er zijn echter processen die niet in detail gekend zijn (b.v. cohesief sediment transport) terwijl andere niet ingebouwd kunnen worden in het model, wegens hun extreem kleine lengte- en tijdschalen (zoals turbulentie) en vereenvoudigd dienen te worden. De vereenvoudigingen of benaderingen die ten grondslag liggen aan de modelvergelijkingen zijn afhankelijk van de toepassingen die men wil modelleren. De zo bekomen partiële differentiaalvergelijkingen kunnen meestal niet rechtstreeks opgelost worden. Wiskundige modellen gebruiken numerieke technieken om de vergelijkingen op te lossen. De numerieke techniek (b.v. eindige differenties of eindige elementen) moet gebruik maken van een numeriek schema dat nauwkeurig is, consistent is met de oorspronkelijke vergelijkingen en dat convergentie garandeert.

In deze dissertatie komen drie, nauw verwante aspecten van numerieke modellering aan bod. Het eerste omvat de numerieke aspecten van een model (numeriek schema, stralingsrandvoorwaarde en advectioneel schema's), het tweede omvat het proces van vergelijking van de modelresultaten met analytisch oplossingen, met de resultaten van andere modellen en met metingen. Het derde aspect beschrijft enkele toepassingen. Al deze drie aspecten vormen een deel van het zogenaamde validatie proces van een model.

## 2. Beschrijving van de numerieke modellen

Het ijs-oceaan systeem wordt beheerst door drie onderling gekoppelde dynamische processen, zijnde de hydrodynamica, de ijsdynamica en de ijsthermodynamica. De weersomstandigheden boven de oceaan vormen een tijdsafhankelijke randvoorwaarde aan het oppervlakte voor elk van die processen. In het vervolg wordt er enkel aandacht geschonken aan het ijs-oceaan gedeelte en worden thermodynamische effecten buiten beschouwing gelaten. Dit is gerechtvaardigd indien men met kleine tijdschalen (dagen) rekent.

De vergelijkingen die door het 2.5D oceaan model opgelost worden, zijn afgeleid van de tijdsafhankelijke driedimensionale momentum- en transportvergelijking. De basishypothese is dat de oceaan als uniform beschouwd wordt in één van de horizontale richtingen ( $y$ ). Daardoor zijn alle partiële afgeleiden naar  $y$  gelijk aan nul. Het model maakt verder gebruik van een constante waterpeilverheffing. De verticale snelheid aan het oppervlakte wordt gelijk gesteld aan nul. Deze benadering wordt gebruikt om oppervlaktegolven te elimineren en laat toe om een grotere tijdstap in de berekeningen te gebruiken. De turbulente processen worden beschreven met behulp van turbulente mengingscoëfficiënten. Het model maakt gebruik van een Cartesisch rooster. De vergelijkingen worden opgelost met behulp van een expliciet eindige differenties-schema.

De ijsdynamica omvat processen van mechanische vervorming en van ijstransport ten gevolge van de schuifspanningen aan het wateroppervlak en aan het ijs/water - contactvlak. De initiële ijsgroei gebeurt steeds thermodynamisch. In de verdere ontwikkeling van ijsvelden kan de groei ook dynamisch gebeuren (zelfs tijdens dooiperiodes). Uitgestrekte ijsvelden worden gefragmenteerd in brokstukken, welke zich het één onder het ander kunnen bewegen en aldus aanleiding geven tot de vorming van ijsruggen, of welke kunnen vloten naar andere zones zodat open water zones gevormd kunnen worden. Deze twee vormen van ijsdynamica worden onderhouden door de actie van de wind, van de golven, van de stromingen en van de interne spanningen in het ijs. De ijsdynamica kan in rekening gebracht worden door het gefragmenteerde ijsveld als een continuüm te beschouwen. De nodige voorwaarde om de continuümbenadering toe te passen, is dat de elementaire lengteschalen van het continuüm voldoende groot zijn in vergelijking met de typische grootte van de ijsschotsen, én voldoende klein zijn ten opzichte van het volledige ijsveld en de aandrijvende krachten. Omdat de verticale beweging van het ijs-medium gedurende mechanische vervormingen van enkele grootte-orden verschillen



ten overstaan van de horizontale bewegingen, mag de beweging van het ijsveld als horizontaal beschouwd worden. De bewegingsvergelijking van het ijsveld-conti-nuüm kan afgeleid worden uit het krachtenevenwicht op een elementair oppervlak, de aanwezige krachten zijn de kracht van de wind werkend op het ijs/luchtcontact-vlak, de kracht van het water werkend op het water/ijscontactvlak, de Coriolis-kracht en de kracht tengevolge van de interne ijsspanningen. De koppeling van het ijsmodel aan het oceaanmodel gebeurt door de schuifspanningstermen aan het oceaan/ijs/atmosfeervlak. De wind brengt zowel de oceaan als het ijsveld in bewe-ging. De kracht die de wind uitoefent is afhankelijk van de fractie van ijsbedekking, en is sterker bij een dichter ijsveld. Bij eenzelfde wind zal de oceaan trager stromen dan het ijsveld. Het water onder het ijs wordt in beweging gebracht door het ijs en/of door de windactie.

In vele numerieke modellen is het nodig om het integratiedomein klein te houden wegens beperkingen in computertijd, intern geheugen of omdat de modelleerder enkel geïnteresseerd is in een lokaal fenomeen. Het rekendomein is dan kleiner dan het gehele oceaanbekken en er dienen randen ingevoerd te worden die geen fysi-sche betekenis hebben. Indien er geen goede open randvoorwaarde wordt geïmple-menteerd kan dit leiden tot foutieve oplossingen van het probleem. Een open rand-voorwaarde is een rekenkundige rand die storingen, ontstaan in het modelgebied, toelaat het domein te verlaten zonder de interne oplossing te verstoren. Perfecte open randvoorwaarden bestaan niet. Open randvoorwaarden die gebaseerd zijn op de Sommerfeld stralingsvoorwaarde werden met succes gebruikt.

Twee veel belovende implementaties van deze randvoorwaarde werden overgeno-men uit de literatuur (Orlanski's en Camerlengo-O'Brien's) en ingebouwd in een bestaand 2D dieptegemiddeld stromingsmodel om vervolgens onderworpen te wor-den aan een reeks numerieke testen. Uit de berekeningen blijkt dat de Camerlengo en O'Brien versie de beste resultaten geeft.

De voorgaande experimenten werden uitgevoerd met een vereenvoudigd model, de advectione en diffusieve termen in de vergelijkingen werden weggelaten. De numerieke formulering van de diffusieve termen op een Euler rooster levert meestal geen problemen op. De Euler benadering van de advectione termen is daarentegen ingewikkelder. Er werd daarom een numeriek experiment opgezet waarin het ge-drag van twee gekende advectione schema's (eerste orde opwaarts en QUICK schema) onderzocht werd in functie van de plaatsing van de open rand. Het numerieke experiment geeft de stroming in een goot weer achter een dam. Het is een typisch voorbeeld waar zowel advectione als diffusie belangrijk zijn. Achter de dam wordt een neer gevormd, terwijl een secundaire neer tegenover de dam ont-

staat. Als open randvoorwaarde werd de Camerlengo en O'Brien voorwaarde gebruikt. De resultaten tonen aan dat deze open randvoorwaarde de oplossing nauwelijks verstoort en dit zowel voor het geval dat de open rand buiten als ter hoogte van de neerzone geplaatst wordt.

### 3. Hydrodynamische effecten van een katabatische windopzet

Katabatische winden worden veroorzaakt door de afkoeling van lucht op een hellend met ijs bedekt terrein. Deze winden kunnen hoge snelheden bereiken in de Antarctische kustzone. Indien de winden sterk genoeg zijn, kunnen kustpolynyas ontstaan. Polynyas zijn open waterzones in een ijsveld en kunnen enkele honderden meters tot honderden kilometers groot zijn.

In dit hoofdstuk worden de resultaten gebundeld van een samenwerking tussen de KUL, de BMM en de UCL in het kader van het ANTAR project (Belgisch Wetenschappelijk Project betreffende het Zuidpoolgebied, Diensten van de Eerste Minister, Wetenschapsbeleid). Het doel van de studie is om de hydrodynamische effecten van een katabatische windopzet bij twee verschillende oceaanmodellen te bestuderen en te vergelijken en om na te gaan of katabatische winden in staat zijn om kustpolynyas te vormen. Daartoe werd een typisch kustprofiel ter hoogte van Adélieland gediscrètiseerd. Omdat een van de hoofddoelen het uitvoeren van een vergelijking tussen modellen is, worden er enkele vereenvoudigingen aangebracht, met name de barocliene effecten worden verwaarloosd. Daardoor is het mogelijk om de modelresultaten te vergelijken met een analytische oplossing (Ekman's oplossing).

De twee 2.5D modellen die deelnemen aan het experiment, lossen dezelfde vergelijkingen op maar maken gebruik van een ander numeriek schema. Het KUL model gebruikt een expliciet eindige differentie schema en beschrijft de bathymetrie met behulp van een Cartesisch rooster. Het BMM model is semi-impliciet en gebruikt  $\sigma$ -coördinaten. Verder zijn er verschillen bij de keuze van de advectione schema's, de plaats van de bodem en toplaag in het rooster en de discretisatie van zowel de advectione als de diffusieve termen aan de boven- en onderranden van het model-domein. De vergelijking van resultaten afkomstig van verschillende modellen met elkaar is belangrijk en geeft een idee van de nauwkeurigheid van het model. De uitkomst van zulk een modelvergelijking kan echter niet gebruikt worden om een uitspraak over de juistheid van de resultaten te formuleren. Dit kan enkel gebeuren door de modelresultaten te vergelijken met metingen of met een analytische oplossing.

De resultaten van de modelsimulaties tonen aan dat er globaal een goede overeenkomst is tussen de modellen en tussen de modellen en de analytische oplossing. Beide modellen simuleren een zeewaarts gericht oppervlaktestroming in de buurt van de kustlijn, wat wijst op het feit dat kustpolynyas gevormd kunnen worden. Er werden echter ook verschillen opgemerkt tussen de twee modellen onderling en tussen de modellen en de analytische oplossing. Voor de snelheden parallel met het verticale vlak zijn de verschillen klein en vooral gesitueerd in de boven- en onderlaag. In de dwarsrichting zijn er grotere verschillen opgemerkt tussen de drie oplossingen. Deze verschillen zijn het gevolg van verschillen in numerieke procedures. Om de verschillen te verklaren worden een aantal bijkomende simulaties uitgevoerd. De sensitiviteit van de modellen werd onderzocht door de tijdstap en de verticale roosterafstand te verkleinen en door de advectione en diffusieve schema's te uniformiseren. De discretisatie van de horizontale advectione en diffusieve termen heeft een geringe invloed op de oplossing. Voor een gegeven verticale roosterafstand kunnen de verschillen tussen de modellen en de Ekman-oplossing gedeeltelijk toegeschreven worden aan de waarde van de horizontale diffusie coëfficiënt. Indien deze laatste in waarde verminderd wordt, convergeert de modeloplossing naar de analytische oplossing. Uit de simulaties blijkt duidelijk dat de grootste verschillen het gevolg zijn van de discretisatie van de verticale termen in de vergelijkingen. Een verbetering van de KUL-oplossing werd bekomen door een tweede orde benadering van de diffusieve term aan het oppervlak te gebruiken. Een beduidende verbetering van beide modelresultaten kon verkregen worden door de verticale roosterafstand te verkleinen.

Het 2.5D model werd uitgebreid tot een 3D model. Het model werd toegepast op een kuststrook ter hoogte van Terra Nova (Antarctica) en de stroming tengevolge van een katabatische wind berekend. Uit de eerste resultaten blijkt ook in het 3D model dat er langsheen bepaalde kustzones sterke naar zee gerichte stromingen ontstaan. Deze stromingen kunnen verantwoordelijk zijn voor de vorming van kustpolynyas.

#### **4. Stromingen aan een ijsrand**

Het kontinentaal plat is een gebied met relatief ondiep water. Aan de rand van het kontinentaal plat treedt er een plotse verandering in bodemhelling op en vormt de overgang naar de oceanen. De stroming aan de rand van het kontinentaal plat wordt beïnvloed door de bathymetrie, de gelaagdheid en de oceaanstromingen.



Langsheen de rand kunnen, afhankelijk van de windrichting, opwaartse of neerwaartse stromingen ontstaan.

Oceanen in arctische gebieden zijn bedekt met een ijslaag. De ijsrand gedraagt zich analoog als de rand van een kontinentaal plat en kan ook opwaartse stromingen genereren. Aan de ijsrand zijn echter twee processen verantwoordelijk voor het verticaal stromingspatroon, zijnde de wind en de ijsbewegingen. De verticale beweging langsheen kontinentale platen en ijsranden heeft een grootte van ongeveer  $10^{-5}$  m/s.

Het doel van dit hoofdstuk is om de verticale beweging langsheen een ijsrand te simuleren en de interacties tussen de kontinentale plaat en de ijsrand te bestuderen met behulp van een 2.5D model. Om de verscheidene effecten, zoals bathymetrie, ijsbedekking, gelaagdheid en windopzet te begroten worden twee sets van experimenten beschreven. Het eerste experiment bestaat uit een kontinentaal plat met een constante diepte van 400m. In het tweede experiment is het kontinentaal plat verbonden met een oceaan. Voor beide experimenten is het plat bedekt met een ijslaag, die ofwel statisch is, ofwel dynamisch kan bewegen. De oceaan heeft ofwel een constante, ofwel een variabele dichtheid. De windrichting is parallel met de kust of de ijsrand. Tengevolge van de Coriolisversnelling wordt er een stroming loodrecht op de kust gegenereerd. Door de opwaartse waterbeweging wordt zwaarder water naar de oppervlakte getransporteerd langsheen de ijsrand of de kust, zodat er een horizontale dichtheidsstroming ontstaat die de verticale stroming afremt.

De op- of neerwaartse stroming langsheen de ijsrand is minder uitgesproken dan langsheen een kontinentale rand omdat de stroming zich onder het ijs voortzet. Opwaartse stroming langsheen de rand van het kontinentaal plat is sterk beïnvloed door de aanwezigheid van een ijsrand. De opwaartse stroming is kleiner in het geval van een stationaire ijsbedekking, maar wordt versterkt indien de ijslaag dynamisch kan bewegen. De initiële stratificatie vermindert de opwaartse stroming. Het zwaarder water dat aan de kontinentale rand opwaarts stroomt wordt afgeleid en versterkt de stroming aan de bodem van het plat. Niettegenstaande het model enkele vereenvoudigingen heeft (zie hoofdstuk 2) worden de processen kwalitatief goed weergegeven. De ijsrand werd door de windopzet ongeveer 16km (experiment 2) tot 24km (experiment 1) verplaatst. Zulke waarden werden ook teruggevonden in literatuurgegevens.

## 5. Cohesief sediment transport in het Scheldeëstuarium

Er zijn verschillende redenen om de slibtransporten in een estuarium te bestuderen. Sedimentatie van slib in toegangsgeulen, havens en scheepvaartgeulen heeft tot gevolg dat er frequent baggerwerken dienen uitgevoerd te worden. Slib fungeert als transportmedium voor verontreinigingen zoals zware metalen en organische stoffen. Verder vormen slibrijke sedimenten in de intertijdsgebieden van estuaria de basis voor een unieke en waardevolle ecologische leefgemeenschap. De kennis van de tijdsafhankelijke en ruimtelijke variaties van het slibtransport en de erosie en sedimentatie van slib zijn daarom niet alleen belangrijk vanuit wetenschappelijk maar ook vanuit zowel maatschappelijk als ecologisch standpunt. Slibtransportmodellen van estuaria kunnen processen, zoals erosie, sedimentatie en transport simuleren op korte tijdschalen. Lange termijn voorspellingen (1 jaar) zijn vandaag nog niet voldoende betrouwbaar. Deze modellen moeten daarom met de nodige zorg gebruikt worden, deels wegens hun beperkte voorspellingsmogelijkheden, deels wegens de complexe hydrodynamica in estuaria en gedeeltelijk wegens de onvoldoende kennis van de verdeling van het slib in suspensie en op de bodem. De betrouwbaarheid van slibtransportmodellen kan vergroot worden indien gegevens voor validatie van de resultaten beschikbaar zijn. In hoofdstukken 6 en 7 wordt aandacht geschonken aan de numerieke modellering van slibtransport in het Scheldeëstuarium. Deze modellen maken gebruik van de literatuurgegevens en metingen die in dit hoofdstuk bijeengebracht en geanalyseerd zijn.

Een estuarium wordt gewoonlijk geklasseerd volgens de menging van het zout- en het zoetwater. Men maakt onderscheid tussen een homogeen, een goed gemengd, een gedeeltelijk gemengd en een gelaagd estuarium. Het Schelde estuarium bestaat essentieel uit drie zones, met name een zone met bijna uitsluitend zoetwater (Boven Zeeschelde), een gedeeltelijk gelaagde zone (Beneden Zeeschelde en opwaarts deel van de Westerschelde) en een goed gemengde zone (afwaartse deel van de Westerschelde). Het getij, dat via de Noordzee het estuarium binnendringt, is halfdagelijks met een periode van 12 uur en 25 minuten bij gemiddeld getij. Het tijverschil en de duur van vloed en eb zijn niet constant over de lengte van het estuarium. De getijasymmetrie wordt veroorzaakt door de stelselmatige vervorming van de getijgolf tijdens haar voortplanting in het estuarium. Het gemiddeld zoetwaterdebiet in de Schelde afwaarts de Rupelmonding bedraagt  $100\text{m}^3/\text{s}$  met extreme waarden van  $20\text{m}^3/\text{s}$  tijdens de zomer en  $600\text{m}^3/\text{s}$  tijdens de winter.

Het zoutgehalte in het Scheldeëstuarium varieert tussen nul in Gentbrugge en na-

genoeg de waarde van zeewater aan de monding. Kenmerkend voor de zoutverdeling in het estuarium is het optreden van zowel langse, zijdelingse als verticale zoutgradiënten. Het langsverloop van het zoutgehalte is een functie van de bovenafvoer en van de getijactie. De bovenafvoer beperkt de zoutindringing, gedurende lage bovenafvoeren dringt de zouttong tot voorbij Rupelmonde, terwijl gedurende natte periodes de indringing van het zeewater beperkt is tot Antwerpen. De halfdagelijkse waterpeilschommelingen en de spring-doodtij tijverschil variaties geven aanleiding tot een periodieke verschuiving van de zoutindringing. Het naar opwaarts afnemend zoutgehalte veroorzaakt een langse dichtheidsgradiënt. Zijdelingse zoutgradiënten treden vooral op in gebieden met uitgesproken eb- en vloedgeulen. Belangrijk zijn de laterale gradiënten die optreden tussen de rivier en artificiële geulen (toegangsgeulen tot sluizen). Verticale zoutgradiënten zijn vooral zichtbaar in de gedeeltelijk gemengde zone en zijn het grootst tijdens hoogwater kentering.

Slibtransporten in een estuarium zijn zeer complex. De slibdeeltjes worden onder invloed van het getij opgewerveld en getransporteerd, om vervolgens tijdens kentering elders weer afgezet te worden. Afhankelijk van de plaats in het estuarium kunnen aldus opwaartse of afwaartse residuele slibtransporten optreden. Karakteristiek voor vele estuaria is het voorkomen van een zogenoemd turbiditeitsmaximum. Dit gebied met hoge slibconcentratie is voornamelijk het gevolg van de getijwerking en van dichtheidsstromingen. Het turbiditeitsmaximum is vaak gesitueerd aan het uiteinde van de zoutindringing en is als dusdanig afhankelijk van de bovenafvoer. Slib in suspensie wordt naast de ruimtelijke variatie, ook gekenmerkt door grote variaties in tijd. De verschillende tijdschalen die dienen beschouwd te worden, zijn het getij, de spring-doodtij cyclus en de seizoenen.

Om een inschatting te kunnen geven van de ruimtelijke en tijdelijke variaties in slibtransport in een deel van het Scheldeestuarium werden een aantal metingen geanalyseerd. Deze metingen verschillen in tijdsduur (6 uur tot meer dan een jaar) en in ruimtelijke spreiding (van een gedetailleerde verticale en horizontale opmeting van een dwarssectie tot een puntsmeting).

In het najaar van 1990 werden door de Antwerpse Zeehavendienst (nu afdeling Maritieme Schelde) van het Ministerie van de Vlaamse Gemeenschap twee 13-uursmetingen (snelheid, richting, zoutgehalte en slibconcentratie) uitgevoerd in een vijftal punten in een raai ter hoogte van de Drempel van Zandvliet. Het betreft één meting tijdens doodtij (27/09/90) en één tijdens springtij (04/10/90).

De snelheidsverdeling over de dwarssectie tijdens eb en vloed is verschillend. De



stroming tijdens eb volgt de hoofdgeul, terwijl de vloedstroming een maximum heeft in de Schaar van Ouden Doel. Uit de metingen blijkt dat het verloop van het zoutgehalte ongeveer 1 uur achter loopt op de waterstand. Een maximum treedt op omstreeks hoogwaterkentering en een minimum omstreeks laagwaterkentering. De minimale zoutwaarden zijn nagenoeg gelijk tijdens doottij en springtij. De maximale waarde tijdens springtij is echter  $\pm 1.5\text{g/l}$  hoger dan tijdens doottij. De verticale zoutverschillen zijn het hoogst tijdens hoogwaterkentering ( $2.8\text{g/l}$  tijdens doottij en  $4\text{g/l}$  tijdens springtij) en kennen een minimum omstreeks laagwaterkentering. Deze verticale gelaagdheid heeft een invloed op het snelheidsprofiel en veroorzaakt een naar afwaarts gerichte snelheidscomponent in de bovenlaag en een naar opwaarts gerichte in de onderlaag. De zijdelingse zoutgradiënt is het gevolg van de bathymetrie (geulen en platen) en kent een maximum omstreeks minimum zoutwaarde (laagwaterkentering).

De slibconcentratie varieert in functie van de tijd, over de verticaal en over de dwarssectie. De verticaal gemiddelde slibconcentratie bedraagt ongeveer  $60\text{mg/l}$  tijdens doottij en  $120\text{mg/l}$  tijdens springtij. De maximale concentraties treden op aan de bodem ( $\pm 120\text{mg/l}$  tijdens doottij en  $\pm 300\text{mg/l}$  tijdens springtij). De variaties kunnen gedeeltelijk gecorreleerd worden aan de snelheden. De grootste slibconcentraties treden op omstreeks één uur na hoog- of laagwaterkentering. De snelheden zijn dan groot genoeg om het slib, dat tijdens kentering afgezet werd in suspensie te brengen. Het slib dat onder deze vloeibare sliblaag ligt, heeft een grotere weerstand tegen erosie. Daardoor neemt de slibconcentratie af met toenemende snelheid. Een duidelijke afname in concentratie door sedimentatie treedt op omstreeks hoogwaterkentering. Er treedt een faseverschuiving op tussen de maximale snelheid en concentratie, wat resulteert in een hysteresis verloop van de concentratie in functie van de snelheid.

Uit de resultaten van twee andere 13-uursmetingen, gelegen ongeveer 5km opwaarts (raai Plaat van Lillo) en 3.5km afwaarts (raai Vaarwater boven Bath) van de meetraai Drempel van Zandvliet, blijkt dat de slibconcentratie naar opwaarts toeneemt.

Gedurende twee halftij metingen (vloed: 19/04/93, eb: 29/04/93) werd aan de ingang van de toegangsgeul naar de Zandvliet-Berendrechtssluisen het snelheidsprofiel met behulp van een BBADCP (Broad Band Acoustic Doppler Current Profiler) opgemeten. Tegelijkertijd werd er in een drietal punten gelegen op de raai het zoutgehalte opgemeten. De metingen toonden aan dat de stroming naar en van de toegangsgeul voornamelijk gedomineerd door dichtheidsverschillen. Het gevolg



hiervan is dat gedurende nagenoeg de volledige getijcyclus de stroming opgesplitst is in twee lagen met tegengestelde richting. Dit heel specifiek stromingspatroon is verantwoordelijk voor een hoge sedimentatie van slib in de toegangseul.

De analyse van de twee 13-uursmetingen ter hoogte van de Drempel van Zandvliet tonen het dynamische karakter van slib in suspensie aan. De slibconcentratie in een punt is een functie van lokale factoren, turbulentie, bezinking, erosie en transport. De slibconcentratie varieert in functie van de tijd (getij, spring-doodtijcyclus), over de verticale en over de dwarssectie. Om de variaties over een lange tijdspanne te kunnen inschatten, werden gedurende de periode september 1992 tot december 1993 continu zoutgehalte, temperatuur, waterstand en slibconcentratie gemeten in de tijpost van Prosperpolder. De gegevens zijn gerangschikt in functie van het tijverschil en opgedeeld in springtij, gemiddeld getij, doottij en stormvloeden. Door middelling over eb, vloed en/of getij kunnen de getijvariaties uit het signaal gefilterd worden. De voornaamste conclusies uit de analyse van deze meetreeks zijn:

Het zoutgehalte is afhankelijk van het bovendebiet. De zoutwaarde bereikt een minimum 5 dagen na het maximum in het bovendebiet. Eenzelfde zoutwaarde kan daarbij optreden voor twee verschillende debietwaarden, afhankelijk van de voorgeschiedenis. Gedurende een jaar varieert het zoutgehalte tussen 1.5g/l tijdens winter en 16g/l tijdens zomer. Deze jaarlijkse variatie heeft een verwaarloosbare invloed op de zoutvariaties die optreden tijdens een getijcyclus en tijdens een doottij-springtijcyclus. De temperatuur heeft een maximum omstreeks laagwater en een minimum omstreeks hoogwater. De seizoenen hebben een voorname invloed op de verschillen tijdens een getij. Het verschil tussen maximum en minimum temperatuur gedurende een getij is groter tijdens de winter (1.9°C) dan tijdens de zomer (1.5°C).

De langdurige meting toont aan dat de slibconcentratie op verschillende tijdschalen varieert, met name het getij, de doottij-springtijcyclus en de seizoenen. Verder worden variaties met een hoge frequentie (grootte orde 10 minuten) opgemerkt. De slibconcentratie tijdens vloed is over het algemeen groter dan tijdens eb. De verhouding tussen vloed- en ebconcentraties wordt bepaald door het tijverschil en is niet seizoengebonden. De piekconcentraties gedurende de winter zijn groter tijdens vloed dan tijdens eb. Gedurende de zomer werd het tegenovergestelde waargenomen. Een verklaring hiervoor wordt gegeven door de verschuivingen van het turbiditeitsmaximum ten gevolge van het bovendebiet. De over een getij gemiddelde slibconcentratie is 1.3 tot 1.7 keer groter gedurende een springtij dan gedurende een doottij. De slibconcentratie tijdens winter is ongeveer het dubbele van de 'zomerconcentratie'. Hiervoor zijn verschillende verklaringen geformuleerd,

zijnde een verschuiving van het turbiditeitsmaximum in functie van het bovendebiet, een hoger sedimenttransport gedurende de winter ten gevolge van een verminderde biologische activiteit en een grotere bodemerosie in het Scheldebekken.

Snelheid, sedimentconcentratie, zoutgehalte en temperatuur variëren duidelijk in functie van het getij. Slibconcentratie, zoutgehalte en natuurlijk temperatuur vertonen daarenboven variaties met de seizoenen. De invloed van de seizoenen is direct gecorreleerd met de klimatologische cyclus. De invloed van de seizoenen op de slibconcentratie en het zoutgehalte is echter indirect door biologische activiteit, regen en landerosie. Voor een verdere kwantificatie van deze variaties en het opstellen van algemene regels en correlaties is het nodig om talrijker en meer en volledige veldmetingen uit te voeren.

## 6. Een 2D model voor cohesief sedimenttransport

Transport van slib wordt bepaald door de uitzakking van slibdeeltjes en door erosie en sedimentatie ten gevolge van de heersende bodemschuifspanning. Het volledige proces van erosie, transport, uitzakken, afzetting en consolidatie is complex, wegens de cohesieve eigenschappen van het slib. Het uitzakken van slibdeeltjes wordt bepaald door de zwaartekracht, de turbulentie en de interactie tussen de slibdeeltjes. De valsnelheden kunnen daarbij variëren tussen een grootte-orde van  $10^{-4}$  en 1mm/s en zijn een functie van de slibconcentratie, de fysico-chemische eigenschappen van het water, de slibsamenstelling en het snelheidsveld. Voor concentraties kleiner dan 5-10g/l zijn de interacties tussen partikels klein en is de valsnelheid onafhankelijk van de concentratie. Sedimentatie is het proces waarbij slibdeeltjes zich vasthechten aan de bodem. Afzetting treedt op als de bodemschuifspanning kleiner is dan een kritische waarde. In het 2D model wordt afzetting berekend met de formule van Krone. Erosie wordt gedefinieerd als het proces dat slibdeeltjes terug in suspensie brengt. De bodemschuifspanning is de voornaamste hydrodynamische factor die de resuspensie bepaalt. De weerstand tegen erosie is een functie van de sedimentsamenstelling, de eigenschappen van het poriënwater, de biologische activiteit in het slib en de wijze hoe het sediment afgezet en geconsolideerd is. De hoeveelheid slib die in suspensie gebracht wordt, is afhankelijk van de kritische schuifspanning voor erosie en de bodemschuifspanning.

Wegens de complexiteit van de processen die slibtransport beschrijven, is er tot nu

toe nog geen volledig systeemmodel ontworpen. In het kader van het MAST G8 Coastal Morphodynamics onderzoeksproject werd een vergelijking van modelberekeningen met laboratoriummetingen uitgevoerd. Het 2D slibtransportmodel TRASIL lost de 2D dieptegemiddelde transportvergelijking op met behulp van een Lagrange techniek. De diffusieve termen werden ingevoerd door een zogenoemde 'random walk' techniek.

De laboratoriummetingen werden door SOGREAH ter beschikking gesteld en werden uitgevoerd in een ovale stroomgoot van 1m breedte, 0.4m diepte en een totale lengte van 84m met twee rechte stukken van 30m en twee bochten van 180° en 12m lengte. Het waterpeil werd constant gehouden gedurende de experimenten. De stroming werd gegenereerd door een Archimedes-schroef, die geplaatst werd in één van de rechte stukken. De snelheids- en slibconcentratietingen werden uitgevoerd in de middellijn van het andere recht stuk. De stroomgoot werd gevuld met slib, dat gedurende een tijdspanne van 0.25 tot 7.6 dagen de mogelijkheid kreeg om te consolideren. Dit komt overeen met een gemiddelde droge dichtheid van 98 tot 309kg/m<sup>3</sup> en een laagdikte van 97 tot 32mm. Er werden twee reeksen van simulaties uitgevoerd. In de eerste werd de erosie van slib onderzocht door de snelheid stapsgewijs te vergroten. In de tweede reeks van experimenten werd de stroming gealterneerd, zodat erosie, sedimentatie en resuspensie bestudeerd konden worden.

De slibbodem is gediscrètiseerd en ingevoerd in het model. De kritische schuifspanning voor erosie is vervolgens uitgedrukt als een functie van de dichtheid van het slib. Uit de erosietesten blijkt dat de modelresultaten beter overeenkomen met de metingen bij een korte tot middellange consolidatieperiode. Bij een lange consolidatietijd van het slib treden er grote verschillen op. De belangrijkste conclusies uit de experimenten kunnen als volgt geformuleerd worden:

De beschikbare erosie en sedimentatiewetten geven een adequate beschrijving van de fundamentele processen in permanente en niet-permanente stroming.

Kwantitatieve verschillen tussen de modelresultaten en de metingen wijzen erop dat de dichtheidsstructuur van de bodem en de resuspensie van verse slibdeeltjes de sleutelparameter zijn.

De bodemschuifspanning is de aandrijving voor erosie en sedimentatie. De kritische schuifspanning voor erosie is een functie van de bodemdiepte en de consolidatietijd. De numeriek beschrijving van het bodemdichtheidsprofiel is van cruciaal belang om de kritische schuifspanning voor erosie te bepalen.

Het 2D slibtransportmodel TRASIL is samen met nog twee andere slibtransportmodellen toegepast op een deel van de Beneden Zeeschelde, met name het gebied



gelegen tussen het baken Meestooft en een raai ter hoogte van Bath. De bathymetrie van het modelgebied is afgelezen van de dieptekaarten opgesteld door de Antwerpse Zeehavendienst. Om het slibtransport te kunnen berekenen dienen er snelheids- en waterstandsgegevens beschikbaar te zijn. Een bestaand 2D dieptegemiddeld hydrodynamisch model werd gebruikt om het stromingsveld te simuleren.

Afijking van het model omvat het proces van parameterschatting en dient om de modelresultaten in overeenstemming te brengen met metingen. Verder dient de afijking om een idee te bekomen van de sensitiviteit van de verscheidene parameters. Om een slibtransportmodel af te ijken moeten er metingen en gegevens beschikbaar zijn omtrent slibconcentratie en slibverdeling en -samenstelling op de bodem en moeten de erosie en sedimentatieparameters gekend zijn. Voor de Beneden Zeeschelde zijn weinig consistente meetgegevens beschikbaar. Uit literatuurgegevens en uit de metingen beschreven in hoofdstuk 5, werd een inschatting gemaakt van de waarde van de verschillende parameters. Uiteindelijk werden de volgende waarden weerhouden: valsnelheid 2mm/s, kritische schuifspanning voor erosie 0.4Pa, kritische schuifspanning voor sedimentatie 0.2Pa en de erosieconstante 0.05g/m<sup>2</sup>s.

De resultaten van de drie slibtransportmodellen tonen aan dat het slibtransport kwalitatief goed weergegeven wordt. De verschillen tussen de modelresultaten zijn het gevolg van numerieke verschillen, met name de waarde van de diffusiecoëfficiënt. De simulaties hebben aangetoond dat de nauwkeurigheid van de resultaten beperkt wordt door de hydrodynamische gegevens. De hoge sedimentatie in de toegangsgeul, zoals waargenomen in natuur, kan niet berekend worden met een 2D model, tenzij men de diffusieparameter 'overcalibreert'.

## **7. Sedimentatie van slib in een toegangsgeul**

De sluizen van Zandvliet en Berendrecht, gelegen ter hoogte van de Drempel van Zandvliet in de Beneden Zeeschelde, vormen de meest belangrijke aanlooproute tot de haven van Antwerpen. De sluizen zijn met de Schelde verbonden door een toegangsgeul. De stroming in de toegangsgeul is complex en uitgesproken driedimensionaal. Door de lage stroomsnelheden is de toegangsgeul een preferentieel gebied voor de sedimentatie van slib.

Bij de wateruitwisseling tussen de Schelde en de toegangsgeul spelen verschillende fenomenen een rol. Ten eerste zorgt de getijwerking voor de vulling en lediging van de toegangsgeul. De stroming in de Schelde geeft aanleiding tot de vorming van



een horizontale neer aan de ingang van de toegangsgeul. Verder veroorzaken zoutverschillen tussen de rivier en de toegangsgeul en de aanvoer van zoeter water door versassing van schepen een dichtheidsstroming. Tenslotte wordt de horizontale stroming afgebogen door de aanwezigheid van de verticale kaaimuren, dit resulteert in de vorming van een verticale neer.

Een gedetailleerd inzicht in de stroming in de toegangsgeul kan bekomen worden door metingen in situ en met behulp van numerieke modellen. De zoutverdeling wordt gewoonlijk gekarakteriseerd door enerzijds een vermindering van de turbulentie door de verticale gelaagdheid en anderzijds door de stroming ten gevolge van de horizontale dichtheidsverschillen. Dit complex en driedimensionaal fenomeen waarbij de stroming en de dichtheid dynamisch gekoppeld zijn, kan enkel gesimuleerd worden met een driedimensionaal model dat rekening houdt met een koppeling tussen stroming en zouttransport. Ook maakt de complexe aard van de stroming in en rond de toegangsgeul het gebruik van een driedimensionaal model noodzakelijk.

De resultaten van het hydrodynamisch-numeriek model worden gebruikt als invoer voor het 3D slibtransportmodel. Het model omvat een deel van de Schelde van nagenoeg 8.5km lengte afwaarts begrensd ter hoogte van de Belgisch-Nederlandse grens, opwaarts ter hoogte van Doel. De bathymetrie is gediscrètiseerd op een rechthoekig equidistant rooster met een cellengte van 50m. De verticale lagen hebben een dikte van minimum 3m dikte. Op ondiepe plaatsen ( $< -12\text{m TAW}$ ) wordt de onderste laag stelselmatig uitgeschakeld, de nieuwe bodemlaag vergroot dan om de juiste diepte te behouden. De dikte van de bovenlaag verandert met het getij, tijdens springtij is dit dan b.v. tussen ongeveer 3m bij laagwater en 9m bij hoogwater. Deze relatief grove verticale resolutie is voldoende voor de Schelde omdat er geen duidelijk afgelijnde grens bestaat tussen zoet en zout water. Het model omvat zowel gesloten randen (oevers, kaaimuren) als open randen. Langs de gesloten randen wordt er een 'free slip' conditie toegepast. Aan de afwaartse open rand, ter hoogte van de Belgisch-Nederlandse grens wordt een waterstand opgelegd, terwijl aan de opwaartse rand (ter hoogte van Doel) het model aangedreven wordt door een snelheidsrandvoorwaarde. Tevens moet aan beide open randen een zoutwaarde opgelegd worden.

De twee datasets van de 13 uursmetingen ter hoogte van de Drempel van Zandvliet (zie hoofdstuk 5) zijn gebruikt voor de calibratie en validatie van het model. Uit deze vergelijking blijkt dat de gemeten verticaal gemiddelde snelheid goed overeenstemt met de snelheid in de bovenste lagen van het model. Daarnaast blijkt dat het snelheidsprofiel afwijkt van het klassieke snelheidsprofiel: aan het oppervlak is een opwaartse component waarneembaar. Dit veroorzaakt tijdens vloed een

afname van de snelheid aan de oppervlakte en tijdens eb een toename ervan. Deze verandering van het snelheidsprofiel wijst duidelijk op de aanwezigheid van een horizontale dichtheidsgradiënt. Door de aanwezige verticale gelaagdheid van het zoutgehalte omstreeks hoogwaterkentering is de stroming in de bovenlaag afwaarts gericht terwijl in de onderlaag het zoutere water nog naar opwaarts stroomt. De bovengenoemde bevindingen worden ook teruggevonden in de meetresultaten.

De berekende snelheden aan de ingang van de toegangsgeul worden vergeleken met de BBADCP metingen. Aangezien op deze meetdagen de getijomstandigheden, de zoutvoorwaarden en de bathymetrie verschilden van de calibratieomstandigheden, is een gedetailleerde vergelijking onmogelijk. Bovendien bestaat de verticale resolutie van het 3D model slechts uit vier lagen, terwijl door de BBADCP metingen werden uitgevoerd elke 0.5m wat resulteert in een veel fijnere weergave van de verticale snelheidsstructuur dan in het model. Niettemin kan worden gesteld dat de stroming kwalitatief en kwantitatief goed wordt berekend in het model.

De stroming in de toegangsgeul is zowel bij spring- als bij doottij alsook bij verschillende zoutgradiënten in de Schelde klein. Dit betekent dat het water dat de toegangsgeul binnenkomt of verlaat nooit snel genoeg stroomt om erosie van slib te kunnen veroorzaken.

Door het in- en uitstromend debiet door de meetraai aan de ingang van de toegangsgeul te integreren over een getij wordt het totaal volume instromend water berekend. Een vergelijking met het getijvolume laat toe om na te gaan in welke mate de horizontale wateruitwisseling, als gecombineerd effect van neervorming en dichtheidsstroming, de dominerende factor is.

Tijdens springtij bedraagt de wateruitwisseling als gevolg van het getij (komberging)  $1.88 \times 10^6 \text{ m}^3$  en bij doottij  $1.40 \times 10^6 \text{ m}^3$ , terwijl de totale wateruitwisseling (komberging + horizontale uitwisseling) ongeveer  $20 \times 10^6 \text{ m}^3$  bedraagt. De totale wateruitwisseling (neer en zoutgradiënt) is een factor 10 tot 12 groter dan de verticale (komberging). Vroegere analyses voor de toegangsgeul van de Zandvlietsluis geven een verhouding aan van 20 tot 25. De grootte van de horizontale zoutgradiënt heeft een invloed op de totale wateruitwisseling. Bij een lagere zoutgradiënt is de uitwisseling van water tussen de toegangsgeul en de rivier met ongeveer 16% en zonder saliniteitsgradiënt met ongeveer 50% verminderd t.o.v. de toestand bij een hoge gradiënt. De dichtheidseffecten veroorzaakt door de aanwezigheid van een horizontale zoutgradiënt spelen een voorname rol bij de wateruitwisseling tussen de toegangsgeul en de rivier. De zoutwaarde heeft een grotere invloed dan de tijverschillen. Zo is bij doottij met een hoge zoutwaarde de wateruitwisseling groter dan bij springtij met een lage zoutwaarde. De gemiddelde hoeveelheid water (overeenkomend met halftij) in de toegangsgeul tijdens springtij

bedraagt ongeveer  $5.5 \times 10^6 \text{ m}^3$  en tijdens doortij ongeveer  $5.2 \times 10^6 \text{ m}^3$ . Dit betekent dat tijdens een springtij bij een hoge saliniteit het water 3.6 keer 'ververst' wordt. Tijdens een springtij bij een lage saliniteit is dit 3.0 keer en tijdens een doortij bij een hoge saliniteit 3.3 keer. Tijdens een springtij zonder zoutgradiënten wordt het water slechts 1.7 keer ververst.

In de toegangsgeul is de structuur van het stromingsprofiel complex. De aanwezigheid van een neer, gecombineerd met de wateruitwisseling ten gevolge van dichtheidsverschillen maakt dat in de toegangsgeul de stroming in de boven- en de onderlaag meestal in tegenovergestelde richting staat. De dikte van deze lagen is niet eenduidig definieerbaar, maar verandert in de loop van het getij. De stroming bij afwezigheid van een zoutgradiënt is nagenoeg constant over de verticaal zodat er geen tweelagen-stroming meer optreedt.

De resultaten van het hydrodynamisch numeriek model worden gebruikt als invoer voor het 3D slibtransportmodel. Uit de modelresultaten blijkt dat tijdens een springtij met een hoge zoutgradiënt er in de toegangsgeul ongeveer  $4.6 \text{ kg/m}^2$  slib per dag sedimenteert. De jaarlijkse hoeveelheid slib die neerslaat in de toegangsgeul is dan gelegen tussen 1.1 en 2.3 miljoen  $\text{m}^3$ . Deze waarde stemt overeen met de baggergegevens. Uit de resultaten blijkt verder dat de hoeveelheid afgezet slib afneemt met dalend tijverschil. De hoeveelheid sedimentatie wordt echter sterk beïnvloed door de aanwezige zoutgradiënt. Zo wordt bij een dalende zoutgradiënt het slib minder ver in de geul afgezet. Indien er geen zoutverschillen zouden zijn in de Schelde, daalt de sedimentatie in de toegangsgeul met nagenoeg 50% en wordt al het slib aan de ingang van de geul afgezet.

## 8. Conclusies

Het hoofddoel van deze thesis is de simulatie van de hydrodynamica en het cohesief sedimenttransport in kustzeeën en estuaria. De numerieke modellen die ontworpen of gebruikt werden, zijn voorgesteld en enkele toepassingen zijn uitgewerkt. Een belangrijk deel van de thesis is gewijd aan validatie van de modellen, door de modelresultaten te vergelijken met analytische oplossingen, met andere modelresultaten of met metingen. In wat volgt zullen een kort overzicht en de belangrijkste conclusies gegeven worden.

In hoofdstuk 2 is een 2.5D ijs-oceaan model voorgesteld. Het model beschrijft de hydrodynamica en de ijsdynamica in een verticaal vlak, waarbij verondersteld wordt dat alle gradiënten loodrecht op dit vlak gelijk zijn aan nul.



Open randvoorwaarden zijn nodig als het modelgebied kleiner is dan de dimensies van het oceaانبekken. Het doel van open randvoorwaarden is om storingen, die in het binnenste van het domein gegenereerd worden, toe te laten het domein te verlaten zonder dat de oplossing verstoord wordt. Uit een tweetal numerieke testen blijkt dat de Camerlengo and O'Brien randvoorwaarde, die gebaseerd is op de Sommerveld stralingsvoorwaarde, de beste resultaten geeft en dit zowel voor stromingen veroorzaakt door windopzet, als in advection-diffusie gedomineerde stromingen.

De stroming veroorzaakt door katabatische winden in de Antarctische kustzone wordt beschreven in hoofdstuk 3. Twee verschillende 2.5D oceaan modellen hebben deelgenomen aan een modelvergelijking, waarbij tevens de modeloplossingen vergeleken worden met een analytische oplossing. De resultaten tonen aan dat er een goede overeenkomst is tussen de modellen en dat er in de nabijheid van de kust beide modellen een zeewaartse stroming berekenen. Deze kuststroming geeft een aanwijzing dat kustpolynyas kunnen ontstaan door katabatische winden. De verschillen tussen de modelresultaten zijn het gevolg van numerieke verschillen, met name andere advection en diffusie discretisaties. Het 2.5D model werd uitgebreid tot een volledig 3D model en toegepast op een kuststrook ter hoogte van Terra Nova.

In hoofdstuk 4 wordt de opwaartse stroming langsheen de rand van een kontinentaal plat, bedekt met een ijslaag beschreven. De respons van de oceaan is duidelijk verschillend indien men met of zonder ijsdynamica rekent. De op- of neerwaartse stromingen langsheen een ijsrand zijn minder uitgesproken dan langsheen een continentale rand. De verticale stroming langsheen de rand van het kontinentaal plat wordt verminderd door de aanwezigheid van een stationaire ijsbedekking en wordt vergroot indien het ijs kan bewegen.

Hoofdstuk 5 beschrijft het cohesief sedimenttransport in een deel van de Beneden Zeeschelde met behulp van enkele metingen. De metingen verschilden in duur en in resolutie. Uit de metingen blijkt dat de snelheid, het zoutgehalte, de slibconcentratie en de temperatuur duidelijk variëren in functie van het getij en de doodspringtij cyclus. Slibconcentratie, temperatuur en zoutgehalte vertonen verder een duidelijk correlatie met de seizoenen. De invloed van de seizoenen kan verklaard worden door variaties in temperatuur, biologische activiteit, bovendebiet en landerosie. Het turbiditeitsmaximum is gelegen in de Beneden Zeeschelde, de juiste plaats is echter afhankelijk van het bovendebiet. Een deel van de waargenomen



seizoengebonden slibconcentratievariaties kan toegeschreven worden aan een verschuiving van het turbiditeitsmaximum onder invloed van het bovendebiet.

In hoofdstuk 6 komt de numerieke modellering van slibtransport aan bod. Een bestaand 2D verticaal gemiddeld slibtransportmodel (TRASIL) werd hiervoor gebruikt. Het model lost de transportvergelijking, uitgebreid met de nodige bron en verliestermen op, met behulp van een Lagrange techniek. Het model werd uitgebreid om diffusieve processen te simuleren, door een 'random walk' model te implementeren. Afijking en validatie van een cohesief sediment transport model is een moeilijke taak. De klassieke twee-staps afijking-validatie procedure lijdt niet noodzakelijk tot nauwkeurige resultaten. Het validatie-experiment, dat in het hoofdstuk beschreven wordt, is een waardevolle stap om tot een kwantificatie van de nauwkeurigheid van deze modellen te komen. Uit de modelresultaten blijkt dat de beschikbare erosie en sedimentatiewetten een adequate beschrijving van de fundamentele processen in permanente en niet permanente stroming geven. De gevonden afwijkingen kunnen voor een groot deel worden toegeschreven aan de beschrijving van het dichtheidsverloop in de bodem en de resuspensie van 'verse' slibdeeltjes.

Het 2D slibtransportmodel TRASIL wordt samen met twee andere slibtransportmodellen toegepast op een deel van de Beneden Zeeschelde. De resultaten van de drie slibtransportmodellen tonen aan dat het slibtransport kwalitatief goed weergegeven wordt. De verschillen tussen de modelresultaten zijn het gevolg van numerieke verschillen, met name de waarde van de diffusiecoëfficiënt. De simulaties tonen aan dat de nauwkeurigheid van de resultaten beperkt wordt door de hydrodynamische gegevens. De hoge sedimentatie in de toegangsgoed, zoals waargenomen in natuur, kan niet berekend worden met een 2D model, tenzij men de diffusieparameter 'overcalibreert'.

De metingen, beschreven in hoofdstuk 5, hebben aangetoond welke processen verantwoordelijk zijn voor de sedimentatie van slib in de toegangsgoed tot de Zandvliet- en Berendrechtstuizen. Het zoutverschil tussen de rivier en de toegangsgoed is daarbij de belangrijkste factor, naast getijeffecten, neervorming en randeffecten. Deze effecten kunnen enkel met een 3D model berekend worden. Een gedetailleerde beschrijving van de stroming en het sedimenttransport met behulp van metingen en numerieke modellen vormt het onderwerp van hoofdstuk 7. In de toegangsgoed is de snelheidsverdeling over de verticaal complex. De aanwezigheid van een neer, gecombineerd met de wateruitwisseling ten gevolge van dichtheidsverschillen maakt dat in de toegangsgoed de stroming in de boven- en de onderlaag meestal

in tegengestelde zin staat. De resultaten van het hydrodynamisch numeriek model worden gebruikt als invoer voor het 3D slibtransportmodel. Uit de modelresultaten blijkt dat tijdens een springtij met een hoge langse zoutgradiënt in de Schelde er in de toegangsgeul ongeveer  $4.6\text{kg/m}^2$  slib per dag sedimenteert. De hoeveelheid sedimentatie wordt sterk beïnvloed door de aanwezige zoutgradiënt. Zo wordt bij een dalende zoutgradiënt het slib minder ver in de toegangsgeul afgezet. Indien er geen dichtheidsverschillen zouden zijn in de Schelde, daalt de sedimentatie in de toegangsgeul met nagenoeg 50% en wordt al het slib aan de ingang van de geul afgezet.



## CHAPTER 1

### OBJECTIVES AND SCOPE OF THE STUDY

#### 1.1. Introduction

The major part of the surface of our planet (i.e. the first few kilometres) consists of water. Water forms river, lakes and oceans. In contrast with the known celestial bodies, the earth is the only place where water is occurring in its liquid state. Water is never pure because it interacts with the solid matter in a variety of ways. Matter can be or in solution in the water (salt) or be transported as solid particles (suspended sediments). Water occurring on earth is in motion. The circulation in oceans and shelf seas is due to two forcing mechanisms, the first one resulting from the energy input in the form of solar radiation (direct as heating of the sea water and indirect as wind stress exerted on the sea surface or atmospheric pressure) and the second one due to (mainly) the simultaneous action of the moon's, sun's and earth's gravitational forces, and the revolution about one another of the earth and moon and the earth and sun. In rivers the main driving force is through gravity due to the slope of the bed.

A large amount of human activities related to water is situated in the very narrow regions of continental shelves and estuaries. Continental shelves are shallow compared to the oceans as they are a part of the continental plates. The shelves are connected to the ocean by a sudden change in bathymetry called the shelf break. This sudden change in bathymetry at a continental margin forms a kind of barrier for the ocean currents and can result, depending on the direction of the currents, in upwelling along the shelf break. Upwelling in oceans is usually induced by wind blowing over the water surface (O'Brien et al., 1977). Oceans at high latitudes are



seasonally covered with sea ice. Along the ice edges oceanic frontal systems occur due to large horizontal density gradients created by melting or freezing or by wind forcing and can result in local up- or downwelling. Marginal ice zones are those regions where sea ice merges into open water. It is in these regions that the ice-ocean and atmosphere system is in non-equilibrium resulting in a highly dynamic system. Marginal ice zones are characterised by strong gradients in physical and biological parameters (Niebauer and Smith, 1989). One of the oceanic features providing the enhanced primary production is upwelling.

Estuaries are places where rivers meet the sea and are as such influenced by the motion in the sea and by the river flow. This creates a specific environment where fresh water is gradually mixed with salty water. Salt water enters the estuary during flood. The salinity at a certain point is varying according to the tide, with maximum salinity occurring at about the time of high water slack. Salinity variations cause variations in density of the water. Density differences are responsible for density induced circulations. The most direct consequence of the salinity intrusion is its effect on the distribution of cohesive suspended sediments and the deposition of mud. A characteristic feature of estuaries is the occurrence of a turbidity maximum. The upstream bottom flow as a result of the density induced circulation, moves sediments landward until the head of the salt intrusion. The sediments in the bottom flow are mainly from marine origin, whereas in the top layers sediments from riverine origin are found. The turbidity maximum is often situated at the landward side of the salt intrusion. In this zone, the much higher concentrations of suspended sediments are due to a number of factors, among which the residual circulation, the availability of cohesive sediments, the distortion of the tidal wave and flocculation. In the turbidity maximum high rates of deposition occur, which can cause problems of shoaling and necessitates dredging to keep the estuary or harbour navigable.

## 1.2. Objectives

Throughout the last decades numerical models have been extensively used to study ocean, shelf seas and estuaries. In the past much of what was known about the aquatic environment was the result of field measurements and observations. The success of numerical models is mainly due to the evolution of computers but can also be explained by the fact that they are based on physical laws which describe the motions in detail. Some processes (e.g. cohesive sediments) are not known in

detail while others cannot be incorporated in the model due the very small time and length scales (turbulence) and have to be introduced by simplification or parameterization. Mathematical models are using numerical techniques to solve the hydrodynamic equations. The hydrodynamic equations can be used in their original form or can be simplified and reduced to a set of equations with less unknowns. The simplifications or approximations which can be used depend on the phenomena which we want to model. The resulting partial differential equations usually cannot be solved directly and are therefore discretised in order to solve them numerically. The numerical techniques (e.g. finite differences or finite elements) have to be such that the resulting 'numerical' equations are accurate, consistent and guarantee convergence.

The main objective of this research is to develop and apply numerical models for the simulation of currents and transport phenomena (salinity and sediments) in shelf seas and in estuaries. In the thesis we have restricted ourselves to the study of cohesive sediments. This does not mean that non cohesive sediments are of lesser importance but especially for the case study (Scheldt estuary) the cohesive sediments form a major problem for navigation and pollution.

Three aspects of modelling, which are closely related, are highlighted. The first one focuses on the numerical aspects (finite difference techniques, open boundary condition and advection schemes), the second deals with comparing the model results with those of other models, with analytical solutions and with field measurements, while the third one describes some applications. All these aspects are a part of the model validation process. A recently published book by the AGU (1994) is dedicated to model validation. Validation is defined by Dee (1994) as *'the process of formulating and substantiating explicit claims about applicability and accuracy of computational results, with reference to the intended purposes of the model as well as the natural system it represents'*. Following this definition validation consists of a wide range of activities. Model validation is a continuous process and as such never finished. It will lead to a more accurate model and to a better evaluation of the constraints and the predictive capacities of the model. In this thesis we will focus on the following techniques to test the quality of a numerical model:

- using numerical test cases to check some specific features of the computational results,
- comparing the model results with analytical solutions,
- intercomparison with other numerical models,
- comparing the model results with measurements.

The first step in model validation, previous to the above listed ones, consists in defining a test case. This step is general and is not depending on how complicated the validation experiment is. Setting up a test case can be defined as the process of information collection in view of designing the validation experiment. This action constitutes of establishing a framework in which some specific or general features of the numerical model can be validated and to define the initial and boundary constraints which limit the generality of the test case.

Two numerical test cases have been setup to check the quality of some radiation open boundary conditions (Orlanski's and Camerlengo and O'Brien's) and advection schemes (Chapter 2). The correct definition of the open boundary condition is of great importance since it determines or influences the interior solution. In the first numerical test case the two above mentioned open boundary conditions have been implemented in a simplified numerical model (no advective and diffusive terms) and have been used in three different situations. The results of have indicated that the Camerlengo and O'Brien condition is performing better. This open boundary condition has then been used in a second test case where specifically the behaviour of it in a advection-diffusion dominated flow problem has been analyzed. The radiation open boundary condition is applied when surface gravity waves occur. In the case of a rigid lid, where these waves are filtered out, the condition at the open boundary is simplified and can be calculated by assuming that the gradient of the open boundary variable is equal to zero.

The hydrodynamic and transport equations are partial differential equations for which no analytical solution exists except for some simplified cases. The analytical solution of Ekman for the hydrodynamic equation has been used to evaluate the 2.5D model results forced by a katabatic wind. The results are described in Chapter 3.

Intercomparison exercises, involving different models, have been proved to be highly valuable as a tool for model validation (see e.g. Yu et al. 1989). Intercomparison of model results can involve different stages as is shown in the thesis. The 2.5D ocean model has been applied to a test case and the results have been compared to those of another model (Chapter 3). Five mud transport models have been used in an intercomparison exercise to simulate a laboratory test case. The conclusions are briefly presented in Chapter 6. In the same chapter three different mud transport models, applied to an actual estuarine problem, are involved in an intercomparison exercise.



Comparison of a numerical model with measurements involves at least two independent data set. The first step is necessary to adjust the model parameter in order to reproduce the measurements (calibration). The second step consists of the validation (in the sense of comparing the results with observations) of the model by simulating another situation using the previous determined parameters. This simple two step calibration - validation procedure has been successfully used in hydrodynamic models (see Chapter 7) but has its limitation in case of cohesive sediment transport. The reason for this is due to the various processes involved, such as erosion, transport, aggregation, settling, deposition and consolidation. Up to now these processes are considered as different process models. A proper integration into a system model asks for detailed knowledge of the processes and their interactions. This can only be achieved through intensive field and laboratory experiments and measurements. Chapter 5 has been devoted to a detailed description of field measurements and observations of cohesive suspended sediments in the Scheldt estuary. This chapter is intended to presents a framework for future measurements needed for calibration purposes of numerical models. In Chapter 6 the results of the TRASIL transport model are compared to the measurements of a laboratory model. The advantage of a laboratory test case is, that a more or less consistent set of various measurements is available.

### 1.3. Structure Of The Text

In *Chapter 2* the formulation of the conceptual and numerical 2.5D ice-ocean model is presented. The model is called 2.5D because it solves the 3D hydrodynamic equation assuming that the derivatives in one of the horizontal coordinate direction are zero so that the domain of integration can be reduced to a vertical plane. The main advantage of a 2.5D model compared to a 3D model is that the CPU-time is small. The program can therefore be run on a PC or a workstation in a reasonable amount of time. The governing equation for the hydrodynamics and ice dynamics cannot be solved analytically, except for some simplified examples. Therefore numerical techniques are commonly used in order to solve the equations. The numerical technique used is the finite difference technique. A description of the ocean model can be found in § 2.2., the ice model is presented in § 2.3.

The domain of integration is very often smaller than the ocean basin and non physical boundaries have thus to be introduced. Numerically this means that an open boundary condition has to be implemented. The choice of the open boundary condition has a very important influence on the solution. In § 2.5. a short literature



review of the most promising open boundary conditions is presented. These open boundary conditions have been implemented in an existing 2D depth averaged hydrodynamic model (Moelans and De Bruyn, 1986) and have been validated by applying the model to some well defined test cases. In agreement with literature, the Camerlengo and O'Brien condition gave the best results. This open boundary condition has therefore been implemented in the ocean model presented and developed in § 2.2. One of the important points during development of a numerical model consists in choosing an accurate and stable numerical scheme for solving the advection terms. A detailed analysis of various advection schemes has been carried out by Yu (1993). In § 2.6. the results of a numerical simulation of a backward facing step (typical example where advection and diffusion plays an important role) in a long channel with the upstream and downstream boundaries open are presented. The aim of this experiment was to investigate the quality of the results as a function of the advection schemes (1<sup>st</sup> order upstream or QUICK) and of the open boundary condition. The length of the domain has been varied in such a way that the open boundary was situated either outside or inside the influence zone of the backward facing step. It was found that the Camerlengo and O'Brien open boundary condition gave good results also when the boundary had been placed in the eddy zone.

In Chapter 3 and 4 the 2.5D model is applied to an (idealized) ocean. *Chapter 3* will discuss the model results of an ice free ocean forced by a katabatic wind. This chapter is the result of the collaboration of the KULeuven, the MUMM and the UCLouvain in the framework of the Belgian Scientific Program on Antarctic. The main goal of the simulations was to carry out an intercomparison of two different 2.5D ocean models applied to the Adélie Land coastal area. The model results have shown that polynyas (open water zones in an ice covered ocean) can be formed by katabatic winds. The preliminary results of a 3D model of the Terra Nova coastal area forced by a katabatic wind show that near the coast strong offshore currents are formed.

In *Chapter 4* some applications are shown where the ocean is covered by an ice layer. The wind blowing over the ocean and the ice will induce up- or downwelling along the ice edge, depending on the direction and the dynamics of the ice layer. Ice edge upwelling has first been reported by Buckley et al. (1979) during a measurement campaign in the Arctic ocean. Numerical studies dealing with ice edge upwelling are usually situated in shallow shelf seas. The applications therefore deals with the behaviour of an ocean in the vicinity of an ice edge and a

continental slope.

The subject of *Chapters 5 to 7* is the study of mud transport in a part of the Scheldt estuary, more precisely in the 'Beneden Zeeschelde' (between Antwerp and the Belgian-Dutch border) using field measurements and numerical models. Numerical models of mud transport should be used with care, reasons for this are given by the limited predictive capabilities of such models, by the complex nature of the hydrodynamic conditions in the estuary and by the lack of knowledge of the distribution of mud in suspension and on the bottom. The need for detailed knowledge of cohesive sediment and hydrodynamic processes has arisen because of the increasing use of numerical models as management tools. The accuracy and reliability of these models can only be increased if data for refinement and for validation are available.

In order to illustrate and explain the great variations in mud concentration found in the Scheldt estuary the results of some field measurements will be presented in *Chapter 5*. Some of these observations have been used to calibrate and validate the numerical models used in Chapters 6 and 7. The mud transport is simulated using a 2D and a 3D model.

In *Chapter 6* the 2D transport model TRASIL is presented. TRASIL is a Lagrangian model and has been developed by Praagman (1986). The model has been validated by comparing the model results to the data obtained from a laboratory model. The validation experiment has been carried out as a part of the MAST G8 research program and has been the subject of an intercomparison exercise. This experiment has shown that the model is able to reproduce qualitatively and quantitatively well the observations, but that even using the controlled validation data of a laboratory model, the predictive capability of the model suffers from a good description and integration of the various physical processes which govern the transport (i.e. erosion, deposition, consolidation, rheological properties). The 2D mud transport model has then been applied to a part of the 'Beneden Zeeschelde'. The model is able to reproduce qualitatively well the sedimentation patterns of cohesive sediments, with regard to the known distributions of mud on the bottom of the estuary (Bastin, 1988; Bastin and Belmans, 1988). The results of the model have been compared to the results of two other mud transport models (Pathirana, 1994; Jabbari, 1994). Differences between the models have been found and explained as being due to numerical factors and due to diffusion. Diffusion was not incorporated in TRASIL and has therefore been implemented using the so-called random

walk method. Simulations with diffusion incorporated give results which are similar to the one obtained by the other models.

The measurements described in Chapter 5 have indicated that density induced currents play an important role, especially in the access channels to the harbour of Antwerp. A 2D depth averaged hydrodynamic model is not able to simulate these currents, therefore a 3D model has been set up. The 3D model which has been used for the study of cohesive sediment transport in the access channel is the 3D tideflow and mudflow model of HR Wallingford. In *Chapter 7* it is shown that the high mud sedimentation in the access channels is due, for an important part, to density gradients existing between the river and the access channel and in the vertical plane. The importance of density effects has already been reported in literature (Wollast, 1973; Sas, 1989). A detailed numerical model study together with a measurement campaign to validate the model has however not been carried out up to now.

Finally, a summary and the conclusions of the study are given in *Chapter 8* together with recommendations for further research.



## CHAPTER 2

### FORMULATION OF THE ICE-OCEAN NUMERICAL MODELS

#### 2.1. Introduction

Approximately 70% of the surface of the earth is covered by water. The average depth of the oceans is roughly 4000m. The continents are surrounded by a shallow continental shelf with a depth of the order of 100 metres. The shelf width is strongly varying from one place to another, on average the width is about 65km (Washington and Parkinson, 1986). At the seaward side of the continental shelf a sudden increase in depth is generally found giving way to a steep continental slope which extends to the deep-sea bottom.

The circulation in oceans and the shelf seas is due to two forcings, the first one resulting from the energy input in the form of solar radiation (direct as heating of the sea water and indirect as wind stress exerted on the sea surface or atmospheric pressure) and the second one (mainly) due to the simultaneous action of the moon's, sun's and earth's gravitational forces, and the revolution about one another of the earth and moon and the earth and sun. The secondary forces, such as the friction forces acting at the boundaries or in the internal of the water column and the Coriolis forces are due to the motion of the fluid.

Following Nihoul and Djenidi (1987) the range of time and length scales which are found in the marine environment can be classified as follows. The quantity  $\mathcal{L}$  is defined as the ratio of typical vertical to typical horizontal length scales in the oceans. *Microscale processes* having a time scale of the order of 1s and a scale  $\mathcal{L}$  of the order of 1mm describe 3D eddy turbulence motions. *Mesialscale processes*

with a time scale of the order minutes and  $\mathcal{L} \geq 1\text{m}$  describe the short internal waves and all turbulent processes affected by stratification. *Mesoscale processes* are characterized by time scale of the order of hours too days and  $\mathcal{L} >> 1\text{km}$ . They consist of inertial oscillations, tides, storm surges and diurnal variations. Higher order frequencies with a time scale of weeks to years are called *synoptical scale and global scale processes*, examples are residual and global ocean circulations and climatic processes.

Approximately 7% of the oceans is covered by sea ice. It exists as a result of the cooling of water below the freezing point and varies from fine ice particles suspended in water to expansive stretches of ice 3m or more in thickness (Washington and Parkinson, 1986). The ice cover is never uniform, because differential motion and cracking and local heat sources in the ocean creates open water areas. The sea ice in the Antarctic is more or less symmetrically distributed around the continent. Generally the Antarctic sea ice is less compact due to the lower latitudes, the presence of diverging motions from predominant winds and the non enclosed nature of the sea ice. Marginal ice zones are those regions where sea ice merges into open water. It is in these regions that the ice-ocean and atmosphere system is in non-equilibrium resulting in a highly dynamic system. Marginal ice zones are characterised by strong gradients in physical and biological parameters (Niebauer and Smith, 1989). One of the oceanic features providing the enhanced primary production is upwelling, along ice edge oceanic jets, oceanic fronts and strong heat exchange between the ocean and the atmosphere (Røed and O'Brien, 1983).

The ice-ocean system is governed by three coupled dynamical processes: the hydrodynamics of the sea, the thermodynamics of the ice and the dynamics of the ice. The weather conditions in the atmosphere form a time dependent boundary condition which is also interactively related to the ice-ocean system. This boundary condition consist of a time varying forcing for the exchange of mass (evaporation and precipitation), of momentum and of heat. In the following chapters we want to focus only on the ice-ocean system. The time scales which will be treated in the following are of the order of days, therefore only the dynamical behaviour of the ice will be taken into account. The main goal of Chapter 2, 3 and 4 is to develop a mesoscale vertical plane ice-ocean model, to validate various aspects of the model and to apply it to an ocean at high latitude.

This chapter presents the formulation of the conceptual and numerical 2.5D ice-

ocean model and 3D ocean model. The model is called 2.5D because it solves the 3D hydrodynamic equation assuming that the derivatives in one of the horizontal coordinate direction are zero so that the domain of integration can be reduced to a vertical plane. The governing equation for the hydrodynamics and ice dynamics cannot be solved analytically, except for some simplified examples. Therefore numerical techniques are commonly used in order to solve the equations. The numerical technique used here is the finite difference technique. A description of the 2.5D ocean model can be found in § 2.2., the ice model is presented in § 2.3., and the coupling between ice and ocean model can be found in § 2.4. A description of the 3D ocean model is given in § 2.5., the model is an extension of the 2.5D model.

The domain of integration is very often smaller than the ocean basin and non physical boundaries have thus to be introduced. Numerically this means that an open boundary condition has to be implemented. The choice of the open boundary condition will have a very important influence on the solution. In § 2.6. a short literature review of the most promising open boundary conditions is presented. These open boundary conditions have been implemented in an existing 2D horizontal model (Moelans and De Bruyn, 1986) and have been tested by applying the model to some well defined test cases. In agreement with literature, the Camerlengo and O'Brien condition gave the best results. This open boundary condition has therefore been implemented in the ocean model presented and developed in § 2.2. and § 2.5.

One of the important points during the development of a numerical model consists in choosing an accurate and stable numerical scheme for solving the advection terms. A detailed analysis of various advection schemes has been carried out by Yu (1993). In § 2.6. the results of a numerical simulation of a backward facing step (typical example where advection and diffusion plays an important role) in a long channel with open upstream and downstream boundaries are presented; the results of these studies have been reported in Fettweis and Yu (1990a). The aim of this experiment was to investigate the quality of the results as a function of the advection schemes (1<sup>st</sup> order upstream or QUICK) and of the open boundary condition. The length of the domain has been varied in such a way that the open boundary was situated or outside or inside the influence zone of the backward facing step. It was found that the open boundary condition (the Camerlengo and O'Brien condition has been used) gave good results also when the boundary had been placed in the eddy zone.



## 2.2. The 2.5D Hydrodynamic Model

### 2.2.1. *The governing equations*

In the introduction a series of various time and length scales have been presented which are relevant for marine environments. Giving the limitations in computer facilities it is yet not possible to resolve all these processes. Setting up a model means thus to set up some restrictions, the restrictions being the phenomena that the model has to be able to resolve.

The basic equations for the 2.5D numerical model are derived from the time-dependent three-dimensional equations of motion of a viscous fluid. The horizontal coordinates are  $x$  and  $y$ , the vertical coordinate is  $z$  and is positive downward from the undisturbed surface. The velocities are respectively  $u$ ,  $v$  and  $w$ .

The basic assumption of the 2.5D model is that the ocean is assumed to be uniform in one of the horizontal directions, i.e. the  $y$ -coordinate. This means that all the derivatives with respect to  $y$  are zero. The domain of integration is thus reduced to the  $x$ - $z$  vertical plane. The variables can only vary in this plane and are constant in the  $y$ -direction.

The pressure  $p$  is assumed to vary hydrostatically. Because the horizontal extent of an estuary or an ocean is much larger than the vertical extent, the vertical motion is much smaller than the horizontal one. In case of predominantly horizontal flow, the vertical accelerations are small compared to the gravitational acceleration and the vertical equation of motion can be reduced to the hydrostatic equation. This approximation thus says that the pressure distribution is more or less equal to the pressure distribution of a stationary body of water. The vertical momentum equation is reduced to:

$$\frac{\partial p}{\partial z} = \rho g \quad (2.1)$$

where  $\rho$  is the density and  $g$  the acceleration due to gravity. In Table 2.1 an indication of the values of the different terms in the complete vertical momentum equation are presented using a typical vertical velocity scale of  $10^{-5}$ m/s, a horizontal velocity scale of  $10^{-1}$ m/s, a vertical grid distance of 10m, a horizontal grid distance of 1000m, a horizontal eddy viscosity  $A_h$  of  $100\text{m}^2/\text{s}$  and a vertical eddy viscosity of  $A_v$  of  $0.01\text{m}^2/\text{s}$ . For comparison the vertical acceleration term is of magnitude  $10\text{m}/\text{s}^2$ . A consequence of this approximation is that the order of the system is reduced, the elliptic equation that has to be solved for pressure is reduced from two dimensions to one dimension.

Table 2.1: Scaling of the different terms in the vertical equation of motion (m/s<sup>2</sup>).

horiz. advection $uw/\Delta x$	vertical advection $w^2/\Delta z$	horiz. diffusion $A_h(w/\Delta x^2)$	vert. diffusion $A_v(w/\Delta z^2)$
$10^{-9}$	$10^{-11}$	$10^{-9}$	$10^{-9}$

The rigid-lid approximation is made, i.e.  $w_{\text{surface}} = w_0$ , where  $w_0$  is a specified value, usually taken as zero. A non-zero value can take into account mass transfer at the water surface due to evaporation or precipitation (Paul and Lick, 1981). The rigid-lid approximation is used to damp surface gravity waves. The time scale associated with gravitational surface waves ( $\Delta x/(gh)^{0.5}$ ) is an order of magnitude smaller than other relevant physical phenomena (advection, diffusion, baroclinic waves). Filtering out the surface gravity waves means that in the numerical model a larger time step can be used. With the rigid-lid approximation, only surface variations associated with surface gravity waves are neglected. Pressure variations along the undisturbed surface and internal gravity waves associated with vertical density variations are permitted.

The Boussinesq approximation is made. This approximation describes the way density variations are written in the equation of motion. Water density will be essentially considered as constants, while the variations of density will introduce a term in the equation of motion which describes Archimedian buoyancy force. In other words, the density variations can be neglected in all terms of the equation of motion (i.e. the variations due to the mass variations with density) but must be retained on the weight of the fluid (i.e. buoyancy effects). A consequence of this approximation is that acoustic waves, which are related with variations in density, are filtered out.

Eddy viscosity and diffusivity coefficients are used to account for the turbulent and molecular diffusion processes in both momentum and salinity equations. Very often turbulence is introduced into numerical models by a relatively simple parameterization. More complicated eddy viscosity formulations based on the production and dissipation of turbulent kinetic energy have been used successfully in hydrodynamic models, see Rodi (1987). The problem with these formulations is that they generally involve a series of empirical coefficient, which have been obtained in a certain applications or in laboratory experiments. Therefore the vertical eddy viscosity and diffusivity has been taken as constant. The remaining assumptions are:

- the horizontal eddy viscosity and diffusivity coefficients are assumed to be constant,
- the variations in bottom topography are accounted for using a Cartesian grid,

the density is assumed to be only a function of salinity.

The hydrodynamic equations and the salt transport equation can be written as follows:

$$\frac{\partial u}{\partial t} + u \frac{\partial u}{\partial x} + w \frac{\partial u}{\partial z} + \frac{1}{\rho} \frac{\partial p}{\partial x} - f v = \frac{\partial}{\partial x} (A_h \frac{\partial u}{\partial x}) + \frac{\partial}{\partial z} (A_v \frac{\partial u}{\partial z}) \quad (2.2)$$

$$\frac{\partial v}{\partial t} + u \frac{\partial v}{\partial x} + w \frac{\partial v}{\partial z} + \frac{1}{\rho} \frac{\partial p}{\partial y} + f u = \frac{\partial}{\partial x} (A_h \frac{\partial v}{\partial x}) + \frac{\partial}{\partial z} (A_v \frac{\partial v}{\partial z}) \quad (2.3)$$

$$\frac{\partial s}{\partial t} + u \frac{\partial s}{\partial x} + w \frac{\partial s}{\partial z} = \frac{\partial}{\partial x} (K_h \frac{\partial s}{\partial x}) + \frac{\partial}{\partial z} (K_v \frac{\partial s}{\partial z}) \quad (2.4)$$

where  $u$ ,  $v$  and  $w$  are the velocity components in  $x$ ,  $y$  and  $z$  directions respectively,  $\rho$  is the density,  $p$  and  $P$  the pressure,  $f$  the Coriolis parameter,  $g$  the acceleration due to gravity,  $s$  the salinity and  $A_h$ ,  $A_v$ ,  $K_h$  and  $K_v$  the horizontal and vertical eddy viscosity and diffusivity respectively. At the sea surface the vertical friction term is written as  $-A_v \partial u / \partial z = \tau_{s,x} / \rho$  and  $-A_v \partial v / \partial z = \tau_{s,y} / \rho$ .  $\tau_{s,x}$  and  $\tau_{s,y}$  are the sum of the wind and ice stresses in  $x$ - and  $y$ -direction respectively (see § 2.4.). The pressure term in equation (2.3),  $\partial P / \partial y$ , is a forcing term, which has to be specified.

The variables which have to be solved are  $u$ ,  $v$ ,  $w$ ,  $s$  and  $p$ . We assume that the density  $\rho$  is only depending on  $s$ . In case of the rigid-lid assumption the hydrostatic equation (2.1) is integrated from the undisturbed surface to the bottom:

$$p = g \int_0^z \rho dz + C \quad (2.5)$$

The constant of integration  $C$  corresponds to the pressure at the sea surface ( $z=0$ ), i.e.  $p_s$  and the pressure on the rigid lid due to the flow, i.e.  $p_l$ , we obtain thus

$$p = p_s + p_l + gz\bar{\rho} \quad (2.6)$$

where

$$\bar{\rho} = \frac{1}{z} \int_0^z \rho dz \quad (2.7)$$

The pressure  $p$  in equation (2.2) is replaced by equation (2.6). By assuming that



the air pressure is constant over the domain the pressure term of equation (2.2) can be replaced by the following with  $\rho_0$  the reference density:

$$\frac{1}{\rho} \frac{\partial p}{\partial x} = \frac{1}{\rho_0} \frac{\partial p_i}{\partial x} + \frac{gz}{\rho_0} \frac{\partial \bar{\rho}}{\partial x} \quad (2.8)$$

Finally the continuity equations reduces to

$$\frac{\partial u}{\partial x} + \frac{\partial w}{\partial z} = 0 \quad (2.9)$$

### 2.2.2. Finite difference equations

The set of equations which we have at our disposal are (2.2) - (2.4) and (2.9). These equations are solved using an explicit scheme, a description of the numerical scheme has been reported in Fettweis et al. (1991b). The variable are described on a staggered grid system (the so-called B-grid), see Figure 2.1. The finite difference representation of the continuity equation, the momentum equations and the transport equation are presented using the notation of Figure 2.1. The subscripts  $i, k$  are the space coordinates of the grid in  $x$  and  $z$  direction respectively, the superscript  $n$  indicates the time level ( $n$  is the known current time level,  $n+1$  is the unknown future time level) and  $\Delta x$  is the horizontal and  $\Delta z$  the vertical distance between two successive  $u/v$  points.  $\Delta z$  is not necessarily constant, in order to make the equations not too complicated it is assumed to be constant in the following description of the finite difference equations. The equations are valid away from the boundaries.

Continuity equation (2.9):

$$(u_{i,k}^{n+1} - u_{i-1,k}^{n+1})/\Delta x + (w_{i,k+1}^{n+1} - w_{i,k}^{n+1})/\Delta z = 0 \quad (2.10)$$

Momentum equations (2.2):

$$\begin{aligned} & (u_{i,k}^{n+1} - u_{i,k}^n)/\Delta t + a u_{i,k}^n - f v_{i,k}^{n+1} - A_h(u_{i+1,k}^n - 2u_{i,k}^n + u_{i-1,k}^n)/\Delta x^2 \\ & - A_v(u_{i,k+1}^n - 2u_{i,k}^n + u_{i,k-1}^n)/\Delta z^2 + \frac{1}{\rho_0} \left( \frac{\partial p_i}{\partial x} \right)_i^{n+1} + \frac{gz}{\rho_0} \left( \frac{\partial \bar{\rho}}{\partial x} \right)_i^n = 0 \end{aligned} \quad (2.11)$$

and momentum equation (2.3):

$$(v_{i,k}^{n+1} - v_{i,k}^n)/\Delta t + a v_{i,k}^n + f u_{i,k}^n - A_h(v_{i+1,k}^n - 2v_{i,k}^n + v_{i-1,k}^n)/\Delta x^2$$

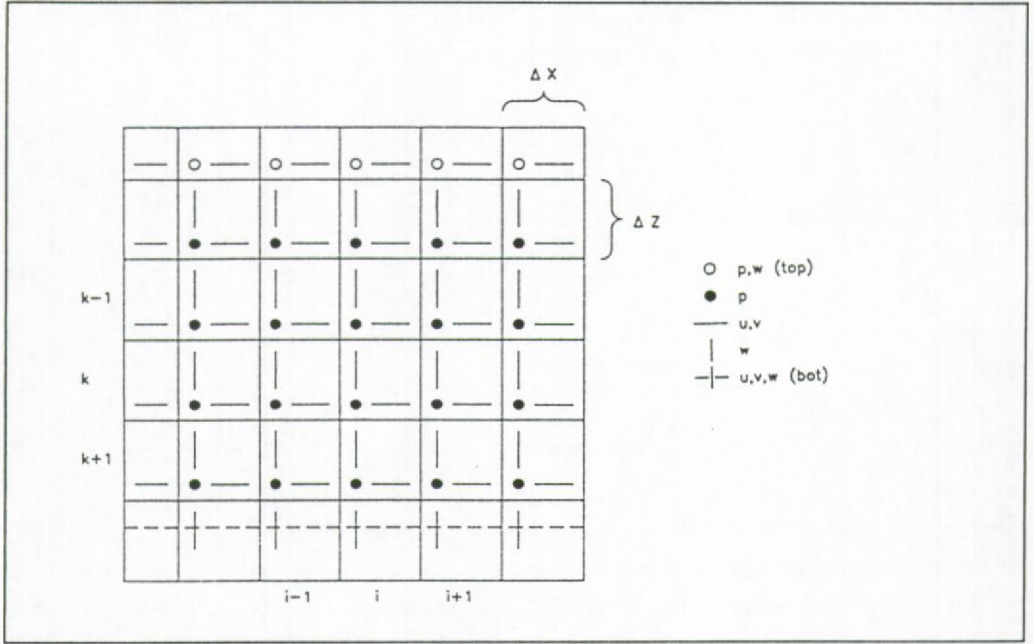


Figure 2.1: Numerical grid used by the 2.5D model.

$$- A_v(v_{i,k+1}^n - 2v_{i,k}^n + v_{i,k-1}^n)/\Delta z^2 + \frac{1}{\rho_0} \left( \frac{\partial p}{\partial y} \right)_i^{n+1} = 0 \quad (2.12)$$

where  $adu_{i,k}^n$  and  $adv_{i,k}^n$  are the advection terms, they are replaced by a 1<sup>st</sup> order upwind scheme (see § 2.7). The pressure term in equation (2.12) is not calculated but can be used as forcing term.

The transport equation is written in finite differences as follows:

$$\begin{aligned} (s_{i,k}^{n+1} - s_{i,k}^n)/\Delta t + ads_{i,k}^n - K_h(s_{i+1,k}^n - 2s_{i,k}^n + s_{i-1,k}^n)/\Delta x^2 \\ - K_v(s_{i,k+1}^n - 2s_{i,k}^n + s_{i,k-1}^n)/\Delta z^2 = 0 \end{aligned} \quad (2.13)$$

where  $ads_{i,k}^n$  are the advection terms (approximated by a 3<sup>rd</sup> order QUICK scheme, the description of the scheme is given in § 2.6.2. eq. 2.40). In order to prevent unstable stratification the vertical advection is implicitly treated using the convective adjustment scheme. If the upper layer has a higher density than the lower one the density value in both layers is replaced by the (weighted) average over both layers.

### 2.2.3. Computational scheme

Equation (2.12) can be solved directly since all the terms, except the time derivative, are explicit. Solving the  $u$ -momentum equation (2.11) takes more computations, it cannot be solved directly because of the pressure gradient term which is implicit. This pressure gradient term is calculated in the following way: The velocity in  $x$ -direction is split in two parts, a part containing the known terms and another one containing the implicit ones:

$$u_{i,k}^{n+1} = u'_{i,k} + u''_{i,k} \quad (2.14)$$

where  $u'$  and  $u''$  are equal to:

$$u'_{i,k} = u_{i,k}^n + (-adu_{i,k}^n + diff_{i,k}^n + fv_{i,k}^{n+1})\Delta t \quad (2.15)$$

$$u''_{i,k} = -\frac{1}{\rho_0} \left( \frac{\partial p_i}{\partial x} \right)_i^{n+1} \Delta t \quad (2.16)$$

$adu_{i,k}^n$  are the advective terms and  $diff_{i,k}^n$  are the diffusion terms. To calculate the pressure gradient, the continuity equation (2.9) is integrated over the vertical (from top  $k = 1$  to  $k = nz - 1$ , with  $nz$  the bottom coordinate). The vertical velocity at the surface and at the bottom is zero (rigid lid condition) so that the vertically integrated continuity equation at timestep  $n + 1$  and written in finite differences takes the form

$$h_{i+1} \sum_{k=1}^{nz-1} (\omega_k u'_{i+1,k}^{n+1}) - h_i \sum_{k=1}^{nz-1} (\omega_k u'_{i,k}^{n+1}) = 0 \quad (2.17)$$

where  $\omega_k$  is a weighting factor depending on the vertical grid size. Equation (2.14) is put in equation (2.17) and together with equations (2.15) and (2.16) the following relation is obtained between the pressure gradient at  $i + 1$  and  $i$ :

$$\left( \frac{\partial p_i}{\partial x} \right)_{i+1}^{n+1} \Delta t = \frac{\rho_0}{h_{i+1}} \left[ h_{i+1} \sum_{k=1}^{nz-1} (\omega_k u'_{i+1,k}) - h_i \sum_{k=1}^{nz-1} (\omega_k u'_{i,k}) + \frac{h_i}{\rho_0} \left( \frac{\partial p_i}{\partial x} \right)_i^{n+1} \Delta t \right] \quad (2.18)$$

Starting from a lateral boundary and using the lateral boundary condition the pressure gradient can be calculated from equation (2.18). Having obtained the pressure gradient, the  $u$ -velocity can be calculated from equation (2.14). After  $u$  and  $v$  have been calculated for the whole domain for  $n + 1$ , the vertical velocity is obtained by solving the continuity equation (2.10) from bottom to top. The vertical velocity is thus the result of fulfilling the continuity equation. The last step consists of solving



the transport equation and calculating the new density values.

## 2.3. The 1.5D Ice Dynamic Model

### 2.3.1. Introduction

The physical system which describes the evolution of the ice is dominated by three mutually connected processes: the hydro- and thermodynamics of the ocean, the thermodynamics of ice and the ice dynamics. The atmosphere consists of a time-dependent boundary condition on the surface of each of the processes and is responsible for the exchange of mass (precipitation and evaporation), for the motion of water and ice and for the heat exchange at the air-water and the air-ice boundaries. A review of coupled ocean and ice models is given in van Ypersele (1989). In Figure 2.2 the processes near the ice margin are displayed.

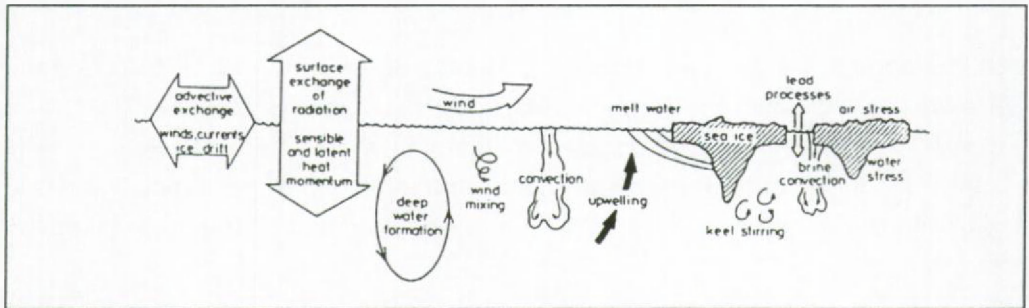


Figure 2.2: Processes near the ice margin (from Lemke, 1986).

The initial growth of the ice is always thermodynamical. When ice is formed or is melting, it affects the upper ocean salt budget. Most of the salt contained in the water is expelled from the ice by the building of ice crystals. Sea ice formation thus increases the density of the under-ice water, which can lead to convection and overturning. Sea ice melting will stabilize the water column.

Sea ice receives momentum from both the ocean and the atmosphere, and moves in response. The ice dynamics describe processes of mechanical deformation and of transport of the ice due to stresses exerted on the ice-ocean and the ice-atmosphere interfaces. These mechanical deformation processes have also an influence on the ice distribution due to ridging and rafting and can create open water zones (polynyas or leads) where new ice can be formed. During a winter season thermodynamic processes can e.g. form an ice layer of 1m whereas due to ridging ice layers of 7m to 8m are common (Wake and Rumer, 1983).

In what follows we will concentrate on the dynamical aspects of sea-ice, since we are interested on small time-scales (order of days).

### 2.3.2. *The governing equations of ice dynamics*

The three dynamical processes (transport, ridging and rafting) can be incorporated by assuming that the fragmented ice layer, formed by discrete ice floes, consists of a continuum. The continuum approximation has been used in Wake and Rumer (1983) and Chieh et al. (1983) for simulating the ice behaviour of the Great Lakes. In case of polar seas the continuum approximation can be simplified (Kollé and Pritchard, 1983), because the time and length scales of the Great Lakes and the polar oceans are different.

The necessary condition to apply the continuum approximation is that the elementary length scales of the continuum should be sufficient big compared to the typical scale of an ice floe and sufficiently small compared to the total ice field and the forces acting on it. This condition is a function of the fragmentation and the homogeneity of the ice field, which are itself a function of the age of the ice and the local and geographical conditions. The surface concentration of ice is expressed as

$$A = A_i / A_t \quad (2.19)$$

where  $A_i$  is the surface in the elementary area covered by ice and  $A_t$  is the total surface of the elementary area. The elementary area has to be chosen in such a way that  $A$  is independent of the surface area  $A_t$ . By treating the ice concentration as a continuous variable, the 'density' of the ice medium is the ice concentration multiplied by the actual density of the sea ice (Røed and O'Brien, 1983).

The continuity equation of ice mass can be deduced from the net ice mass transport across an elementary surface together with the growth or depletion of ice mass due to thermodynamical processes in the elementary surface as:

$$\frac{\partial(\rho_i A d)}{\partial t} + (\rho_i A d) \nabla V_i = E_s \quad (2.20)$$

where  $\rho_i$  is the ice density (910 kg/m<sup>3</sup>),  $V_i = (u, v)$  the ice velocity vector,  $d$  the ice thickness defined as the mean ice thickness integrated over the fraction of the elementary surface covered by ice and  $E_s$  the variations of ice mass due to melting or freezing.

The equation for ice mass conservation is an exact equation. In order to determine the ice concentration separately an empirical ice concentration equation is used (see e.g. Mellor and Kantha, 1989):

$$\frac{\partial A}{\partial t} + A \nabla V_i = E_s - R_s \quad (2.21)$$

with  $R_s$  the variation of ice concentration due to mechanical redistributions. In the following the thermodynamic terms will be taken as zero. The above two equations describe the continuity of ice mass and ice concentration in a two-dimensional system. As in the ocean model (§ 2.2) we assume that the gradients in the along-shore direction ( $y$ ) are zero.

Because the vertical movements of the ice are orders of magnitude smaller than the horizontal movements the ice dynamics can be approximated as two dimensional. The momentum equations of the ice continuum is deduced from the equilibrium of forces acting on an elementary surface taking into account that the derivatives with respect to  $y$  are zero. Let  $u_i$  and  $v_i$  be the horizontal ice velocities in  $x$  and  $y$  direction and  $A$  the ice concentration, the ice momentum equations can be written as (Røed and O'Brien, 1983):

$$\rho_i dA \left[ \frac{\partial u_i}{\partial t} + u_i \frac{\partial u_i}{\partial x} - f v_i \right] = -\frac{\partial \sigma}{\partial x} + A (\tau_{ai,x} + \tau_{wi,x}) \quad (2.22)$$

$$\rho_i dA \left[ \frac{\partial v_i}{\partial t} + u_i \frac{\partial v_i}{\partial x} + f u_i \right] = A (\tau_{ai,y} + \tau_{wi,y}) \quad (2.23)$$

where  $\tau_{ai,x}$  and  $\tau_{ai,y}$  represent the components in  $x$  and  $y$  direction of the atmospheric stress exerted by the wind on the air-ice interface and  $\tau_{wi,x}$  and  $\tau_{wi,y}$  represent the components in  $x$  and  $y$  direction of the stress exerted by the ocean on the ice.  $\sigma$  is the internal stress of the ice. Hibler (1979) included in his model the forcing terms due to ocean tilt, according to him this forcing is only important on long time scales (order of years) and has therefore been omitted. The air-ice and the water-ice stresses are only acting on that fraction of the area which is covered by sea ice, therefore they have been multiplied by  $A$ , the ice concentration.

The air-ice stress can be written similar to the air-water stress using a quadratic friction formulation:

$$\tau_{ai} = \rho_a C_{ai} |W| W \quad (2.24)$$

where  $W$  is the wind velocity vector,  $\rho_a$  is the air density ( $1.2 \text{ kg/m}^3$ ) and  $C_{ai}$  is the



drag coefficient between air and ice. It is generally agreed (Røed and O'Brien, 1983 and Niebauer and Smith, 1989) that the drag coefficient over pack ice is about the double of the drag coefficient over open water.

The interfacial drag between water and ice is written using a linear formulation as (Hibler, 1979):

$$\tau_{wi} = \rho C_{wi} (V - V_i) \quad (2.25)$$

where  $C_{wi}$  is the water-ice drag coefficient,  $\rho$  is the upper layer water density and  $V$  and  $V_i$  are the water and the ice velocity vectors respectively.

The internal ice stress  $\sigma$  takes into account forces generated by ice-ice interactions and they are generally expressed in terms of deformational characteristics of the ice field. The constitutive law describes the stress-strain relationship and is necessary in order to close the system. The ice is usually treated as a plastic material. The ice models generally differ in the way the pre-yielding behaviour is defined. The AIDJEX group (Arctic Ice Dynamics Joint Experiment, see e.g. Rothrock, 1975) developed a model which assumed elastic behaviour while Hibler (1979) assumed a viscous behaviour. A review of yield curves and flow rules for pack ice can be found in Ukita and Moritz (1995). Røed and O'Brien (1981) have used for the marginal ice zone a simplified version of Hibler's constitutive law where the internal stress is given by an uncompensated pressure and where the pressure is only a function of the areal mass. The internal ice stress term can then be written as (Røed and O'Brien, 1983):

$$\frac{\partial \sigma}{\partial x} \frac{1}{\rho_i A d} = \frac{c^2}{A} \frac{\partial A}{\partial x} \quad (2.26)$$

with  $c$  the propagation speed of disturbances written as:

$$c^2 = c_0^2 A e^{1-k(1-A)} \quad (2.27)$$

with

$$c_0^2 = \frac{k^2 p^* / (\rho_i d_0)}{e^{-k} + k - 1} \quad (2.28)$$

and  $c_0$  a typical speed for 100% ice cover,  $d_0$  a typical thickness of the pack ice and  $p^*$  a typical value of the plastic strength (5000N/m).  $k$  is the dispersivity coefficient and is of the order of 15-20.

The final equations of sea ice motion can now be written as:

$$\frac{\partial u_i}{\partial t} + u_i \frac{\partial u_i}{\partial x} - f v_i + \frac{c^2}{A} \frac{\partial A}{\partial x} = [\tau_{ai,x} + \rho C_{wi}(u - u_i)] / (\rho_i d) \quad (2.29)$$

$$\frac{\partial v_i}{\partial t} + u_i \frac{\partial v_i}{\partial x} + f u_i = [\tau_{ai,y} + \rho C_{wi}(v - v_i)] / (\rho_i d) \quad (2.30)$$

### 2.3.3. Numerical scheme of the 1.5D ice model

Equations (2.29) and (2.30) are solved explicitly at each time step of the ocean model. The transport of ice is then calculated by equations (2.20) and (2.21). If the new ice concentration in an area is higher than 100% then the ice thickness will be increased in order to conserve ice mass.

## 2.4. Coupling Of The 2.5D Ocean And The 1.5D Ice Model

The sea ice model is coupled to the ocean and vice versa by the stress on the water ice interface  $\tau_{wi}$  (eq. 2.25). In ice free regions ( $A=0$ ) the surface forcing of the ocean is only given by the air-water stress  $\tau_{aw}$ . In ice covered areas, the atmospheric forcing is depending on the fraction of open water ( $1-A$ ) and the stress exerted by the ice on the water depending on the fraction of ice covered water ( $A$ ). The stresses  $\tau_{s,x}$  and  $\tau_{s,y}$  that act on the surface of the ocean are then calculated as

$$\tau_{s,x} = \tau_{aw,x}(1-A) + \tau_{iw,x}A \quad (2.31)$$

$$\tau_{s,y} = \tau_{aw,y}(1-A) + \tau_{iw,y}A \quad (2.32)$$

The ice-water stress is acting in such a way that in case of larger ice velocities the water is accelerated by the ice whereas the ice is decelerated by the water.

## 2.5. Open Boundary Conditions

### 2.5.1. *Introduction*

In many numerical models it is necessary to restrict the domain of integration because of restrictions in computer time, internal memory of the computer or because the modeller is only interested in some local phenomena. The integration domain is in those cases much smaller than the whole ocean basin and boundaries with no physical meaning have to be introduced. This can lead to a wrong solution of the problem. In order to integrate the equations for a restricted domain it is necessary to define meaningful conditions at the open sea boundaries.

The computational boundaries can be subdivided into natural and artificial boundaries. Natural boundaries are continental boundaries. Artificial boundaries can be further subdivided into open boundaries and specified boundaries. For the latter kind of boundaries one or several variables are a priori determined and are independent of the values of the same variables in the interior of the domain. The specified boundary has a great influence on the evolution of the model solution. This kind of boundaries are *e.g.* used in hydrodynamic tidal models which are forced by specifying the horizontal or vertical tide at the boundary.

A common approach is the grid refinement technique: a bigger domain is discretised with a coarse grid size and the values of the dependent variables at the fine/coarse grid boundary are used as boundary condition for the fine grid domain (see *e.g.* Yu et al. 1988b). This technique is in many cases not appropriate because it does not allow for disturbances generated in the fine domain to be included in the boundary condition.

A second approach consists in the use of an open boundary condition (OBC). OBC have to be defined in such a way that the influence of the boundaries is minimal in the interior domain. Røed and Cooper (1986) defined an open boundary as a 'computational boundary at which disturbances originating in the interior of the computational domain are allowed to leave it without disturbing or deteriorating the interior solution'. Unfortunately perfect open boundaries do not exist (Chapman, 1985), every open boundary condition introduces disturbances in the numerical solution. In the following a short review of different open boundary conditions is given. The open boundary conditions mentioned in literature can be divided into three types:



- Extrapolation formulas (e.g. Kreiss, 1966 and Chen, 1973).
- Sponge Filter layers (e.g. Israeli and Orszag, 1981).
- Formulas based on the Sommerfeld radiation condition.

Open boundary conditions based on the Sommerfeld radiation conditions have been used most widely. The Sommerfeld radiation condition can be formulated as follows

$$\frac{\partial \phi}{\partial t} + c_{\phi} \frac{\partial \phi}{\partial x} = 0 \quad (2.33)$$

where  $\phi$  is the dependent variable which has to be specified at the boundary,  $c_{\phi}$  is the propagation speed,  $t$  is time and  $x$  is the coordinate perpendicular to the boundary. Equation (2.33) is an advection equation, specifying the transport of some quantity.

Orlanski (1976) suggested to calculate the phase speed explicitly by evaluating its value from values of  $\phi$  at neighbouring grid points inside the domain using a leapfrog finite difference scheme. If the phase speed is positive (outflow) the value is calculated using a finite difference representation of (2.33). The calculated phase speed is limited to  $\Delta x/\Delta t$  in order not to violate the stability criterion. If the phase speed is negative (inflow) the boundary value is either unchanged or specified. Camerlengo and O'Brien (1980) simplified the Orlanski method, they proposed to use only the extreme phase speed values. This method seems to yield better results when simulating the outflow of Kelvin waves for a free-wave experiment, but does not have the long-time stability of a perfect open boundary. Miller and Thorpe (1981) tested different numerical formulations of the Sommerfeld radiation condition. They showed that the Orlanski formulation can be made more accurate when using an upstream finite difference scheme instead of the leapfrog scheme. Blumberg and Kantha (1985) incorporated the possibility of external forcing. They developed a damped Sommerfeld radiation condition which can be used for tidal or meteorological forcing. The phase velocity is fixed  $((gh)^{0.5})$  and the value of  $\phi$  (e.g. tidal elevation) at the boundary is forced to some known value  $\phi_k$  in a certain time scale. Bills and Noye (1987) concluded that the Blumberg and Kantha method is not appropriate in case of pure tidal forcing. They proposed a modification, which uses the Orlanski scheme to calculate the phase speed. This condition gives better performances but 'seems unnecessarily complicated in comparison to the Orlanski condition'. The success of this condition is mainly due to its separation of tidal motion in ingoing and outgoing flows.

### 2.5.2. Numerical experiments of open boundary conditions

Some numerical experiments with the Orlanski and the Camerlengo and O'Brien implementation of the radiation condition have been carried out in case of wind forcing, see Fettweis et al. (1989). The 2D horizontal model used for these experiments is based on the solution of the 2D depth integrated shallow water equations on a C-grid using a falsified alternating direction implicit scheme, without advection or diffusion terms. A description of the model can be found in Moelans and De Bruyn (1986), Yu et al. (1988a), Yu et al. (1989) and Yu (1993).

Rearranging equation (2.33), the phase velocity is calculated as

$$c_{\phi} = -\frac{\partial \phi}{\partial t} / \frac{\partial \phi}{\partial x} \quad (2.34)$$

Equation (2.34) is evaluated for the points situated along the open boundary just inside the domain (thus not directly at the boundary). If  $c_{\phi} < 0$  then the flow is ingoing, if  $c_{\phi} > 0$  the flow is outgoing. Orlanski (1976) restricted the value of  $c_{\phi}$  so that:

- |  |  |
|--|--|
| if $c_{\phi} < 0$                      | then $c_{\phi}$ is set to zero,                  |
| if $0 < c_{\phi} < 2\Delta x/\Delta t$ | then $c_{\phi}$ keeps the calculated value,      |
| if $c_{\phi} > 2\Delta x/\Delta t$     | then $c_{\phi}$ is set to $2\Delta x/\Delta t$ . |

Camerlengo and O'Brien (1980) proposed to take only the extreme phase speed values:

- |                   |  |
|-------------------|--|
| if $c_{\phi} < 0$ | then $c_{\phi}$ is set to zero,                  |
| if $c_{\phi} > 0$ | then $c_{\phi}$ is set to $2\Delta x/\Delta t$ . |

The value of  $c_{\phi}$  is put in equation (2.34) to calculate the value of  $\phi$  at the boundary. For an ingoing wave ( $c_{\phi} < 0$ ) both schemes are reduced to the value of  $\phi$  at the boundary at the previous time-step.

The open boundary conditions of Orlanski and Camerlengo and O'Brien are applied to the sea surface elevation in the 2DH model. To examine the effect of the open boundary conditions in the model, three numerical experiments have been carried out:

- barotropic relaxation (no forcing),
- alongshelf wind stress,
- forcing at the open boundary.

A long channel (600km x 1200km) with a simple bathymetry was chosen as a test basin, see Figure 2.3. The dimension of the basin, the value of the different parameters in the numerical model and the set up of the experiments was taken from Røed and Smedstad (1984).

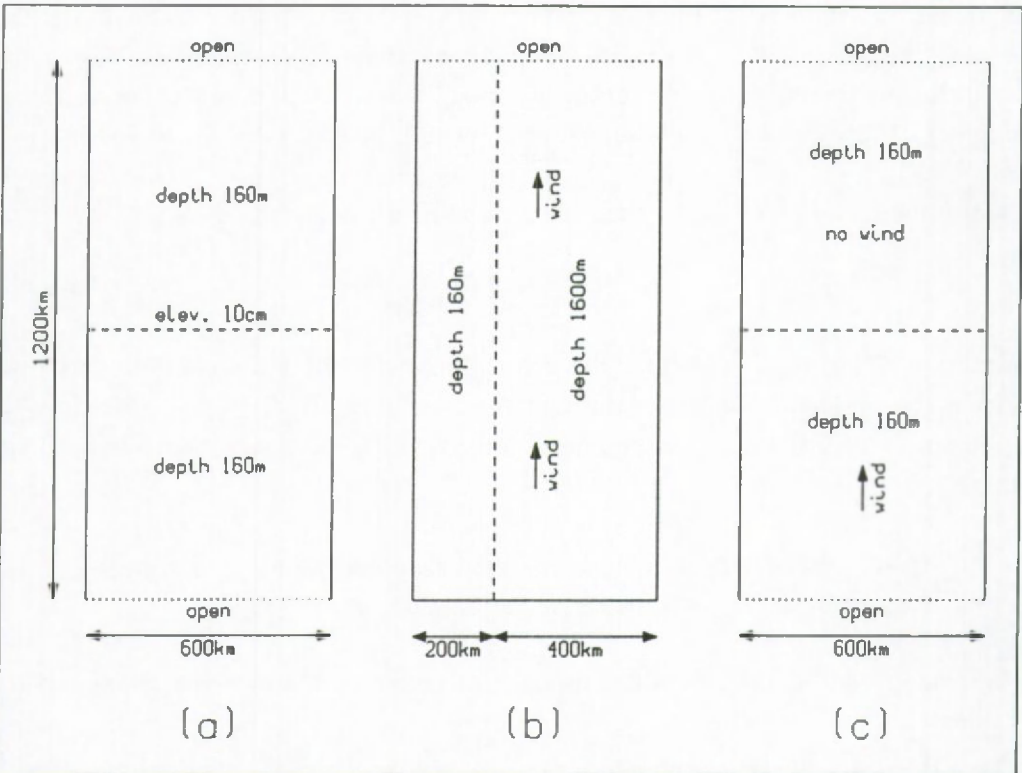


Figure 2.3: The geometry of the three test basins. (a) barotropic relaxation, (b) alongshelf wind stress and (c) forcing at open boundary.

#### 2.5.2.1. Barotropic Relaxation

In this simulation no forcing is applied. The fluid is initially at rest with the sea surface elevated 10cm in the middle of the computational domain. The upper and the lower boundary are open (i.e. the short sides of the basin), see Figure 2.3a. This experiment allows the investigation of the wave reflection properties of the open boundary condition. Adjustment takes place by dispersive Poincaré waves and non-dispersive Kelvin waves (Gill, 1976). The channel has a constant depth of 160m. In Figure 2.4 the deviation of the surface elevation is shown for different



time-steps for the Orlanski open boundary condition. After 16 hours most of the disturbances have past the open boundary. Hardly any difference exists between the Orlanski and the Camerlengo and O'Brien condition.

#### 2.5.2.2. *Alongshelf wind stress*

The channel has now a shelf region with a water depth of 160m and a width of one-third of the channel from the right-hand wall, the rest of the channel consist of a deep ocean of 1600m, see Figure 2.3b. Only the upper boundary is open. Wind stress is applied along the channel axis in northward direction in the lower half of the channel and is turned on for 8 hours and then set to zero.

In consequence of the wind action different kind of waves are formed: the topography generates dispersive shelf waves and when the wind is turned off a non-dispersive Kelvin Wave is generated. The sequence of events is illustrated in Figure 2.5 for the Orlanski open boundary condition and in Figure 2.6 for the Camerlengo and O'Brien condition. The results have been compared with those of a closed channel with such a length that the fastest wave and its reflection did not disturb the solution within the region of interest during the computation. Compared with that solution (not shown) the condition of Camerlengo and O'Brien gives better performance than the Orlanski condition.

#### 2.5.2.3. *Forcing at the open boundary*

This experiment was set up in order to check the response of the water to wind forcing in case an open boundary is situated in a forced region. The basin has the same dimensions as in the previous experiment, the depth is constant and set to 160m. The wind is blowing in the lower half of the channel in northward direction. The southern boundary and northern boundary are open, see Figure 2.3c. After an adjustment time a steady state sea surface elevation sets up and generates an alongshelf current. The adjustment time is a function of the water depth and the friction coefficient. After 8 hours, the wind is turned off and a geostrophic flow is developed, except for some oscillations (see Figures 2.7 - 2.8). After 32 hours an alongshelf flow is present for the Camerlengo and O'Brien condition in contrast with the Orlanski condition.

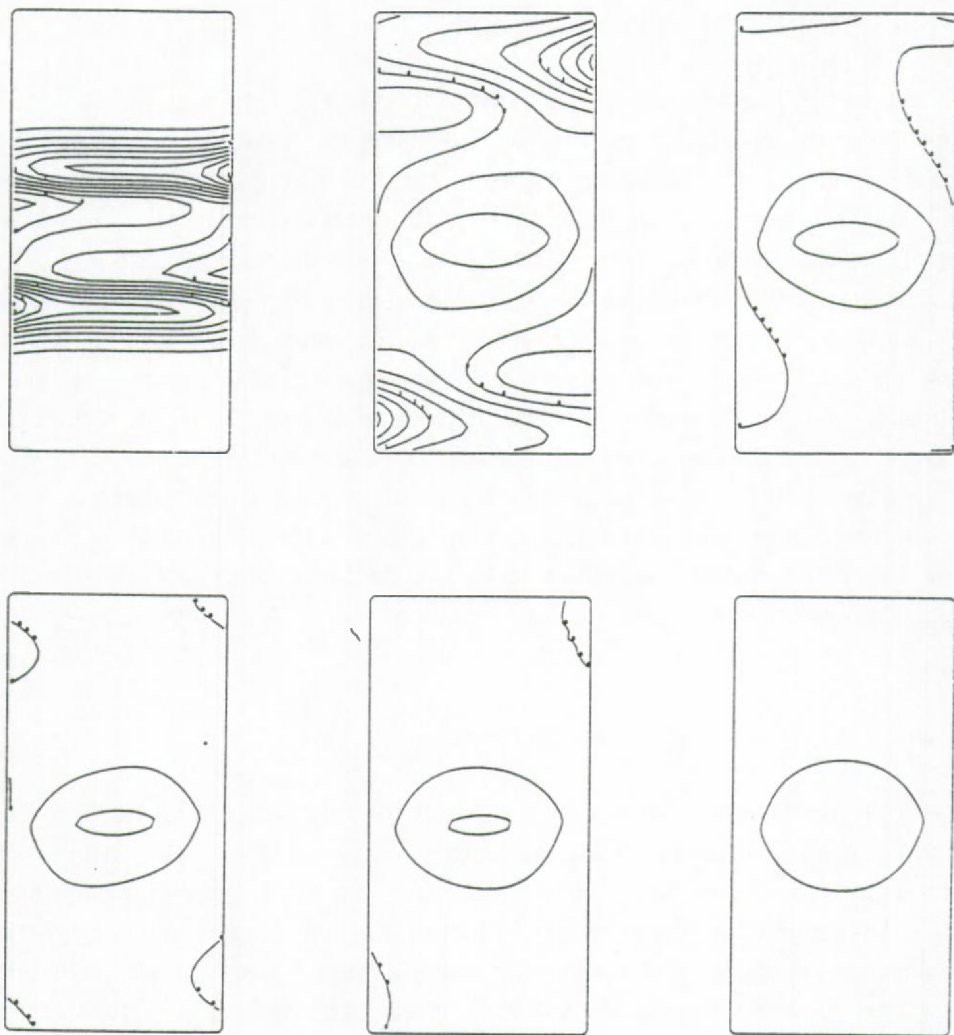


Figure 2.4: Surface elevation in cm (interval 0.25cm) for the barotropic relaxation experiment (Camerlengo and O'Brien condition). The solution is shown after 2, 5, 8, 11, 16 and 32 hours.

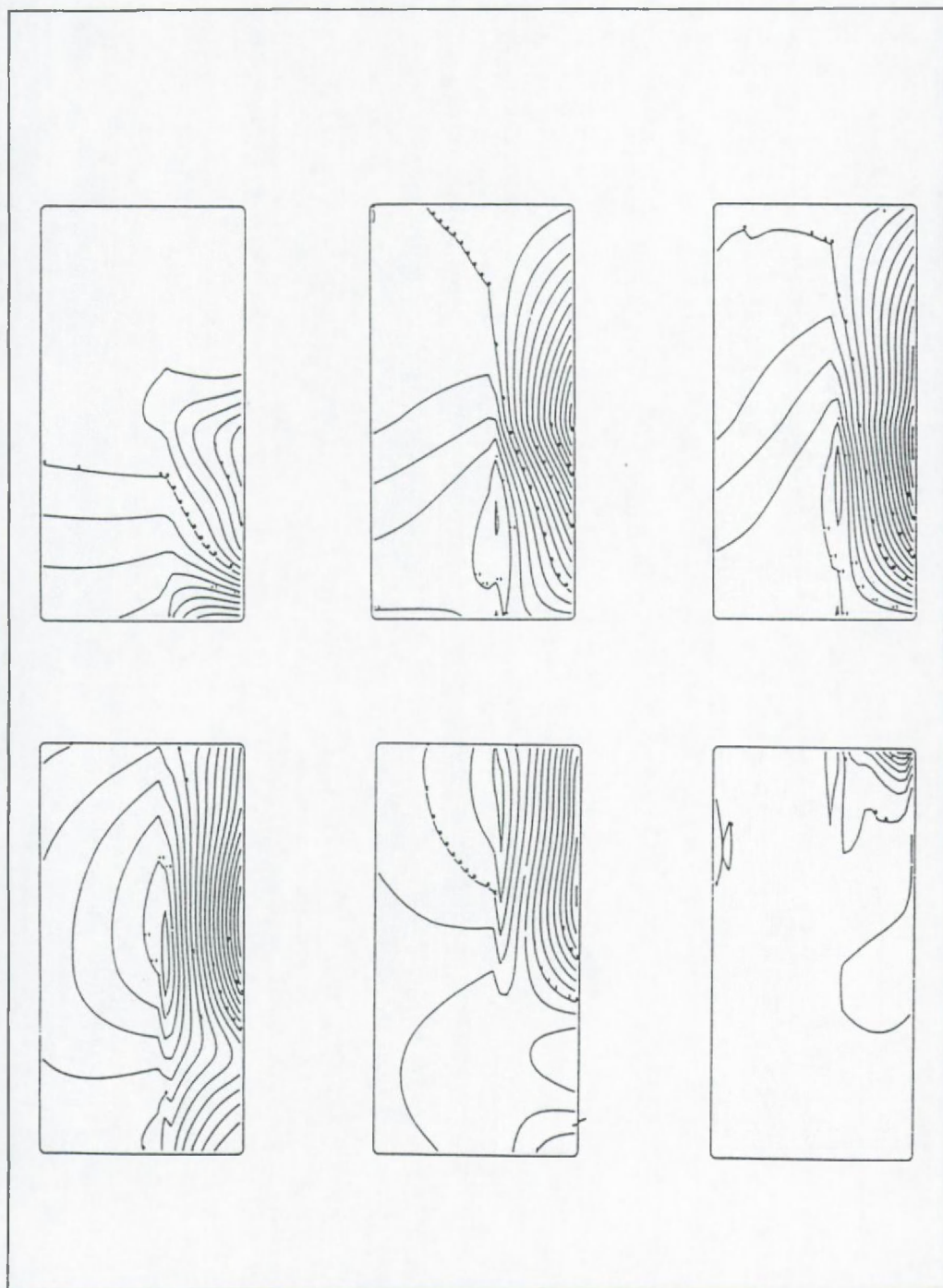


Figure 2.5: Surface elevation in dm (interval is 2.5cm) for the alongshelf wind stress experiment. The Orlanski condition has been used. The solution is presented after 2, 6, 8, 11, 17 and 32 hours.



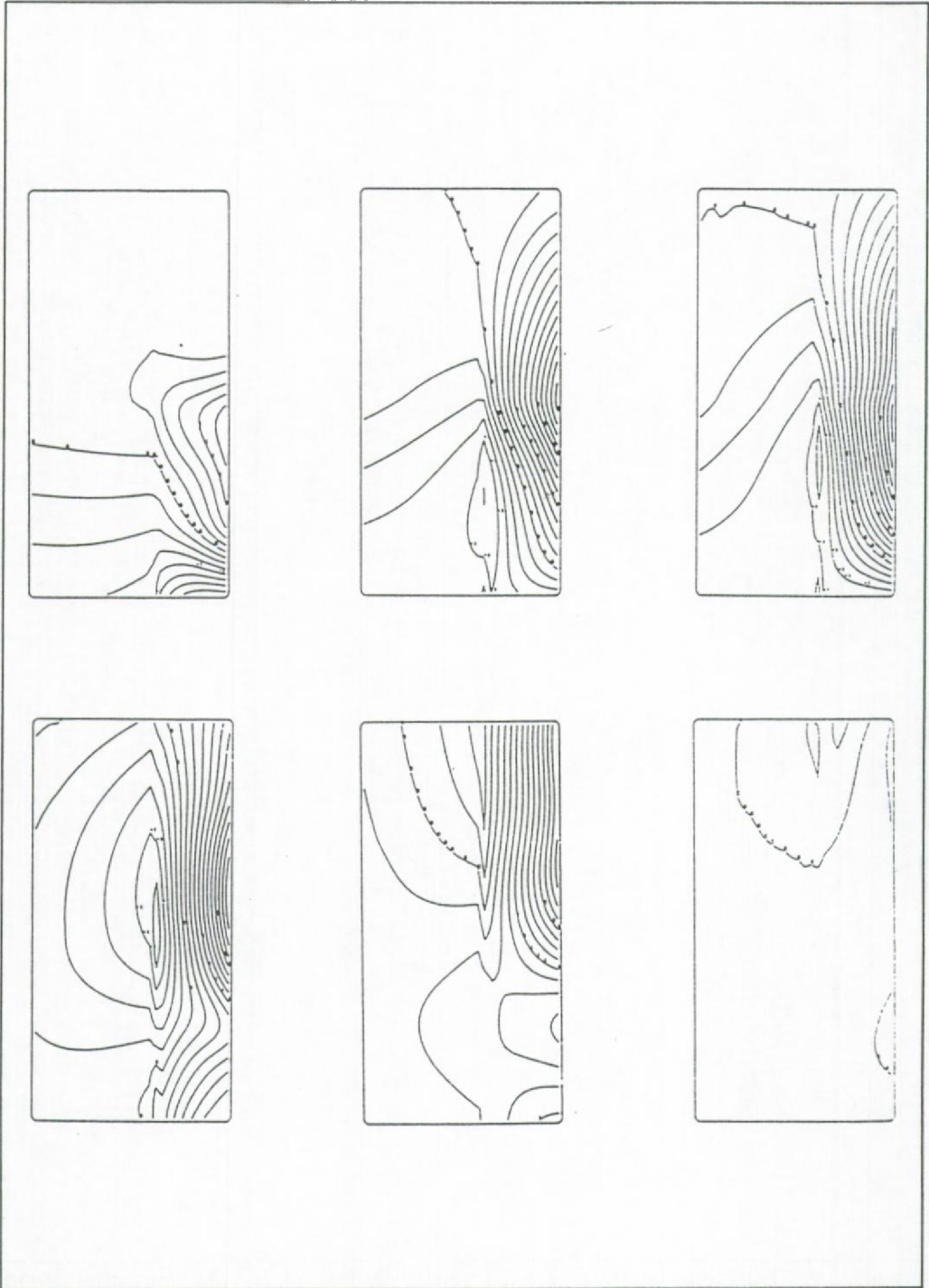


Figure 2.6: idem figure 2.5 except that the Camerlengo and O'Brien condition has been used.

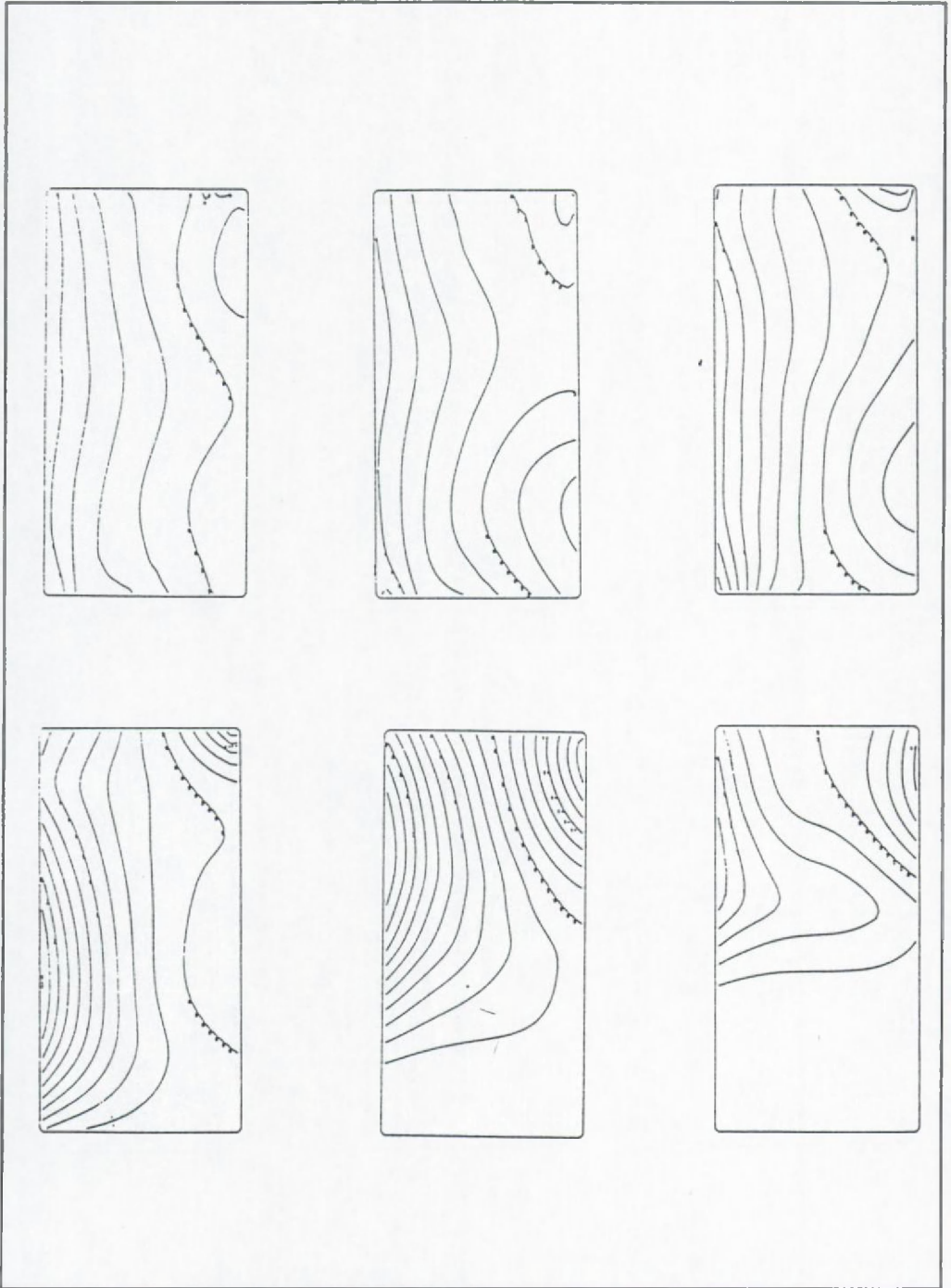


Figure 2.7: Surface elevation in dm (interval is 5cm) for the forced wave experiment. The Orlanski condition has been used. The solution is presented after 3, 6, 8, 16, 24 and 32 hours.

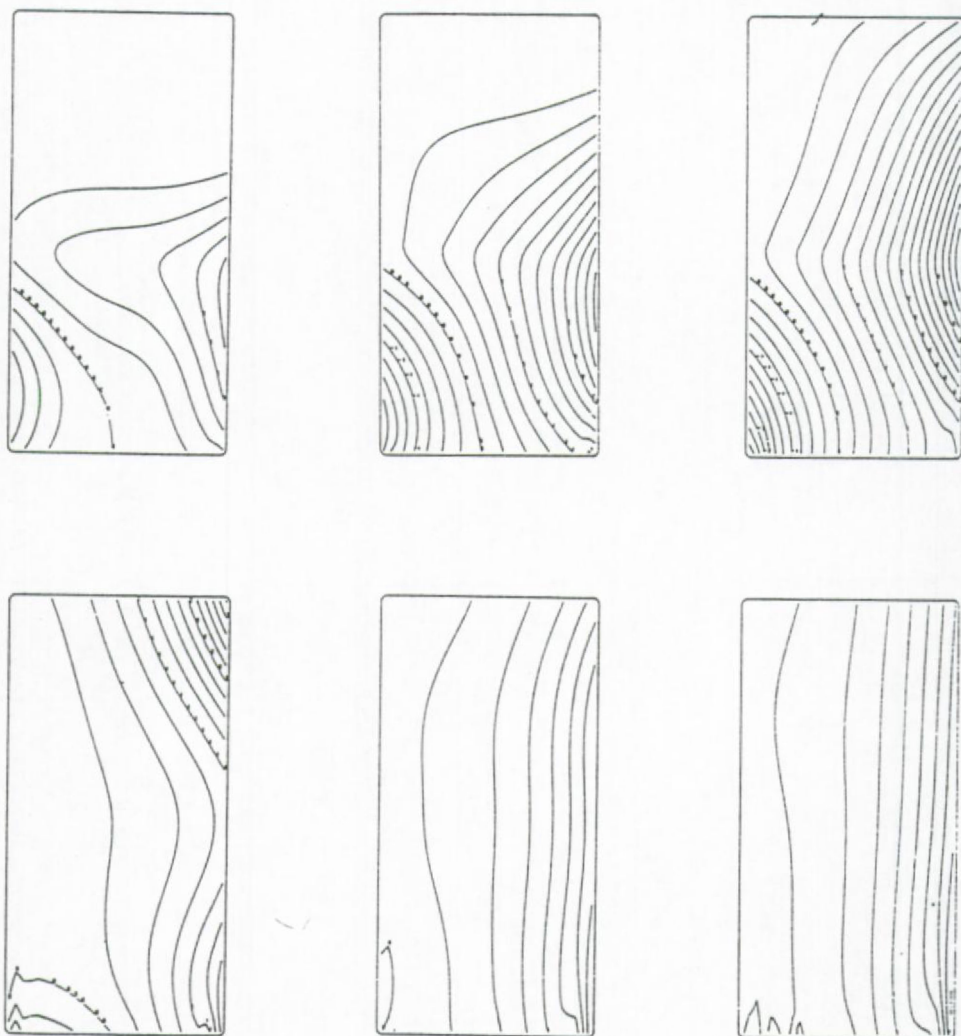


Figure 2.8: idem figure 2.7 except that the Camerlengo and O'Brien condition has been used.



### **2.5.3.        *Conclusions***

The results of three different simulations have been presented. Along the open boundary a radiation condition has been applied. The result of a literature study have indicated that the Orlanski and the Camerlengo and O'Brien open boundary conditions are the most promising ones. The numerical experiments have shown that the Camerlengo and O'Brien condition gives better results than the Orlanski condition. The Orlanski condition is behaving similar when no forcing is applied (barotropic relaxation). In the following the Camerlengo and O'Brien condition will therefore be used to describe the open boundary condition.

### **2.6.        Numerical Experiments Of Advection-Diffusion Dominated Flow Problems And Open Boundary Condition**

The results of the experiments presented in the previous section have shown that the Camerlengo and O'Brien (1980) approach of the Sommerfeld radiation condition is the most suitable. The experiments have, however, been carried out with a simplified model, since the advection and diffusion terms in the equations have been omitted. The numerical formulation of diffusion processes on a Eulerian grid (the velocity or scalar quantity is calculated at the discrete nodal points of the grid) is rather succesful. The Eulerian approximation of the advection terms is much more difficult to implement. The discretisation of the advective terms has since long been a major research topic.

In this paragraph two common and well known advection schemes, i.e. the 1<sup>st</sup> order upwind and the 3<sup>rd</sup> order QUICK scheme, have been used to simulate the flow behind a backward facing step in a long channel. The backward facing step is a typical example where advection and diffusion plays an inportant role. The aim is to investigate the behaviour of these two advection schemes in the vicinity of an open boundary described by the Camerlengo and O'Brien condition. This experiment forms a rigourous test of the open boundary condition. The results have been presented in Fettweis and Yu (1990a and 1990b). The simulations have been carried out using a 2D horizontal model as described below. The results of the model for the backward facing step problem (as presented by Gresho and Sani, 1988) will be discussed.

### 2.6.1. *Governing equation and numerical procedure*

For the simulation of flows without external forcing the 2D Navier-Stokes equations can be written as:

$$\frac{\partial V}{\partial t} + \nabla V^2 + \nabla p = \frac{1}{Re} \nabla^2 V \quad (2.35)$$

$$\nabla V = 0 \quad (2.36)$$

where  $Re$  is the Reynolds number,  $p$  the pressure and  $V$  the velocity vector. The equations are solved using the artificial compressibility method (Peyret and Taylor, 1983). The equations are discretised on a so-called Arakawa B-grid, *i.e.* the pressure  $p$  is situated on the corner points (integer index) and the  $u$  and  $v$  velocity components in the centre of a grid cell (at half integer index). The artificial compressibility method uses the momentum equation and the continuity equation in the following form:

$$\frac{V^{n+1} - V^n}{\Delta t} + V^n \nabla V^n + \nabla p^n - \frac{1}{Re} \nabla^2 V^n = 0 \quad (2.37)$$

$$\frac{p^{n+1} - p^n}{\Delta t} + c^2 \nabla V^{n+1} = 0 \quad (2.38)$$

The idea of the method consists in finding the steady state solution using the unsteady state equations in the limit when time tends to infinity. The solution of the continuity equation (2.38) has only a physical meaning when the time derivative of the pressure is equal to zero, *i.e.* the continuity equation is only fulfilled at convergence,  $c$  is an arbitrary constant. As is described by Peyret and Taylor (1983) equations (2.37) and (2.38) can be used to approximate the unsteady solution when  $c^2 \ll 1$ . Along the solid boundaries a no-slip condition is implemented, at the open boundary the velocity is either prescribed or calculated using the Camerlengo and O'Brien (1980) formulation of the radiation condition.

### 2.6.2. *Approximation of the advection and diffusion terms*

The finite difference approximation of the advective terms should be chosen carefully, since the accuracy of the solution and the possibility of induced instabilities depends strongly on the finite difference scheme. Shyy (1983) investigated the accuracy of the above described approximations for the advective-dominated flow

in case of steady state. This is the most difficult case to prevent instabilities. The 2<sup>nd</sup> order central difference operator is the commonly used algorithm. Bella (1970) found that this operator may give rise to oscillating results when the advective dominated flow is not in a well defined direction, e.g. recirculation in 2D problems as in the backward facing step. The central difference approximation results in an unconditionally unstable finite difference scheme in case of pure advective flow. The 1<sup>st</sup> order upwind scheme gives rise to large numerical diffusion resulting in a strong damping of the peak values, the scheme is however conditionally stable, see the experiments of Backhaus (1983), Falconer and Liu (1988) and Yu (1993). An advantage of the 1<sup>st</sup> order upwind scheme is that no phase lag occurs for pure advective flows and that it is oscillation free along the computational directions, because the operators are dependent on the local velocity directions. The QUICK scheme is a 3<sup>rd</sup> order upwind scheme combining the advantages of the upwind scheme and a higher accuracy and thus of a lower numerical diffusion.

The accuracy not only depends on the advection scheme but is strongly influenced by the treatment of it at the boundary. The points which fall outside the domain cannot be used and there exists different techniques to approximate the advection terms at the boundary. One consists in taking a lower order or one-side difference approximation; this technique is suited for the higher-order schemes, such as the QUICK scheme.

The 1<sup>st</sup> order upwind and the 3<sup>rd</sup> order Quick scheme for  $\partial u/\partial x$  are presented below (similar equations can be written for  $\partial u/\partial y$ ,  $\partial v/\partial x$  and  $\partial v/\partial y$ ):

1<sup>st</sup> order upwind scheme:

$$(u \frac{\partial u}{\partial x})_{i-\frac{1}{2},j-\frac{1}{2}} = u_{i-\frac{1}{2},j-\frac{1}{2}} (u_{i-\frac{1}{2},j-\frac{1}{2}} - u_{i-\frac{3}{2},j-\frac{1}{2}}) / \Delta x, \quad u_{i-\frac{1}{2},j-\frac{1}{2}} > 0 \quad (2.39)$$

3<sup>rd</sup> order QUICK scheme:

$$(u \frac{\partial u}{\partial x})_{i-\frac{1}{2},j-\frac{1}{2}} = u_{i-\frac{1}{2},j-\frac{1}{2}} (3u_{i-\frac{1}{2},j-\frac{1}{2}} - 3u_{i-\frac{1}{2},j-\frac{1}{2}} - 7u_{i-\frac{3}{2},j-\frac{1}{2}} + u_{i-\frac{5}{2},j-\frac{1}{2}}) / 8\Delta x, \\ u_{i-\frac{1}{2},j-\frac{1}{2}} > 0 \quad (2.40)$$

The diffusion terms can be easily approximated by a 2<sup>nd</sup> order central difference operator.



### 2.6.3. Discussion of the backward facing step results

The experiment has been set up by Gresho and Sani (1989) as a test problem for open boundary conditions. The domain is a rectangle of 1 unit wide and 15 units long for the long mesh, and 7 units long for the short mesh, with flow entering over half of the width only. The inlet boundary condition is a parabola for  $u(y)$  with a maximum of 1.5:  $u(y) = 24y(0.5 - y)$  and  $v(y) = 0$ . Except for the outflow end, the remainder of the domain has a no-slip boundary condition, see Figure 2.9.

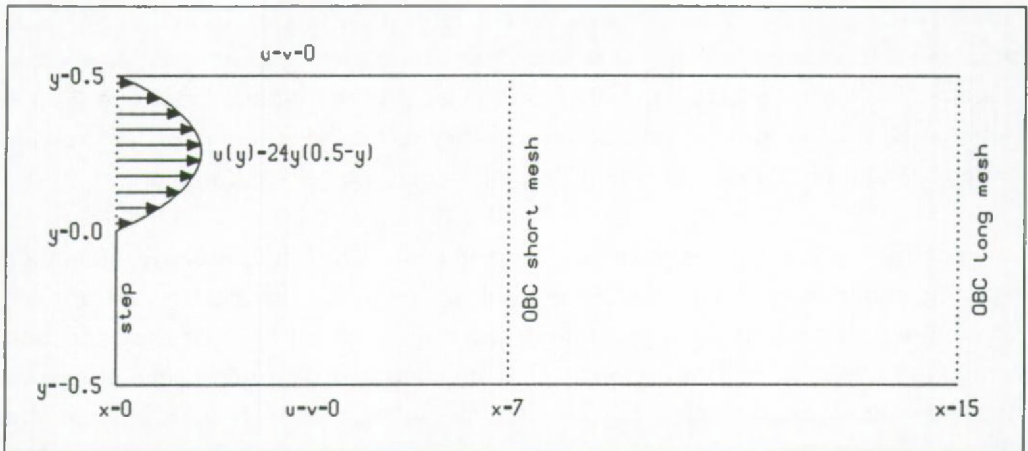


Figure 2.9: The geometry of the basin for the backward facing step problem, (OBC = open boundary condition).

When using the 1<sup>st</sup> order upstream scheme one can see that the eddy situated at the top ( $y = 1/2$ ) is absent and the eddy attached to the step is shorter, see Figure 2.10a. A more accurate solution (longer eddy at the step and secondary eddy at the opposite side) is obtained with the QUICK scheme, see Figure 2.10c. The velocity profile at the outflow end obtained with the 1<sup>st</sup> order upwind scheme is, in contrast with the results of the model using the QUICK scheme, a parabola and symmetric with respect to the  $y$ -axis. The 1<sup>st</sup> order upstream schemes gives almost the same results when the number of grid cell is doubled (half the original grid size), see Figure 2.10b. The starting and ending points of the eddies can easily be seen in the shear stress diagram ( $\partial u / \partial x$  vs.  $x$ ) along the top and bottom walls, see Figure 2.11.

In order to test the ability of the open boundary condition a long (15 units) and a short (7 units) mesh have been used. The open boundary of the long mesh is situated at a place ( $x = 15$ ) where the flow is again unidirectional and outgoing. Open boundary conditions which are based on extrapolation of values of interior

grid points towards the boundary can handle this case. The short mesh however has its open boundary through the centre of the secondary eddy (at  $x = 7$ ), the flow there is bidirectional and an open boundary condition based on the separation into ingoing and outgoing is needed. In Figure 2.12 the velocity vectors are displayed for the short domain and for both advection schemes. These results should be compared with those of Figure 2.10. Notice that the grid size in Figure 2.10b, 2.12b and 2.12c in the  $x$ -direction is half as large as that of Figures 2.10a, 2.10c and 2.12a.

The Courant number ( $C = u\Delta t/\Delta x$ ) is small, the cell Peclet number ( $Pe = u\Delta x Re$ ) is 600 for the coarse grid size mesh. It is known (Shyy, 1983) that for high Peclet numbers the Quick scheme can show some oscillations or wiggles in the solution. Following this author, these inaccuracies are not only dependent on the grid size, they can be influenced by the boundary condition and placement. For the Quick scheme model numerical wiggles occur when the short mesh together with the coarse grid size is used. The fine grid size calculations, Figure 2.12c, however are not exciting oscillations and show a result which is similar to the long mesh / coarse grid size solution (Figure 2.9c).

The solution by the 1<sup>st</sup> order upwind scheme is free of oscillation, the grid size influences however the accuracy of the solution. A (weak) secondary eddy (see Figure 2.12b) can be observed in case the fine grid has been used in contrast with the coarse grid result of Figure 2.12a. Similar results can be observed with the long mesh calculations, see Figure 2.10.

## 2.7. Conclusion and Summary

In this chapter an ice-ocean model has been presented. The ocean model enters the class of the so-called 2.5D models. These models are calculating the 3D velocity field in a vertical plane, assuming that the gradients perpendicular to this plane are zero. The assumption on which the model equations have been developed are: hydrostatic pressure distribution, rigid-lid approximation, Boussinesq approximation, eddy viscosity and diffusivity concepts. The governing equations are solved using an explicit scheme. The 1.5D ice model only takes into account the dynamics of ice. Thermodynamic processes have been ignored, because we are only interested in mesoscale phenomena.

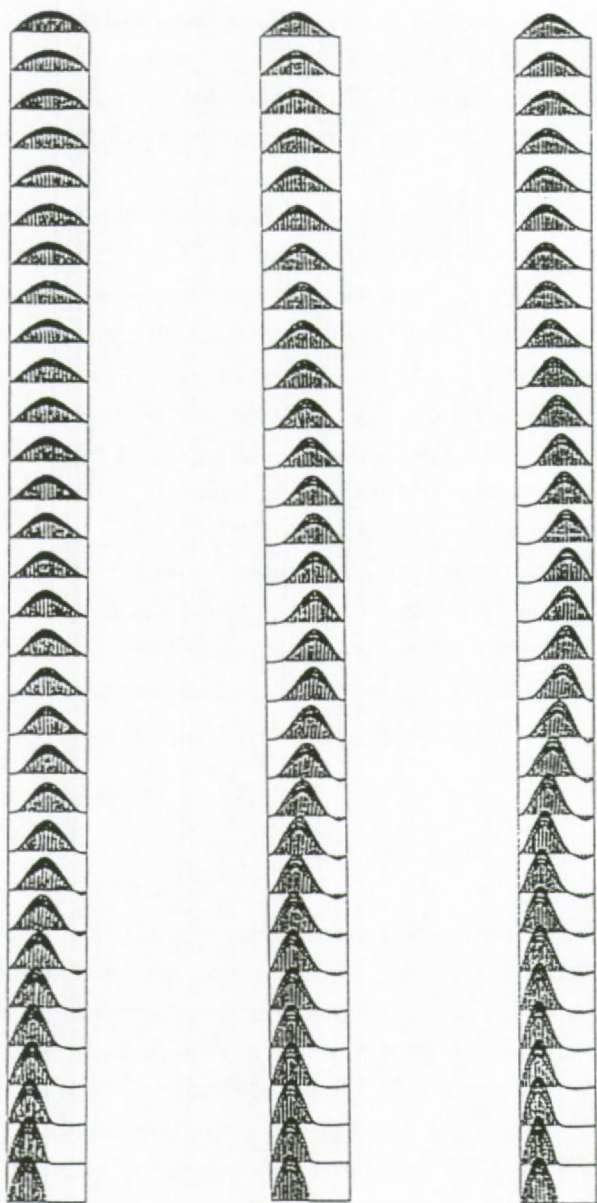


Figure 2.10: Backward facing step, long mesh. (a) 1<sup>st</sup> upstream scheme and coarse grid, (b) 1<sup>st</sup> upstream and fine grid and (c) QUICK scheme and coarse grid.



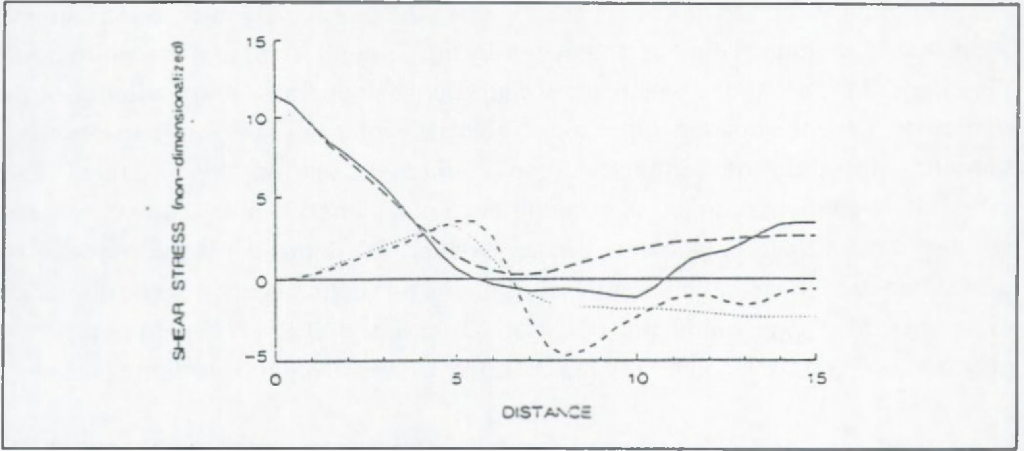


Figure 2.11: Shear stress along walls, coarse grid. Quick scheme at  $y = 1/2$  (solid) and  $y = -1/2$  (short dash). 1<sup>st</sup> upwind scheme at  $y = 1/2$  (long dash) and  $y = -1/2$  (dot).

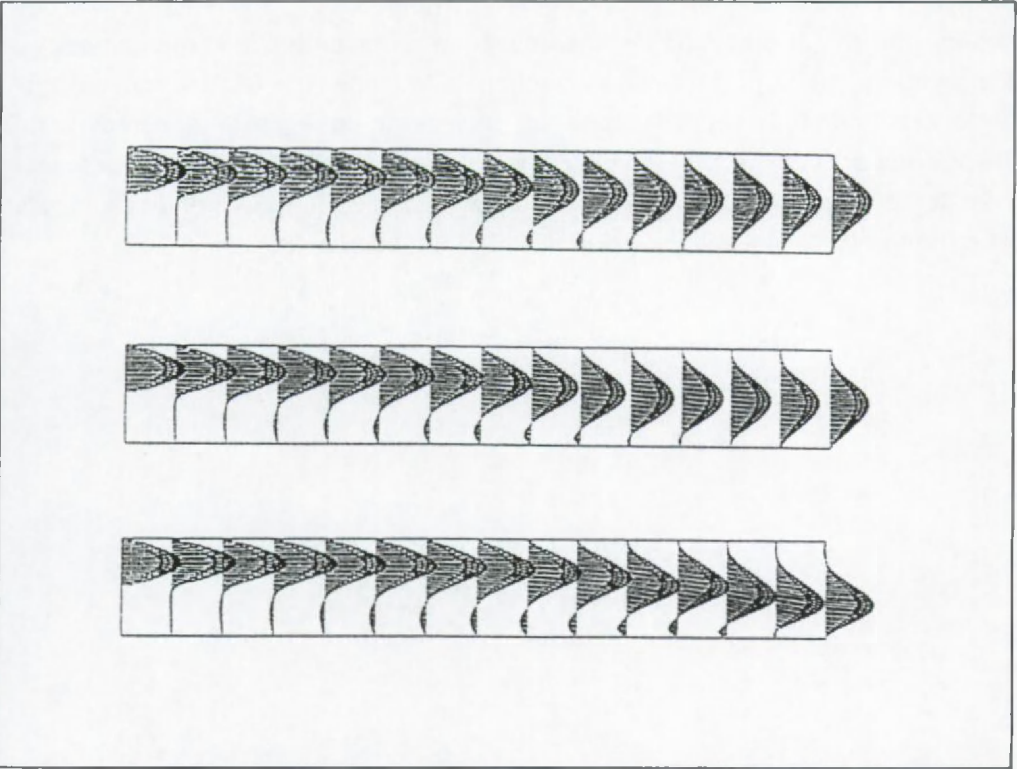


Figure 2.12: Backward facing step, short mesh. (a) 1<sup>st</sup> upwind scheme and coarse grid, (b) 1<sup>st</sup> upwind scheme and fine grid and (c) QUICK scheme and fine grid.

Open boundary conditions are necessary when the domain of integration is smaller than the geographical dimensions of the basin. The most appropriate open boundary conditions are those which allow disturbances generated in the interior of the domain to leave the domain without disturbing the interior solution. Open boundary condition based on the Sommerfeld condition have been most widely used. Two different implementation of this condition, i.e. Orlanski's and Camerlengo and O'Brien's have been implemented in an existing 2D depth averaged model. The performance of these open boundary conditions has been tested in some numerical experiments. It was found that the Camerlengo and O'Brien implementation is giving equal or better quality results than the Orlanski implementation.

The Camerlengo and O'Brien open boundary condition has been implemented in a 2D horizontal flow model. The model has been developed to calculate the flow at a backward facing step and to investigate the performance of an open boundary condition in a convection-diffusion dominated flow. Behind the step an eddy is formed, while a secondary eddy can be seen opposite to the step. It has been shown that the discretisation of the advection terms determines the accuracy of the solution. Higher order upstream schemes, such as the QUICK scheme, give better results than lower order schemes. In order to get a similar accuracy with a lower order scheme as with a higher order one, the grid size has to be decreased. The Camerlengo and O'Brien open boundary conditions gave good results also when the open boundary had been placed in the eddy zone.

## CHAPTER 3

### HYDRODYNAMIC RESPONSE TO KATABATIC WIND FORCING

#### 3.1. Introduction

Katabatic winds are formed by cooling air on a sloped ice covered surface. These winds can reach very high velocities in the coastal zone of the Antarctic continent. If the winds are strong enough coastal polynyas can be formed. Polynyas are openings in sea ice. They range in size from a few hundred metres to hundreds of kilometres. Traditionally polynyas are characterized according to their mechanism of formation, i.e. latent heat and sensible heat polynyas (Schneider and Budéus, 1995). In the first type, the forming ice or the existing ice floes are continually removed from the region by currents and winds. An example is a coastal polynya formed by offshore winds. In the second type, the sensible heat polynya, oceanic heat from warmer deeper layers enters a region in sufficient quantity to prevent local ice formation. In these open water zones important energy exchanges occur between the water and the air leading to the formation of sea ice and dense water.

The content of § 3.2.-3.6. is the summary of the results of a collaboration between the KUL (Hydraulics Laboratory), the MUMM and the UCL (Institut d'Astronomie et de Géophysique G. Lemaître) in the framework of the Belgian Scientific Research Programme on Antarctic, see Fettweis et al. (1991b). The aim of the study was to compare the hydrodynamic response to katabatic wind forcing using two different ocean models and to investigate whether the currents induced by katabatic winds can be responsible for the formation of coastal polynyas. The ocean was supposed to be ice free and barotropic. In this chapter the emphasis is on the hydrodynamic part. The simulation of the katabatic wind field and the



development of the atmospheric model have been prepared by the UCL, therefore only the results of the atmospheric model will be presented here. The calculated wind field has been used as input for the two ocean models. The aim of the study can be summarized as follows:

- setting up a realistic case to simulate the currents in a vertical plane driven by katabatic winds and to look especially at the near shore oceanic response in order to explain whether coastal polynias can be formed by these winds.
- using this case for a comparison study between two 2.5D vertical plane models of the KUL and the MUMM and an analytical solution in order to validate the model.
- analyzing the results as a function of the differences in numerical solution techniques.

The first item, i.e. setting up a realistic case, needs to be clarified in more detail. A realistic case study of this phenomena would imply at least a coupled ice-ocean model including density induced flows and thermohaline effects. Since one of the primary goals of this experiment was to compare the results of two numerical ocean models, the case study has been restricted here to a model intercomparison using a realistic bathymetry and a realistic wind forcing but excluding all baroclinic effects. Due to this simplification it was possible to compare the model results with an analytical solution.

The two 2.5D ocean models are both solving the same equations using the finite difference method, but differ in the way the equations are discretised. The KUL model applies an explicit scheme using a Cartesian coordinate system, whereas MUMM's model is semi-implicit and calculates the currents in a  $\sigma$ -plane. Intercomparison of models is important and interesting in order to get an idea of the quality of the model results. Since measurements are scarce in the ocean surrounding the Antarctic continent, much of what is known about the oceanographic characteristics has been obtained through models. Intercomparison of models allow to get an idea about reliability and accuracy of the results, it does not prove however that the model results are correct. This can only be achieved through the comparison of the model with measurements or with an analytical solution of the simplified governing equations.

In § 3.7 the preliminary results of a 3D model study forced by a katabatic wind in the Terra Nova coastal area are presented.

### 3.2. Katabatic Wind Simulation

The atmosphere is simulated with the UCL hydrostatic mesoscale primitive equation model, assuming homogeneity of the dependent variables along the coast (the so-called 2.5D approach). The model makes use of the  $\sigma$ -coordinate system. A detailed description of the model can be found in Gallée et al. (1989) and Fettweis et al. (1991b). In this paragraph the simulation of a katabatic wind over the Adélie Land terrain profile are presented. The model domain covers 2000km of ocean and 2000km of land. The ocean is chosen to be ice free. The choice of a such large domain allows to perform a long simulation (5 days) without any influences of the boundaries on the simulated atmospheric circulation. Moreover, the quasi-steady state atmospheric circulation obtained at the end of such a long simulation could be considered as varying little over the long time during which it is used to force the oceanic model.

The main results of the simulation are shown in Figure 3.1 (x dependence of the horizontal components of the wind) and Figure 3.2 (x dependence of the friction velocity and the horizontal wind norm). The strongest winds are simulated near the coast. In this area the winds are blowing from the south-east (direction southeasterly winds). A reversal in the wind direction is found at roughly 200km off the coast.

### 3.3. Description Of The 2.5D Ocean Models

The 2.5D models solve the 3D hydrodynamic equations in the form presented in Chapter 2, see equations (2.2), (2.3), (2.5) and (2.9). All the gradients with respect to the  $y$ -direction are considered to be zero. The pressure is assumed to be hydrostatic and the energy loss due to friction is parameterized by means of eddy viscosity coefficients. The models are barotropic.

The boundary conditions have been chosen as follows. At the coastal walls the  $u$ - and  $v$ -velocity components are supposed to be zero, at the bottom all the three velocity components are zero (no-slip condition). At the open boundaries the velocity gradients are set to zero.

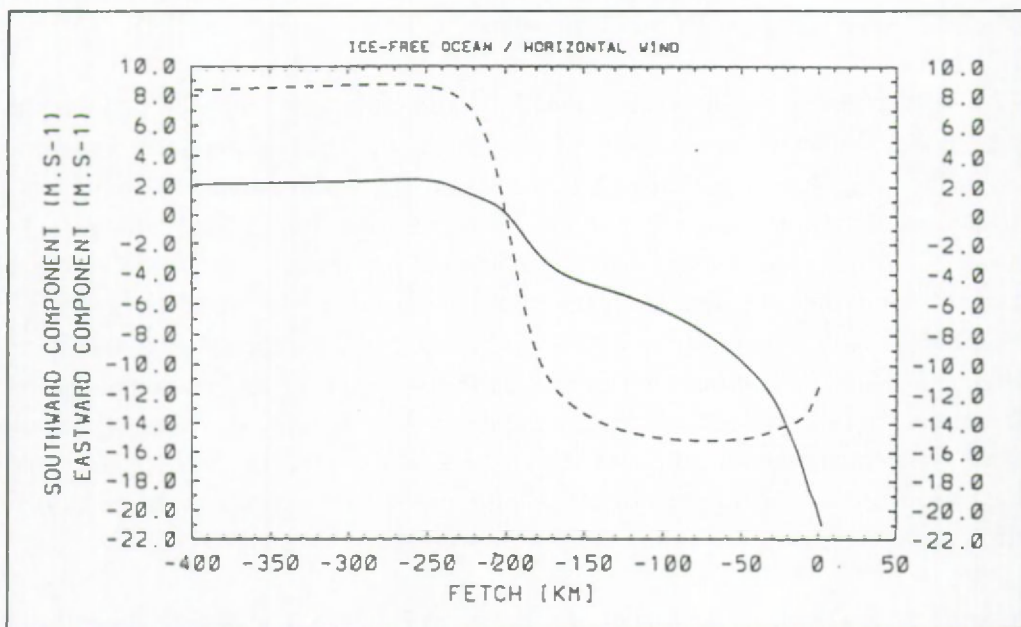


Figure 3.1:  $x$  dependence of the horizontal wind component. Southward ( $u$ , full line) and eastward component ( $v$ , dashed line), positive distances are on land.

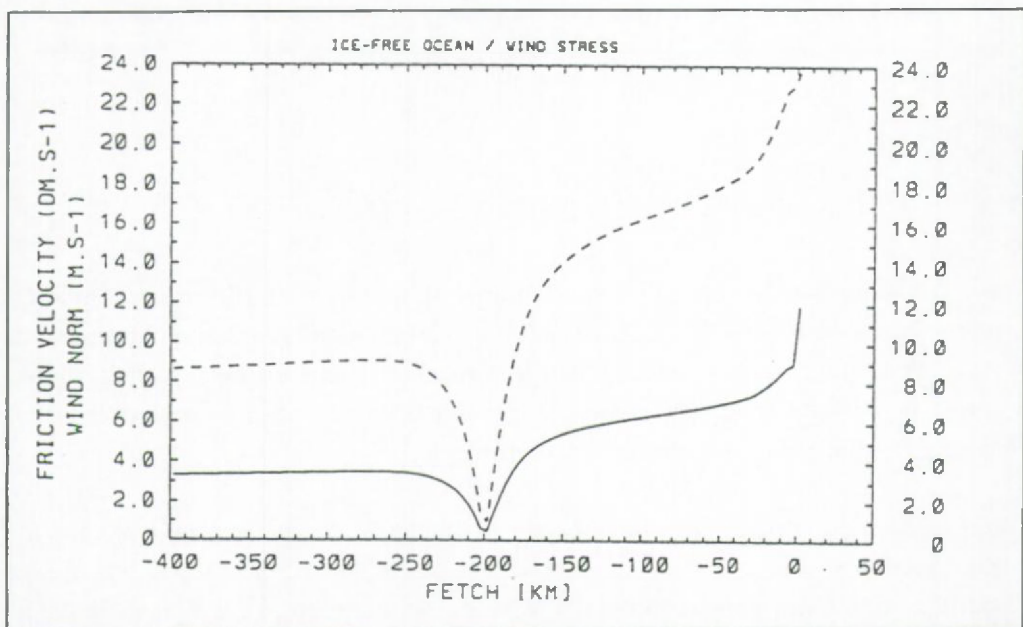


Figure 3.2:  $x$  dependence of the friction velocity and the horizontal wind norm. Friction velocity (full line) and horizontal wind norm (dashed line), positive distances are on land.



The two models participating in the intercomparison exercise are the KUL model, described in § 2.2. and the MUMM model. For a description of this latter model the reader is referred to Spitz et al. (1987) and Fettweis et al. (1991b).

### 3.4. Differences Between The Models

In this section the differences between the two models concerning the numerical solution of the equations are outlined. The differences are summarized in Table 3.1 together with the characteristics of the Ekman solution, which will be described in § 3.5.2.1.

Table 3.1 Differences between both models and the Ekman solution.

	KUL	MUMM	Ekman
Grid	B	B	-
Vert. coord.	Cartesian	$\sigma$	-
Bottom	through w-points	through u/v-points	-
Horizontal advection	explicit 1 <sup>st</sup> order upwind	explicit 2 <sup>nd</sup> order central	no
Vertical advection	explicit 1 <sup>st</sup> order upwind	semi-implicit 2 <sup>nd</sup> order central	no
Horizontal diffusion	explicit 2 <sup>nd</sup> order central	explicit 2 <sup>nd</sup> order central	no
Vertical diffusion	explicit 2 <sup>nd</sup> order central 1 <sup>st</sup> order 1 <sup>side</sup> at top & bottom	semi-implicit 2 <sup>nd</sup> order central 2 <sup>nd</sup> order 1 <sup>side</sup> at top & bottom	yes
Coriolis term	implicit (u) explicit (v)	semi-implicit	yes

The models solve the equations on a staggered so-called B-grid using finite differences. The KUL model is basically using an explicit scheme (some terms, e.g. Coriolis and pressure term in *u*-momentum equation are treated implicitly) and uses Cartesian coordinates, whereas the MUMM model is semi-implicit (Crank-Nicholson scheme) using  $\sigma$ -coordinates in the vertical plane. Although both models make use

of a B-grid, differences occur in the position of the bottom. The bottom is going through w-points in the KUL model, whereas in the MUMM model the bottom has been placed through  $u/v$ -points.

The treatment of the advection and diffusion terms is different. The advection terms are approximated by an explicit first order upwind scheme in the KUL model and by an explicit second order central scheme in the MUMM model. At a boundary the second order central scheme is replaced by a second order one side difference scheme.

Beside the explicit/semi-implicit approach there exist differences in the treatment of the vertical diffusion terms in the surface layer: the MUMM model makes use of second order one-side and the KUL model of first order one-side differences.

The Coriolis term is treated semi-implicitly in the MUMM model. The KUL model has an explicit Coriolis discretisation in the  $v$ -momentum equation and an implicit one in the  $u$ -momentum equation.

### 3.5. Comparison Of The Model Results

#### 3.5.1. *Description of the test cases*

The area of Adélie coast has been chosen as example for the intercomparison exercise. Four different cases have been set up, for all of them the vertical plane is 500km long.

The domain is bounded in the south by a coastal boundary. The northern boundary is an open sea boundary. The bathymetry in the four cases differs: Case 1 has a constant depth of 400m, whereas for the other ones the shelf is interrupted by a shelf break with a slope of 5%. The depth outside the shelf and the shelf slope is 4000m.

Three different placements of the shelf break have been proposed. Case 2s has a short shelf (80km), Case 2o a medium shelf (160km) and case 2l a long shelf (280km), see Figure 3.3. The length of the shelf of case 2o corresponds with the information read from the map. These oceans are forced by a katabatic wind. The wind is such that coming from the coast it is decreasing to zero at about 200km and is then blowing in opposite direction (eastward), see Figure 3.1. This zero wind velocity point is situated above the shelf slope in case 2o, in case 2l the shelf slope is north of it, whereas in case 2s it is south of this point.

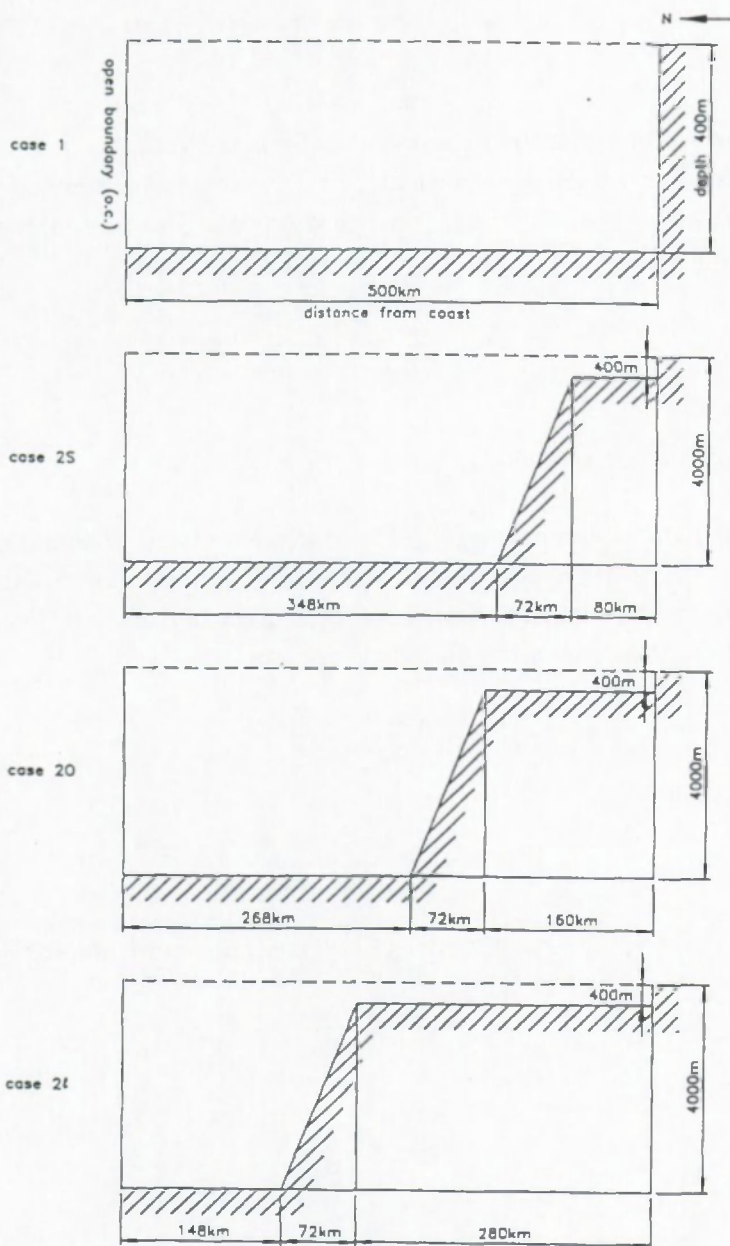


Figure 3.3: Dimension of the basins.



The horizontal grid size is 4km, the horizontal eddy viscosity coefficient  $A_h$  is 200m<sup>2</sup>/s, the vertical eddy viscosity  $A_v$  is constant and has a value of 0.01m<sup>2</sup>/s, the acceleration due to gravity  $g$  is 9.81m/s<sup>2</sup> and the Coriolis parameter  $f$  has been taken at 67.5°S ( $-1.34 \cdot 10^{-4} \text{ s}^{-1}$ ). A Katabatic wind is blowing over the water surface.

As was discussed in § 3.4, the two models differ in the vertical coordinate system used. Therefore it has been decided to focus for the detailed comparison on the flat bottom case (case 1). The vertical grid size is constant for both models and has been set to 10m.

### 3.5.2. Case 1: Flat bottom

#### 3.5.2.1. Ekman's solution

The general equations can be simplified to obtain an analytical solution for  $u$  and  $v$ , see Ekman (1905). If the adjustment to the wind forcing leads to a steady state the time dependent terms can be skipped. Dropping the horizontal diffusion and the advection terms, the momentum equations become:

$$f v = A_v \frac{\partial^2 u}{\partial z^2} - \frac{1}{\rho_0} \frac{\partial p}{\partial x} \quad (3.1)$$

$$-f u = A_v \frac{\partial^2 v}{\partial z^2} - \frac{1}{\rho_0} \frac{\partial p}{\partial y} \quad (3.2)$$

At the surface and bottom the following boundary conditions are applied:

Top: 
$$-A_v \frac{\partial u}{\partial z} = \frac{\tau_{sw,x}}{\rho_0} \quad (3.3)$$

$$-A_v \frac{\partial v}{\partial z} = \frac{\tau_{sw,y}}{\rho_0} \quad (3.4)$$

Bottom: 
$$u = v = 0 \quad (3.5)$$

where  $\tau_{sw,x}$  and  $\tau_{sw,y}$  are the components of the wind stress.

In order to solve the equations two more conditions are necessary to calculate the pressure gradient terms  $\partial p / \partial x$  and  $\partial p / \partial y$ . For the pressure gradient along  $x$  we

impose:

$$\bar{U} = \int_0^h U \, dz = 0 \quad (3.6)$$

where  $h$  is the height of the water column. The pressure gradient along  $y$  is assumed to be zero:  $\partial P / \partial y = 0$ .

Introducing a complex velocity and a complex wind stress with ( $i^2 = -1$ ):

$$U = u + iv \quad (3.7)$$

$$\tau = \tau_{sw,x} + i\tau_{sw,y} \quad (3.8)$$

and combining equations (3.1) and (3.2) we obtain:

$$\frac{\partial^2 U}{\partial z^2} - \alpha^2 U = \frac{1}{A_v \rho_0} \frac{\partial \rho}{\partial x} \quad (3.9)$$

where

$$\alpha = \sqrt{if/A_v} \quad (3.10)$$

with the boundary conditions at the surface and at the bottom:

$$-A_v \frac{\partial U}{\partial z} = \frac{\tau}{\rho_0} \quad (3.11)$$

$$U = 0 \quad (3.12)$$

The solution of the problem can be readily calculated by:

$$U = \frac{\tau}{\rho_0 A_v \alpha} \left[ \frac{\sinh(\alpha(h-z))}{\cosh(\alpha h)} \right] - \frac{i}{f \rho_0} \frac{\partial \rho}{\partial x} \left[ 1 - \frac{\cosh(\alpha z)}{\cosh(\alpha h)} \right] \quad (3.13)$$

### 3.5.2.2. Results of the simulations

The results described in this chapter have been obtained with the two models presented in § 3.3. No attempts have been made to unify some of the features of the numerical scheme.

The initial conditions have been described in § 3.5.1. The models start with the calculation at  $t=0$  and continue until 50 days have been simulated. The results have been stored at this time and compared to each other and to the Ekman solution. The results have reached nearly steady state after 50 days of simulation.

The path of the pressure gradient with distance is shown in Figure 3.4. As can be seen from the figure the pressure gradient for the three proposed solution is different. The absolute value of the pressure gradient is on the whole lower for the KUL model than for the MUMM model. Ekman's solution is, except in the region around 200km and near the closed boundary where horizontal diffusion and advection play a significant role, in between the solution of the numerical models.

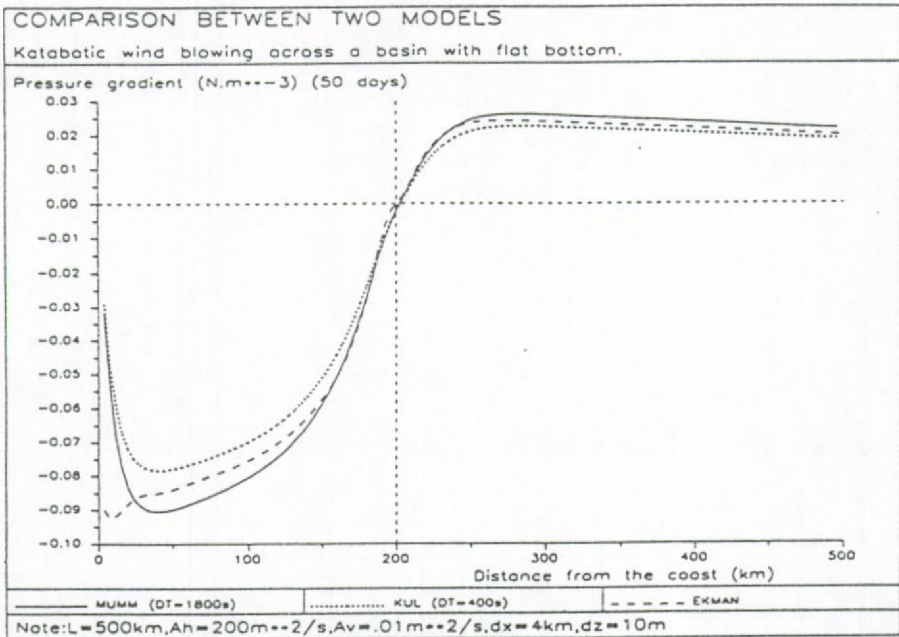


Figure 3.4: Pressure gradient with distance (longitudinal direction) after 50 days for case 1. The vertical grid size is 10m.

In Figure 3.5 the flow fields in the vertical plane are shown (northward and vertical currents). The flow pattern consist of two major cells, in the first 200km the flow is directed on-shore in the top layer, except close to the continent, with downwelling at the continental margin, off-shore flow at the bottom and upwelling around 200km. At about 50m depth and close to the continental boundary a vertical eddy exists. For the second cell (from 200km to 500km) the flow is in opposite direction, off-shore at the top and on-shore at the bottom. Figure 3.6 gives an enlargement of the first 80km of the basin. It is noticeable on this figure that, although the flow in the surface layer is directed on-shore, a seaward flow exists at the surface in the first 10km. This behaviour of the surface flow near the coast, in agreement with the Ekman theory, can give an indication of the formation of

coastal polynyas. Of course, as was already mentioned in the beginning, the formation of coastal polynyas cannot be fully explained by this flow structure. Further away from the coast the surface flow is directed towards the coast. Differences between the two model solutions can be observed at the continental boundary. The horizontal extension of the off-shore directed flow in the surface layer close to the continent is shorter in the KUL model than for the MUMM model. The layer at the continental margin where downwelling occurs is thinner for the KUL model, this results also in a different shape and placement of the vertical eddy between the two models.

In what follows  $u$  and  $v$  velocity profiles at 8km, 100km and 300km and a  $w$  profile at 8km are presented. The velocity profile at 8km is near the closed boundary, the 100km profile is in the middle of the first cell and the 300km profile is in the centre area of the second cell.

The northward velocity profiles (i.e.  $u$ -velocity) are presented in Figure 3.7. It can be seen that the results of the two models are nearly identical. Differences occur however at the surface and at the bottom.

For the point close to the continent (8km profile) the KUL model underestimates the surface and the bottom velocity. The results of both models are getting closer to the Ekman solution as the distance towards the coast increases. In other words the importance of the non linear terms is decreasing in direction of the open sea. At 100km and 300km the results of the models are nearly perfectly matching Ekman's solution, except in the top and the bottom layer.

The eastward velocity profiles (i.e.  $v$ -velocity) are given in Figure 3.8. At all locations a difference can be observed between the three solutions, the absolute value of KUL's solution is lower than Ekman's solution and the absolute value of MUMM's solution is higher than Ekman's one. These differences are proportional to the differences in pressure gradient occurring between the three solutions, see Figure 3.4. The northward pressure gradient ( $\partial p / \partial x$ ), computed in such a way to ensure a transport equal to zero in that direction, influences directly through the Coriolis term the transport in the eastward direction.

The vertical velocity profile is only shown at 8km from the coast because in this point the differences between both model results are high, see Figure 3.9. The shape of the profiles is similar but the two curves are not matching. These differences reflect the differences which were found in the continental boundary layer between the two model results.



### 3.5.3. Case 2: Shelf/ocean

As mentioned above three different cases have been treated consisting all of a shelf and a deep ocean part. The dimensions of the basin have been given in Figure 3.4. We want to present only the general flow pattern in the vertical plane. The differences between the results of the two models as discussed in the previous section remain for these cases. Besides the numerical differences, the resolution of the vertical plane is different. Due to the  $\sigma$ -coordinates used by the MUMM model the number of wet points in the vertical plane is constant, whereas in the KUL model the number of wet points depends on the local waterdepth. The different vertical grid sizes are responsible for some of the differences observed in the results since the vertical resolution is not the same in the two models.

The results of the models have been obtained after 20 days of simulation. The time scale for horizontal momentum to diffuse to the bottom can be expressed as  $E_v^{-1/2}/f$ , where  $E_v$  is the vertical Ekman number ( $E_v = A_v/fh^2$ , the Ekman number is a non-dimensional ratio of the friction terms to the Coriolis term),  $f$  the Coriolis parameter and  $A_v$  the vertical eddy viscosity coefficient, see Niebauer (1982). In the shelf ocean case these spin up time scales are between 4 days (shelf) and 40 days (ocean). This means that the 20 days simulation is too short in order to form a fully developed bottom Ekman layer in the deep part of the model domain. Indeed, as was found from the results, the solution was not yet stationary. In both models a strong surface and bottom Ekman layer is developed in the shelf zone (cfr. case 1), whereas the flow in the deep ocean part is almost zero except at the top. Due to the finer resolution of the bottom and top in the KUL model the boundary layers are better resolved in the deeper part of the basin. The differences resulting from different vertical grid sizes can be clearly seen in the figures presented below.

In case 2s (short shelf), the shelf and the slope are situated in the area where the wind is blowing in northward direction (Figure 3.3). Downwelling occurs along the slope followed by upwelling at about 150km off shore, i.e. the beginning of the slope, see Figure 3.10. The magnitude of this upwelling flow is gradually decreasing with decreasing depth. The flow on the coastal side of the shelf is similar with the results of case 1.

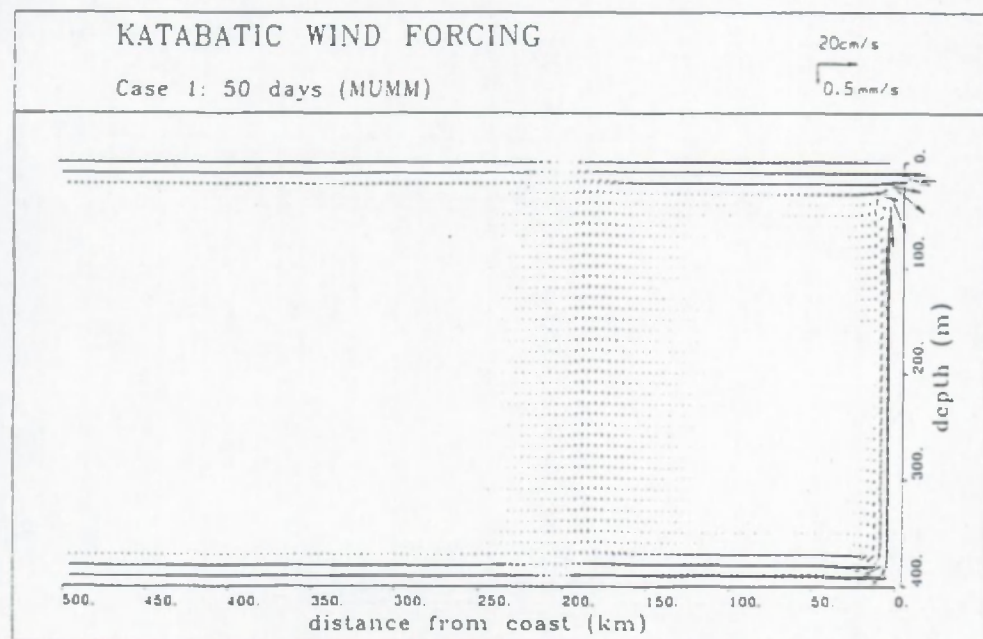
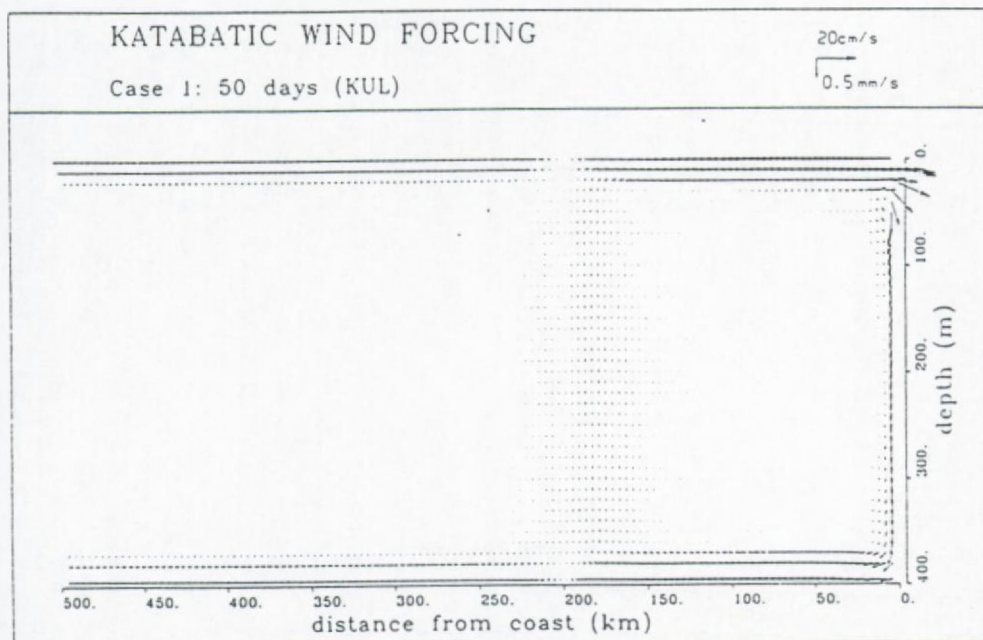


Figure 3.5: Flow field in the vertical plane ( $u$  and  $w$  components) for case 1, (a) KUL's results and (b) MUMM's results. The vertical grid size is 10m.

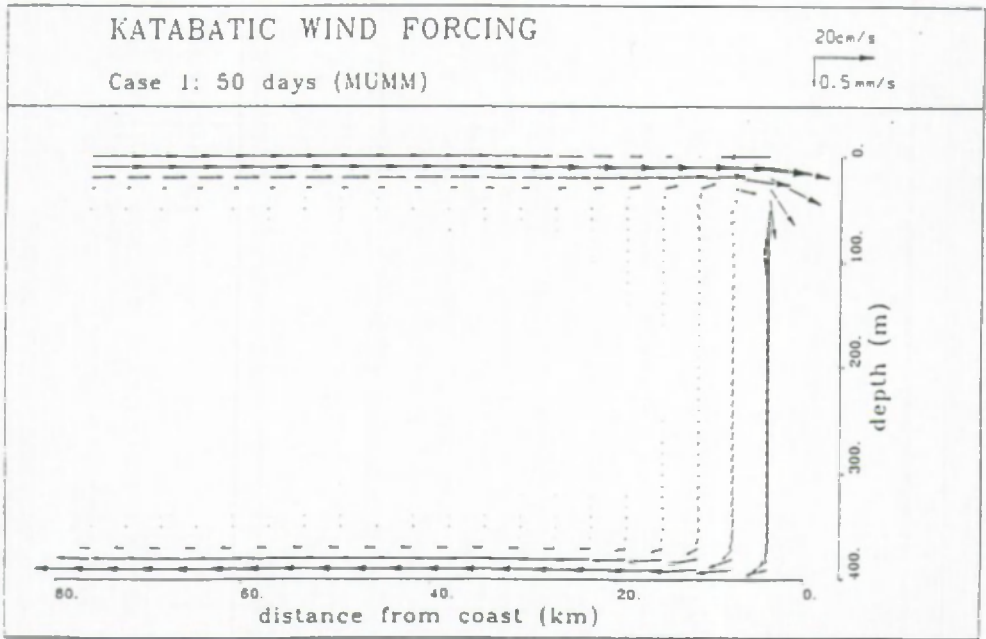
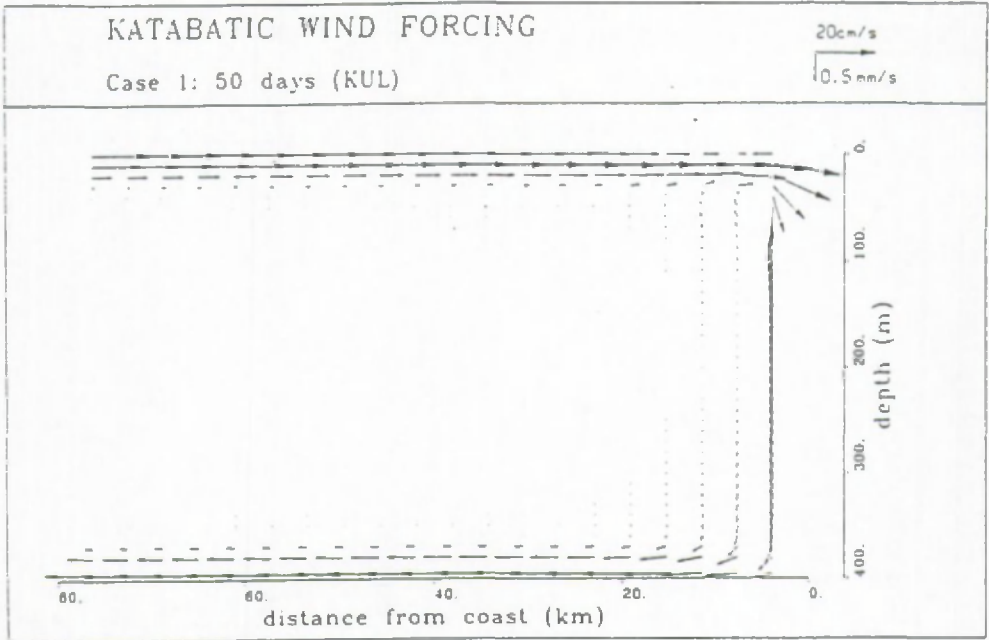


Figure 3.6: Enlargement of figure 3.5, (a) KUL's results and (b) MUMM's results.

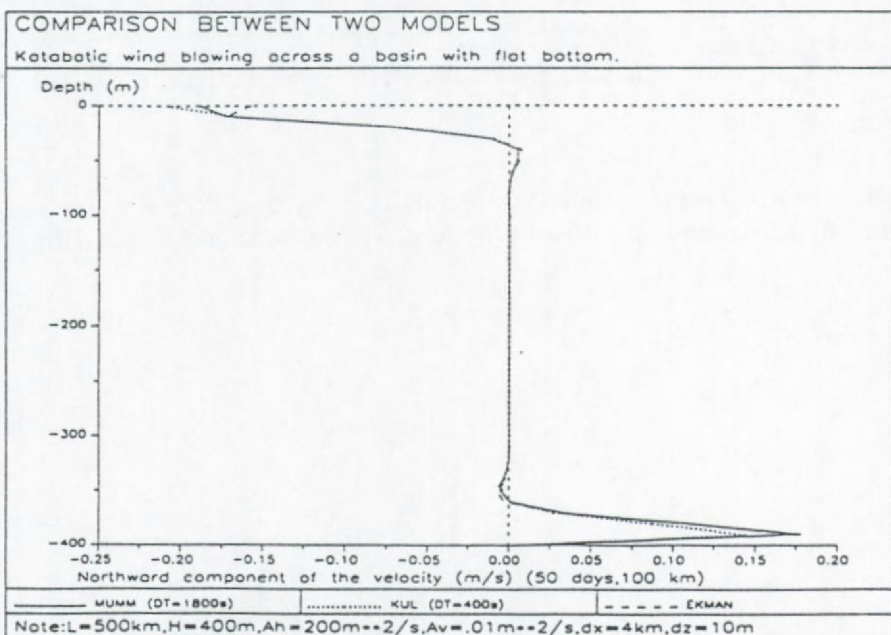
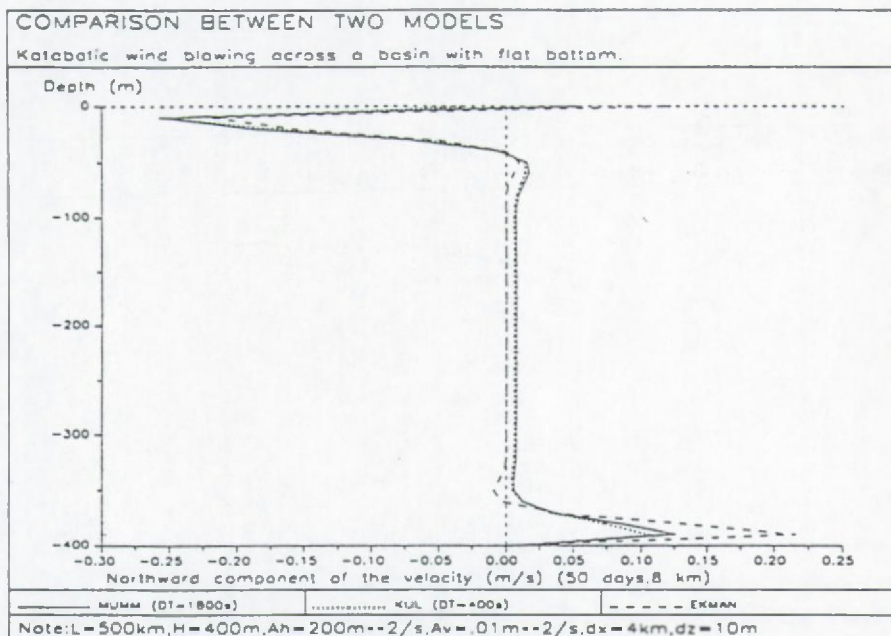


Figure 3.7: explanation see next page.



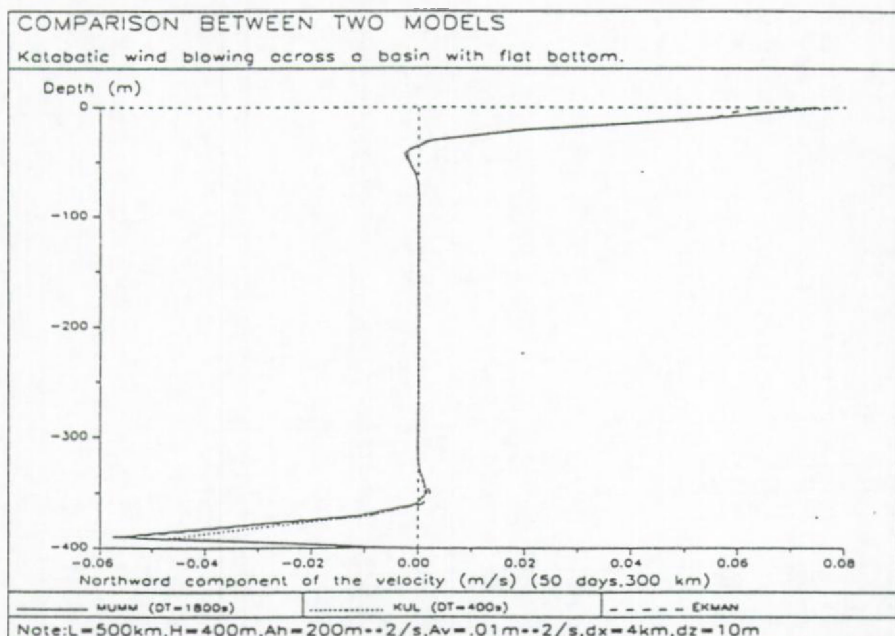


Figure 3.7: Northward ( $u$ ) velocity component profile after 50 days for case 1 at (a) 8km, (b) 100km and (c) 300km off shore. The vertical grid size is 10m.

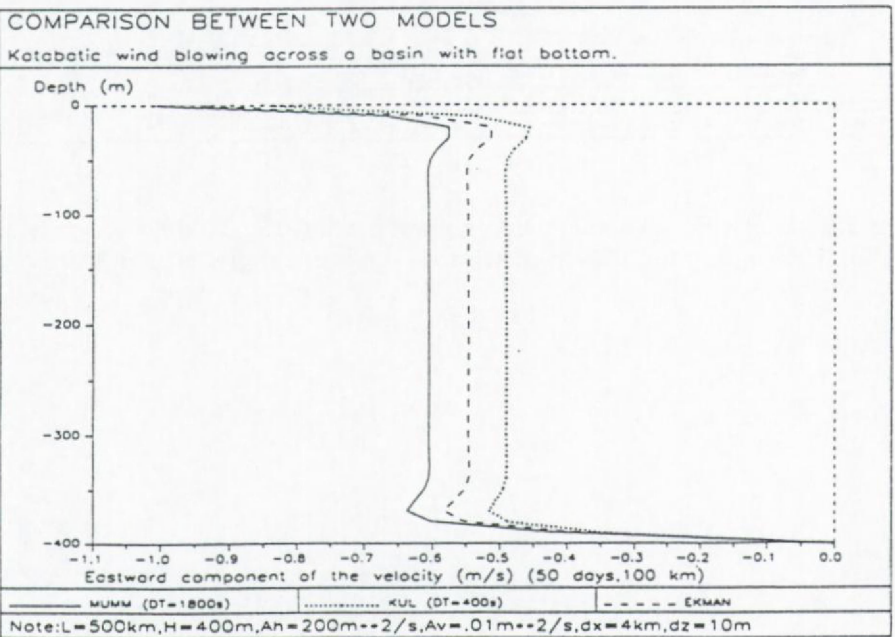
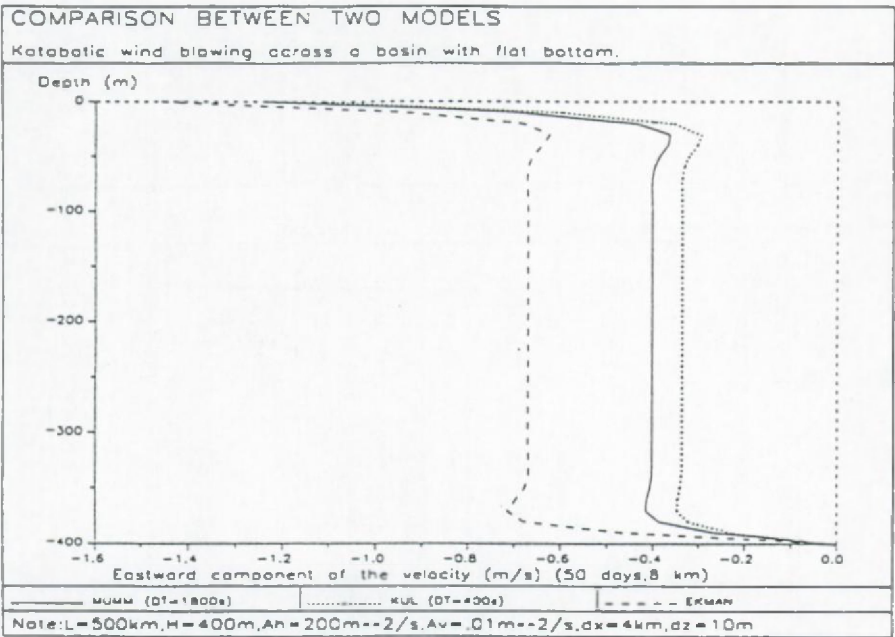


Figure 3.8: explanation see next page.

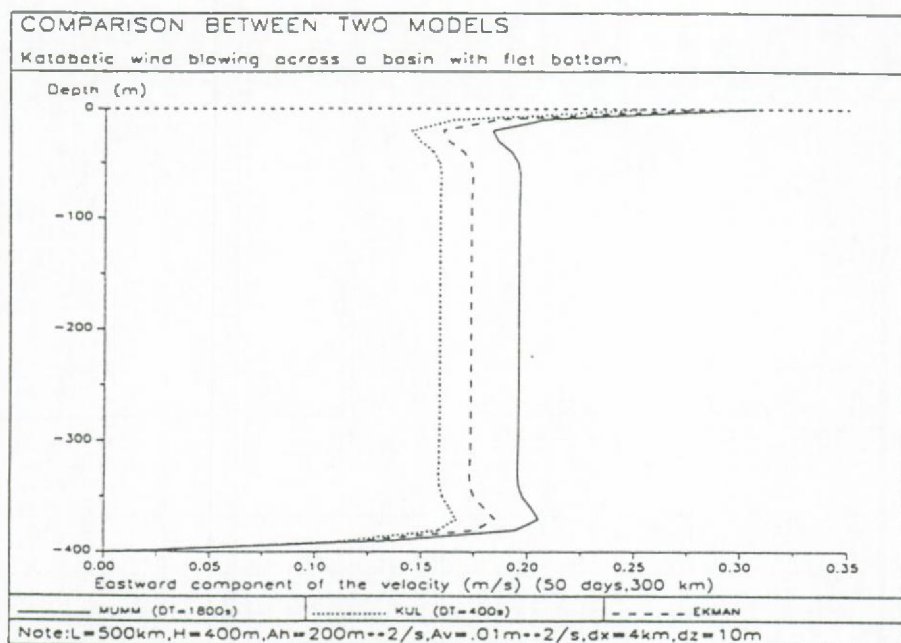


Figure 3.8: Eastward ( $v$ ) velocity component profile after 50 days for case 1 at (a) 8km, (b) 100km and (c) 300km off shore. The vertical grid size is 10m.

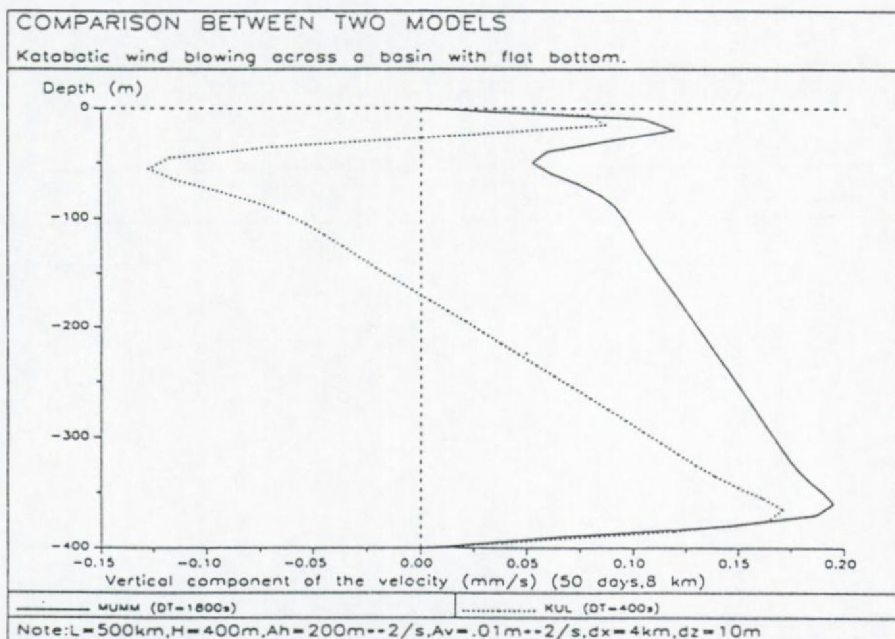


Figure 3.9: Vertical ( $w$ ) velocity component profile after 50 days for case 1 at 8km off shore. The vertical grid size is 10m.

The 200km point, where the wind direction changes from northwest to southeast is situated in the middle of the slope for case 2o. We can therefore observe in Figure 3.11 that in the shallower part of the slope downwelling occur and in the deeper part upwelling occurs followed by downwelling at the bottom of the slope.

The slope for the long shelf case (case 2l) is completely situated in the south-eastern wind blowing zone, see Figure 3.12. The wind is blowing in opposite direction over the shelf slope resulting in upwelling along the slope and downwelling in the ocean.

### 3.6. Discussion

The differences between the results of the KUL model, the MUMM model and Ekman's solution have been discussed in § 3.5.2. for case 1. For the northward component of the velocity the discrepancies are small and mainly situated in the top and bottom layers. In the transversal (eastward component) direction we have noticed important discrepancies between the three results. These differences are



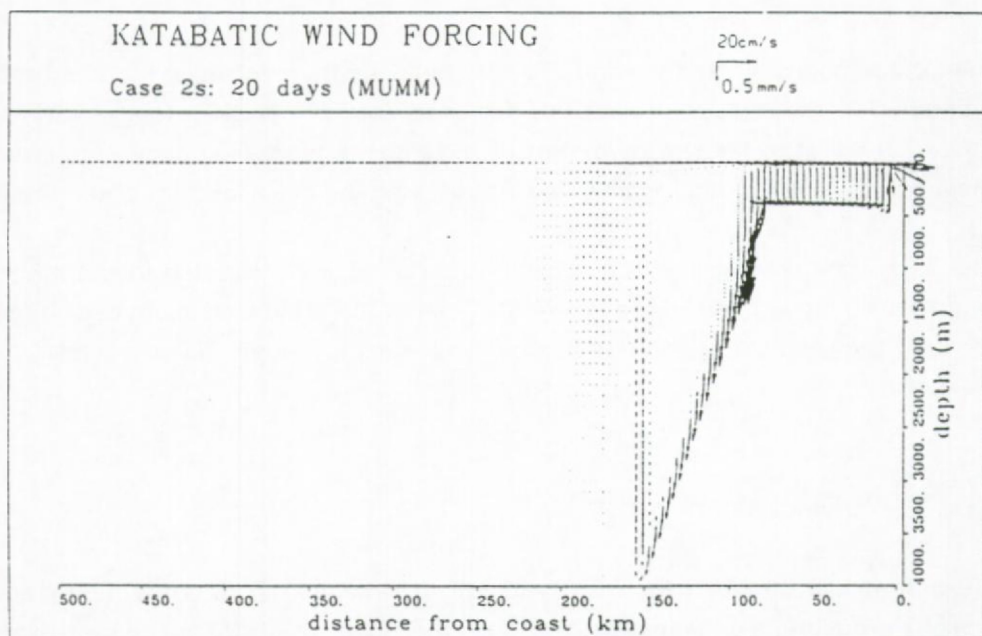
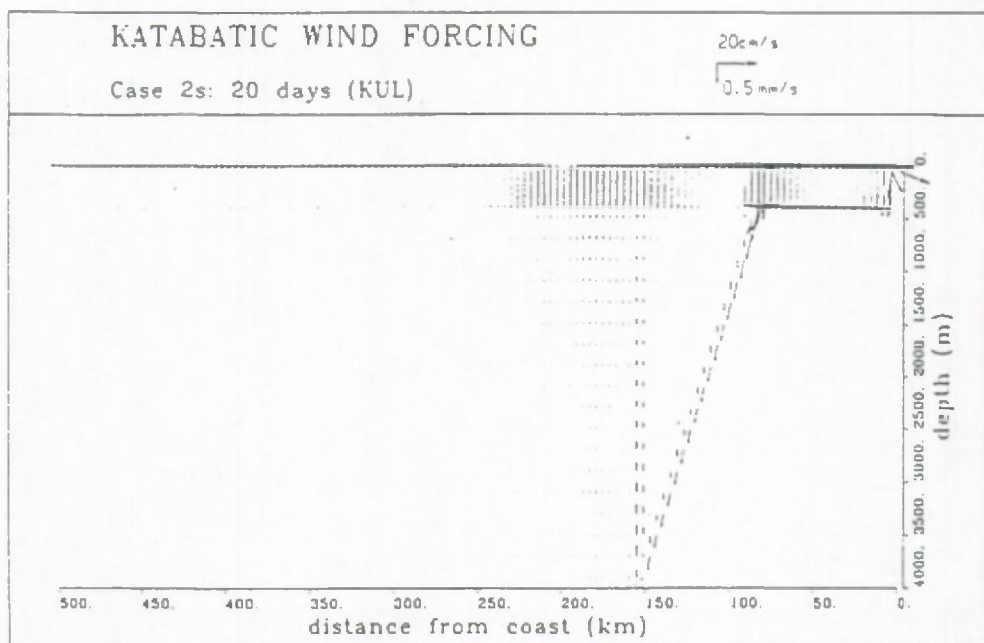


Figure 3.10: Flow field in the vertical plane after 20 days for case 2s (a) KUL's and (b) MUMM's results.

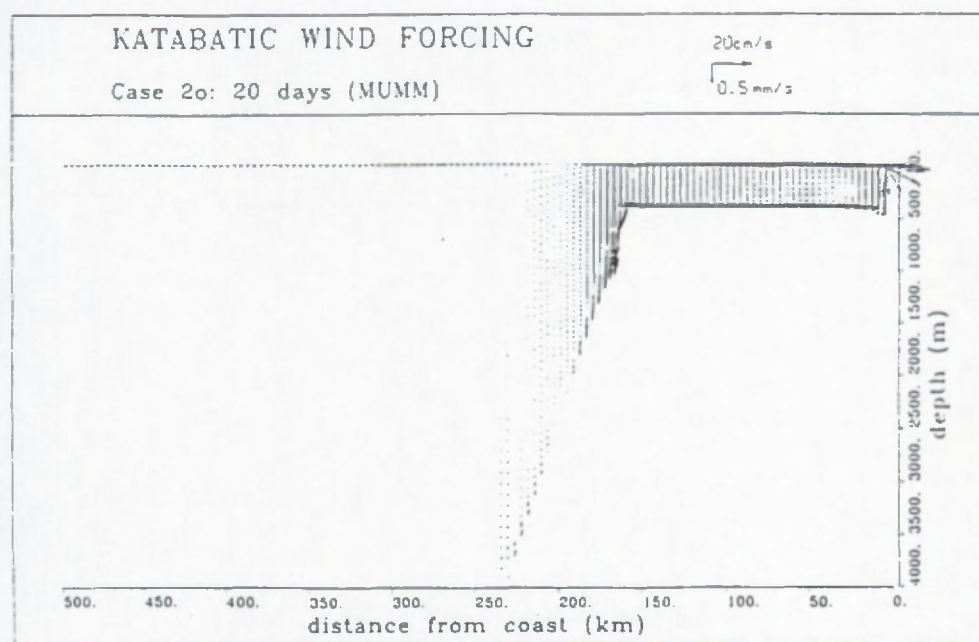
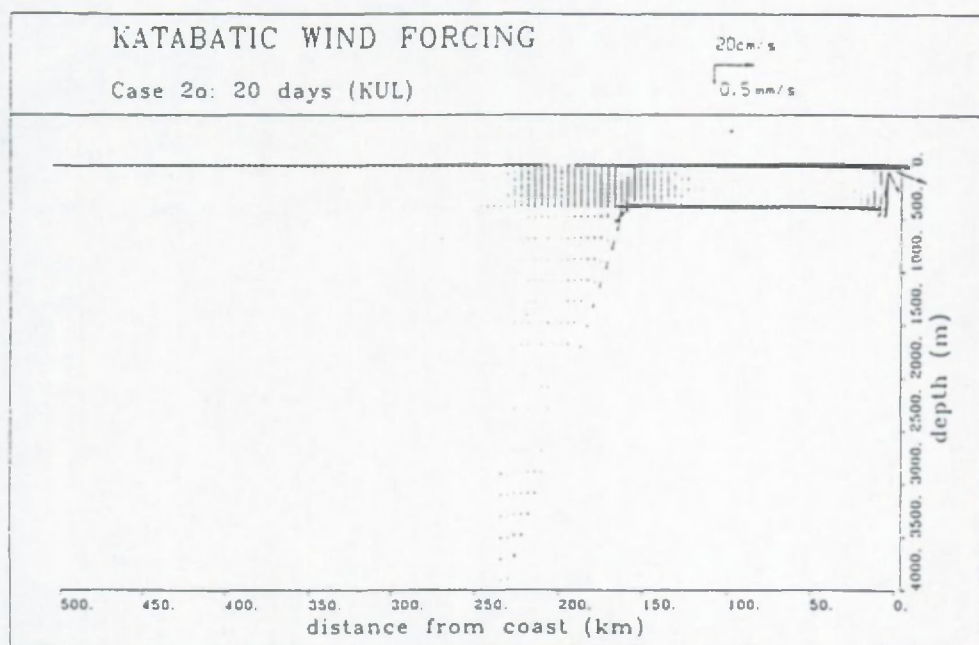


Figure 3.11: Flow field in the vertical plane after 20 days for case 2o (a) KUL's and (b) MUMM's results.

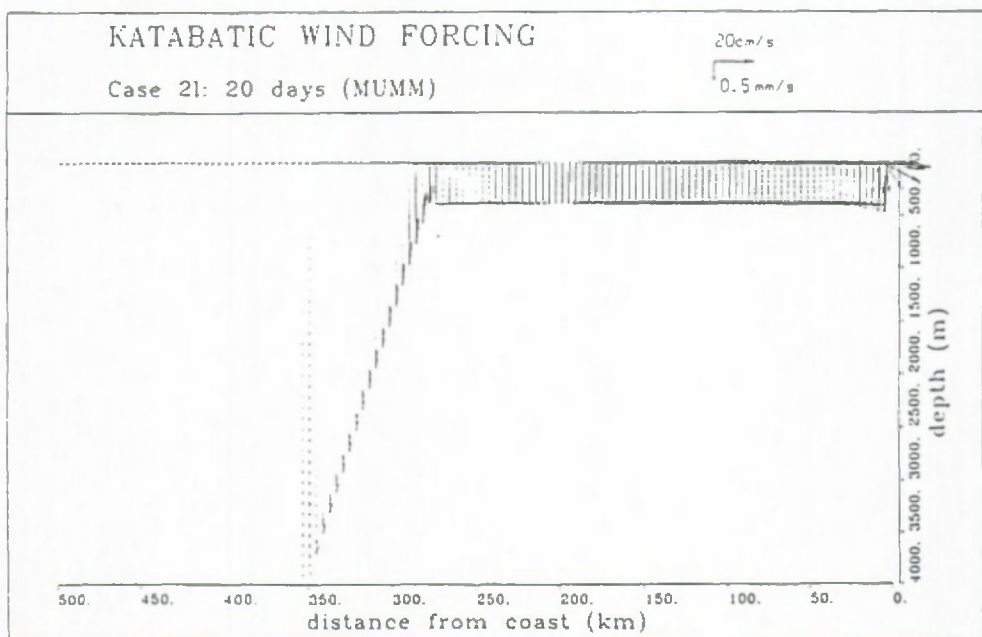
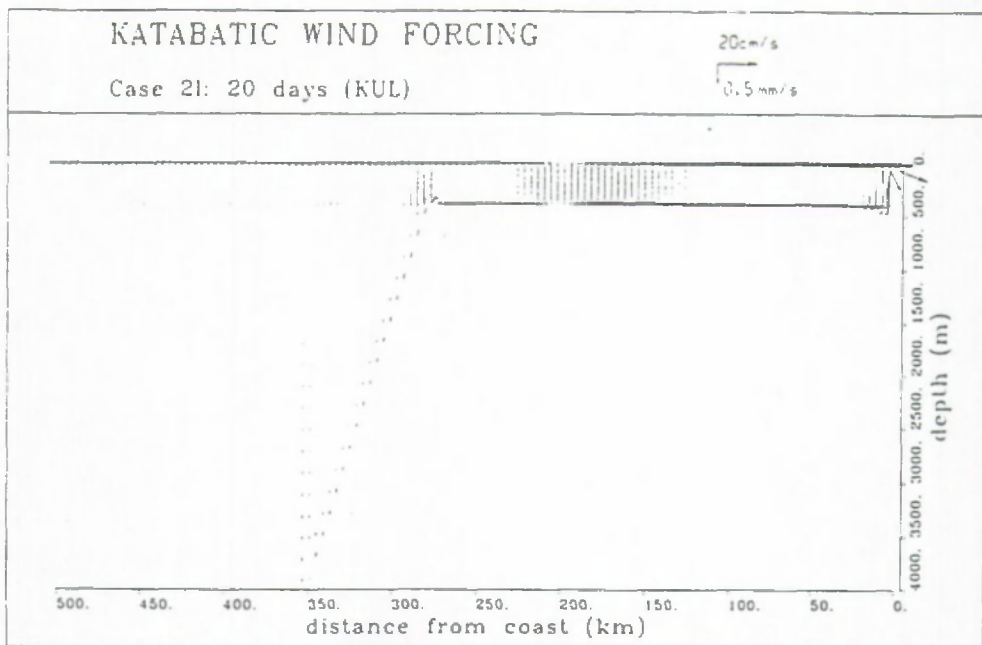


Figure 3.12: Flow field in the vertical plane after 20 days for case 21 (a) KUL's and (b) MUMM's results.

related to the differences in pressure gradient between the three solutions. In this paragraph we want to summarize the work which has been carried out in order to find an explanation for the discrepancies found between the results.

The sensitivity of the models has been tested by using different timestep and vertical grid sizes. All the test runs have been performed with the flat bottom case (case 1). The first solution of the problem as presented in § 3.5.2.2. is referred to as standard.

### **3.6.1.        *Advection - diffusion***

In order to diminish the numerical differences between the models, the vertical diffusion scheme of the KUL model has been changed to second order accuracy at the surface and later the advection scheme has been replaced by a second order central one. The influence of advection or diffusion schemes is, as was expected, small on the pressure gradient and cannot be responsible for the differences found between the three solutions in the standard case.

Changing the first order diffusion scheme to a second order one at the surface has an influence on the northward component of the velocity: the KUL solution is approaching the MUMM solution.

### **3.6.2.        *Timestep size***

The timestep size has only little influence on the solution, reducing the timestep to 60s (instead of 400s) for the KUL model does not reduce fundamentally the discrepancies found between the standard solutions of both models.

### **3.6.3.        *Ekman's solution***

The solution of Ekman is characterized by the fact that the advection and the horizontal diffusion terms are zero. In order to equalize the conditions between the model and the analytical solution two runs have been performed with the KUL model, one where  $A_h = 0$  and one where the horizontal diffusion and the advection terms have been set to zero. The results of these runs are not explaining the differences found in the standard runs, however the solutions are approaching Ekman's one with decreasing horizontal diffusion. Similar results have been



observed with the MUMM model (Petit, 1991).

3.6.4. Vertical resolution

In order to test the effect of different vertical grid sizes the standard models have been taken but the vertical grid size has been changed from 10m to 5m. The results of these runs are presented in Figure 3.13 (pressure gradient), Figure 3.14 (northward velocity) and Figure 3.15 (eastward velocity). The influence of the vertical grid size appears clearly on these figures. The agreement between model results and the Ekman solution is better than in the standard run. This result should be expected. Indeed, the thickness of the surface Ekman layer is relatively small (20m) and a high resolution is required to resolve this layer. The differences in the surface layer for the eastward velocity component between both models are partially due to the first order scheme used for vertical diffusion at the surface of the KUL model.

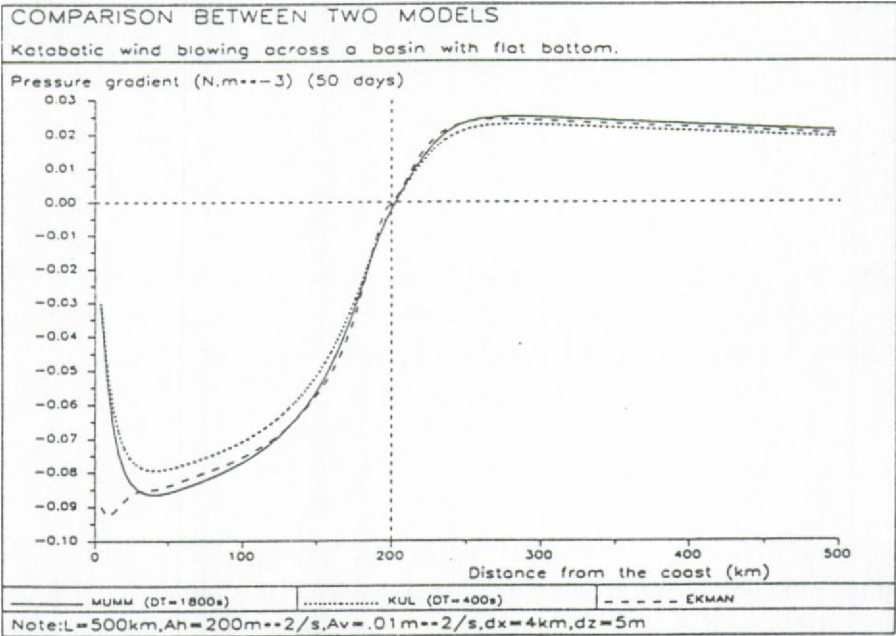


Figure 3.13: Pressure gradient with distance (longitudinal direction) after 50 days (case 1). The vertical grid size is 5m.

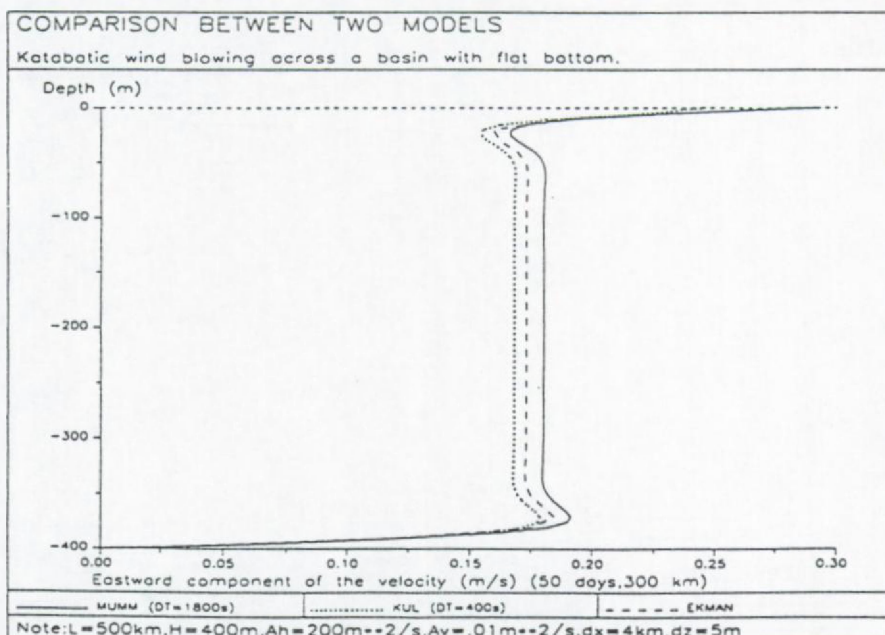
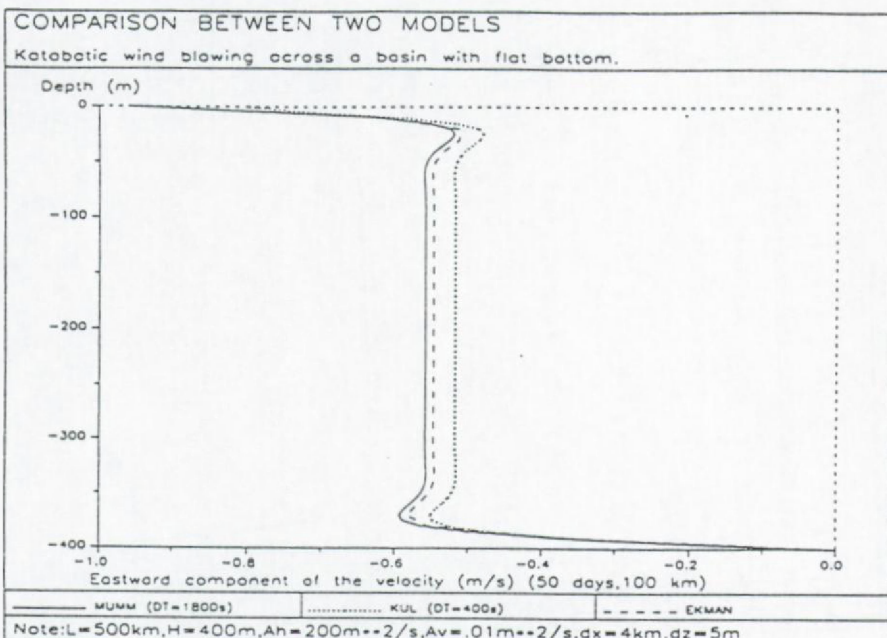


Figure 3.14: Northward ( $u$ ) velocity component profile after 50 days for case 1 at (a) 100km and (b) 300km off shore. The vertical grid size is 5m.

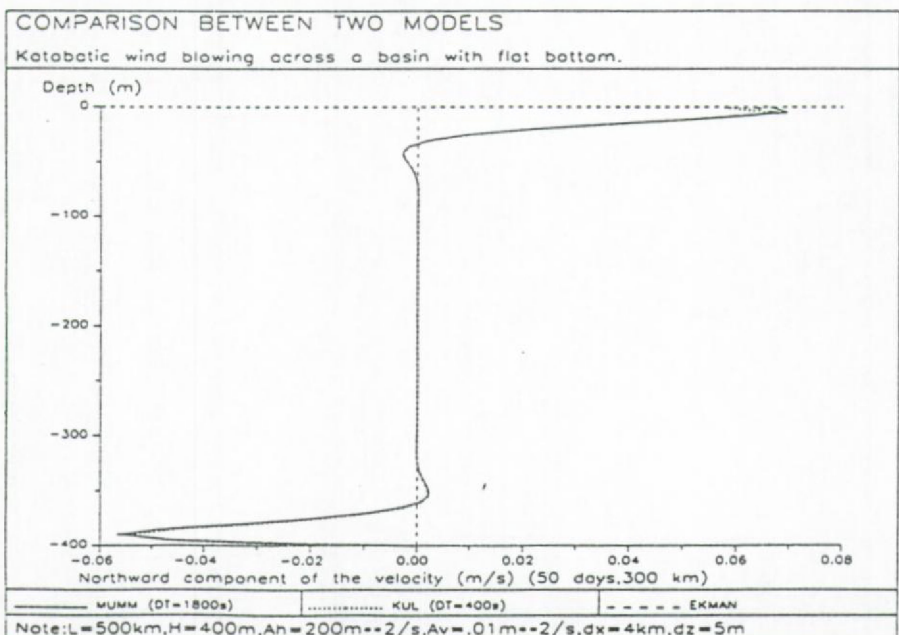
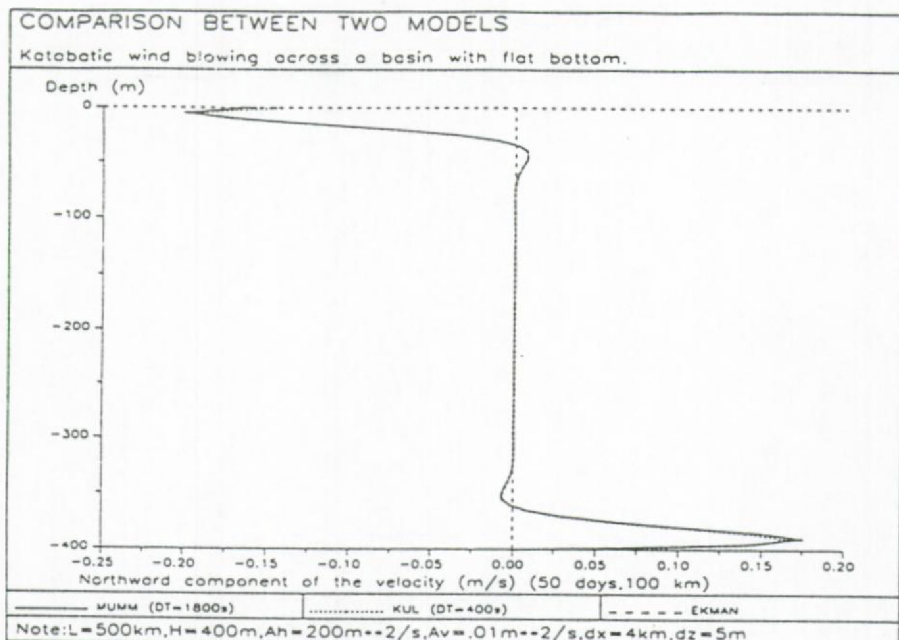


Figure 3.15: Eastward ( $v$ ) velocity component profile after 50 days for case 1 at (a) 100km and (b) 300km off shore. The vertical grid size is 5m.

### 3.7. 3D model of the Terra Nova coastal area

#### 3.7.1. Description of the 3D model

The model solves the 3D Navier-Stokes equations. These equations are an extension of the 2.5D equations in the sense that the partial derivative terms with respect to the  $y$ -direction are included in the model. The assumptions and simplifications made are the same as for the 2.5D model (see § 2.2.1.), i.e. hydrostatic pressure, Boussinesq approximation, the use of eddy coefficients for the turbulent momentum fluxes and the use of a rigid lid. The hydrostatic assumption reduces the effort to calculate the pressure from a three dimensional elliptic equation to a two dimensional one. The model as presented is barotropic, density effects are thus not accounted for. The equations of continuity and momentum in Cartesian coordinates are:

$$\frac{\partial u}{\partial x} + \frac{\partial v}{\partial y} + \frac{\partial w}{\partial z} = 0 \quad (3.14)$$

$$\frac{\partial u}{\partial t} + u \frac{\partial u}{\partial x} + v \frac{\partial u}{\partial y} + w \frac{\partial u}{\partial z} + \frac{1}{\rho} \frac{\partial p}{\partial x} - f v = \frac{\partial}{\partial x} (A_h \frac{\partial u}{\partial x}) + \frac{\partial}{\partial y} (A_h \frac{\partial u}{\partial y}) + \frac{\partial}{\partial z} (A_v \frac{\partial u}{\partial z}) \quad (3.15)$$

$$\frac{\partial v}{\partial t} + u \frac{\partial v}{\partial x} + v \frac{\partial v}{\partial y} + w \frac{\partial v}{\partial z} + \frac{1}{\rho} \frac{\partial p}{\partial y} + f u = \frac{\partial}{\partial x} (A_h \frac{\partial v}{\partial x}) + \frac{\partial}{\partial y} (A_h \frac{\partial v}{\partial y}) + \frac{\partial}{\partial z} (A_v \frac{\partial v}{\partial z}) \quad (3.16)$$

the hydrostatic equation is

$$\frac{\partial p}{\partial z} - \rho g = 0 \quad (3.17)$$

where  $t$  is time,  $x$  the coordinate in northward direction,  $y$  the coordinate in eastward direction,  $z$  the vertical coordinate (positive downward),  $u$ ,  $v$ ,  $w$  are the velocity components in  $x$ ,  $y$ ,  $z$  direction respectively,  $p$  is the pressure,  $\rho$  is the density of the water,  $A_h$ ,  $A_v$  are the horizontal and vertical eddy viscosity coefficients respectively,  $g$  is the gravitational acceleration and  $f$  is the Coriolis parameter.

Considering the boundaries of the model, the velocity at the coastline is set equal to zero (no-slip) and at the open boundary the Camerlengo and O'Brien radiation condition is used. At the sea surface wind is blowing and at the bottom the no-slip condition is used.



### 3.7.1.1. Finite difference equations

An explicit finite difference scheme is used to define the discretisation in time. The finite difference equations are presented using the notation of Figure 3.16. The equations are discretised on a so-called Arakawa C-grid. The advantage of a C-grid is that less averaging is needed for deriving the Poisson equation (see below). Using a C-grid can result in the generation of spurious boundary layers, these effects can be avoided by using the 'wet points only method', as proposed by Jamart and Ozer (1986). The subscripts  $i, j$  and  $k$  are the space coordinate indices of the grid in  $x, y$  and  $z$  direction respectively, the superscript  $n$  indicates the time level and  $\Delta x, \Delta y$  and  $\Delta z$  are the horizontal and the vertical space distances between two successive grid points.  $\Delta z$  is not constant, in order to simplify the equations it is assumed to be constant. The equations are valid away from the boundaries.

Continuity equation (3.14)

$$(u_{i,j,k}^{n+1} - u_{i-1,j,k}^{n+1})/\Delta x + (v_{i,j+1,k}^{n+1} - v_{i,j,k}^{n+1})/\Delta y + (w_{i,j,k+1}^{n+1} - w_{i,j,k}^{n+1})/\Delta z = 0 \quad (3.18)$$

Momentum equations (3.15-16)

$$\begin{aligned} & (u_{i,j,k}^{n+1} - u_{i,j,k}^n)/\Delta t + \overline{adu}_{i,j,k}^n - \overline{f\bar{v}}_{i,j,k}^{n+1} - A_h(u_{i+1,j,k}^n - 2u_{i,j,k}^n + u_{i-1,j,k}^n)/\Delta x^2 \\ & - A_h(u_{i,j+1,k}^n - 2u_{i,j,k}^n + u_{i,j-1,k}^n)/\Delta y^2 - A_v(u_{i,j,k+1}^n - 2u_{i,j,k}^n + u_{i,j,k-1}^n)/\Delta z^2 \\ & + \frac{1}{\rho_0} \left( \frac{\partial p}{\partial x} \right)_{i,j}^{n+1} = 0 \end{aligned} \quad (3.19)$$

and

$$\begin{aligned} & (v_{i,j,k}^{n+1} - v_{i,j,k}^n)/\Delta t + \overline{adv}_{i,j,k}^n + \overline{f\bar{u}}_{i,j,k}^{n+1} - A_h(v_{i+1,j,k}^n - 2v_{i,j,k}^n + v_{i-1,j,k}^n)/\Delta x^2 \\ & - A_h(v_{i,j+1,k}^n - 2v_{i,j,k}^n + v_{i,j-1,k}^n)/\Delta y^2 - A_v(v_{i,j,k+1}^n - 2v_{i,j,k}^n + v_{i,j,k-1}^n)/\Delta z^2 \\ & + \frac{1}{\rho_0} \left( \frac{\partial p}{\partial y} \right)_{i,j}^{n+1} = 0 \end{aligned} \quad (3.20)$$

where  $\overline{adu}_{i,j,k}^n$  and  $\overline{adv}_{i,j,k}^n$  are the advective terms, they are replaced by a 1<sup>st</sup> order upstream scheme.  $\overline{u}_{i,j,k}$  and  $\overline{v}_{i,j,k}$  are equal to:

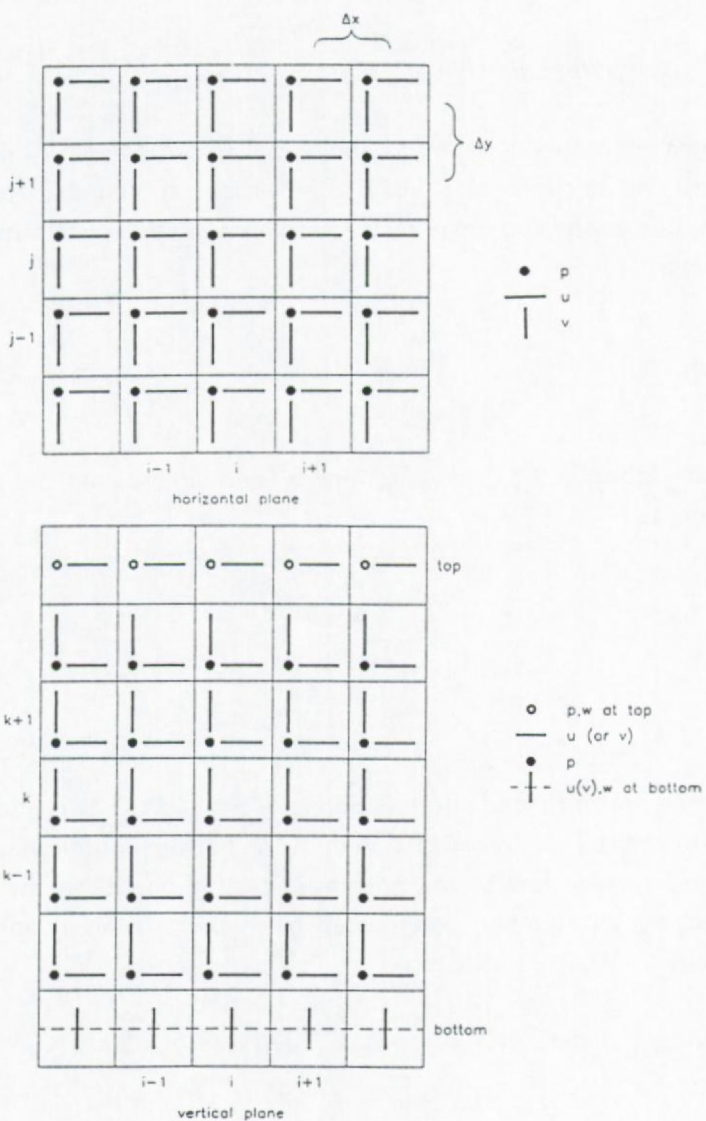


Figure 3.16: Numerical grid (Arakawa C) used by the 3D model.

$$\bar{u}_{ij,k} = (u_{ij,k} + u_{i-1,j,k} + u_{i,j-1,k} + u_{i-1,j-1,k}) / 4 \quad (3.21)$$

$$\bar{v}_{ij,k} = (v_{ij,k} + v_{i-1,j,k} + u_{i,j-1,k} + u_{i-1,j-1,k}) / 4 \quad (3.22)$$

### 3.7.1.2. Computational scheme

The numerical procedure is based on the so-called MAC method, see Peyret and Taylor (1986) and Jamart et al. (1982). The idea is to split the horizontal velocities in two parts, one containing the pressure gradient term and one containing the rest (explicit terms).

$$u_{ij,k}^{n+1} = u_{ij,k}^I + u_{ij,k}^{II} \quad (3.23)$$

$$v_{ij,k}^{n+1} = v_{ij,k}^I + v_{ij,k}^{II} \quad (3.24)$$

where  $u^I$  and  $v^I$  contain the explicit,  $u^{II}$  and  $v^{II}$  contain the (implicit) pressure term and is written as

$$u_{ij,k}^{II} = -\frac{1}{\rho_0} \left( \frac{\partial p_I}{\partial x} \right)_{ij}^{n+1} \Delta t \quad (3.25)$$

$$v_{ij,k}^{II} = -\frac{1}{\rho_0} \left( \frac{\partial p_I}{\partial y} \right)_{ij}^{n+1} \Delta t \quad (3.26)$$

To calculate the pressure gradient the continuity equation (3.14) is integrated over the vertical (from top  $k = 1$  to  $k = nz - 1$ , with  $nz$  the bottom coordinate). The vertical velocity at the surface and at the bottom is zero (rigid lid) so that the vertical integrated continuity equation at timestep  $n + 1$  and written in finite difference takes the form

$$\begin{aligned} & (h_{i+1,j} \sum_{k=1}^{nz-1} (\omega_k u_{i+1,j,k}^{n+1}) - h_{ij} \sum_{k=1}^{nz-1} (\omega_k u_{ij,k}^{n+1})) / \Delta x + (h_{i,j+1} \sum_{k=1}^{nz-1} (\omega_k v_{i,j+1,k}^{n+1}) \\ & - h_{ij} \sum_{k=1}^{nz-1} (\omega_k v_{ij,k}^{n+1})) / \Delta y = 0 \end{aligned} \quad (3.27)$$

where  $\omega_k$  is a weighting factor depending on the vertical grid size: in case of

constant vertical grid distance:  $\omega_1 = 0.5 \Delta z / h_{ij}$  and  $\omega_2 \dots \omega_{nz-1} = \Delta z / h_{ij}$ . Equations (3.23-24) are put in equation (3.27) and together with equations (3.26-27) the following relationship is obtained (we suppose that  $\Delta x = \Delta y$ )

$$\begin{aligned} & h_{i+1,j} \sum_{k=1}^{nz-1} (\omega_k u'_{i+1,j,k}) - \frac{h_{i+1,j}}{\rho_0} \left( \frac{\partial p_I}{\partial x} \right)_{i+1,j}^{n+1} \Delta t - h_{ij} \sum_{k=1}^{k=nz-1} (\omega_k u'_{i,j,k}) \\ & + \frac{h_{ij}}{\rho_0} \left( \frac{\partial p_I}{\partial x} \right)_{ij}^{n+1} \Delta t - h_{i,j+1} \sum_{k=1}^{nz-1} (\omega_k v'_{i,j+1,k}) + \frac{h_{i,j+1}}{\rho_0} \left( \frac{\partial p_I}{\partial y} \right)_{i,j+1}^{n+1} \Delta t \\ & - h_{ij} \sum_{k=1}^{nz-1} (\omega_k v'_{i,j,k}) + \frac{h_{ij}}{\rho_0} \left( \frac{\partial p_I}{\partial y} \right)_{ij}^{n+1} \Delta t = 0 \end{aligned} \quad (3.28)$$

If we replace the pressure gradients by

$$\left( \frac{\partial p_I}{\partial x} \right)_{ij} = \frac{p_{i+1,j} - p_{i,j}}{\Delta x} \quad (3.29)$$

and

$$\left( \frac{\partial p_I}{\partial y} \right)_{ij} = \frac{p_{i,j} - p_{i,j-1}}{\Delta y} \quad (3.30)$$

we obtain the following Poisson equation for pressure (in case of constant depth)

$$4p_{ij} - (p_{i+1,j} + p_{i,j+1} + p_{i-1,j} + p_{i,j-1}) = -G \frac{\Delta x}{\Delta t} \quad (3.31)$$

with  $G$  equals to

$$G = h_{i+1,j} \sum_{k=1}^{nz-1} (\omega_k u'_{i+1,j,k}) - h_{ij} \sum_{k=1}^{nz-1} (\omega_k u'_{i,j,k}) + h_{i,j+1} \sum_{k=1}^{nz-1} (\omega_k v'_{i,j+1,k}) - h_{ij} \sum_{k=1}^{nz-1} (\omega_k v'_{i,j,k}) \quad (3.32)$$

Equation (3.31) is only valid for interior points. Since pressure points are never situated at the boundary a similar equation can be used where the appropriate boundary conditions for velocity are incorporated. As an example, consider a continental boundary at the southern edge of the basin. The summation over the vertical of  $v_{i,j,k}$  is equal to zero and we can drop this term from equation (3.27) resulting in an equation for the surface pressure along this line. The treatment for open boundaries is similar and also depending on the chosen boundary condition for velocity.



method implemented here is the Conjugate Gradient Method, see Golub and Van Loan (1989).

### 3.7.2. *Description of the model area*

The model area is situated along the coast of Terra Nova (Antarctica). The dimensions are 500km in Northward direction and 175km in eastward direction. The Coriolis parameter has been taken at 70°S. The horizontal grid size is 5km, the depth is constant and equal to 1000m. This value is equal to the depth found off the coast of Terra Nova. The horizontal eddy viscosity is 1000m<sup>2</sup>/s and the vertical one 0.01m<sup>2</sup>/s. The model is forced by a katabatic wind, calculated by the UCL 3D atmospheric model (Gallée et al., 1993). In Figure 3.17 the wind forcing is displayed. Interesting to notice is the high values of the katabatic winds in certain areas along the coast. The differences with the 2.5D wind field are situated in the more extreme and less continuous values of the forcing. At about  $x = 200\text{km}$  the wind speed reaches up to 20m/s near the coast and is quickly decreasing to nearly zero stress. These strong variations are not found in the 2.5D wind forcing. The model starts the calculations at time 0 and continuous until 20 days have been simulated.

### 3.7.3. *Results of the simulation*

In Figures 3.17-18 the horizontal flow field in the surface layer and at 20m depth is shown. The flow field in the surface layer is characterised by the presence of small and local areas with high current velocities. At about  $x = 200\text{km}$  the water reaches a velocity of nearly 0.5m/s. The wind and the flow pattern near the coast are in agreement with the idea of coastal polynya formation by a combination of strong seaward winds and currents. At about  $x = 200\text{km}$  and  $x = 430\text{km}$  this seaward flow is clearly existing. The velocity is decreasing quickly with depth. The strong non uniform wind induces divergence or convergence in the coastal zone resulting in upwelling or downwelling away from the boundaries. The formation of dense water in the surface layer of the polynya will result in density induced currents and will influence the vertical flow structure. This subject must be investigated by a baroclinic model.

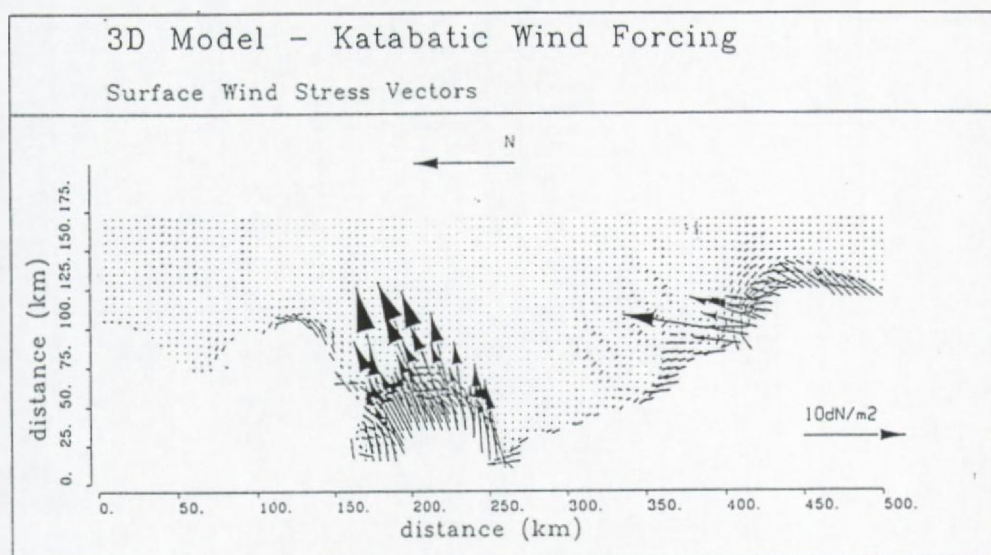


Figure 3.17: Katabatic wind over Terra Nova coastal area, after Gallée et al. (1993).

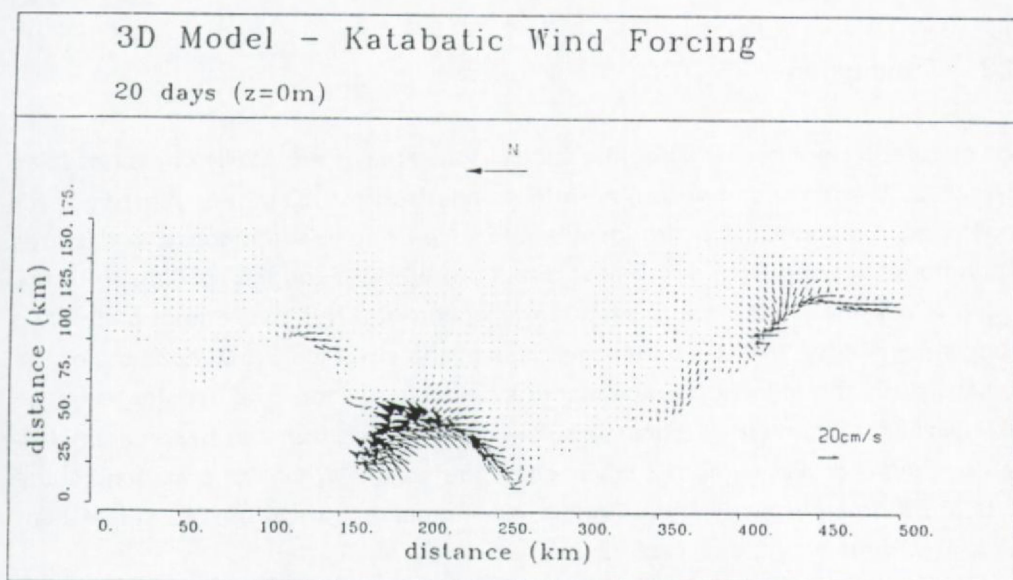


Figure 3.18: 3D model, flow field in the surface layer after 20 days of katabatic wind forcing.

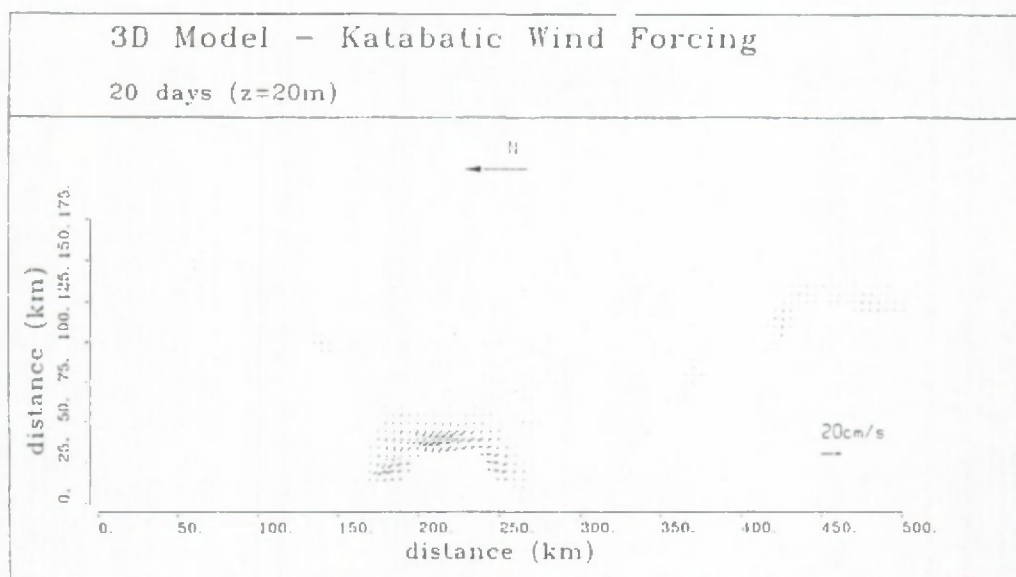


Figure 3.19: 3D model, flow field at 20m depth after 20 days of katabatic wind forcing.

### 3.8. Conclusion

The circulation induced by katabatic winds in the area of the Adélie coast has been chosen as test case to perform an intercomparison exercise between two 2.5D coastal ocean models. The strongest wind is occurring near the coast. In this area the wind is blowing from south-east direction, while at roughly 200km from the coast, a reversal in the wind direction is occurring. The two ocean circulation models used in the exercise enter the class of the so-called 2.5D models. For the present study the following simplifications have been made. The density has been taken as constant and the vertical turbulent flux of momentum has been parameterized by means of a constant eddy viscosity coefficient. While the governing equations are the same for the two models, the numerical procedures to solve them differ in various ways, see Table 3.1.

In a first stage, a set of simulations has been carried out using the models in their original configuration. In these simulations, the forcing is the same but the bottom topography is different (either constant or variable). The results of those first model runs show that an overall agreement exists between the model solutions and es-

pecially that both models predict a seaward flow at the surface close to the continental margin. However, some discrepancies have been observed. The discrepancies have to be ascribed to differences in numerical procedures. Therefore a set of additional simulations has been realized as an attempt to identify where the differences came from. These simulations dealt with the simplest bottom topography (flat bottom) for which the Ekman solution can be taken as the reference outside the lateral boundary layer. The differences between the finite difference analogues of the horizontal advection and of the horizontal diffusion do not contribute significantly to the discrepancies between the model results. For a given vertical resolution, the differences between the model solutions and the Ekman solution are partially due to the value of the horizontal diffusion coefficient. If this latter is reduced, both model results converge towards the Ekman solution. It appeared clearly that the crux encountered came from the numerical procedures used along the vertical. An improvement of the results of the KUL model has been obtained by introducing a second order accurate analogue of the vertical diffusion term at the surface and at the bottom. A significant improvement of the two model results is obtained by reducing the vertical grid size. The results obtained with a vertical grid size equal to 5m agree significantly better with the Ekman solution than those obtained with a coarser vertical resolution.

As an extension a brief presentation of the 3D model results of a katabatic wind forcing off the Terra Nova have been presented. Interesting to note is that in both models a seaward flux exist near the coast. This results is supporting the idea of coastal polynya formation by a combination of wind and surface flow.





## CHAPTER 4

### WIND-DRIVEN CIRCULATION ALONG AN ICE EDGE

#### 4.1. Introduction

The continental shelf is a region of relatively shallow water. At the continental margin an abrupt change in slope occurs (shelf break). The width of the continental shelf is typically of the order of 50 - 200km, the continental slope extends over a distance of the order of 100km. Wind-driven currents on continental shelves have been an important research item since the 1970's. Reviews on wind-driven circulations on continental shelves have been written by Allen (1980) and Brink (1991).

The motion of the water over the shelf and the continental slope is influenced by the topographic constraints (coastline and slope), the density stratification, and the offshore currents. The sudden change in bathymetry at a continental margin can result, depending on the wind direction, in up- or downwelling along the shelf break. Upwelling in an open ocean is usually induced by wind blowing over the water surface (O'Brien et al., 1977).

Oceans in high latitudes are seasonally or continuously covered with sea ice. The first to report about ice edge upwelling, as a result of a measurement campaign in the Arctic ocean, were Buckley et al. (1979). Niebauer (1982) concludes from a numerical model study that wind forcing is responsible for upwelling. Following this author the ice edge is acting similarly to a continental boundary. Røed and O'Brien (1983) and Røed (1983) argued that the ice edge upwelling can also be explained by the motion of the ice alone. Modelling the marginal ice zone requires thus a coupled ice-ocean model.

Upwelling can be defined as a process that involves vertical motion. Upwelling processes can be found in some coastal regions (especially on the western sides of some continents), in the open ocean (e.g. along the equator) and along marginal sea ice edges (Wooster, 1981 and Buckley et al. 1979). Following Wooster the term 'upwelling' should be restricted to the upward motions concentrated within the first hundreds of metres of the surface, see also Pond and Pickard (1986).

The vertical motion is estimated to have a magnitude of about  $10^{-3}$  cm/s, this value is the result of continuity estimates from horizontal motion. It seems likely (Wooster, 1981) that the motion is concentrated in plumes where the speed is one or two orders of magnitude higher. Upwelling can also be described as a vertical displacement of water with a higher density into water of lower density due to some external forcing. The upwelling is primarily forced by winds, an explanation for this process can be found in Ekman's theory. Smith (1980) concluded from measurements done in the coastal region off Oregon, northwest Africa and Peru that the flow pattern are consistent with this theory. As a rule, upwelling is associated with high primary production, and coastal upwelling regions are associated with large concentrations of fish. Up- or downwelling will be used below to describe vertical motion induced directly or indirectly by wind forcing.

Modelling upwelling along the shelf break requires the incorporation of the bathymetry, the stratification of the ocean, time variability and the effect of the bottom friction in the model. A review of numerical models of shelf break dynamics is presented by Johnson and Rockliff (1986). They divide the various models depending on their complexity, i.e. from simple steady state barotropic models to continuously stratified unsteady models.

Previous studies about ice edge upwelling have been carried out by Niebauer (1982) who investigated the response of a shallow sea covered with a non moving ice layer to wind forcing. Røed and O'Brien (1983) and later Smedstad and Røed (1985) used a vertical plane ice-ocean coupled model to investigate the ice-ocean interaction in the marginal ice zone. The main findings are that for wind directions of  $52^\circ$  and  $232^\circ$  the ocean response is essentially nil while for wind direction of  $117^\circ$  and  $232^\circ$  the response is maximal. Niebauer and Smith (1989) used a simplified dynamic ice model (the time dependent, non-linear and internal ice stress terms have been omitted) to investigate the physico-biological interactions in the Fram strait marginal ice zone.

The purpose of this paragraph is to present the results of simulating the vertical

motion along an ice edge and the interaction occurring at a shelf break with a shelf covered with sea ice. In order to separate the different effects, such as varying bathymetry, ice cover, density stratification and wind forcing, two sets of experiments have been set up with different bathymetries. The first test case (§ 4.2.1.) consist of a shelf sea with a constant depth of 400m. In the second series of experiment (§ 4.2.2.) the shelf is coupled to a deep ocean by a shelf break. For both sets of experiments the shelf is or covered with a stationary ice layer, or covered with an ice layer which is allowed to respond dynamically to the wind and ocean forcings, or is ice free. Since the ice is more effectively influenced by the wind, the response of the ocean with a moving ice layer will be different than in the case of a stationary ice cover. In order to carry out the simulations, we consider a highly idealized ice-ocean model as formulated in Chapter 2. The model is idealized in the sense that the vertical eddy viscosity and diffusivity coefficients are constant, that the currents in the alongshore direction are considered to be constant and that no thermodynamic processes are incorporated in the model.

## 4.2. Model Results

The upwelling along ice edges is depending on the ice movements, the wind direction, force and duration. Røed and O'Brien (1983) have found that upwelling favourable winds on a rigid non moving ice cover have the opposite effect in case of a dynamic ice cover. For a stationary ice cover, the conditions for up- or downwelling are similar as in the case of a shelf break or continental margin. The reason for this opposite behaviour may be understood by means of continuity requirements.

The purpose of this experiment is to examine the effect of bathymetry, density and ice on the wind induced upwelling. Two cases have been set up, the first one consist of a flat basin 500km long and 400m deep. For the second one a shelf, shelf break and ocean are considered. The shelf is 400m and the ocean 4000m deep. The shelf zone extends over 160km and is interrupted by a continental slope of 5 percent (i.e. 3800m in 72km), see Figure 4.1. These dimensions are an idealization of the ones found off the coast of Adélie land in Antarctica (see also Chapter 3). In this paragraph simulations of a shelf sea, partly covered by sea ice are presented. The ocean model is time dependent and includes non-linear terms. The sea ice is attached to the continental side of the basin and covers one third of it. At the open sea boundary, a radiation condition (Camerlengo and O'Brien, see Chapter 2)



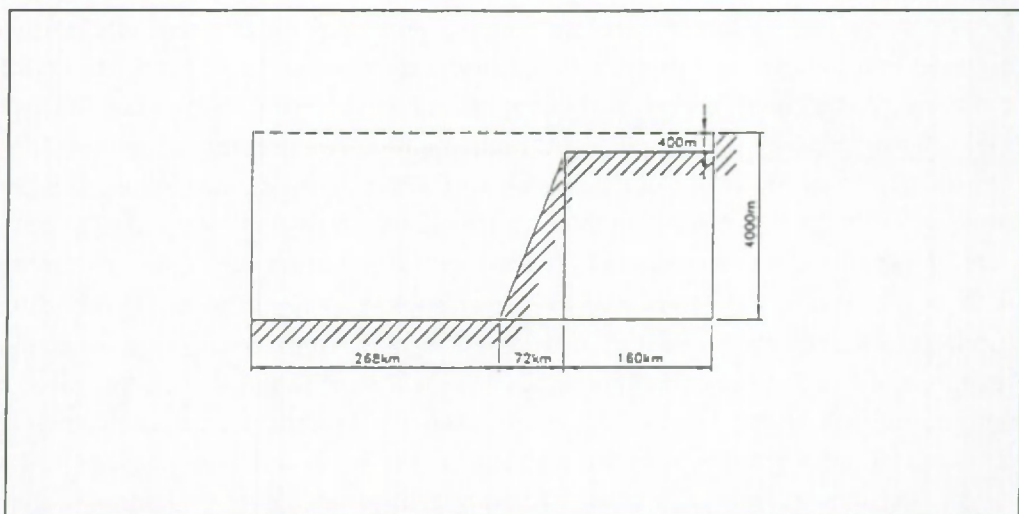


Figure 4.1: Dimension of the basin for case 2 (shelf-ocean), case 1 has the same horizontal extension but the depth is constant and equal to 400m.

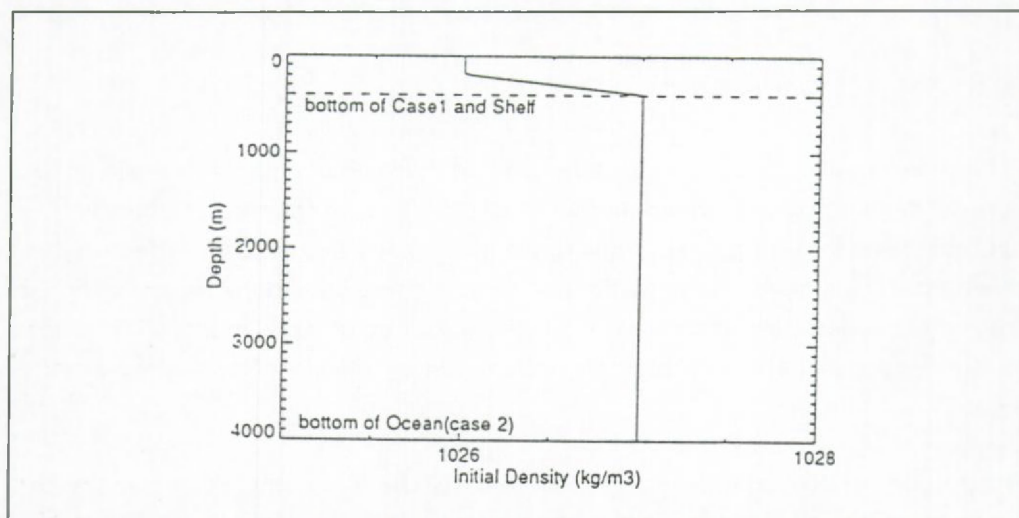


Figure 4.2: Initial density stratification for case 1 and 2.

is applied. The horizontal grid size is 4km and the vertical one is 10m for case 1 and 20m to 200m for case 2. The Coriolis parameter is constant (at  $67^\circ$  South), the horizontal eddy viscosity has been set to  $200\text{m}^2/\text{s}$ , the vertical one to  $0.01\text{m}^2/\text{s}$ , the horizontal eddy diffusivity is  $100\text{m}^2/\text{s}$  and the vertical one  $0.001\text{m}^2/\text{s}$ . The eddy diffusivities are low, so that advection is the predominant process for densities variations. The ocean has or a constant density or is stratified with density varying between 1026 and  $1027\text{kg}/\text{m}^3$ , see Figure 4.2. The surface of the ocean can be covered by a moving or a non-moving ice layer. The ice cover

is 160km long and is thus covering the whole shelf zone in case 2. Two sets of experiments are considered, see Table 4.1. In the first one the ice cover is considered to be stationary, whereas in the second one the ice is allowed to move. The simulations with a stationary ice cover have been described in Fettweis et al. (1990c and 1991a). A wind of 10m/s is blowing parallel to the ice edge in an upwelling or downwelling favourable direction with respect to the shelf break upwelling. The flow field is shown after 2 days of simulation.

Table 4.1      Overview of the different simulations.

		Case 1 (§ 4.2.1.)	Case 2 (§ 4.2.2.)
ice free	- no stratification	-	Fig. 4.6
	- stratification	Fig. 4.3	Fig. 4.7
ice fixed	- no stratification	-	-
	- stratification	Fig. 4.4	Fig. 4.8
ice moves	- no stratification	Fig. 4.10	-
	- stratification	Fig. 4.5	Fig. 4.9

4.2.1.      *Case 1 (shelf - flat bottom)*

In order to separate the effects of ice and wind direction different runs have been carried out. In Figure 4.3 the flow field due to an up- and downwelling favourable wind is shown for the ice free shelf. One can distinguish a relatively strong top and bottom Ekman layer and up- or downwelling at the coast. Due to the vertical currents near the coast the pycnocline is transported up- or downward, resulting in a wider up- or downwelling zone. The higher density in the deeper part of the sea is restricting the vertical currents and we can observe a smaller vertical velocity in the lower 200m.

For the next run the ocean is covered by a non moving ice layer and is simulated as an area where the wind stress is zero. The ice cover is acting similarly to a continental boundary and is inducing up- or downwelling. The same remarks as for the ice free case are valid, i.e. the density stratification is decreasing the vertical velocity but horizontally extending the up- or downwelling zone. The flow field in case of up- or downwelling favourable wind direction is shown Figure 4.4. The response of the ocean to an ice cover which is allowed to move dynamically (see § 2.3.) according to the wind and ocean shear is shown in Figure 4.5. Interes-

ting to notice is that at the ice edge the up- or downwelling are reversed as compared to the stationary ice cover case, but that the coastal up- or downwelling is qualitatively equal to the ice free case. The reversal of the up- or downwelling is explained by the fact that the water under the ice is moving faster than the water in the ice free part of the sea. In case of a surface flow off the coast, one can see that the ice is transported away from the coast forming thus a coastal polynya.

#### 4.2.2. *Case 2 (shelf - ocean)*

In this section the results of the shelf/ocean model are presented. Again in the first runs the ocean is ice free. The flow field for the two different wind directions in case of constant density is shown in Figure 4.6. We can see that along the slope and the coast up- or downwelling is occurring. The flow in the deep part is almost zero except at the surface.

The density stratification has a strong influence on the upwelling. In case of stratification the up- or downwelling at the shelf break is strongly reduced as is shown in Figure 4.7. A double vertical eddy has been formed at both sides of the continental break for the constant density case. With varying density the flow is slowed down by the pycnocline and the eddy is much weaker and not reaching the surface. The very weak vertical velocities in the first 400m at the shelf break for the stratified case is partly the result of the fact that the currents are not yet in a stationary state. If the simulations are carried out until steady state one can observe also an up- or downwelling in the stratified case, but again the vertical velocities are 3 to 5 times smaller than in the non-stratified case.

In case the shelf is covered by a non-moving ice layer, we observe a little smaller up- or downwelling along the shelf edge and slope than in the ice free situation. The reason can be found in the fact that the ice is protecting the water from the wind. The surface flow near the ice edge is then smaller giving thus smaller upwelling. The flow field in the shelf break region is presented in Figure 4.8.

The up- and downwelling favourable wind forcing in case of a moving ice cover is shown in Figure 4.9. It can be seen that the up- or downwelling at the slope is stronger than in the ice free and stationary ice cover case. This stronger up- or downwelling is the result of the stronger currents over the shelf generated by the shear forces exerted by the ice floes on the water. The downwelling (Figure 4.9a) and the upwelling (Figure 4.9b) along the ice edge is smaller than in the stationary ice case. Interesting to notice is that the ice edge up- or downwelling is not qualitatively influencing the down- or upwelling along the shelf break.



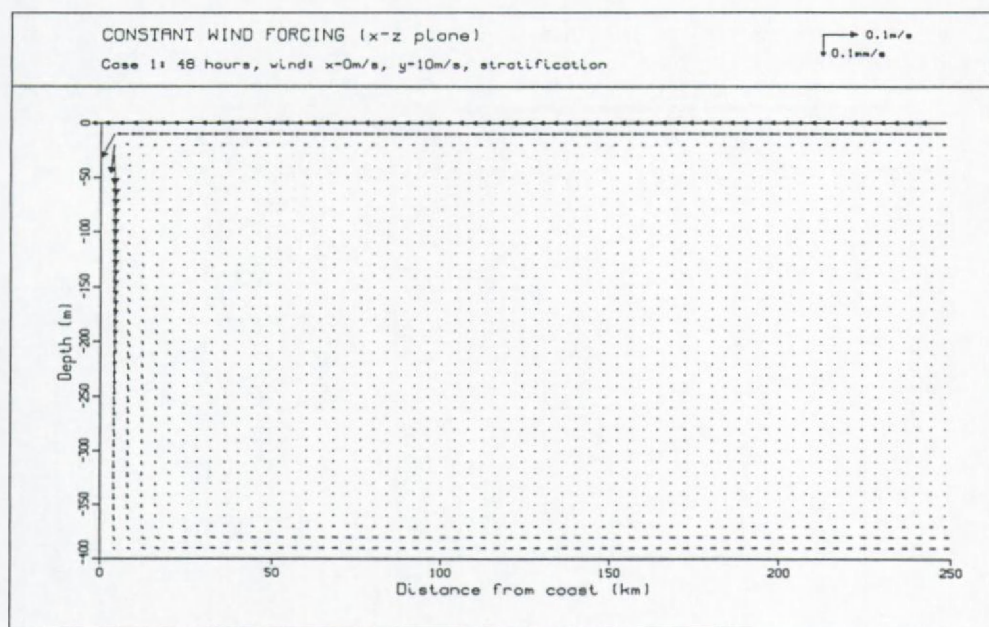
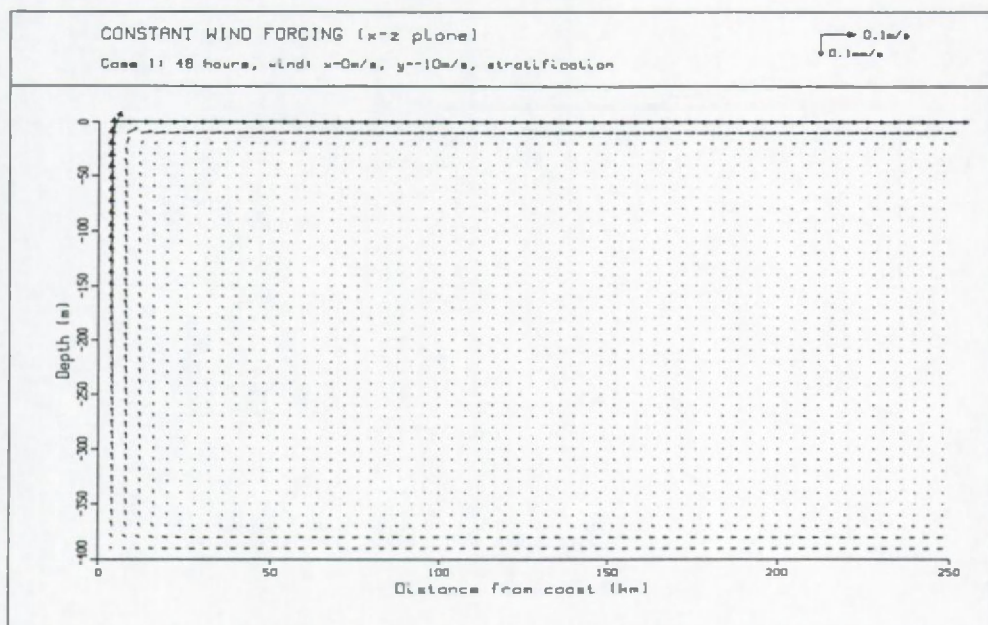


Figure 4.3: Flow field for the ice free shelf case. (a) upwelling and (b) downwelling favourable wind forcing.



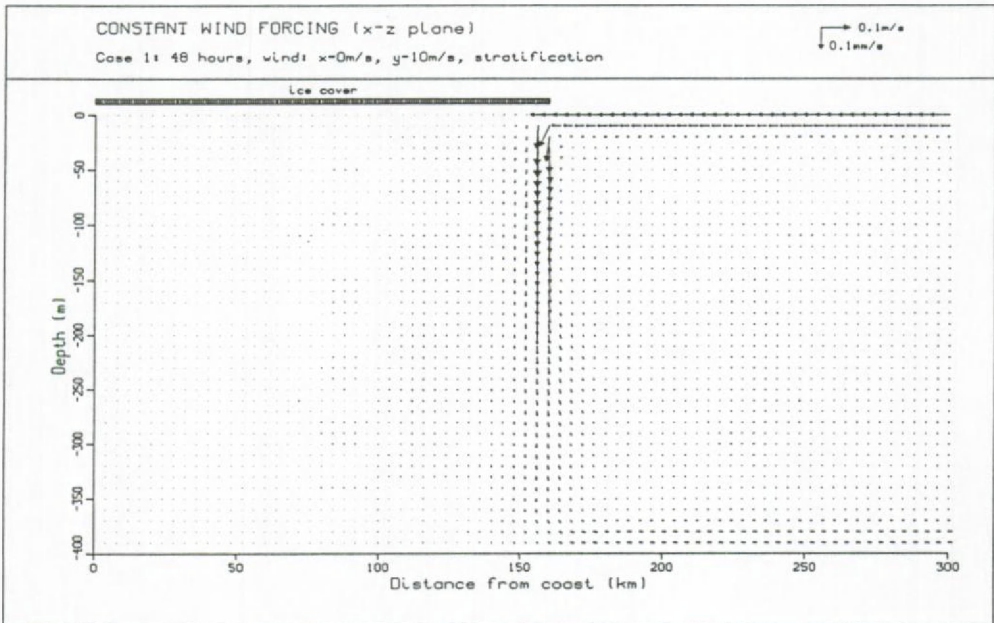
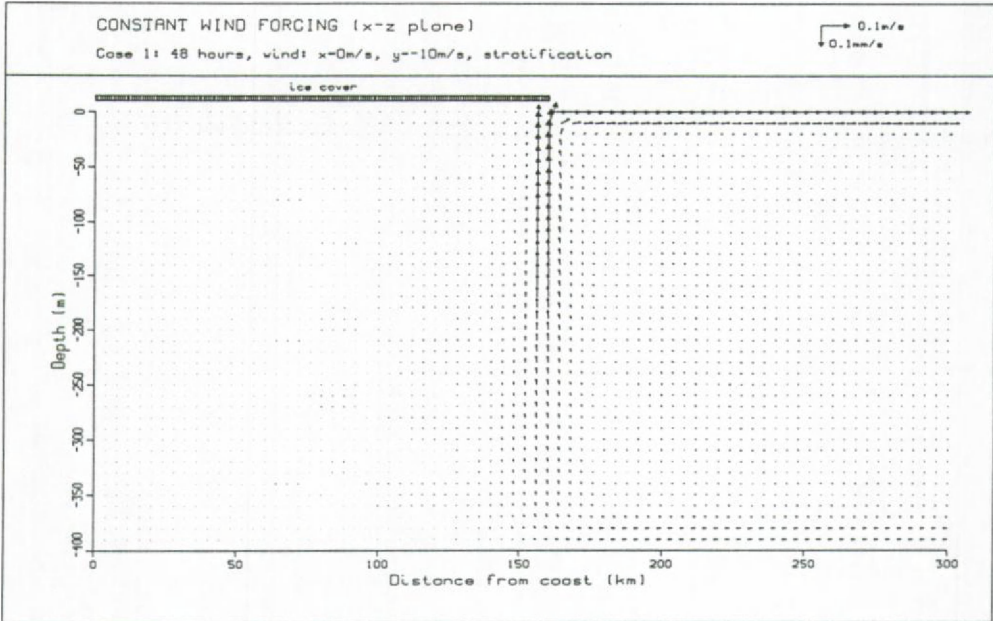


Figure 4.4: Flow field for the shelf case with a non moving ice cover. (a) upwelling and (b) downwelling favourable wind forcing.

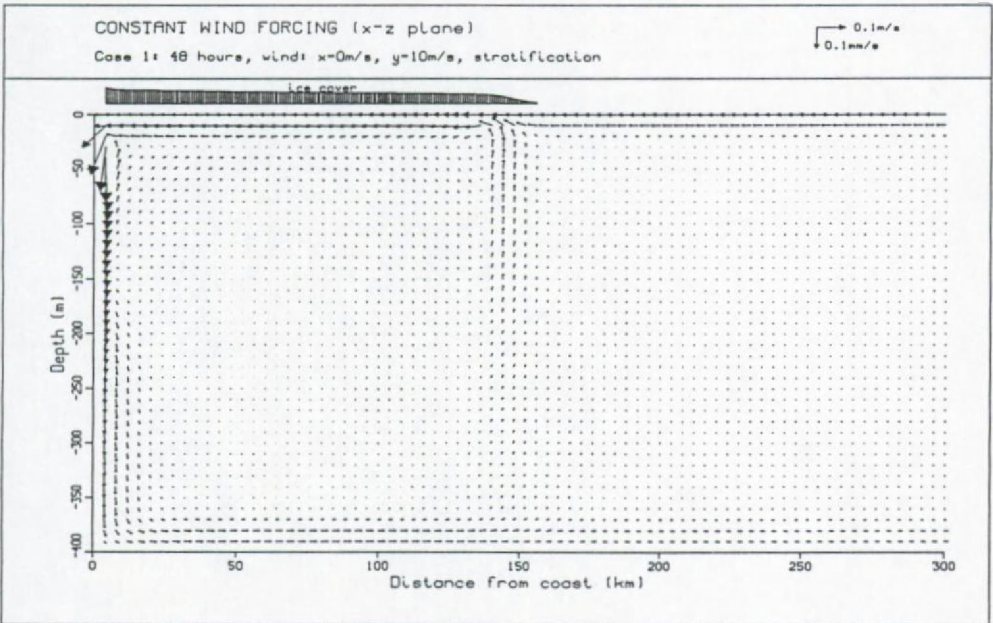
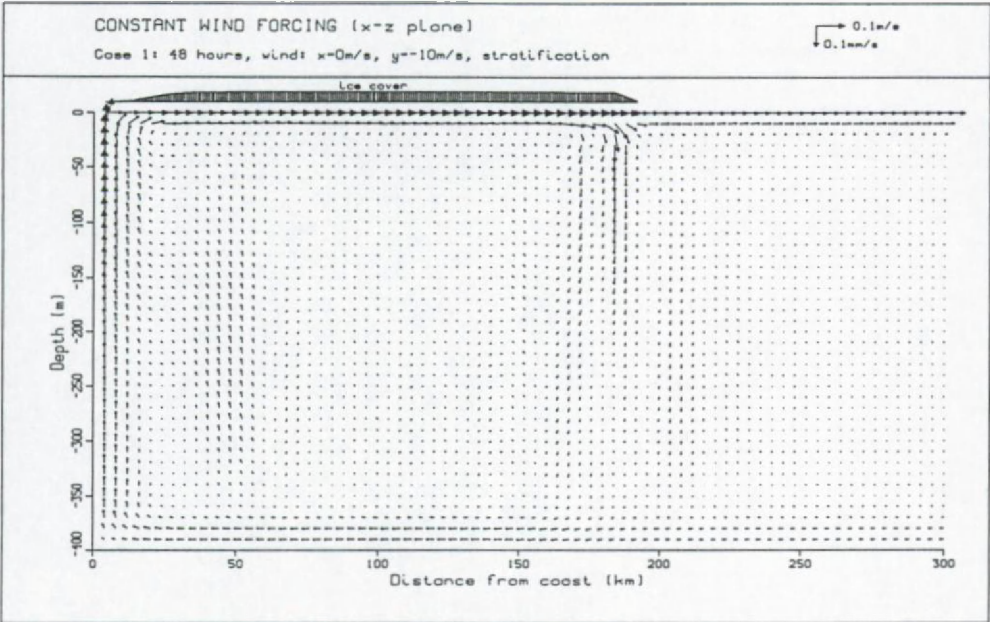


Figure 4.5: Flow field for the shelf case with a dynamic ice cover. (a) upwelling and (b) downwelling favourable wind forcing.

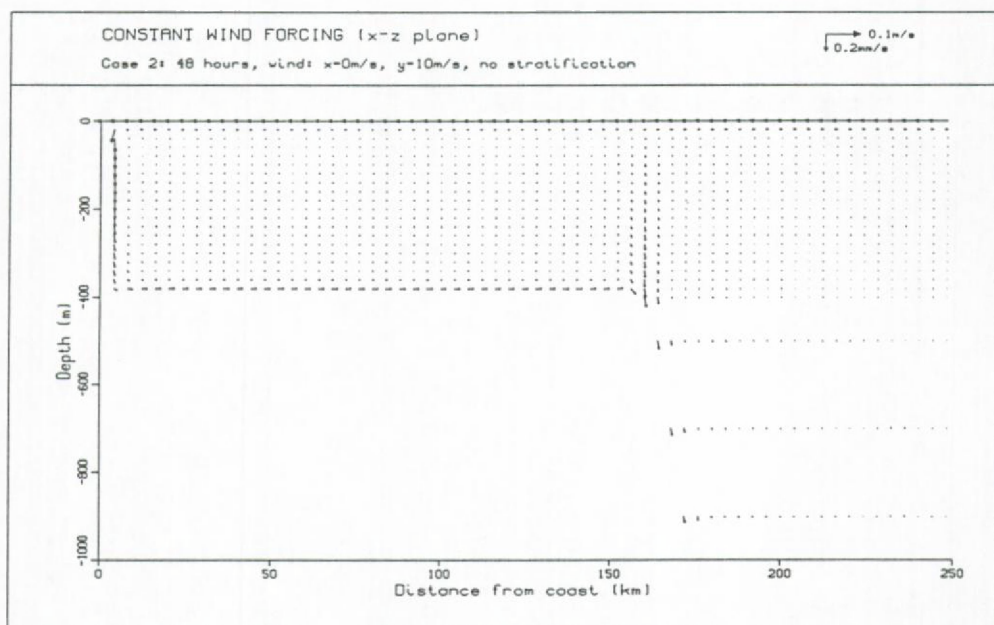
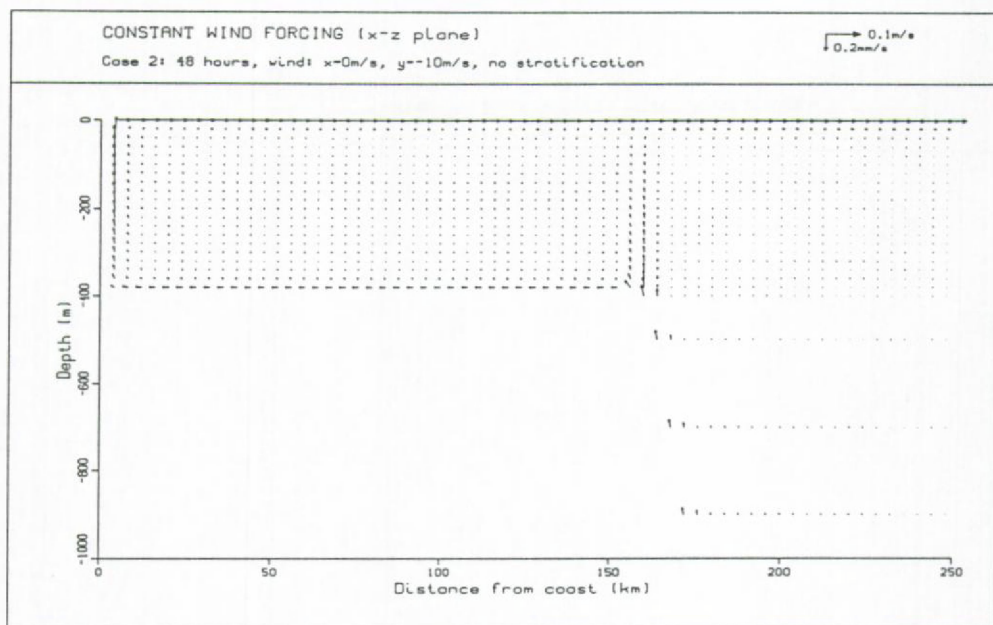


Figure 4.6: Flow field for the non stratified ice free shelf-ocean case. (a) upwelling and (b) downwelling favourable wind forcing.



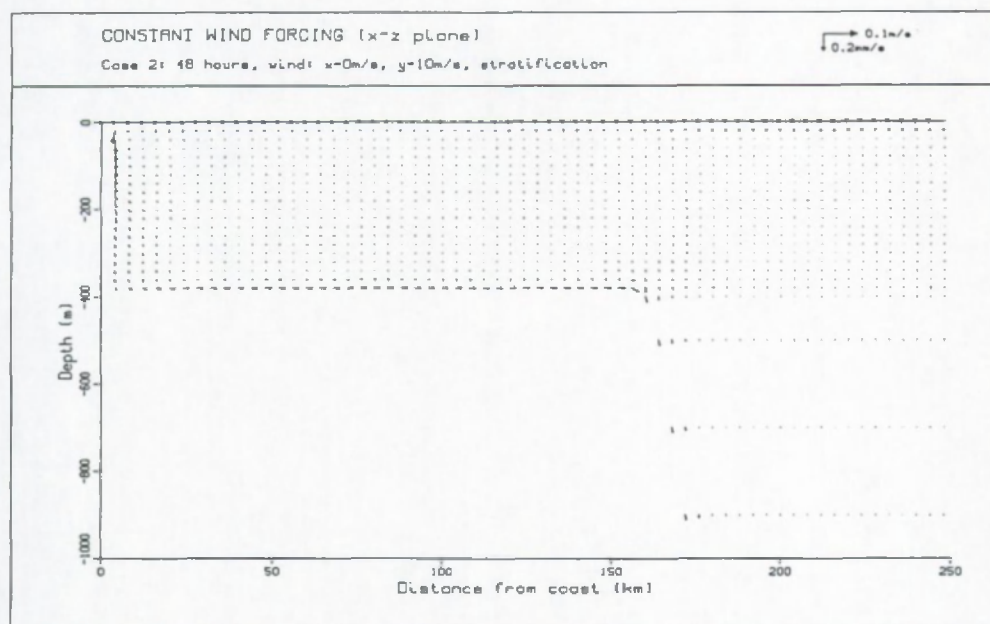
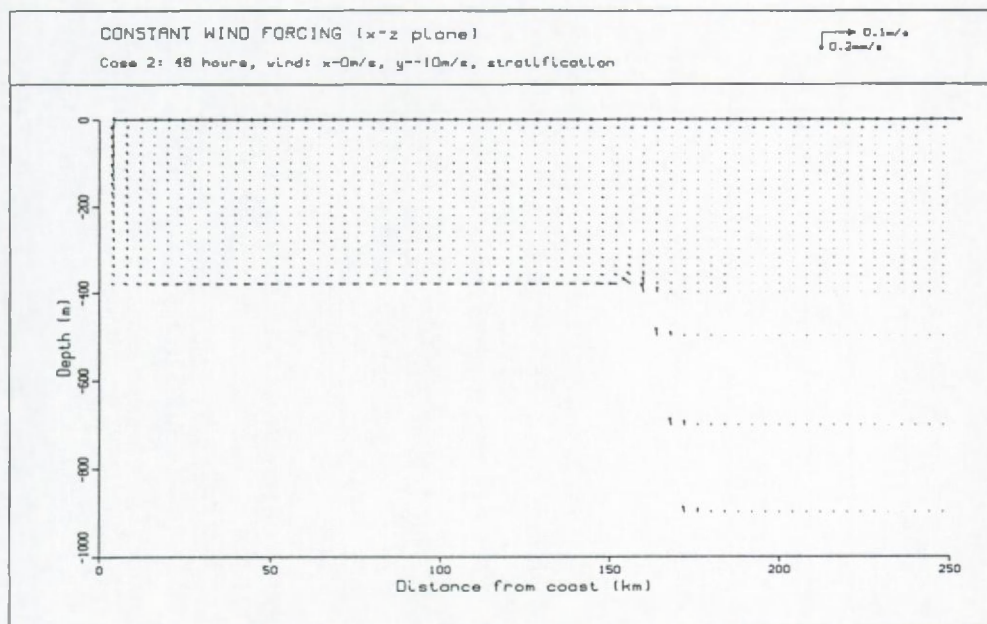


Figure 4.7: Flow field for the stratified ice free shelf-ocean case. (a) upwelling and (b) downwelling favourable wind forcing.



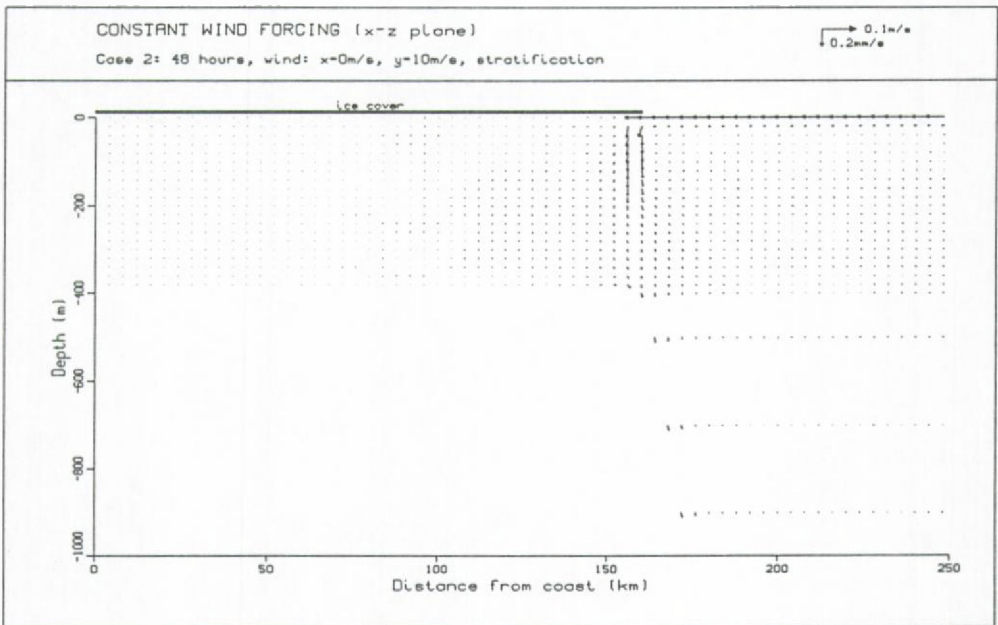
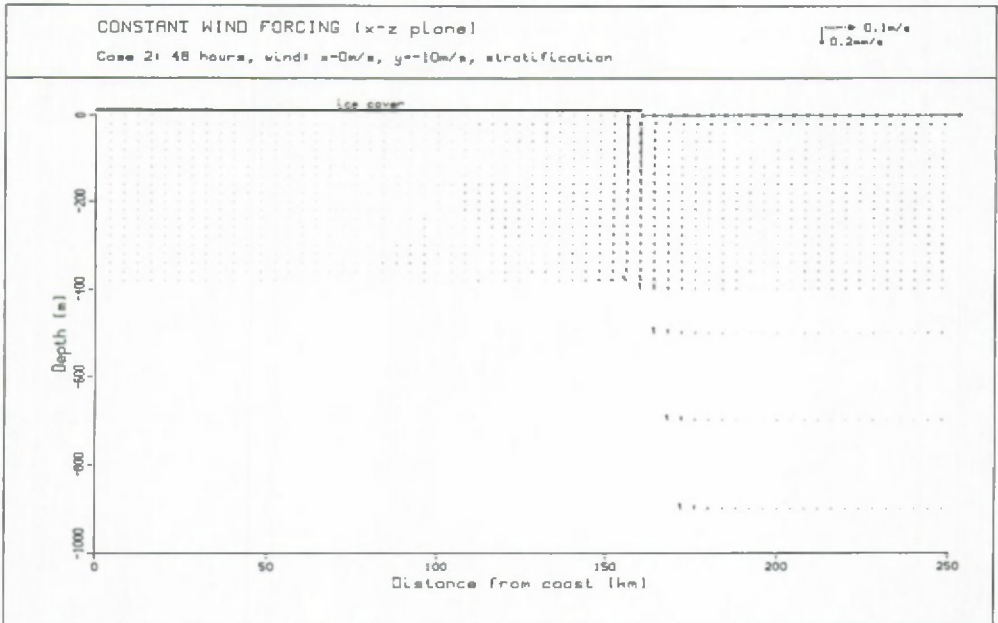


Figure 4.8: Flow field for the stratified shelf-ocean case with a non moving ice cover. (a) upwelling and (b) downwelling favourable wind forcing.

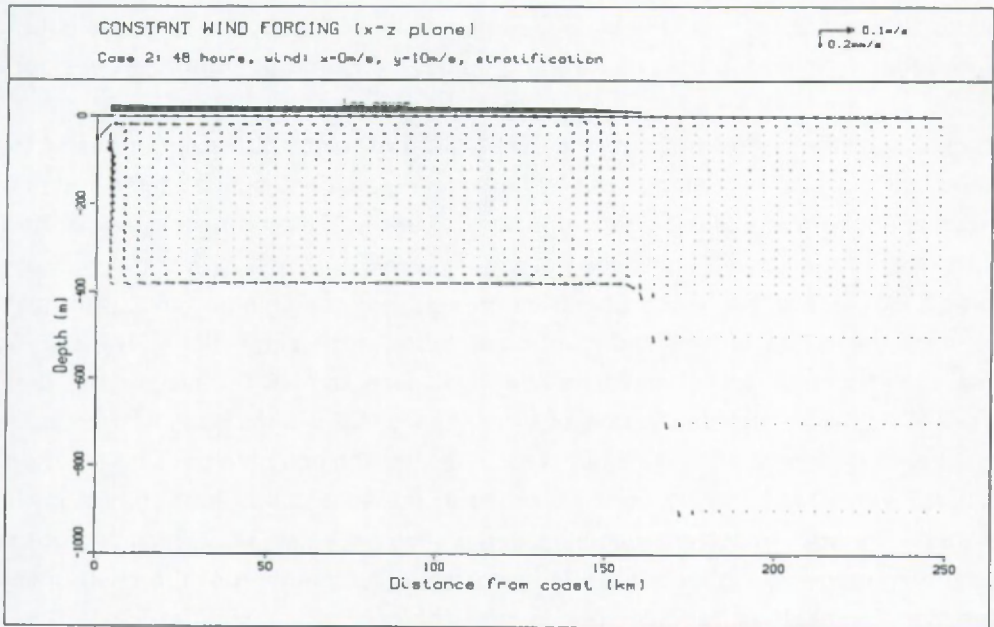
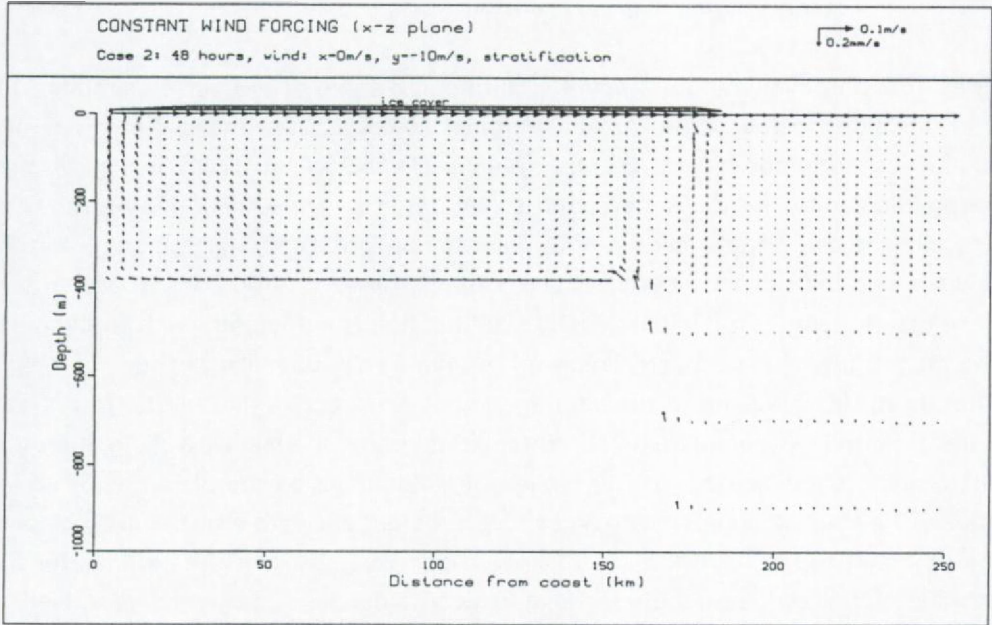


Figure 4.9: Flow field for the stratified shelf-ocean case with a dynamic ice cover. (a) upwelling and (b) downwelling favourable wind forcing.

### 4.3. Discussion And Conclusion

The 2.5D baroclinic model presented in chapter 2 has been used to simulate the currents along a shelf slope and at a marginal ice edge. The wind is blowing parallel to the ice edge/coast in a direction favourable for up- or downwelling. A flow perpendicular to the ice edge/coast is generated due to the Coriolis force. The upwelling is carrying denser water upward, a horizontal density gradient is formed and the resulting density current decreases the upward flow. For the flat bottom case (shelf, case 1) the initial density stratification is sufficiently high to decrease the magnitude of the upward flow and to enlarge the upwelling zone.

The up- or downwelling at the ice edge is not as effective as the one found at a coastal boundary, because the currents extend under the ice. Upwelling along the shelf slope (shelf-ocean, case 2) is strongly influenced by the presence of an ice cover. The shelf slope upwelling is reduced substantially with a stationary ice cover and is enhanced in case the ice is allowed to move. The initially vertical density stratification is reducing the upwelling flow. The denser water which is upwelling at the break is deviated and increasing the bottom flow over the shelf compared to the constant density case. Although the ice and the ocean (constant eddy viscosities and diffusivities) is simulated in a simplified way, the model is able to reproduce the main features occurring at an ice edge and at a continental slope.

The study of the relative importance of the different terms in the equations of the numerical model can be carried out by considering time and space scales and non-dimensional numbers, see Pond and Pickard (1986). The time necessary for horizontal momentum to diffuse to the bottom is given by  $E_v^{-0.5} f^{-1}$ , with  $E_v = A_v f^{-1} h^{-2}$  the vertical Ekman number. For time scales greater than the spin-up times, a bottom Ekman layer will be formed and must be included in the simulations. The spin-up time scale is equal to 4.1 days for the shelf case and 40.6 days for the deep ocean. This means that the 2 days of simulation is in the same order of magnitude as the spin-up time for the shelf but is too short for the ocean to develop a bottom Ekman layer. This has also been observed in the simulations (not shown in the figures). The bottom current velocities in the deep ocean are very small and of the same magnitude as higher in the water column. The intention of the shelf-ocean case was not to simulate the response of the deep ocean to wind forcing but was focused on the shelf edge processes which are in the right order of spin-up time scale.

The internal Rossby radius of deformation is a length scale associated with the spin-up time scale and represents the horizontal scale at which rotation effects



become as important as buoyancy effects and is written as  $\lambda_i = (g'D_0)^{0.5}f^{-1}$ , with  $g'$  the reduced gravity and  $D_0$  the upper layer thickness. The value of  $\lambda_i$  is about 11 km in this case. The majority of the variations in currents occur within the Rossby radius of deformation when the ice cover is stationary. When the ice is allowed to move the currents are over-run or blown away from the up- or downwelling structure and the length scale is distorted.

The ice edge in the experiments moved about 16 km (case 2) to 24 km (case 1) away from its initial position in case the wind induces an off-shore current. The magnitude of the horizontal displacements of the ice edge are in the same order as reported from literature. Buckley et al. (1979) observed that the ice edge around Spitsbergen moved several tens of kilometres in a few days. The model results for the off-shore currents reveal the formation of a coastal polynya. The ice-ocean coupled model explains one of the causes of polynya formation. The ice model only takes into account dynamic processes. A coastal polynya is, however, the result of off-shore ice drift and of the formation of new ice. Both processes have opposite effects and are in equilibrium (Ou, 1988). The wind speed and direction is usually not constant and can therefore have countering effects. The author argued therefore that the width of a polynya is primarily a function of the air temperature. The non-linear terms in both the ice and the ocean momentum equations are not important, except near the coast or at the ice edge. The Rossby number, which is represented by the ratio of non-linear terms divided by the Coriolis term is generally smaller than 0.1 except near the ice edge and at the coastal boundary. There the advective terms cannot be neglected.

A characteristic feature of marginal ice edges is the development of an along ice edge jet. The jet is attributed to Coriolis force. After about 12 hours the jet has been diffused away. The disappearance of the along ice jet is a function of the value of the horizontal diffusion coefficient. The occurrence of an along ice jet in case of non moving ice cover has already been described by Niebauer (1982). Interesting to notice is the formation of a coastal jet in case of an ocean with a moving ice layer forced by an off coastal current favourable wind (see Figure 4.5). This coastal current is present as long as the coastal polynya has not been formed, see Figure 4.10a. The coastal jet is a consequence of the Coriolis force and the stress exerted on the water by the ice and the wind forcing. As the ocean becomes more and more ice free along the coast, the ice stress on the water decreases and the wind is directly acting on the water. Since the ice/ocean stress is higher than the air/water stress, the alongshore current decreases in magnitude in course of

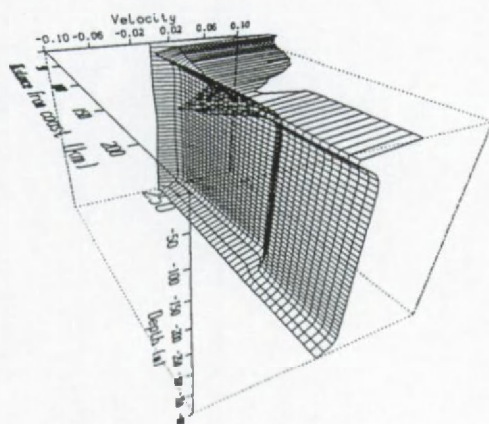


time, as can be seen in Figure 4.10b. At the ice edge one can observe a sharp reduction in along-shore surface currents after 12 hours of wind forcing (Figure 4.10a). An along ice jet occurs just beneath the surface layer with opposite current direction. This along ice jet is diffused away as time is going on (see Figure 4.10b).

The internal ice stress is small where the ice concentration is less than 80%. The internal ice stress terms are thus only important where the ice concentration is high. The influence of the internal ice stress can be seen at the continental boundary in case of on-shore currents, elsewhere the term can be neglected.

CONSTANT WIND FORCING (x-z plane)

Case 1: 12 hours, wind:  $x=0\text{m/s}$ ,  $y=10\text{m/s}$ , no stratification



CONSTANT WIND FORCING (x-z plane)

Case 1: 48 hours, wind:  $x=0\text{m/s}$ ,  $y=10\text{m/s}$ , no stratification

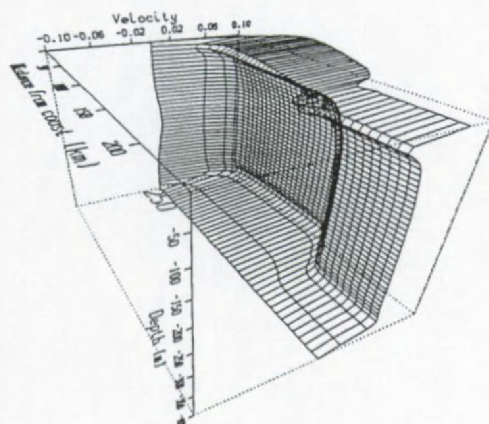


Figure 4.10: Flow field perpendicular to the vertical plane after (a) 12 hours and (b) 48 hours of wind upwelling favourable forcing (moving ice cover) showing the occurrence of an alongshore and along ice jet. (direction is reversed).



## CHAPTER 5

### COHESIVE SEDIMENT TRANSPORT IN THE SCHELDT ESTUARY

#### 5.1. Introduction

The goal of Chapters 5 to 7 is the study of mud transport in an estuary using field measurements and numerical models. As case study a part of the Scheldt estuary, more precisely the 'Beneden Zeeschelde' (between Antwerp and the Belgian-Dutch border), has been chosen. The knowledge of temporal and spatial variations of processes which influences the transport, erosion and sedimentation of mud is important not only from a scientific but also from an engineering or from an environmental point of view.

Mud transport models of estuaries are able to reproduce specific features on limited time scales (erosion/deposition, turbidity maximum, variations as a function of tide or neap-spring cycle). Long term predictions are, to our opinion, not very reliable. Numerical models of mud transport should therefore be used with care, partly because of the limited predictive capabilities of such models, partly because of the complex nature of the hydrodynamic conditions in the estuary and partly because of the lack of knowledge of the distribution of mud in suspension and on the bottom. The reliability of these models can be increased if data for refinement and validation are available. In order to illustrate and explain the great variations in mud concentration found in the Scheldt estuary the results of field measurements will be presented in Chapter 5.

The mud transport is simulated using a 2D (Chapter 6) and a 3D model (Chapter 7). The 2D model has been validated by comparing the results to data obtained from a laboratory model. The validation experiment has been carried out as a part of the MAST G8 research program and has been the subject of an intercomparison



exercise. The experiment has shown that the model is able to reproduce well the observations, but indicated that even using data from a controlled environment of a laboratory, the predictive capability of the model suffers from a good description and integration of the various physical processes which governs the transport (i.e. erosion, deposition, consolidation, rheological properties). The 2D mud transport model has then been applied to a part of the 'Beneden Zeeschelde'. The model is able to reproduce qualitatively well the erosion and sedimentation patterns. The results of the model have been compared to the results of two other mud transport models. Differences between the models have been found and explained as being due to numerical factors and different diffusion coefficient used.

The measurements (Chapter 5) have indicated that density induced currents play an important role, especially in the access channels to the harbour of Antwerp. A 2D model is not able to simulate these currents, therefore a 3D model has been set up (Chapter 7). It is shown that the high mud sedimentation in the access channels is mainly a consequence of the density gradients existing between the river and the access channel. A detailed numerical model study together with a measurement campaign to validate the model has not been carried out up to now.

Chapter 5 is intended to define the processes responsible for the distribution of suspended cohesive sediments in the Scheldt estuary, to illustrate the great variations of mud concentration in time and space and to set up a frame for the analysis of the measurements discussed below. In order to do so a literature review of processes relevant to the distribution of suspended mud in the Scheldt estuary is given in § 5.2. Although the different processes have been readily identified, there is still a lack of knowledge concerning the detailed distribution of suspended mud in time and space in the Scheldt estuary. In § 5.3.-5.6. a detailed analysis of measurements which are all situated in the Beneden Zeeschelde is given. The observations were taken by the Antwerpse Zeehavendienst in the framework of the project Morphological Study of the Northern Container Terminal. The study has been carried out by the consortium I.M.D.C.-W.L.B. and was financed by the Antwerpse Zeehavendienst. The measurements have been published in various reports (see reference list). A detailed scientific analysis has, however, not been carried out up to now, and has therefore been the subject of this thesis. The observations consist of ebb and flood, of through tide and of long term measurements:

During flood and ebb current velocity and salinity have been measured in a cross section at the access channel to the Zandvliet and Berendrecht locks (see § 5.5.). The flow field in the access channel is mainly induced by horizontal and vertical salinity differences. In the access channel high sedimentation of mud occurs.

A detailed analysis of two through tide measurements (neap and spring tide) at the

'Drempel van Zandvliet' is described in § 5.3. The analysis focuses on the variation of current velocity, salinity and mud concentration in time (tide, ebb and flood) and in space (vertical and lateral). Two other whole tide measurements ('Plaat van Lillo' and 'Vaarwater boven Bath') will be briefly introduced in § 5.4 and compared with the measurements at the 'Drempel van Zandvliet'.

Long term observations of salinity, temperature and mud concentration at Prosperpolder are presented in § 5.6. These measurements allowed to quantify the variation of suspended mud as a function of ebb and flood, tidal range and seasons.

## 5.2. The Scheldt Estuary

'An estuary is an area where sea water is measurably diluted with fresh water derived from land drainage' (Pritchard, 1967). This definition does not take into account the fresh water zones of the river system influenced by the tides. The salinity intrusion in a river is generally less extended upstream than the influence of the tidal wave and is a function of the fresh water discharge. Therefore the definition of an estuary is remains somewhat arbitrary. In what follows we will use the word 'estuary' as the whole part of the river system influenced by tides. Pritchard classified estuaries based on the mixture between the fresh and the sea water and defined four classes: homogeneous (no horizontal or vertical salinity gradients), well mixed (no or weak vertical stratification), partially mixed and highly stratified (strong vertical stratification, two-layered flow). An estuary does not necessary belong to one class alone but can consists of different parts with each a specific vertical stratification belonging to one of the above mentioned classes. In the Scheldt estuary three different zones can be distinguished: Homogenous, partial mixed and well mixed (Peters, 1975; Nihoul et al., 1978). Estuaries are particularly complex environments. The transition between fresh water and sea water under influence of tidal action results in a complicated interaction between physical, chemical and biological processes. The tidal wave entering the estuary is gradually distorted by interactions with the channel geometry, friction, non-linear advection and by the fresh water flow of the river system. The difference in salinity and in sediment concentrations results in a density gradient along the estuary and thus in density induced circulations (baroclinic circulation). The hydrodynamic situation has specific consequences on the behaviour of dissolved and suspended materials transported by the currents. Characteristic for estuaries is the presence of a turbidity maximum, this is a region where fine grained sediments are trapped. In the Scheldt estuary the turbidity maximum is situated in the vicinity of the harbour

of Antwerp. The transport and the dynamics of cohesive sediments in estuaries are influenced by a wide range of physical, chemical and biological processes. Markofsky et al. (1986) and Lang et al. (1989) mention in general the following processes which are known to be important, baroclinic circulation, transport due to tidal pumping, resuspension and deposition, flocculation and floc breakup and the death of microorganism in the brackish water zone. The relative importance of these processes is a function of the hydrodynamic factors (tidal range, horizontal current velocities, wave action and fresh water flow). Factors which influence the erosive strength of the sediments are the composition (mineralogy, organic and sand content), the consolidation and the flocculation (Nichols, 1984).

### **5.2.1.      *Hydrodynamic aspects***

The drainage basin of the Scheldt estuary covers an area of nearly 22000km<sup>2</sup> and is situated in the North-West of France, the West of Belgium and the South-West of the Netherlands. The Scheldt basin consist of the Scheldt river, which has its source in France and its tributaries, the most important being the Rupel, the Dender and the Durme, see Figure 5.1. In appendix 1 a list of locations and their distance from the mouth is given.

The tide in the estuary is essentially semi-diurnal with a period of 12 hours 25 minutes at mean, 12 hours 20 minutes at mean spring and 12 hours 41 minutes at mean neap tide. The tidal wave penetrates the estuary up to Gentbrugge (155.6 km from the mouth). The amplitude of the tidal wave as well as the duration of rising and falling tide is not constant over the reach of the estuary. The differences in magnitude and duration between ebb and flood tidal currents (tidal asymmetry) are produced by the distortion of the tidal wave propagating from the continental shelf to the estuary. The mean tidal range is 3.85m at the mouth (Flushing) and increases up to 5.24m at Schelle (91.2km from mouth). Further upstream it decreases to a value of 1.89m at Gentbrugge (155.6km). The ratio between the duration of rising to falling tide decreases from 0.88 at Flushing to 0.75 at Schelle and 0.39 at Gentbrugge (Claessens and Belmans, 1984). The average fresh water discharge at Schelle is about 100m<sup>3</sup>/s, with extreme values of 20m<sup>3</sup>/s during summer and 600m<sup>3</sup>/s during winter (Belmans, 1991).

The estuary can be classified in different zones using the hydraulic ratio (flood volume divided by the fresh water volume during a tidal cycle) and the geometrical parameter (width divided by average cross sectional area). Peters (1975) and Nihoul et al. (1978) distinguished three zones. A zone of practically fresh water



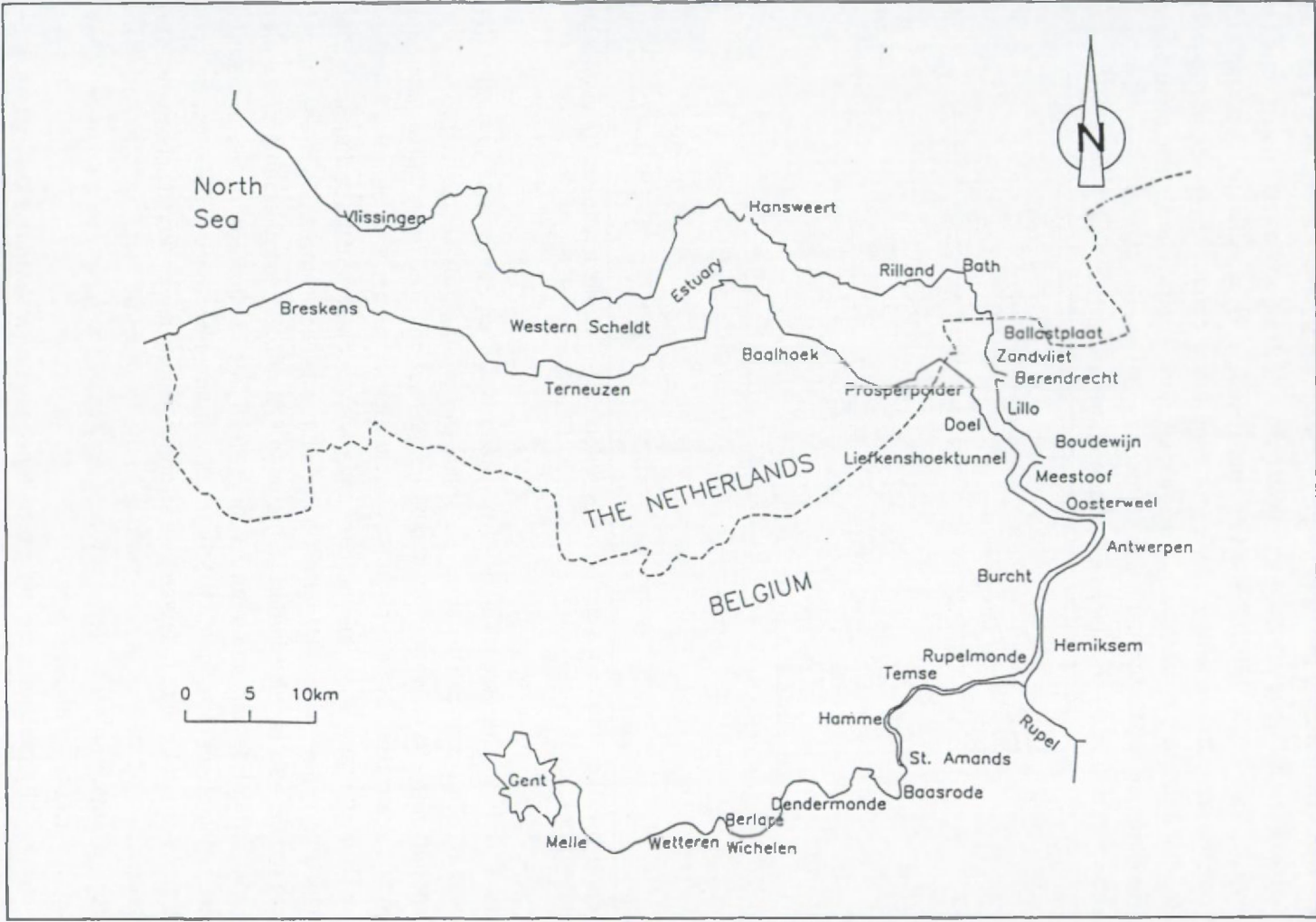


Figure 5.1: Scheldt estuary.



between Gentbrugge (155.6km) and Rupelmonde (92km), a partially mixed zone between Rupelmonde (92km) and Walsoorden (39km) and a well mixed zone between Walsoorden (39km) and Flushing (0km). This classification corresponds roughly with the transition between a simple one channel river (Gentbrugge to Rupelmonde) to a system with one main channel, flood channels and sand banks (Rupelmonde to Walsoorden) to a complex region of multiple channels (flood and ebb channels) and sand banks (Walsoorden to mouth).

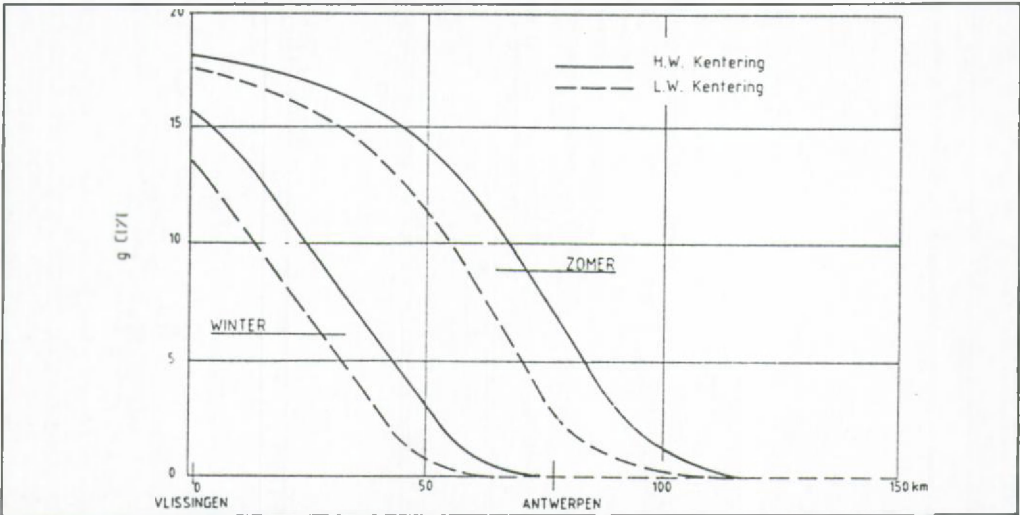


Figure 5.2: Longitudinal salinity distribution in the Scheldt estuary (solid = high water slack, dash = low water slack), after Claessens (1988).

The salinity in the estuary varies from fresh water at Gentbrugge to nearly the value of sea water at Flushing. The shape of the longitudinal salinity profile is a function of the fresh water flow and of the tidal actions. The fresh water discharge limits the intrusion of salt, during low river run-off the salt can penetrate further than Rupelmonde. The semi-diurnal changes in water level and the spring-neap tidal amplitude variations result in a periodical shift of the salt intrusion. The averaged longitudinal salinity distribution is shown in Figure 5.2. Measurements of salinity in the Scheldt estuary between Flushing and Temse indicate that the gradient is very regular (van Maldegem, 1995): an almost linear decrease in the western part of the Western Scheldt followed by a stronger, almost linear decrease between the eastern part of the Western Scheldt up to the fresh water zone ( $< 2\text{g/l}$ ) and then a further asymptotical decrease towards upstream. The zero salinity point can shift over a distance of about 40km.

Lateral salinity gradients are most pronounced in regions where a distinct separation between flood and ebb channels exist. At the 'Drempel van Zandvliet' (see §

5.3.5.) the lateral difference in salinity is highest at around low water and has a value of 1.5g/l at neap tide and 2.5g/l at spring tide. Important for engineering works are the lateral salinity gradients which occur between the river and some artificial channels, such as the entrance channels to the locks of the harbour of Antwerp (see § 5.5.3). Vertical salinity gradients are most pronounced in the partially-mixed region and are highest during high water slack, values up to 4g/l during spring tide have been measured (Fettweis et al., 1994).

## **5.2.2.      *Lithology and Morphology***

The geological substratum of the Scheldt estuary consists of essentially 'Oligocene to Pliocene and Quarternary sands, clayey sands and clay, covered by a 2m thick peat layer overlaid by clay (Dunkerque transgression)' (Wartel, 1977). The river is incised in a very cohesive clay layer (Rupelian) between Schelle and Hoboken, this clay layer is overlaid by Quarternary gravel and coarse sand deposits. The distribution of recent sediments is controlled by the input of materials from upstream, the hydrodynamic conditions and the human activities. An overview of the bottom sediments in the estuary can be found in Wartel (1977). The bottom sediments of the main channel between Schelle and Antwerp (the area with a maximum current velocity) consists mainly of medium and coarse sands and sometimes gravel. At some places the clay layer (Rupelian) is not covered by recent sediments. Between Antwerp and Zandvliet the decreasing transport capacity of the flow results in a reduction of the grain sizes of the bottom sediments, the bottom consists of sand, sandy mud, mud and fluid mud (see also Bastin, 1986). The drillings carried out by the Bestuur Geotechniek (BG, 1993) north of the access channel to the Zandvliet lock indicate that along the banks a mud layer of  $\pm 0.5\text{m}$  exist, which is underlain by peat ( $\pm 2\text{m}$ ) and Quarternary sand and sandy clay or clay of variable thickness. Towards the river, in the deeper parts, the Quarternary layers are absent (erosion) and the bottom consists of recent deposits of fine sand, which are directly in contact with the Tertiary sands (Sand of Merksem). Downstream of Zandvliet the mud contents is much reduced and the sediments consist mainly of medium to coarse sands. On the tidal flats the sediments cover a range from well sorted medium sands to heterogeneous poorly sorted clayey silts. The entrance channels to the locks consist mainly of mud and fluid mud.

The morphology of the Scheldt estuary is a result of the geological substratum, geological processes, the natural dynamics of the system (including sediment supply from inland or coastal region) and the influences of human activities (engin-

eering works, dredging activities). The sediment supply and transport depends on several factors among which the fresh water discharge, the sediment characteristics, the wind waves, the current velocity distribution and its variation during a tidal cycle (Dronkers, 1986). Fresh water discharge has an influence, through the creation of density differences, on the vertical distribution of the current velocity, tending to increase the flood currents near the bottom and decrease them near the surface and vice versa during ebb. This aspect has an important effect on cohesive sediment transport and will be discussed and illustrated below.

### 5.2.3. *Cohesive sediments*

Mud is defined as a sediment with cohesive properties build up of a variety of components (Allen, 1985). The most important components are clay minerals, followed by organic materials (organic molecules and microorganism) and other rock forming minerals (quartz, carbonites). The cohesive properties of a sediment start to become important when the sediment contains more than 5 to 10% of clay by weight (Dyer, 1986). Mud in suspension exists in the form of particles, flocs or aggregates. Van Leussen (1994) made a distinction between flocs and aggregates, floc is a general name for particles or groups of particles that are bound together, aggregates are defined as flocs with a loosely packed structure. We did not have at our disposal measurements or information which gave us the possibility to follow van Leussens's definitions, therefore the word 'particle' has been used in a general way leaving the possibility open whether particle, floc or aggregate is meant. The words 'floc' or 'aggregate' have been used to stress that some kind of packing between particles has occurred due to flocculation or aggregation. Because of the cohesive characteristics of mud it is not possible to give a specific grain size. Clay minerals have dimensions lower than  $2\mu\text{m}$ , mud flocs or aggregates can however be substantially bigger ( $\pm 1\text{mm}$  or more). Very often mud is characterised by a grain size of less than  $63\mu\text{m}$ , i.e. silt and clay particles. This definition results from the fact that the bindings between the various components of mud in an aggregate is very weak and is easily destroyed by sampling and sieving.

#### 5.2.3.1. *Origin of mud in the estuary*

The mud which is found in the estuary is partly of marine and partly of riverine origin. The mud can be on the bottom or in suspension. The total amount of



mud in suspension in the Scheldt estuary has been estimated by van Maldegem (1993): A maximum is found during spring tide at maximum current velocity ( $0.4 \times 10^6 \text{ t}$ ) and a minimum occurs during neap tide at low water slack ( $0.1 \times 10^6 \text{ t}$ ). The amount of mud on the bottom varies between the different morphological units. Mud is deposited in areas where the current velocities are low (harbour entrances) or where the deposition part of the tidal cycle is more important than the erosion part (tidal flats, some parts of channels). Intertidal areas are one of the major sources and sinks in estuaries.

In order to understand the mud transport in the estuary mud balance models have been set up (see e.g. van Maldegem et al. 1993 and Vereeke 1994). These models are based on information of the origin and the amount of mud entering and leaving the estuary. An accurate estimate of the mud fluxes in the estuary is important because of pollution related problems and in order to increase the reliability of prediction concerning the impact of human activity on the sedimentation and erosion of mud in the estuary. The mud fluxes in the mud balance models are determined from the mixing of marine and riverine mud, from amounts of mud taken out of the estuary or displaced by dredging works, from accumulation or erosion of mud in the various morphological units and from suspended mud measurements. All the amounts entering the balance are estimated values and have thus high uncertainties. If we just consider mud concentration measurements, we have found (see analysis of measurements in this chapter) that big variations occur over different time and length scales. These variations are related to a wide range of factors (tides, tidal amplitude, seasons, mud sources) and only intensive measurements, in time and space, can lead to more accurate estimations. Furthermore, observations which have been collected in the past can have limited value today, due to the impact of human activities in the estuary (dredging, harbour extension etc.). A first estimate of the amount of riverine mud input at Rupelmonde varied between  $1.0 \times 10^6$  and  $2.2 \times 10^6 \text{ t/yr}$  (Wartel, 1977). Later Wollast and Marijns (1981) estimated the amount as  $0.75 \times 10^6 \text{ t/yr}$ . In I.M.D.C. (1993a) an update of the different sources of riverine mud input has been presented. These sources are waste water (industrial, domestic and agricultural), surface erosion of cohesive soils and precipitation. The amount of riverine mud entering the system is estimated by I.M.D.C. (1993a) as  $0.8 \times 10^6 \text{ t/yr}$ . The amount entering from the sea is not known in detail and is derived indirectly as a closing parameter. The riverine/marine mud ratio is an important parameter and is determined by various tracers. The following have been used:  $\text{CaCO}_3$ ,  $^{15}\text{N}/^{14}\text{N}$ ,  $^{239+240}\text{Pu}$ ,  $^{238}\text{Pu}$ ,  $^{12}\text{C}/^{13}\text{C}$ ,  $^{137}\text{Ce}$ ,  $^{210}\text{Pb}$  and Cr, see W.L. (1975), Swart (1987), Wartel et al. (1993), ten Brinke (1994). The researches all indicate, quite evidently, that in the Belgian part of the estuary



(Beneden Zeeschelde) the mud is mainly from riverine origin. In the eastern part of the Western Scheldt the mud is from riverine as well as marine origin. In the western part of the Western Scheldt most of the mud on the bottom (tidal flats and channels) is from marine origin. The mud in the ebb channels is relative richer in riverine mud than the mud in the flood channels. There exist, however, differences between the results of the different tracers, resulting in high variations of the marine/riverine mud ratio. Studies based on only one or a limited amount of tracers give high uncertainties. The high variations in mud concentration occurring during a year at e.g. Prosperpolder (see § 5.6.4.) are partly interpreted as a result of the shift of the turbidity maximum as a function of the fresh water discharge and partly due to higher sediment loads of the tributaries of the Scheldt as a function of river run-off. These long term variations are a good indication for the fact that the ratio marine/riverine mud contents is probably not constant at a place and that frequent measurements in time have to be carried out in order to evaluate accurately the mixing of mud from both sources and to evaluate the applicability of the tracers.

#### 5.2.3.2. *Suspended mud distribution*

In most medium and high tidal range estuaries a turbidity maximum is found. The turbidity maximum consists of an area where a large amount of cohesive sediments are accumulated and where these sediments are continually deposited and resuspended by the tidal flow. The turbidity maximum area is usually situated in the region with a strong increase in salinity in longitudinal direction or at the limit of the saline intrusion (Darbyshire and West, 1993). Dyer (1986) considered two main mechanism for the formation of the turbidity maximum, i.e. tidal transport and gravitational circulation due to density induced currents.

The influence of tidal transport is explained by the longer distance a mud particle travels during flood than during ebb. This difference in distance is due to two processes: asymmetry in slack waters and currents. The asymmetry in duration of high and low water slack influences the resuspension and settling behaviour of mud particles. Differences in magnitude of the ebb and flood currents can result in an upstream transport of mud in suspension. This landward transport will continue up to a point where the river flow will be dominant so that the direction changes towards the sea. Tidal asymmetry in estuaries has been discussed by Aubrey and Speer (1985), Dronkers (1986) and Friederichs and Aubrey (1988). The neap-spring cycle is affecting the transport of mud on a larger time scale due to the difference in magnitude of the currents. During neap tide the concentration

of mud in the water is lower because of the higher sedimentation, during spring tide more mud is resuspended resulting in higher concentration and transport.

Density induced circulation is an important mechanism for the trapping of fine sediments. The less saline water flows above the denser sea water towards the sea and the sea water flows near the bottom towards upstream. Riverine mud particles which are settling are then transported upstream and because of the mixing of fresh and salt water can be again brought into the upper layers where the net circulation is towards the sea. The process then restarts. Erosion of sediments creates a vertical sediment gradient, with higher concentrations near the bottom. This vertical gradient will increase the formation of density gradients.

The relative importance of density induced circulation and tidal transport in the formation of the turbidity maximum is depending on the ratio between tidal and fresh water flow and thus on the spring-neap cycle and the fresh water discharge. In a macro tidal estuary such as the Scheldt estuary the tidal transport is of the same order of importance as the density induced circulation (Iten Brinke, 1992).

A minor, although necessary process, in the formation of a turbidity maximum is the agglomeration of fine particles into flocs and aggregates (van Leussen, 1994). Without aggregation or flocculation, and the resulting increase in fall velocity, the sedimentation of mud would be much smaller. The formation of flocs and aggregates results from collisions between particles and from the cohesive properties of the particles and is limited by breaking mechanisms due to turbulence. A stable density stratification results in an inhibition of turbulence. This reduction of turbulent energy will favour the formation of mud aggregates or flocs. Turbulence plays also a role in the formation of aggregates because it increases the collision frequency. According to van Leussen (1994) aggregation is due to various mechanism, among which turbulence (increase of collision frequency and breakup), processes influencing the electrostatic equilibrium (salt flocculation, metallic coatings on the particles), organic aggregates and bioflocculation (action of microorganism) and pellitization (action of macroorganism i.c. filter feeders).

The averaged longitudinal profile of mud concentration in the Scheldt estuary, based on observations between 1970 and 1990, can be seen in Figure 5.3 (Van Eck et al., 1991). Peters and Sterling (1976) are mentioning turbidity values of 30mg/l between Flushing and Bath, increasing to 150-200mg/l at Rupelmonde. They found that the longitudinal course of turbidity has strong variations during the year. Swart (1982) presents values for the yearly averaged mud concentration of 60mg/l at the Belgian-Dutch border decreasing to 30-40mg/l downstream of the 'Verdrongen Land van Saeftinge' and further a rather flat course down to the mouth. The highest concentrations occur between Antwerp and Zandvliet, the tur-

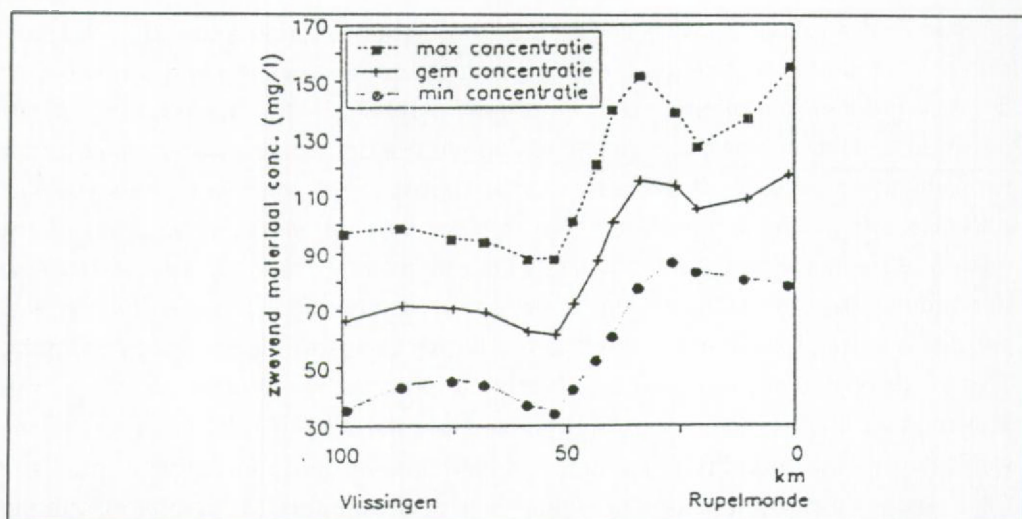


Figure 5.3: Longitudinal mud concentration in the Scheldt estuary, averaged values over 1970-1990, from Van Eck et al. (1991).

bidity maximum is situated in the vicinity of Oosterweel according to Wartel (1977). The exact location is, however, a function of the salinity and thus of the fresh water discharge. Wollast and Marijns (1981) and before them Peters (1972) have shown that the turbidity maximum in the Scheldt estuary is situated during low river run off at about 110km and during high river run off at about 50km from the mouth. In case of a river run-off greater than  $70\text{m}^3/\text{s}$  two maxima have often been observed in the turbidity maximum area. The existence of multiple turbidity maxima has also been observed in the Tay estuary, see Dobereiner and McManus (1983). Wollast (1973), Peters (1975) and Wollast and Peters (1979) explain the presence of the turbidity maximum in the Scheldt estuary as a result of the hydrodynamic conditions (residual circulation), the density induced currents and the flocculation processes. By calculating the time a particle remains in the estuary at different places Wollast (1973) has shown that the residual currents have a minimum in the area of the port of Antwerp (50-80km from mouth). The residual currents in this area are therefore specifically sensitive to variations in fresh water discharge. The salinity gradient is responsible for the deformation of the velocity profile (see § 5.3.). During flood an increase of the velocity near the bottom is observed whereas during ebb the velocity is decreased near the bottom. This results in favourable conditions for resuspension of sediments during flood and in upstream transports. Recent measurements (van Maldegem, 1995) of suspended mud along the Scheldt estuary have shown that at low water slack the turbidity maximum is absent (the course of mud from Flushing towards upstream increases)



but that a turbidity maximum is present during maximum flood flow between Prosperpolder and Hemiksem. The above cited researches indicate that the position of the turbidity maximum is highly variable and is depending mainly on the fresh water discharge superposed by variations occurring on time scales given by the tides and the neap-spring cycle.

The mechanism leading to residual mud transport have been described by Manni (1986). The horizontal circulation is not constant over the cross section, mud particles are thus moving with different velocities in the cross section. Due to salinity differences in longitudinal and vertical direction the velocity profiles during ebb and flood are different (see above) resulting in a net upstream transport near the bottom. In case of multiple channels or ebb and flood channels the current velocities differ much during flood and ebb. During flood the mud can be stored in the shallow parts of the estuary. During ebb the currents can be such that no or only part of the mud, which has been deposited during flood, is resuspended and again transported, resulting in an upstream transport of mud. Storage of mud in the shallow areas is a function of the seasons. The storage capacities during summer are generally increased due to biological activities (growth of algae) who tends to stabilize the mud on the bed. During winter the biological activity is reduced and the critical erosion shear stress decreases, resulting in a reduction of the storage capacity. This phenomenon is believed to influence the differences in suspended mud concentration in the estuary between summer and winter. Another mechanism, which results in differential mud transport is the formation of eddies due to irregular geometries. The mud in these eddies is isolated from the rest of the river, exchanges between the eddy and the other waters occurs through turbulent diffusion. Eddy formation is of importance in the access channels to the harbour of Antwerp. The differences in distance a particle is travelling during flood and ebb together with the non symmetric tides (neap-spring cycles, storm surges) and the above mentioned processes make it very difficult to predict the residual circulation of mud in the estuary. Furthermore the calculation of residual circulation or transport is depending on the length of the data record and is not necessarily equal from one period to the other. It is therefore clear that the residual circulation or transport in estuaries is to a certain extend only useful as a qualitative instrument to explain certain processes and phenomena.

The amount of mud in suspension as well as the longitudinal gradient show besides spatial variations also big variation in time. A general presentation of the various time scales and the variations in mud concentration is given by Van Eck et al. (1991). The smallest time scale which they consider are the tides, they estimate that the depth averaged mud concentration during a tidal cycle varies by a factor



two. The next time scale is given by the variations occurring during a spring-neap tidal cycle. The differences due to the seasons are for the Western Scheldt estuary estimated as a factor 3. The time variations in mud concentration depend on the length of the record and the geographical location of the measurement station. Estimates as those presented by van Eck et al. (1991) give thus general indications of how suspended mud varies in the estuary, locally the situation can be different: The long term measurements at Liefkenshoek (I.M.D.C., 1989), e.g. gave values for the ratio between mean to maximum mud concentration of 1.65 during flood and 2.30 during ebb. The mud concentration during neap tide was  $\pm 50\%$  and during spring tide 125% of those at mean tide. Recent measurements at Prosperpolder (see § 5.6.4.) indicate that the influence of the season is given by a factor of 2. This value has also been reported in van Maldegem (1993). In the following emphasis will be put on these mud concentration variations.

### 5.3. Through Tide Measurements At 'Drempel Van Zandvliet'

On 27/09/90 (neap tide) and on 04/10/90 (spring tide) two through tide measurements have been carried out in five points over a cross section at 'Drempel van Zandvliet' (I.M.D.C.-W.L.B., 1992a and 1992b). Points 1 and 2 are situated in the navigation channel (ebb channel), point 3 on the 'Plaat van Doel' (a sand bank) and points 4 and 5 in the 'Schaar van Ouden Doel' (a flood channel), see Figure 5.4. The 'Plaat van Doel' is separated from the main channel by a submerged dyke. This dyke has been constructed to concentrate the ebb flow in the main channel. The neap tide measurements started at high water slack whereas the spring tide measurements started at low water slack.

A detailed vertical profile of current velocity and direction, salinity and suspended mud concentration has been measured every 20 or 30 minutes. If possible the points were distributed over the vertical as follows: at 0.5m, 1m and 2m from the bottom, at 1/3, 1/2 and 2/3 of the depth and at 3m and 1m from the water surface. The velocity was measured with an Ott- or NBA- current meter, the conductivity with a NBA-sensor. Mud concentration was measured with a optical Partech turbidity sensor. Optical turbidity measurement devices are based on the scattering and attenuation of light waves (Thevenot and Kraus, 1993). The attenuation of a beam of light is measured by comparing the intensity of the beam of light before and after transversing a known length. The attenuation coefficient is linearly related to the concentration. The Partech optical suspended solid sensor has a near-zero response to the presence of sand ( $> 63\mu\text{m}$ ) in suspension, it measures

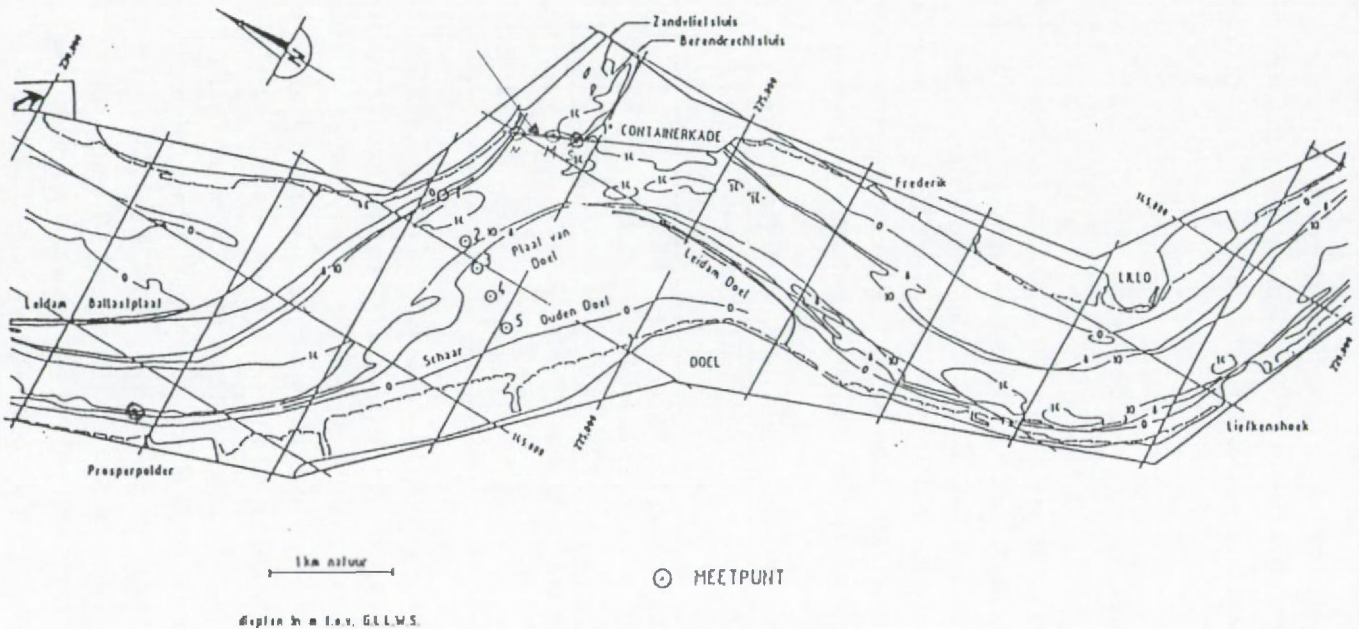


Figure 5.4: Location of the measurement points.

hence suspended silt and clay and not the total suspended solid concentration (Shuttler et al., 1993). The value measured is depending on the particle size and therefore site specific calibration measurement are necessary. The Partech sensor has been calibrated by taking regularly water samples during the measurements. Further calibration has been done by taking a mud sample from the bottom and preparing in a laboratory solutions with different (known) concentrations.

**5.3.1.        *Tides, currents and discharges***

The tidal curves measured in the tidal station of Zandvliet are shown in Figures 5.5-6. The times of low and high water, the water elevation and the tidal range are displayed in Table 5.1. TAW (Tweede Algemene Waterpassing) is the Belgian reference level. The tidal coefficients have been calculated by comparing the tidal range with the mean tidal range at Zandvliet during the period 1971-1980, the tidal coefficient of a mean spring tide is 1.128 and of a mean neap tide 0.832.

Table 5.1.    Tidal variations during the measurement days.

Date, Tidal station	Time (MET)	Water level (m + TAW)	Tidal Range (m)	Tidal coefficient
27/09/90, Prosperpolder	HW: 7h43	4.30	ebb    3.93 flood   3.89	0.810
	LW: 14h03	0.37		0.802
	HW: 20h13	4.26		
04/10/90, Prosperpolder	LW: 9h21	0.26	ebb    5.27 flood   5.57	1.087
	HW: 15h02	5.53		1.148
	LW: 21h52	-0.04		

The vertical averaged velocities are presented in Figures 5.5-6. The flood flow is written as negative and the ebb flow as positive. The curves show an asymmetric course. At spring tide a double peak in the velocity curve is observed during flood, whereas during ebb the velocities are more regular. This double peak in the flood curve is almost absent at neap tide.

The flow during flood is concentrated in the 'Schaar van Ouden Doel', whereas the ebb flow follows the main channel. The maximum flood velocity is situated near points 4 and 5 (neap tide  $\pm 0.8\text{m/s}$ , spring tide  $\pm 1.2\text{m/s}$ ) and the maximum ebb velocity in the vicinity of point 1 (neap tide  $\pm 0.8\text{m/s}$ , spring tide  $\pm 1\text{m/s}$ ), see Figures 5.7-8. The moment of low water slack is not occurring at the same time. The currents change their direction first in the shallower parts of the cross section (points 3-5). The phase lag in low water slack is about 1 hour. High water slack



passes much more synchronous over the width of the river. Only in point 1 during spring tide is the moment of high water slack about 1 hour earlier than in the other points. These differences in slack water moments are a consequence of the fact that the ebb flow is concentrated in the main channel whereas the flood flow has its maximum in the 'Schaar van Ouden Doel'.

Some typical velocity profiles are shown in Figure 5.9. The profiles are distorted with respect to the theoretical logarithmic profile. A downstream component can be observed near the surface and an upstream component near the bottom resulting in a decrease of the surface velocity at flood and an increase during ebb. The distortion of the profile is due to the horizontal and vertical salinity differences (see below). The influence of the stratification makes that during flood the saltier water penetrates faster into the river in the bottom than in the surface layer. During ebb the velocity in the lower layer is retarded. The distortion of the velocity profile can be calculated by taking the ratio of the surface to the vertical averaged velocity and comparing it to the ratio of the theoretical velocity profile. This ratio is equal to  $v_{sur}/v_{avg} \approx 1.1$  and has been calculated in Table 5.2: the 'ebb ratio' is greater than and the 'flood ratio' is smaller than the theoretical value.

Table 5.2 Mean ratio  $v_{sur}/v_{avg}$  for ebb and flood in the measurement points.

Point	1		2		3		4		5	
	ebb	flood	ebb	flood	ebb	flood	ebb	flood	ebb	flood
27/09/90	1.22	0.94	1.31	0.94	1.14	1.06	1.27	0.97	1.31	1.09
04/10/90	1.27	0.77	1.24	0.77	1.20	0.99	1.28	1.06	1.24	1.09

During high water slack the velocity currents in the bottom layer are directed towards upstream whereas in the surface layer water flows towards the sea (Figure 5.9). At the moment of low water slack the variations in flow directions are more irregular and a clear two-layered flow is more difficult to identify. The reason for this behaviour is that at high water a pronounced vertical stratification of salinity exists whereas at low water the vertical salinity gradient is much smaller.

The calculated discharges in every point are separated in ebb and flood values and are presented in Tables 5.3 (neap tide) and 5.4 (spring tide). The duration of ebb and flood has been set to the time between the two slack waters and is thus not equal for all points (the duration of ebb is  $\pm 6.5$  hours and that of flood  $\pm 6$  hours). The ebb and flood averaged discharge is  $3410\text{m}^3/\text{s}$  and  $3560\text{m}^3/\text{s}$  during neap tide, and  $4180\text{m}^3/\text{s}$  and  $4760\text{m}^3/\text{s}$  during spring tide respectively. The difference between ebb and flood is the residual flow which is equal to the sum of the river run off and the tidal residual. This value is the result of a subtraction of two very big



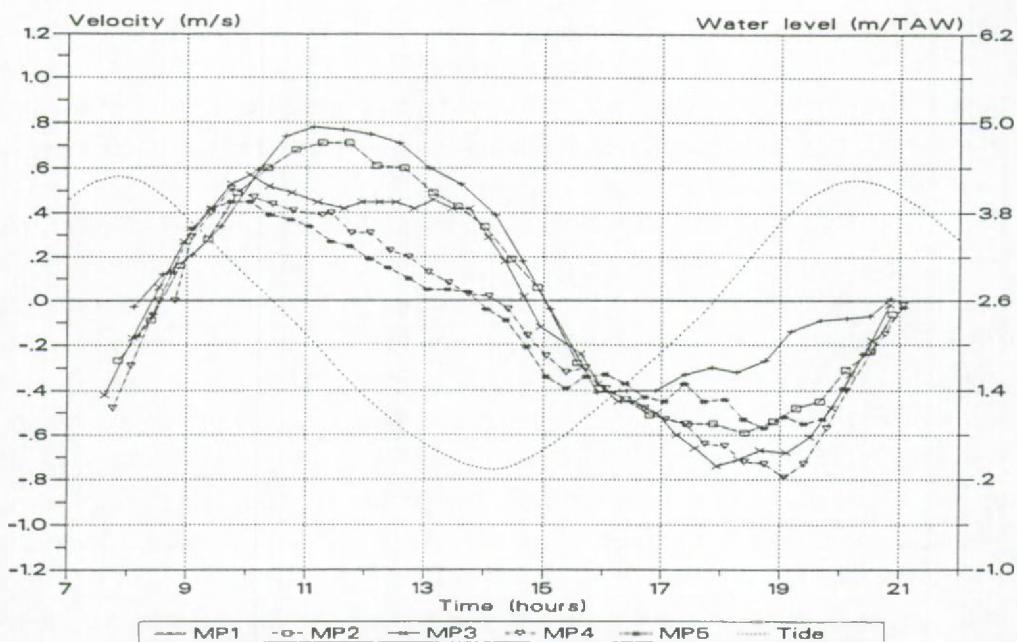


Figure 5.5: Neap tide (27/09/90), vertical averaged velocities at the 'Drempel van Zandvliet'.

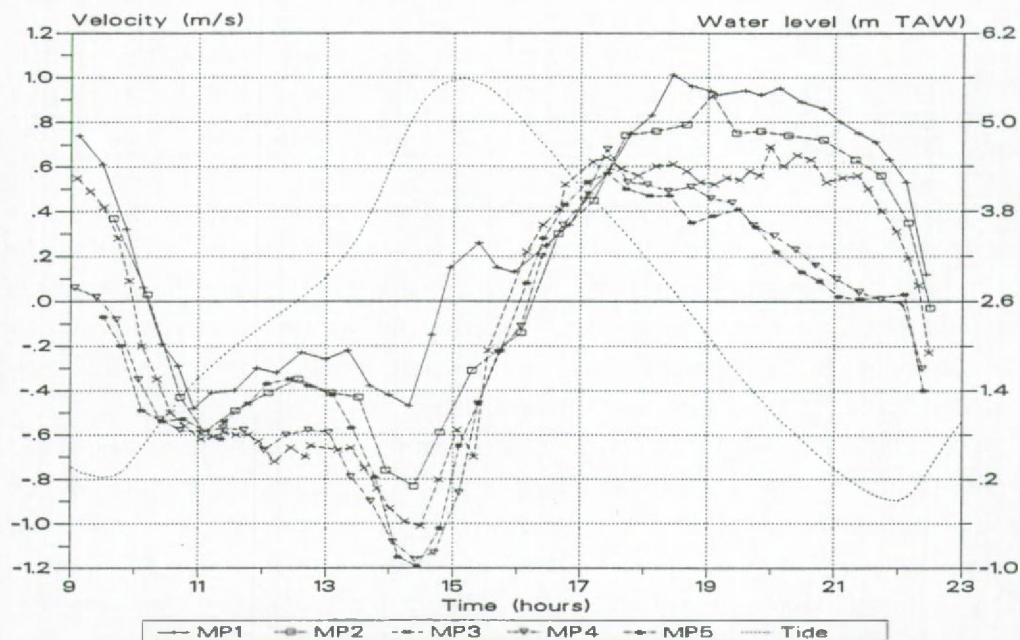


Figure 5.6: Spring tide (04/10/90), vertical averaged velocities at the 'Drempel van Zandvliet'.

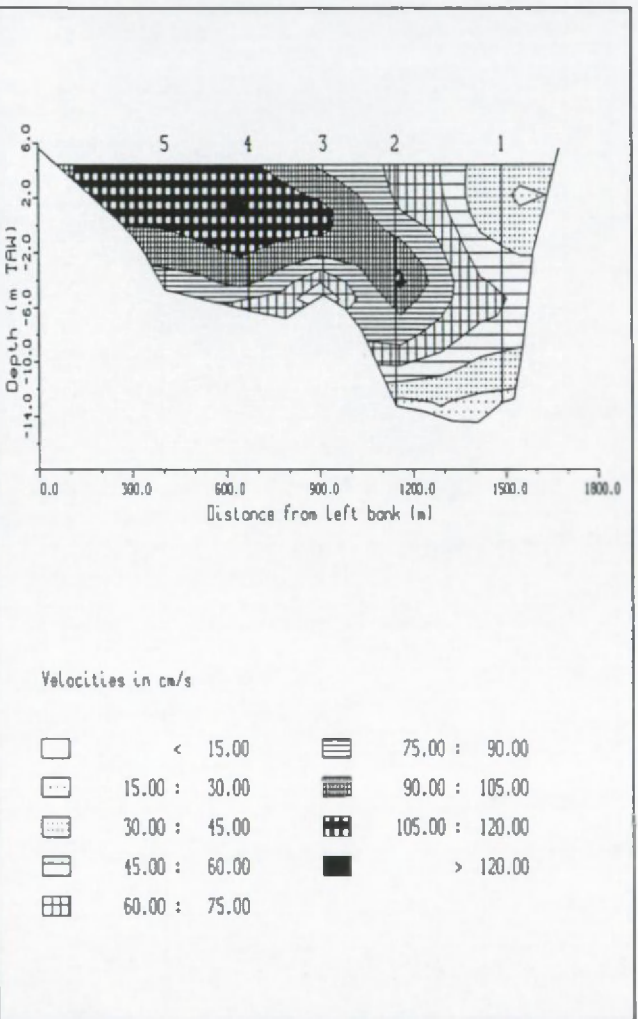


Figure 5.7: Spring tide (04/10/90), maximum velocity during flood over the cross section at the 'Drempe! van Zandvliet'.

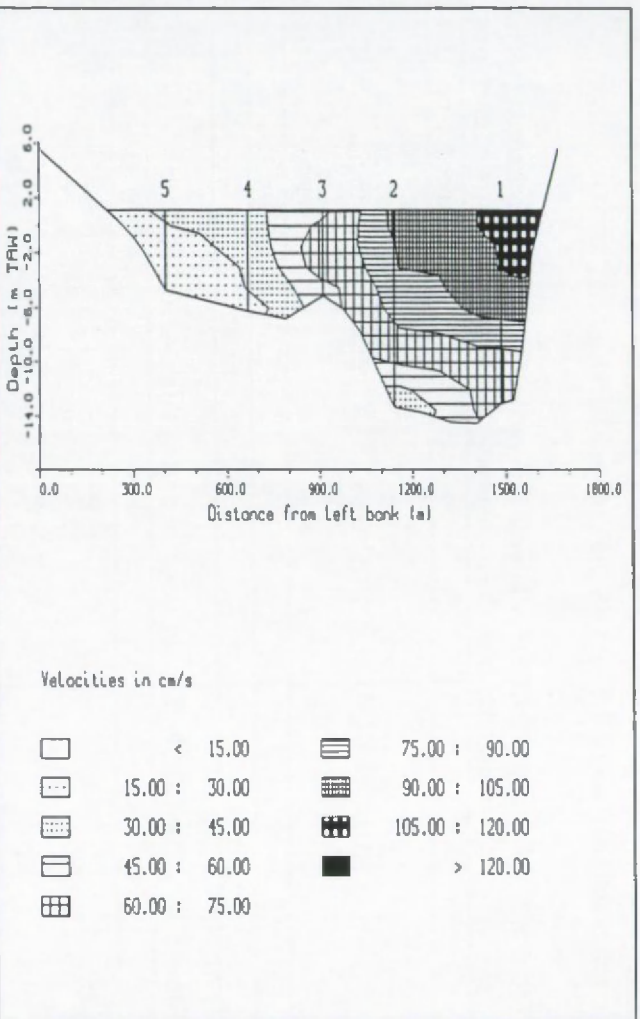


Figure 5.8: Spring tide (04/10/90), maximum velocity during ebb over the cross section at the 'Drempe! van Zandvliet'.

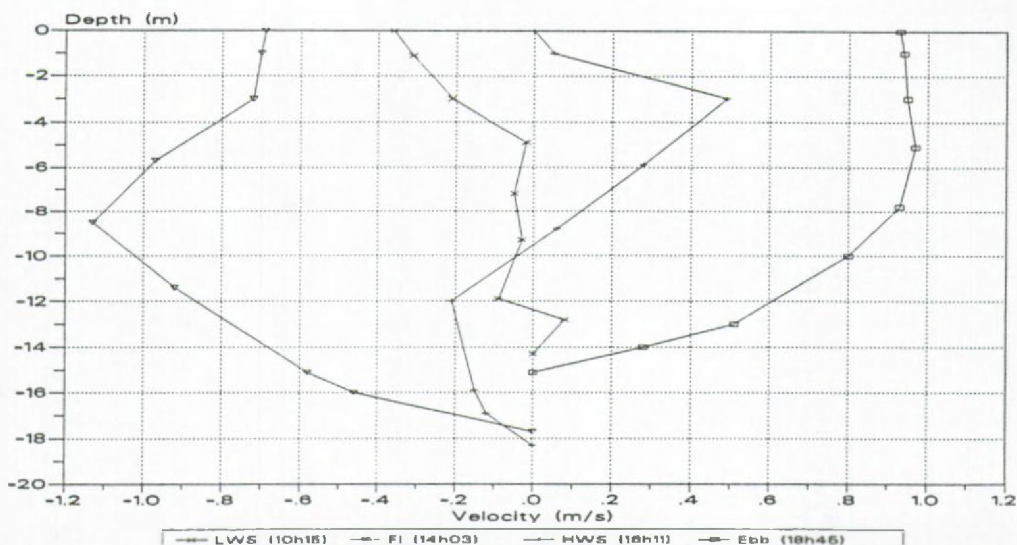


Figure 5.9: Spring tide (04/10/90), velocity profile at point 2, 'Drempel van Zandvliet' (HWS = high water slack, LWS = low water slack).

and almost equal numbers, the accuracy is therefore very small. Converting the residual discharge to  $\text{m}^3/\text{s}$  we obtain for neap tide a value of  $52\text{m}^3/\text{s}$  and for spring tide a value of  $121\text{m}^3/\text{s}$ . The monthly averaged fresh water discharge for September and October was  $45.5$  and  $58.3\text{m}^3/\text{s}$  respectively (A.Z., 1991).

Table 5.3 Neap tide 27/09/90, lateral and vertical averaged discharges ( $10^8\text{m}^3$  per ebb/flood) with the measurement point in the centre of each part.

Point	ebb	flood
1	29.36	-14.68
2	25.86	-23.25
3	10.56	-13.33
4	7.02	-14.45
5	4.94	-9.71
total	77.75	-75.41
ebb-flood	+ 2.34	

Table 5.4 idem Table 5.3 but now for spring tide 04/10/90.

Point	ebb	flood
1	38.60	-13.10
2	33.42	-27.53
3	13.63	-17.17
4	9.71	-22.00
5	7.45	-17.55
total	102.81	-97.35
ebb-flood	+ 5.46	



### 5.3.2. *Salinity*

The Scheldt estuary is considered as being well mixed with a mean vertical salinity difference of 1g/l. The measurements indicate that a higher vertical stratification exist at the place of the cross section. Wollast (1973) mentioned already that in the 'Beneden Zeeschelde' a pronounced vertical and lateral salinity gradient occurs. According to this author the maximum vertical stratification is situated at Doel (km 62), some 4km upstream of the measurement cross section. The Scheldt estuary in this area is thus well-mixed to partially stratified. The salinity in the river is variable, the main factors are the tides, the spring-neap cycle and the fresh water discharge of the river. High fresh water discharges occur during winter (Nov - Apr) low ones are in general during summer (May - Oct). The highest salinity values are perceptible in autumn (Sep - Oct). The lowest ones occur during winter (Dec - Feb). The measurements discussed here are typical for high salinity values. The horizontal salinity gradient between Prosperpolder and Oosterweel during 1990 has a maximum of 0.50g/l per km in November and decreases at the end of the winter (March) to 0.25g/l per km (values based on A.Z., 1993b). According to Peters (1975) values up to 0.75g/l per km can occur in the vicinity of the Belgian-Dutch border. The variation of salinity during a tidal cycle and the mean vertical difference in salinity has a maximum between Bath and Antwerp. We can describe this area as a 'salinity gradient maximum'. It is in this area that a clear stratification occurs resulting in a two-layered flow at the moment of high water slack. This moment corresponds with the maximum in the vertical salinity stratification. The vertical averaged salinity as a function of time is shown in Figures 5.10-11. From the figures can be seen that the maximum and minimum in salinity is not occurring at the same moment over the cross section and that the extrema are maintained during a certain period (0 - 2 hours). Furthermore differences in duration and in time related to high or low water of these extreme values are found between neap and spring tide. Nevertheless we can say that in the main channel the period of maximum salinity occurs in general later than in the points situated on the 'Plaat van Doel' and the 'Schaar van Ouden Doel'. The salinity is minimal at about 1-2 hours after low water. Here too a difference can be observed between the 'Plaat van Doel' and the 'Schaar van Ouden Doel' and the main channel. The salinity in the vicinity of the 'Plaat van Doel' is at about low water on the average higher than in the main channel. The submerged dyke together with the ebb and flood channels protects the water of being easily mixed with the less saltier water from upstream. During high water the salinity does not show big variations over the cross section.



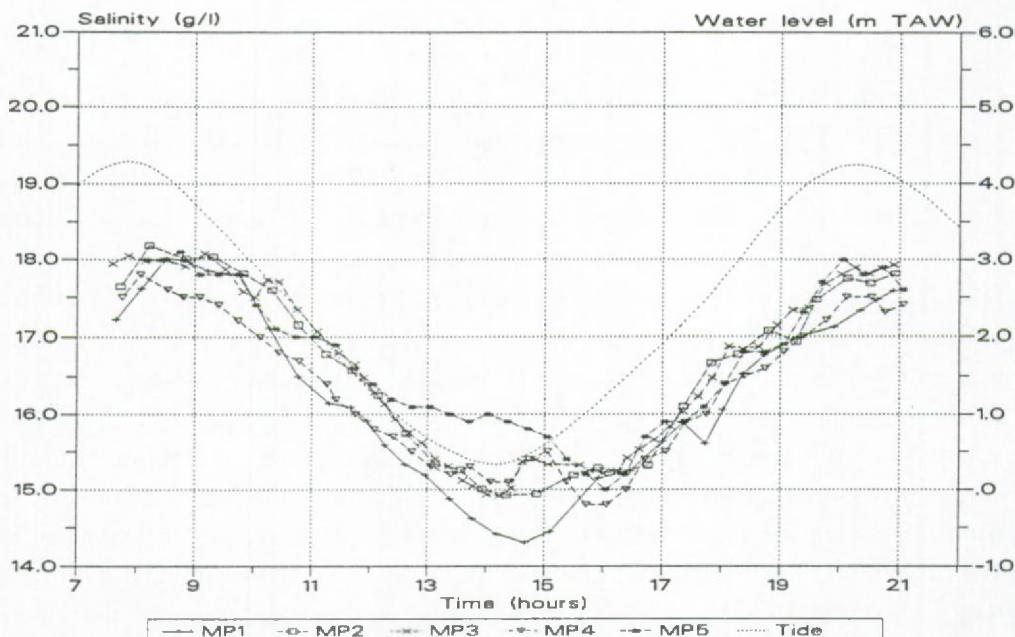


Figure 5.10: Neap tide (27/09/90), vertical averaged salinity at the 'Drempel van Zandvliet'.

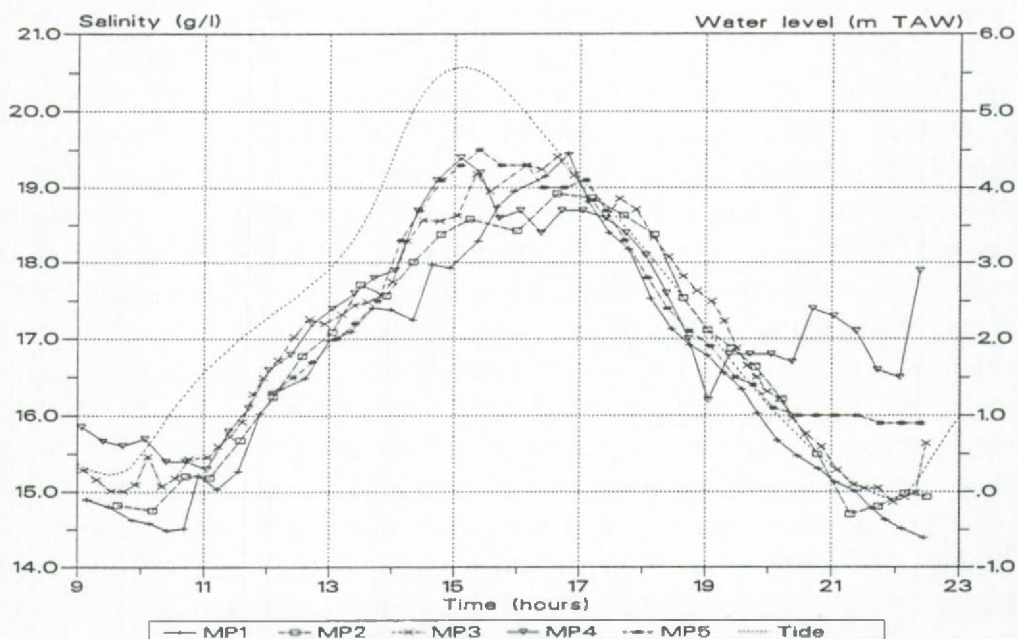


Figure 5.11: Spring tide (04/10/90), vertical averaged salinity at the 'Drempel van Zandvliet'.

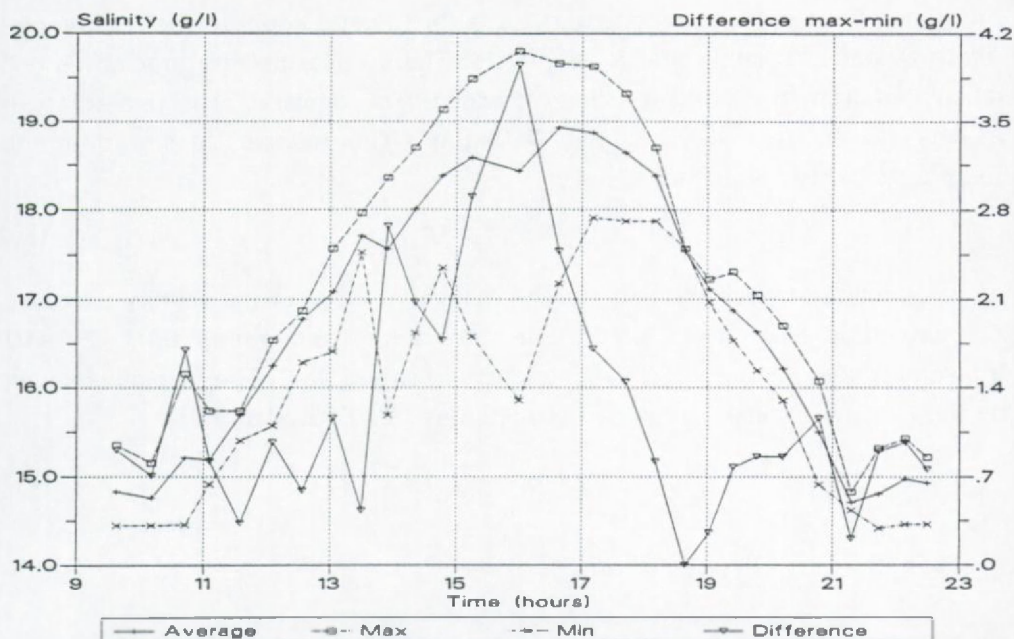


Figure 5.12: Spring tide (04/10/90), salinity in point 2 at 'Drempel van Zandvliet.

The vertical averaged difference between maximum and minimum salinity is about 3.0g/l for neap and 4.5g/l for spring tide, see Table 5.5. The time gradient during ebb and flood is (taking a duration of 6 hours for ebb and flood)  $1.6 \times 10^{-4}$  g/l/s during neap tide and  $2.1 \times 10^{-4}$  g/l/s during spring tide. The horizontal salinity gradient may be calculated indirectly by relating time scales to length scales:

$$\frac{dS}{dx} = \left( \frac{dS}{dt} \right) \frac{1}{V} \tag{5.1}$$

where  $S$  is salinity,  $t$  time,  $x$  horizontal distance and  $V$  velocity. The vertical, lateral and time averaged velocity during neap and spring tide is respectively 0.4m/s and 0.5m/s. The horizontal salinity gradient is then 0.42g/lkm during spring and 0.35g/lkm during neap tide.

The mean, maximum (bottom) and minimum (surface) salinity in point 2 as presented in Figure 5.12 gives a view of the vertical stratification. From the figure appears that the highest stratification occurs at around high water slack and that the stratification is low during the rest of the tide. The difference in salinity between bottom and surface is depending on the location (maximum in point 3). This difference reaches a maximum of 2.8g/l during neap and 4g/l during spring tide, see Table 5.6. The averaged difference is  $\pm 1$ g/l for neap as well as spring tide. The biggest

difference between bottom and surface is thus nearly equal to the difference in depth averaged salinity over a tidal cycle. The vertical density gradient can be calculated from the vertical salinity gradient. The density ( $\rho$ ) is related to the salinity ( $S$ ) by  $\rho = 0.75 S + 1000\text{kg/m}^3$ . The relative density difference ( $\rho_{rel} = \Delta\rho/\rho$ ) is then equal to:

$$\rho_{rel} = 0.75 \Delta S/\rho \tag{5.2}$$

$\rho_{rel}$  is calculated from the mean and the maximum value of the salinity difference  $\Delta S$ , which is equal to  $7.5\times10^{-4}$  (mean of neap- and spring tide),  $2.1\times10^{-3}$  (maximum neap tide) and  $3.0\times10^{-3}$  (maximum spring tide). The velocities caused by this density difference can be calculated as (I.M.D.C., 1988b):

$$V_d = 0.4 \sqrt{\rho_{rel} g h} \tag{5.3}$$

Table 5.5 Extreme salinity values (g/l) at 'Drempel van Zandvliet'.

Point	vertical averaged			top			bottom		
	min	max	diff	min	max		min	max	
Neap Tide 27/09/90									
1	14.3	18.0	3.7	14.3	16.8	2.5	14.4	18.4	4.0
2	14.9	18.2	3.3	14.4	17.4	3.0	15.1	18.6	3.5
3	14.9	18.0	3.1	14.6	17.4	2.8	15.0	18.7	3.7
4	14.8	17.8	3.0	14.4	17.2	2.8	15.1	18.0	2.9
5	15.0	18.1	3.1	14.9	17.7	2.8	15.2	18.4	3.2
Spring Tide 04/10/90									
1	14.4	19.5	5.1	14.3	17.9	3.6	14.5	19.9	5.4
2	14.8	18.9	5.1	14.5	17.9	3.4	15.2	19.8	4.6
3	14.9	19.4	4.5	14.6	18.5	4.1	15.0	20.2	5.2
4	15.3	19.4	4.1	14.7	19.4	4.7	16.0	19.7	3.7
5	-	19.5	-	-	19.3	-	-	19.6	-

Table 5.6 Vertical salinity stratification (g/l) at the 'Drempel van Zandvliet'.

Point	1	2	3	4	5
Neap Tide 27/09/90					
averaged	1.0	1.0	1.2	0.7	0.6
maximum	2.3	2.0	2.8	1.8	1.2
minimum	0.1	0.0	0.3	0.0	0.0
Spring Tide 04/10/90					
averaged	1.0	1.2	1.1	0.8	-
maximum	3.2	3.9	4.0	3.2	1.5
minimum	0.0	0.0	0.0	0.0	-



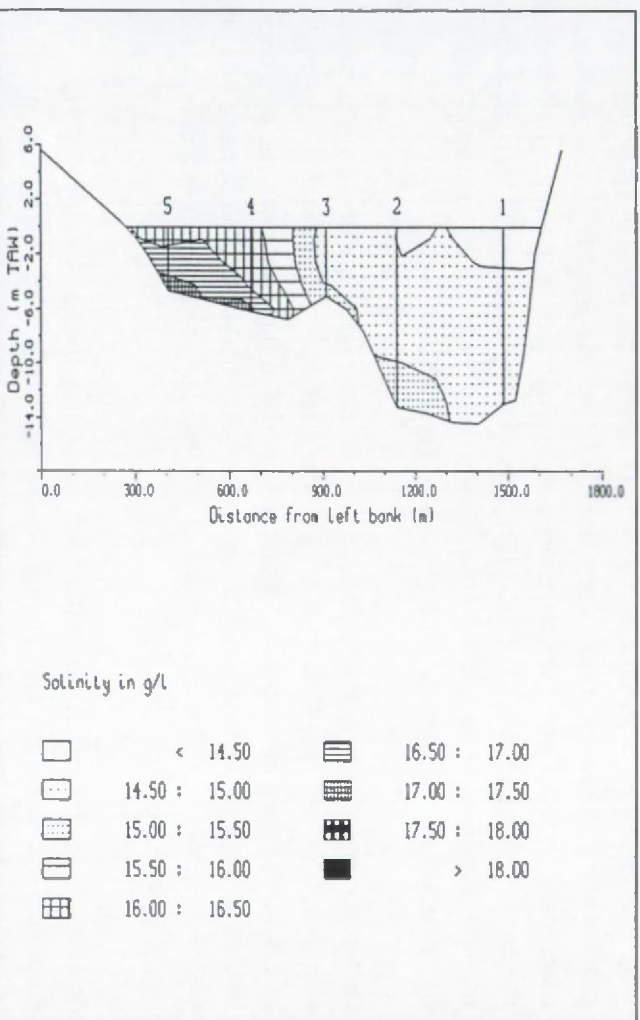


Figure 5.13: Spring tide (4/10/90), salinity distribution at about low water over the cross section at the 'Drempel van Zandvliet'.

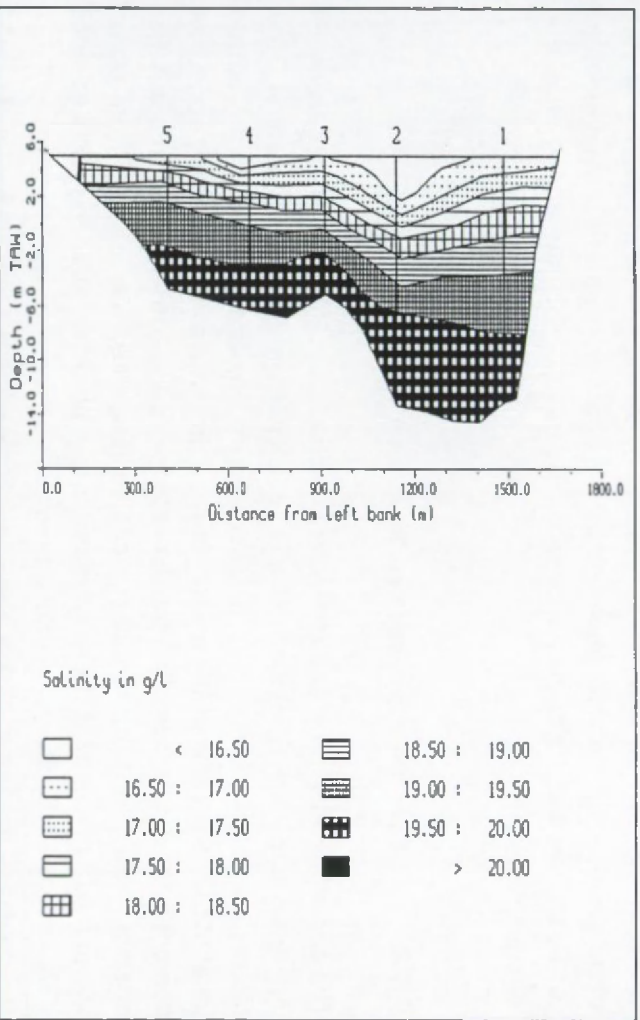


Figure 5.14: Spring tide (4/10/90), salinity distribution at about high water over the cross section at the 'Drempel van Zandvliet'.



where  $V_d$  is the velocity due to the density difference,  $g$  the acceleration due to gravity and  $h$  the water depth. For a depth of 15m the velocity  $V_d$  has an average magnitude of  $\pm 0.13\text{m/s}$ , which is directed downstream in the upper half and upstream in the lower half of the profile. This velocity component reaches a maximum of  $0.2\text{m/s}$  at neap and  $0.3\text{m/s}$  at spring tide. These values explain mostly the deformation of the velocity profiles seen in Figure 5.9.

Due to differences in velocity and depth over the cross section a lateral salinity gradient is formed, see Figures 5.13-14. The lateral salinity differences are higher at spring tide than at neap tide. The maximum differences between the two banks occurs during minimum salinity ( $\pm$  low water) and is about  $1.5\text{g/l}$  at neap tide and  $2.5\text{g/l}$  at spring tide. The occurrence of a lateral salinity gradient is a consequence of the local bathymetry.

The salinity differences found between neap and spring tide are mainly due to variations in tidal amplitude. The depth averaged maximum and minimum salinity is  $18.0\text{g/l}$  and  $14.8\text{g/l}$  during neap and  $19.3\text{g/l}$  and  $14.9\text{g/l}$  during spring tide. The maximum salinity is thus  $1.3\text{g/l}$  higher at spring than at neap tide whereas the minimum salinity is roughly the same. A river flow of  $50\text{m}^3/\text{s}$  represents about 2 to 3% of the tidal volume during respectively spring and neap tide. The vertical stratification is thus mainly governed by the tidal volume (or tidal amplitude) and not by the relative higher importance of the fresh water flow during neap than during spring tide.

### 5.3.3. *Cohesive suspended sediments*

The concentration varies in a characteristic way with tides, notably resuspension during periods with high velocities and sedimentation during slack waters. Other factors play also an important role, such as the presence of mud on the bottom (related to the position of the measurement point), the composition and consolidation age of the mud, the difference in velocity during ebb and flood, the duration of slack water, and the turbulence and salinity. The input of mud from up- or downstream makes that the concentration can be different during ebb and flood independent of the above mentioned factors.

The course of mud concentration as a function of time is shown in Figures 5.15-16 (vertical averaged values) and 5.17-18 (values at bottom, notice the different scales). The mud concentration is clearly stratified over the vertical. The highest

concentrations are observed at the bottom. The big difference between the bottom and the surface mud concentration is a reflection of the erosion- sedimentation cycle. Resuspension of mud during high current velocities results in an increase of the concentration in the bottom layer. Due to diffusion the mud is then distributed over the vertical. Local effects can lead to a sudden increase in concentration in a certain measurement point without being visible in the other points. These local increases are difficult to explain (no direct observations of the bottom layer are available) but could be related to phenomena such as mass erosion. A maximum in mud concentration at spring tide during flood occurs shortly after low water slack and corresponds not with the maximum in flood velocity, which occurs at about 1 hour before high water. At maximum flood velocity the concentration shows a peak value but this value is smaller than the first concentration maximum. This behaviour during a spring tide flood can be explained by the fact that first the soft mud layers, which have been deposited during the previous slack water are eroded (it cannot be answered from these measurements however how the erosion takes place). The mud which is then in contact with the water has a higher critical erosion stress and resuspension will decrease. This behaviour of concentration has also been identified by Helsloot et al. (1988) at 'Middelgat', but has not, following these authors been reported from other estuaries. The concentration of mud during ebb has a similar behaviour.

The ratio between the near bottom ( $C_{\text{bottom}}$ ) and vertical averaged concentration ( $C_{\text{mean}}$ ) is given in table 5.7. This ratio gives an indication of the influence of sedimentation and erosion and reflects the asymmetry of the velocities during a tidal cycle. The table shows that the near bottom concentration is on the average 1.5 (ebb) to 1.7 (flood) and 1.6 (ebb) to 2.2 (flood) times higher than the averaged concentration during neap and spring tide respectively. The long term measurements at Liefkenshoek (I.M.D.C., 1989) resulted in a ratio between the averaged and the maximum mud concentration of 1.65 during flood and 2.30 during ebb. The linear correlation coefficient between the bottom and the averaged concentration has been calculated. According to Nichols (1984) a high correlation coefficient suggests that the concentration in the water column is mainly controlled by processes which act in the vicinity of the bottom (sedimentation and erosion) and to a lesser extend by advection. A low correlation means that transport of mud plays a dominant role in setting up the vertical concentration distribution. The correlation coefficients for the measurement points are all situated between 0.36 and 0.57, with slightly higher values during spring than during neap tide. This suggests that erosion and sedimentation is of minor importance and that transport of mud plays an significant role in establishing the observed suspended mud profiles.

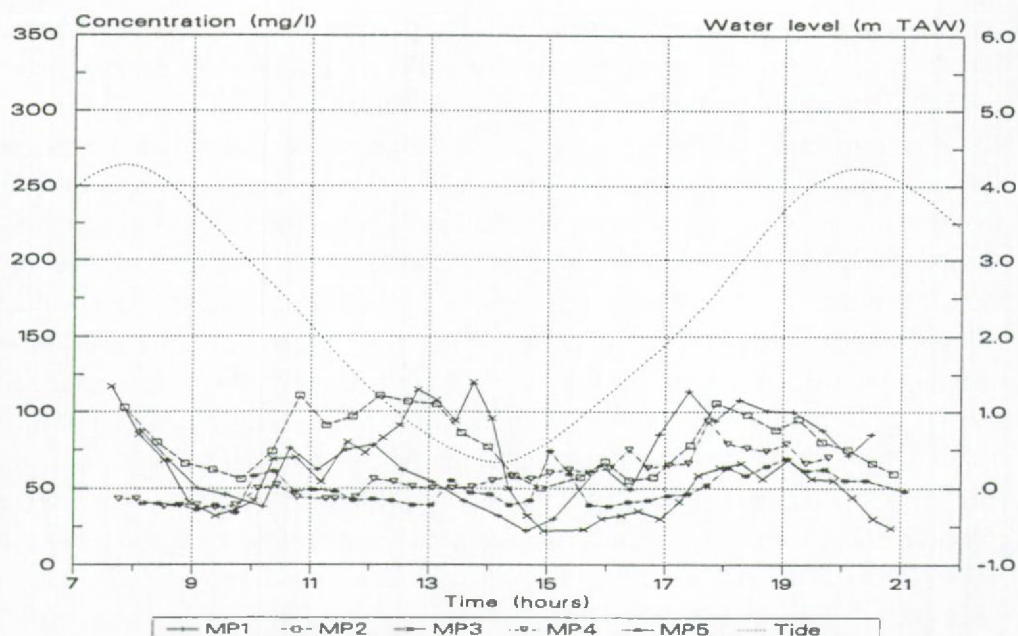


Figure 5.15: Neap tide (27/09/90), vertical averaged mud concentration at the 'Drempel van Zandvliet'.

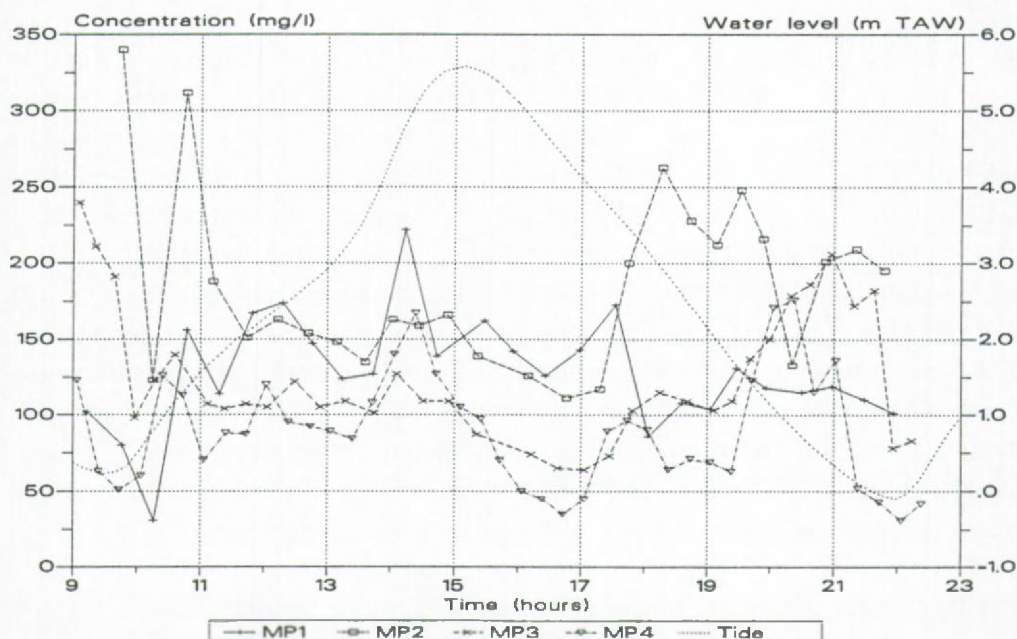


Figure 5.16: Spring tide (04/10/90), vertical averaged mud concentration at the 'Drempel van Zandvliet'.



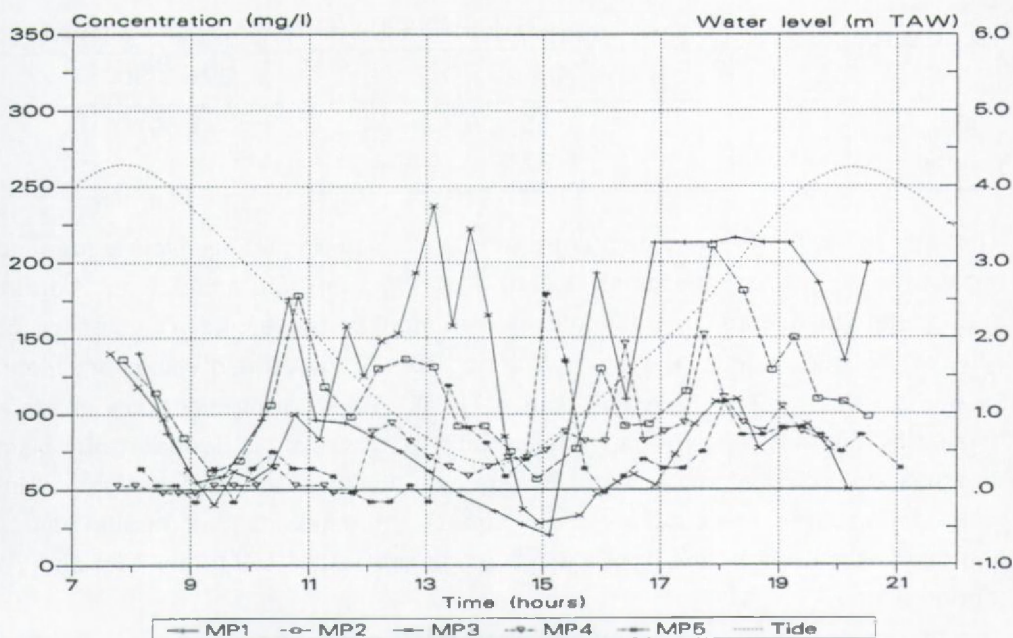


Figure 5.17: Neap tide (27/09/90), mud concentration at bottom, 'Drempel van Zandvliet'.

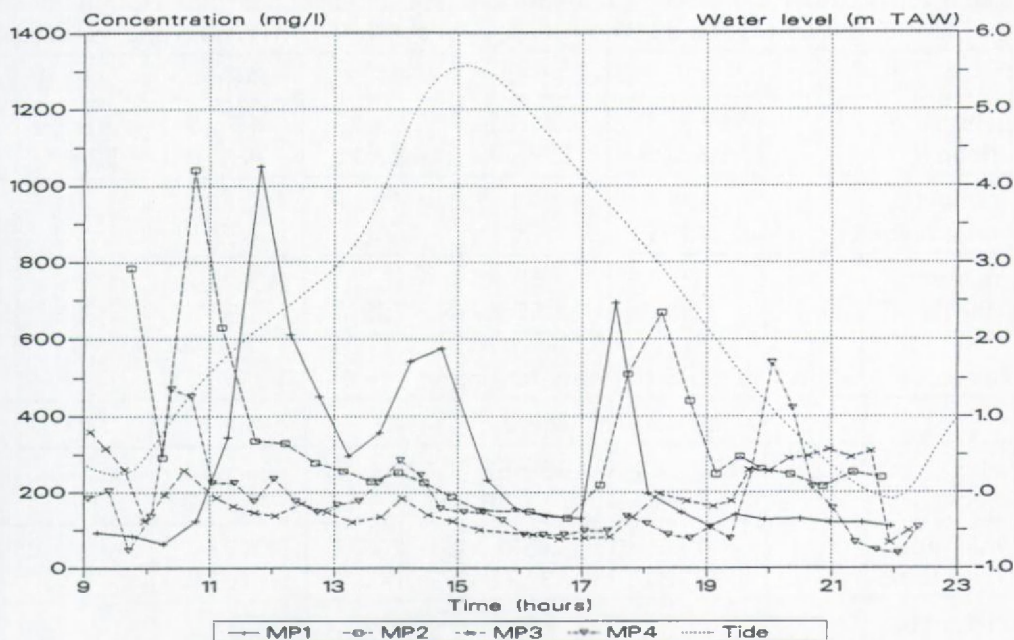


Figure 5.18: Spring tide (04/10/90), mud concentration at bottom, 'Drempel van Zandvliet'.



Table 5.7 Mean ratio  $C_{\text{bottom}}/C_{\text{mean}}$  during ebb and flood.

	27/09/90	04/10/90
ebb	1.45	1.59
flood	1.67	2.19

The ratio of depth averaged concentration  $C_{\text{max}}/C_{\text{min}}$  during a tidal cycle is (depending on the position of the point) 1.5 to 4 during neap tide and 1.6 to 7 during spring tide. The average over the five measurement points results in a value for this ratio of 2.5 during neap tide and 3.5 during spring tide. These values are higher than the value of 2 of Van Eck et al. (1991). These differences are probably caused by the fact that we have looked only at a very short period at one place whereas Van Eck et al. used averaged data over a wide range of places and during longer time scales. The depth averaged concentration has its maximum in point 2 and decreases towards the right and left bank, see Tables 5.8 (neap tide) and 5.9 (spring tide).

The tables indicate that the vertical averaged concentration is about a factor 2 smaller during neap tide than during spring tide.

Table 5.8 Neap tide 27/09/90. Depth averaged mud concentration (mg/l): mean value ( $\pm$  standard deviation) over ebb/flood, maximum and minimum.

	MP 1	MP 2	MP 3	MP 4	MP 5
ebb	$57 \pm 19$	$82 \pm 22$	$73 \pm 27$	$46 \pm 6$	$45 \pm 8$
flood	$83 \pm 25$	$78 \pm 17$	$43 \pm 16$	$68 \pm 6$	$52 \pm 11$
max ebb	78	111	120	56	61
max flood	114	106	66	94	74
min ebb	22	50	32	37	34
min flood	30	55	22	51	38

Table 5.9 idem Table 5.8 but now for spring tide 04/10/90.

	MP 1	MP 2	MP 3	MP 4	MP 5
ebb	$124 \pm 24$	$189 \pm 51$	$120 \pm 46$	$84 \pm 44$	-
flood	$140 \pm 49$	$171 \pm 49$	$111 \pm 13$	$97 \pm 30$	-
max ebb	173	263	206	176	-
max flood	222	312	140	167	-
min ebb	86	111	64	31	-
min flood	31	135	87	50	-

### 5.3.4. *Effective fall velocity*

The effective fall velocity  $w_{s,eff}$  is calculated according to van Leussen (1994) as:

$$w_{s,eff} = -\frac{(\partial C/\partial t) h}{C} \quad (5.4)$$

with  $C$  the depth averaged concentration,  $h$  the waterdepth and  $t$  time. The effective fall velocity is, according to the author not a property of the sediment because vertical upward fluxes of sediments by turbulent mixing is incorporated in the calculation, so that the real settling velocities will be much higher. The value of the fall velocity will, however, give an indication of the magnitude of the fall velocity, which will be used in the mud transport model (see § 6.4.1.2.). The depth averaged effective fall velocity has been calculated according to eq. (5.4). The value of the fall velocity is strongly varying in magnitude as well as in sign. Positive fall velocities are an indication for deposition, negative ones for erosion. The fact that a significant part of the suspended mud is not due to local erosion and/or deposition but from transport (see § 5.3.6.) and because of the incorporated effects of turbulent mixing in the calculations can give an explanation of the observed chaotic course of the fall velocity as a function of time. Generally the positive fall velocities occur during periods with decreasing velocity. The effective fall velocities in the five points for neap and spring tide are presented in Table 5.10. The effective fall velocity is situated between 0 and 5mm/s.

Table 5.10 Effective fall velocities (mm/s) during decreasing velocity.

		MP 1	MP 2	MP 3	MP 4	MP 5
Neap tide	ebb	1.1 - 3.0	0.1 - 2.3	0.3 - 3.4	0.1 - 0.4	0.1 - 0.7
	flood	0.1 - 2.5	0.6 - 2.0	1.0 - 2.7	0.2 - 1.4	0.0 - 0.8
Spring tide	ebb	0.2 - 2.9	0.5 - 2.1	0.7 - 3.7	0.2 - 4.6	-
	flood	2.3 - 4.5	0.3 - 2.0	0.0 - 1.5	0.8 - 3.1	-

### 5.3.5. *Erosion and sedimentation*

A characteristic property of suspended mud under tidal action is that a phase shift occurs between the velocity and the concentration peaks. This results in a typical hysteresis curve of the concentration and the transport with respect to the velocity. Nichols (1984) distinguish several time shifts which are responsible for the asymmetrical transport:

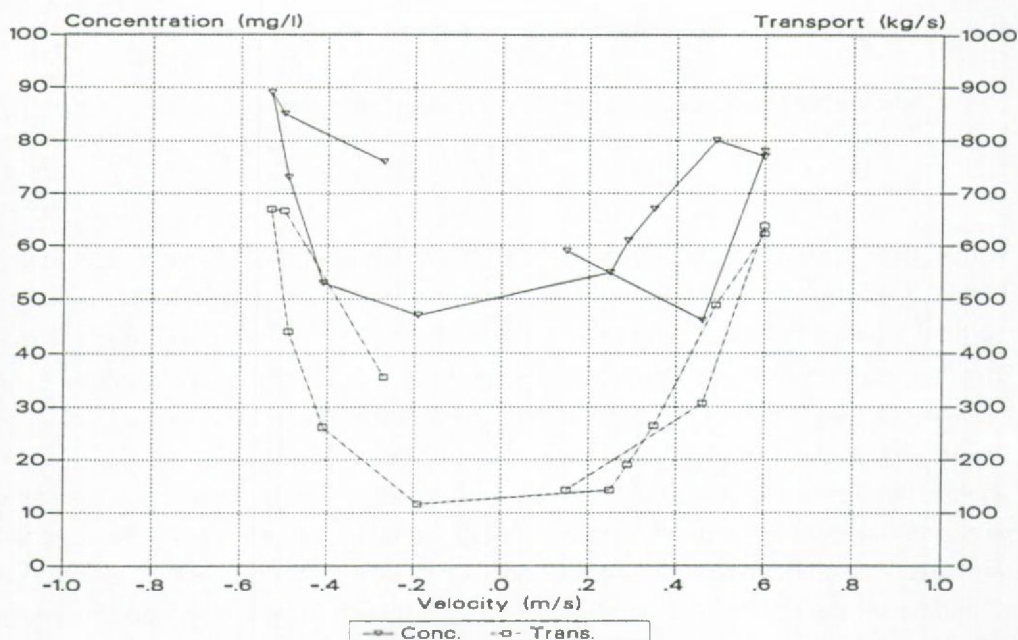


Figure 5.19: Neap tide (27/09/90), erosion/sedimentation cycle of mud at the 'Drempel van Zandvliet'.

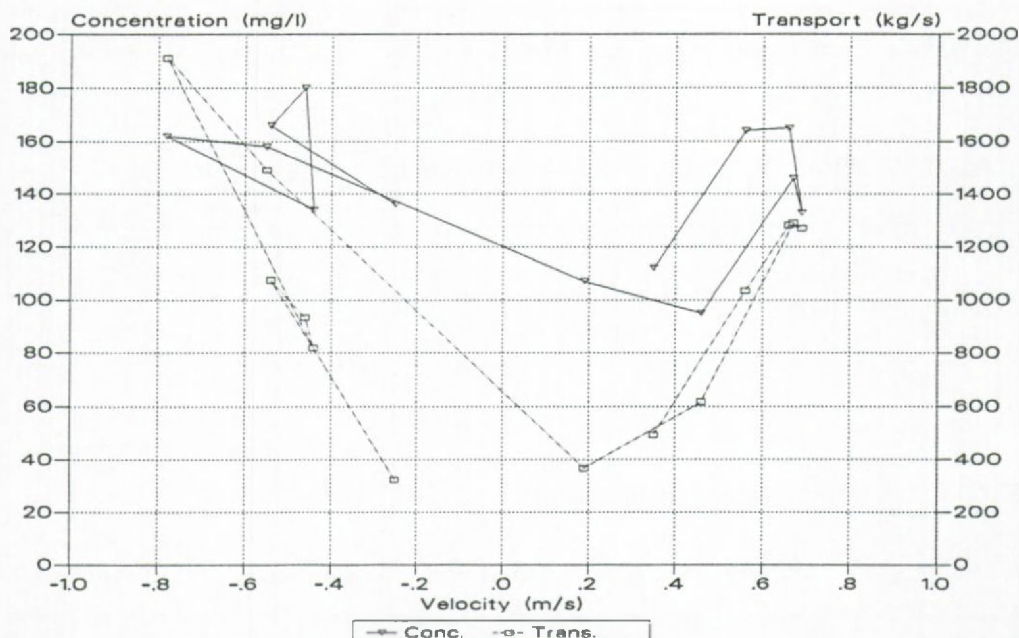


Figure 5.20: Spring tide (04/10/90), erosion and sedimentation cycle of mud at the 'Drempel van Zandvliet'.



The mud particles or flocs are still transported over a certain distance before being attached to the bottom after the bed shear stress has dropped below the critical value for sedimentation. This time shift is inversely proportional to the fall velocity. The critical shear stress necessary to bring mud particles or flocs in suspension is higher than the critical velocity for sedimentation.

The mud particles or flocs which have been brought into suspension need a certain time before they are distributed over the vertical. Vertical stratification reduces this dispersion. The vertical and lateral averaged mud concentration and transport as a function of velocity is shown in Figures 5.19-20 (upstream is negative, downstream is positive, the quantities are vertical and lateral averaged). The maximum concentrations and transports during flood are higher than the concentrations and transports during ebb (especially during spring tide). This is a consequence of the higher flood velocities and indicates the flood dominant character of the concentration. Notice that these figures do not take into account the time difference between ebb and flood, the higher flood transports are thus not necessarily indicating higher transports over whole the flood. The figures show that the concentration and also the transport are lower in magnitude during increasing than during decreasing velocities. These differences in transport between ebb and flood are responsible for the residual transport of mud during a tidal cycle. During flood as well as during ebb the figures indicate a strong decrease in concentration after the velocity has reached its maximum value. The decrease in concentration during decreasing velocities could be related to the formation of larger mud flocs.

### **5.3.6. *Velocity, sediment and transport profiles***

The erosion and sedimentation pattern of mud has a complex three dimensional behaviour. This is presented in Figure 5.21 where velocity-, concentration- and transport profiles are shown for spring tide in measurement point 2 (situated at the border of the main channel). The figure starts with low water slack. At the beginning of the flood (at about 11h00) a sudden increase of the concentration and the transport at the bottom can be observed. The concentration and transport profiles are later more homogeneously distributed over the vertical, a vertical gradient however remains. It can be clearly seen that the mud particles are more and more distributed over the water column during flood. The concentration and also the transport are more homogeneously distributed over the profile during ebb than during flood. A small increase in concentration at the bottom can be seen at about 3 hours after high water (18h01). The surface concentration is very small



during flood, whereas during ebb a significant concentration at the surface can be observed. This can be explained by the fact that the vertical salinity gradient is higher during flood than during ebb, resulting in an inhibition of the vertical mixing.

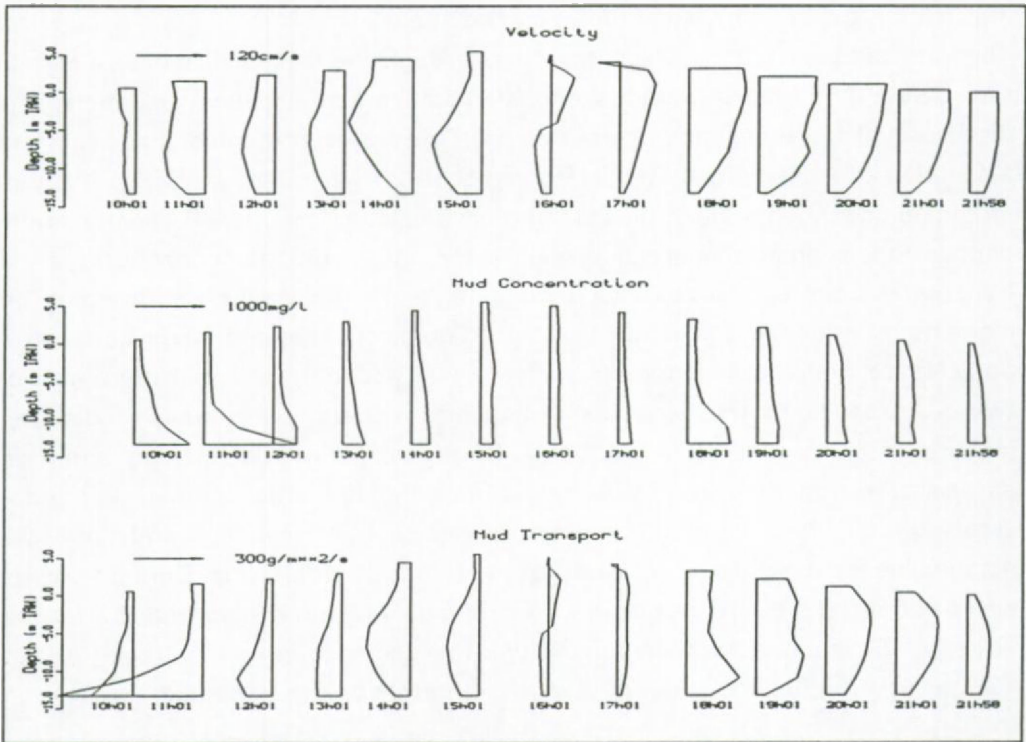


Figure 5.21: Spring tide (04/10/90), vertical profiles of velocity, mud concentration and mud transport in point 2 at the 'Drempel van Zandvliet'.

### 5.3.7. Transport of suspended sediments

The total transport of mud during ebb and flood has been calculated, see Table 5.11. The transport of mud during flood and ebb is important and is the result of an alternation of erosion and sedimentation during a tidal cycle. The residual mud transport over one tidal cycle is very small compared to the ebb and flood transports. The values indicate that a net transport of mud exists in downstream direction. The net transport is 1.1kg/s (neap tide) and 5.4kg/s (spring tide). Separating the transport into ebb and flood results in a three times higher transport during spring than during neap tide. It is not possible to formulate a general balance of the mud transport based on these measurements in the Scheldt river. In order to do so a more extended (in space and time) measurement campaign should be undertaken.

Table 5.11 Total mud transport during neap and spring tide at the 'Drempel van Zandvliet'.

	neap tide (ton)	spring tide (ton)
ebb	5255	13661
flood	-5206	-13418
tide	49	243

### 5.3.8. Conclusions

An overview of the observations at the 'Drempel van Zandvliet' is presented in Figures 5.22-24 showing the isolines of velocity, salinity and mud concentration as a function of time during spring tide.

Figure 5.22 shows the different velocity distributions during flood and ebb. The ebb current follows the main channel (points 1 and 2), whereas the maximum flood velocity is in the 'Schaar van Ouden Doel' (points 4 and 5). The figure also shows the distorted velocity profile during ebb and flood as well as the differences in duration of the slack waters. The asymmetry of the tidal currents can be seen through the not equally spaced isolines at about high water slack and low water slack.

The extreme values of salinity are about one hour later than the extreme water levels. The differences between minimum and maximum salinity is about 3g/l during neap and about 4.5g/l during spring tide. During a major part of the tidal cycle a vertical stratification of salinity is present (Figure 5.23). The vertical gradient has its maximum at about high water and is minimal at about low water. The maximum difference in salinity between bottom and surface occurs at the moment of salinity maximum (2.8g/l at neap and 4g/l at spring tide). The horizontal salinity gradient is about 0.35g/l per km during neap and 0.42g/l per km during spring tide. This gradient is responsible for the distortion of the velocity profile. The lateral salinity differences have their maximum at salinity minimum (1.5g/l during neap and 2.5g/l during spring tide). The minimal salinity values are nearly the same for spring and neap tide, whereas the maximum salinity is about 1.5g/l higher during spring tide than during neap tide.

Figure 5.24 shows that the mud concentration is varying as a function of time, over the vertical and over the cross section. The figure gives an indication of the erosion and sedimentation cycle of mud. The variations can partly be correlated to the current velocities. The highest mud concentration are found at the bottom at about one hour after high or low water slack. The current velocities are then high

enough to erode the mud which has been deposited at the previous slack water. The mud under these soft mud layers has a higher critical shear stress for erosion. This results in a decreasing concentration with increasing velocity. A clear decrease of concentration is visible at about high water slack (sedimentation of mud). The concentration is then nearly equally distributed over the water profile. The concentration is on the average the highest in the main channel (point 2). The ratio between averaged and bottom concentration is about 1.5 during neap and 2 during spring tide. The vertical averaged mud concentration is twice as high during spring than during neap tide. Between the peaks in velocity and in concentration and transport a phase shift occurs which results in a hysteresis curve of the concentration and transport as a function of velocity. The concentration as well as the transport is lower at increasing than at decreasing velocity. The net transport during neap tide is about 1.1kg/s and during spring tide 5.4kg/s. The total transport during flood or ebb is about 2.5 higher at spring tide than at neap tide.

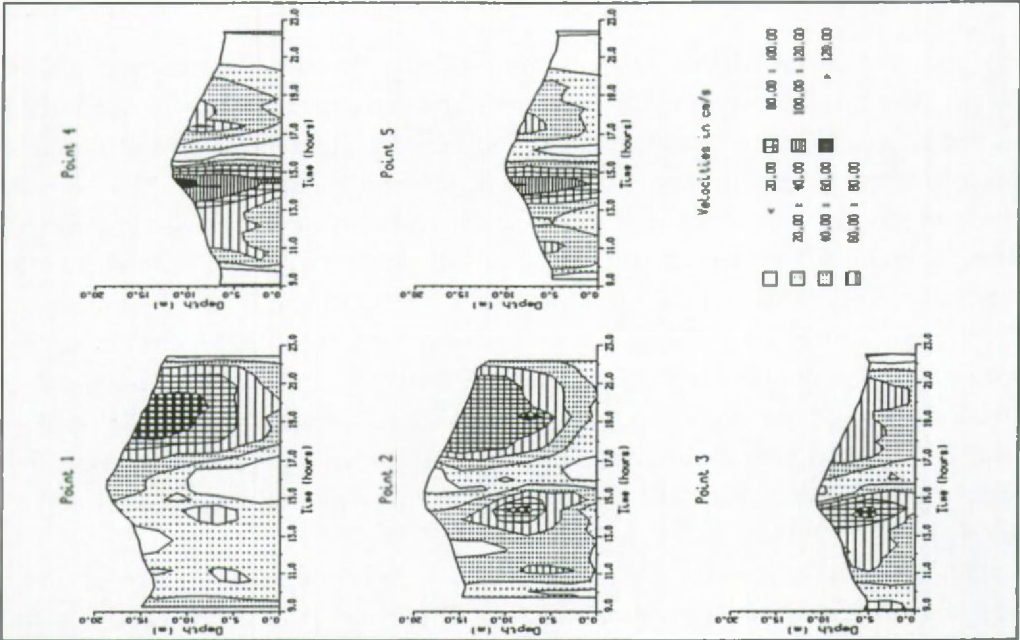


Figure 5.22: Spring tide (04/10/90), contourlines of velocity as a function of time and waterdepth, 'Drempe van Zandvliet'.



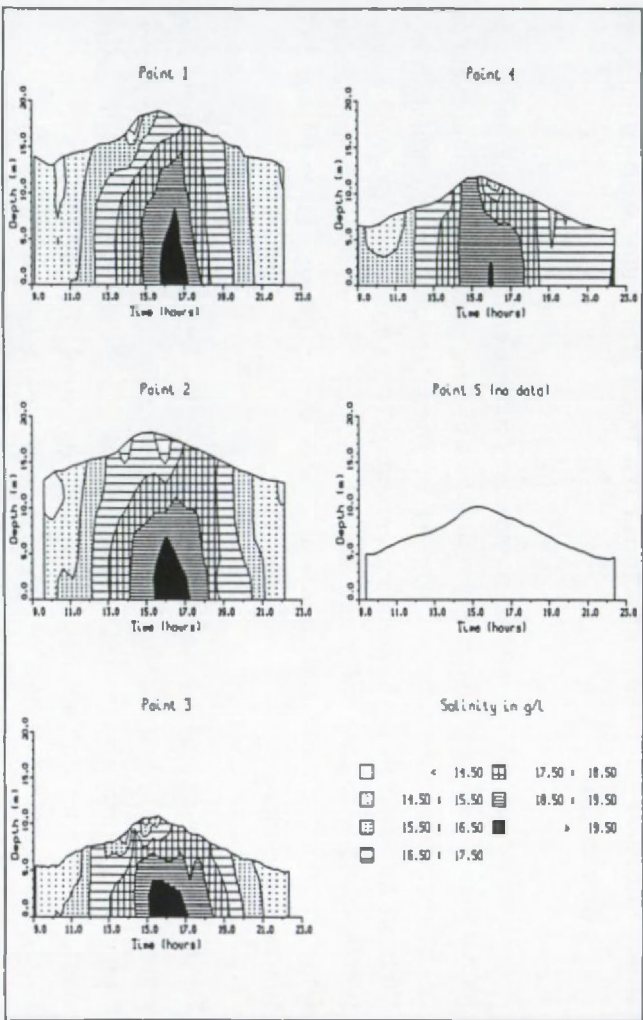


Figure 5.23: Spring tide (04/10/90), contourlines of salinity as a function of time and waterdepth, 'Drempeel van Zandvliet'.

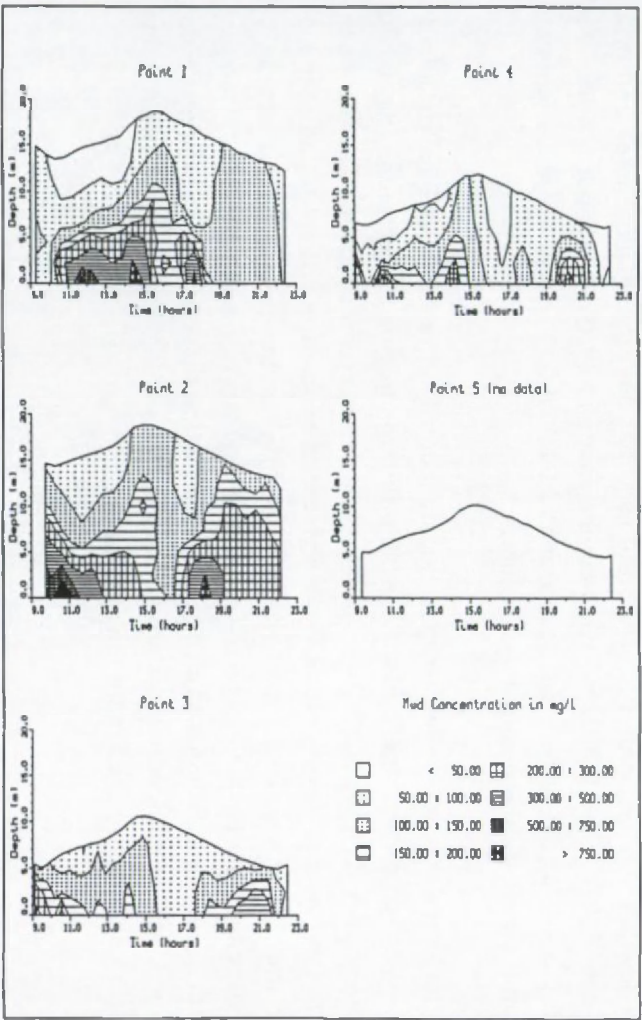


Figure 5.24: Spring tide (04/10/90), contourlines of mud concentration as a function of time and waterdepth, 'Drempeel van Zandvliet'.



#### 5.4. Through Tide Measurements At 'Plaat Van Lillo' And 'Vaarwater Boven Bath'

A detailed description of various parameter (current velocity, discharge, salinity, mud concentration and transport) in function of time over a whole tidal cycle has been presented in the previous paragraph. The intention of this paragraph is to illustrate qualitatively the longitudinal variation of mud concentration. We underline that the comparison can only be qualitative, because the measurement are covering a too short time interval and have been carried out at different dates (influence of seasonal variations).

The measurement cross sections are situated at the 'Plaat van Lillo' and at 'Vaarwater boven Bath' and are situated respectively 5km upstream and 3.5km downstream of the cross section 'Drempel van Zandvliet' (see § 5.3). The measurements are through tide and have been carried out on 13/06/91 (I.M.D.C.-W.L.B., 1993) and 11/07/91 (R.W.S, 1991). A map with the location of the cross sections is given in Figure 5.1.

The tides on the two measurement days were both spring tides, the tidal range of 13/06/91 (ebb: 5.70m, flood: 5.69m) is higher than the tidal range of 04/10/90 (ebb: 5.27m, flood: 5.57m), whereas the range of 11/07/91 (flood: 5.46m, ebb: 5.52m) is of the same order as the one of 04/10/90. The two measurements are both situated during summer conditions.

The lateral and vertically averaged mud concentration values have been calculated in function of time for the four available through tide measurements. The results are shown in Figure 5.25. The curves show a decrease of suspended mud concentration towards downstream. The highest mud concentrations are found at the location 'Plaat van Lillo', the lowest at 'Vaarwater boven Bath'. This course of suspended mud as a function of longitudinal position is in agreement with literature data, see § 5.2. The figure also indicate that at the most upstream location ('Plaat van Lillo') the peak concentrations during flood are substantially higher than in the cross section situated more downstream.

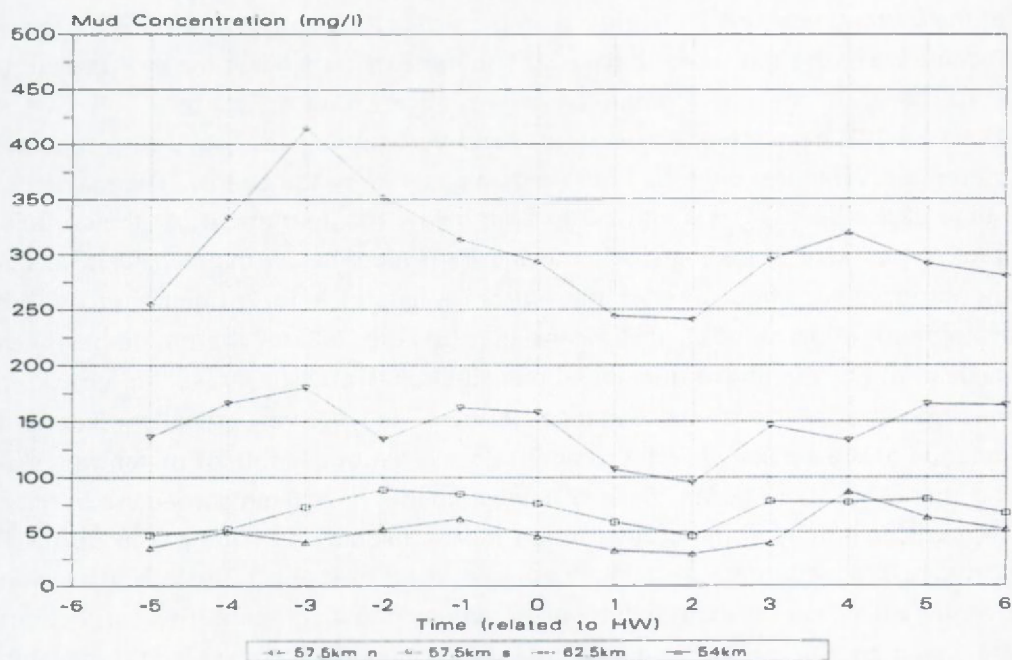


Figure 5.25: Mud concentration at 'Drempel van Zandvliet' (57.5km n: neap tide, 57.5km s: spring tide), 'Plaat van Lillo' (62.5km) and 'Vaarwater boven Bath' (54km).

## 5.5. Measurements In An Access Channel

On 19 and 29/04/94 two measurements have been carried out at the entrance of the Zandvliet-Berendrecht access channel using a Broad Band Acoustic Doppler Current Profiler (BBADCP). Both campaigns covered half of a tidal cycle. On 19/04/93 the velocities during flood and on 29/04/93 during ebb were recorded (A.Z., 1993c). A map with the location of the cross section is given in Figure 5.3.

The BBADCP measurement system (RD Instruments, 1989) was mounted on the survey vessel. The instrument allows to record continuously the velocity profile. The BBADCP transmits four identical pulses, these pulses are reflected by particles in the stream (it is assumed that the particles move with the same velocity as the water). The Doppler frequency shift of the backscattered pulses is proportional to the three-dimensional velocity field. The BBADCP produces current velocity data in a series of bins. The vertical size of the bins determines the vertical resolution

of the current measurements (minimum bin size is 25cm). The four transducers on the outside of the instrument have a 30° orientation. As a result the beams diverge horizontally. At maximum range the beams span  $\pm 55\text{m}$  horizontally.

The BBADCP calculates the horizontal and vertical velocity, assuming that the currents are uniform over the entire region covered by the beams. The maximum range of the BBADCP is about 35 to 55m below the instrument. At the surface, data are lost due to the installation of the transducer below the ship. This loss at the surface was about 3m. At the bottom a loss of 1 to 2m occurred. With a waterdepth of 15 to 20m, this means that 66% to 75% of the profile has been measured. For the above mentioned measurements a vertical resolution of 0.5m was chosen, the horizontal distance between successive vertical profiles is a function of the ship speed and was about 25m. The total length of the entrance of the channel is about 600m. Salinity measurements have been carried out in three different points along the cross section (north, middle and south). The BBADCP software produces data of velocity splitted in an East-West and a North-South component. Since the instrument was not coupled to a compass, these directions are equal to the velocity components perpendicular and parallel to the ship direction. The raw data have further been treated and extended by assuming no-slip at the bottom and no velocity gradients towards the surface.

#### 5.5.1. *Currents*

The predicted time of low and high water, the tidal elevation and the range during the two measurement days for the station Prosperpolder are given in Table 5.12 (D.D.K. and A.Z., 1993). Comparing the tidal range with the mean tidal range during the period 1971-1980 (Claessens and Belmans, 1984) results in a tidal coefficient for the campaign of 19/04/93 of 1.17 and of 29/04/94 of 0.96. The tide on 19/04/93 corresponds thus with a greater than average spring tide (coefficient = 1.13) and the tide on 29/04/93 with a somewhat smaller than an average mean tide.

Table 5.12 Measured tidal variations at Zandvliet during the measurement days.

Date	Time (MET)	Water level (m + TAW)	Tidal Range (m)	Tidal coefficient
19/04/93	8h12	-0.37	flood: 5.66	1.17
	14h09	5.29		
29/04/93	7h57	4.96	ebb: 4.68	0.96
	14h25	0.28		



Some results of the measurement campaigns are displayed in Figures 5.26-31. The figures consist of two parts. The 'East-West Velocity' part gives the horizontal velocity perpendicular to the cross section and the 'North-South Velocity' part displays the horizontal velocity in the cross section. East, west, north and south are thus not corresponding to the points of the compass (the North in the figure is rotated 23° counterclockwise to the real North). Positive and negative east-west current velocities refer to a flow leaving (outflow) or entering (inflow) the access channel. Positive and negative north-south current velocities indicate a flow directed towards downstream (North) or upstream (South). In the following a summary of the results is given.

In the beginning of the flood (Figure 5.26, 5h before HW) the outflow occurs in the surface layer and the inflow in the bottom layer. The currents are almost all directed towards the North. As the water level rises the current directions are reversed (Figure 5.27, 1h before HW). Inflow takes place in the surface layer and outflow in the bottom layer. The water is leaving the channel towards upstream (South) in the bottom layer and is entering the channel from downstream (North). The flow field at about high water slack is presented in Figure 5.28. The 'East-West' velocities are small with a separation of in- and outflow over the horizontal. In the southern part of the cross section outflow occurs and in the northern part water is entering the access channel.

A major difference between the ebb and the flood flow field is that no pronounced two layered flow over the cross section is observed during ebb. Outflow occurs in the southern part and inflow in the northern part of the cross section over the whole water depth (Figures 5.29-30) or a separation in outflow in the surface layer and inflow in bottom layer (Figure 5.31) is observed. The flow is generally directed towards the North. The currents in the northern part of the cross section do not show a separation into two velocity layers with opposite direction as is observed in the southern and middle part of the cross section.

The 'east-west' current velocities field are in general stronger during flood than during ebb. This can be explained by the presence of a pronounced eddy in the access channel having the main current velocities in the 'North-South' direction. During flood no or a weaker eddy is found.



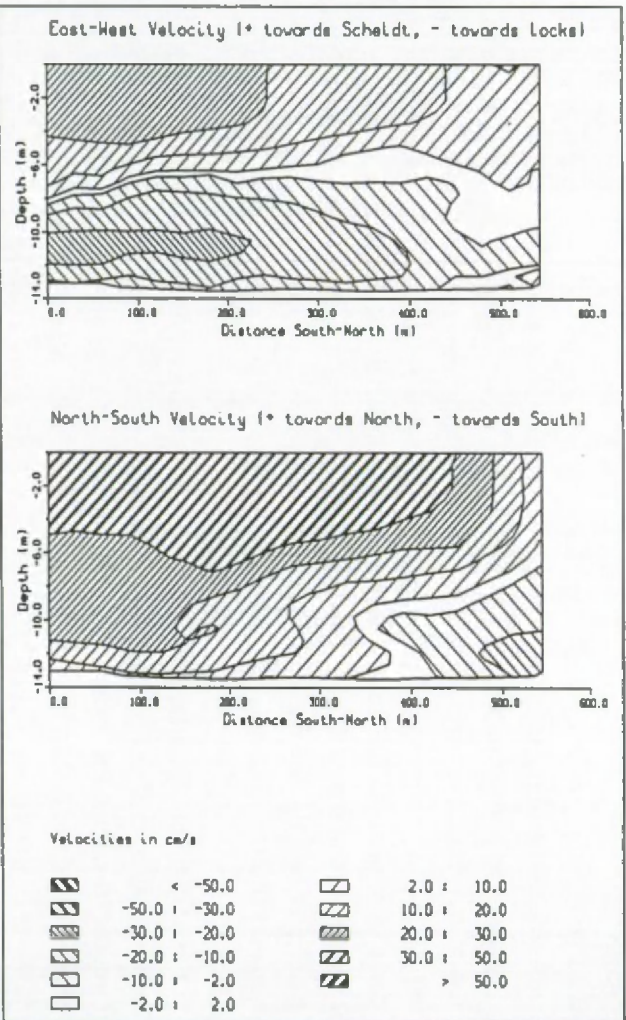


Figure 5.26: BBADCP measurements (19/04/93 - flood), 8h40, 5h31 before HW, Zandvliet-Berendrecht access channel.

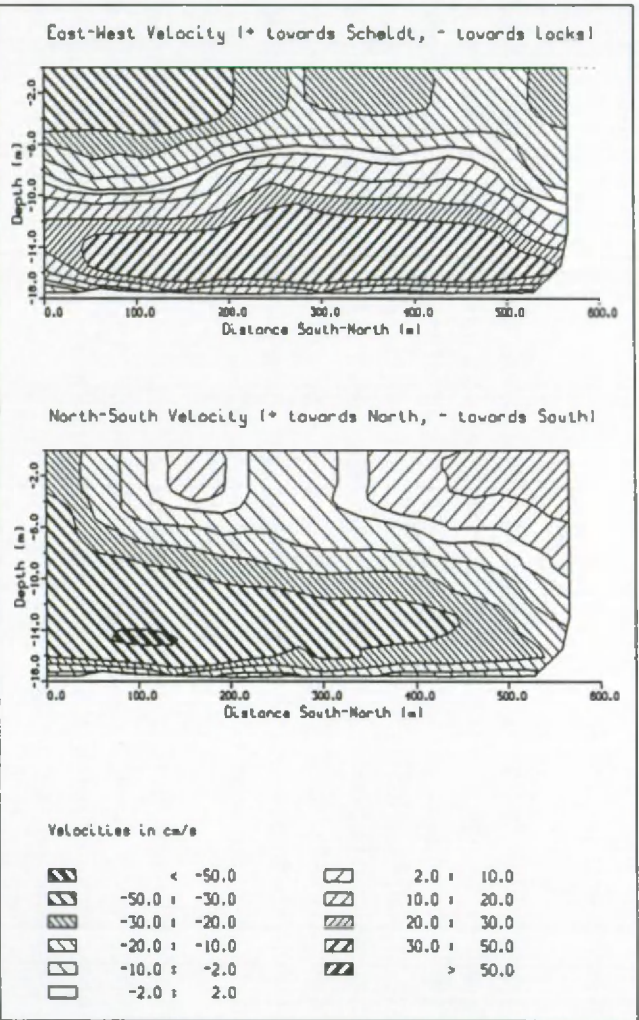


Figure 5.27: BBADCP measurements (19/04/93 - flood), 13h04, 1h06 before HW, access channel Zandvliet-Berendrecht.

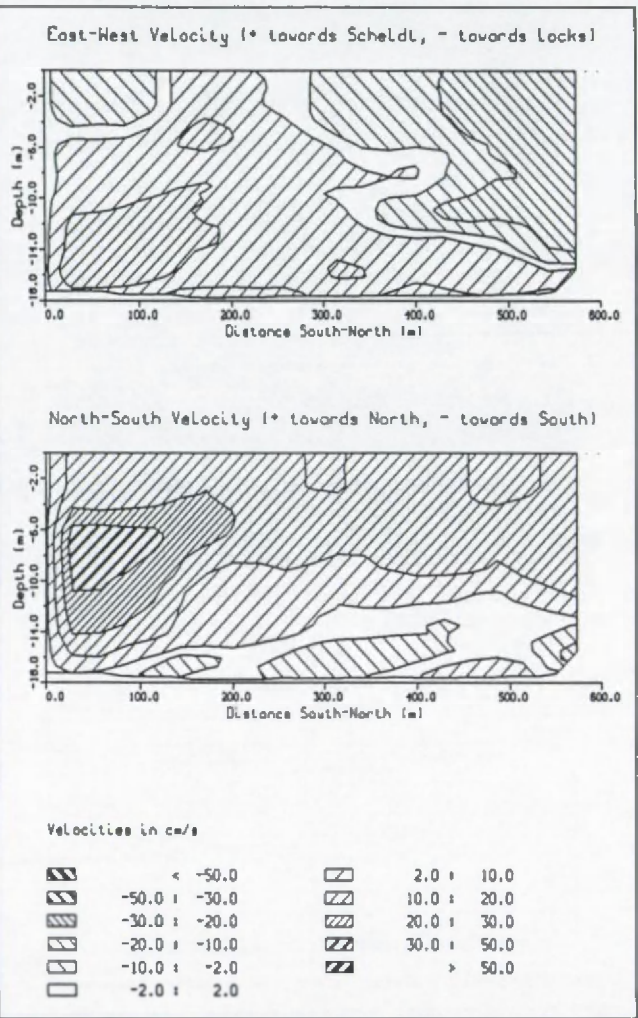


Figure 5.28: BBADCP measurements (19/04/93 - flood), 15h31, 1h21 after HW, access channel Zandvliet-Berendrecht.

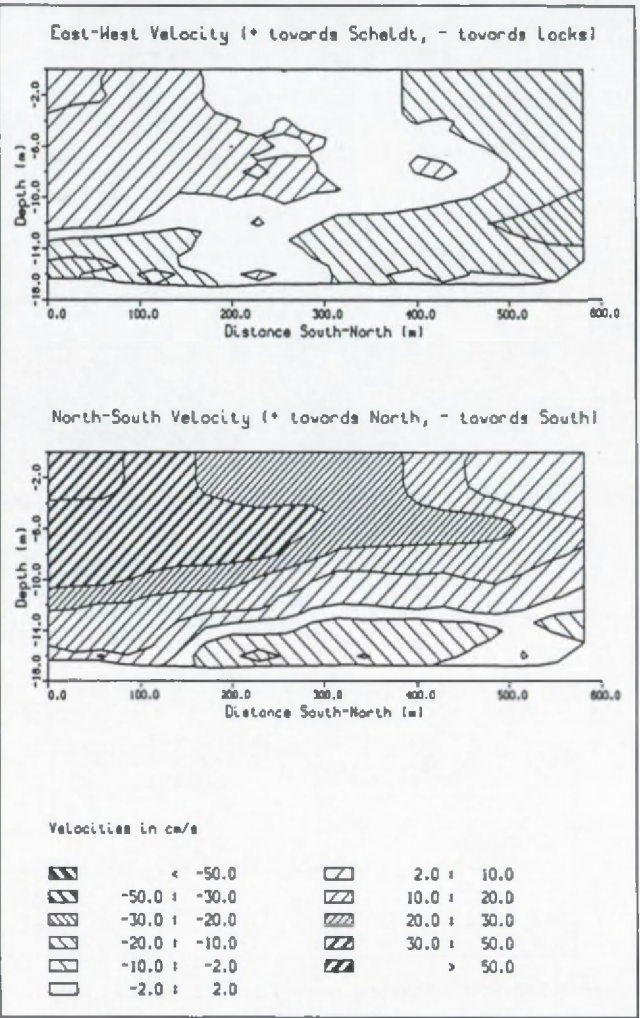


Figure 5.29: BBADCP measurements (29/04/93 - ebb), 10h02, 2h04 after HW, access channel Zandvliet-Berendrecht.



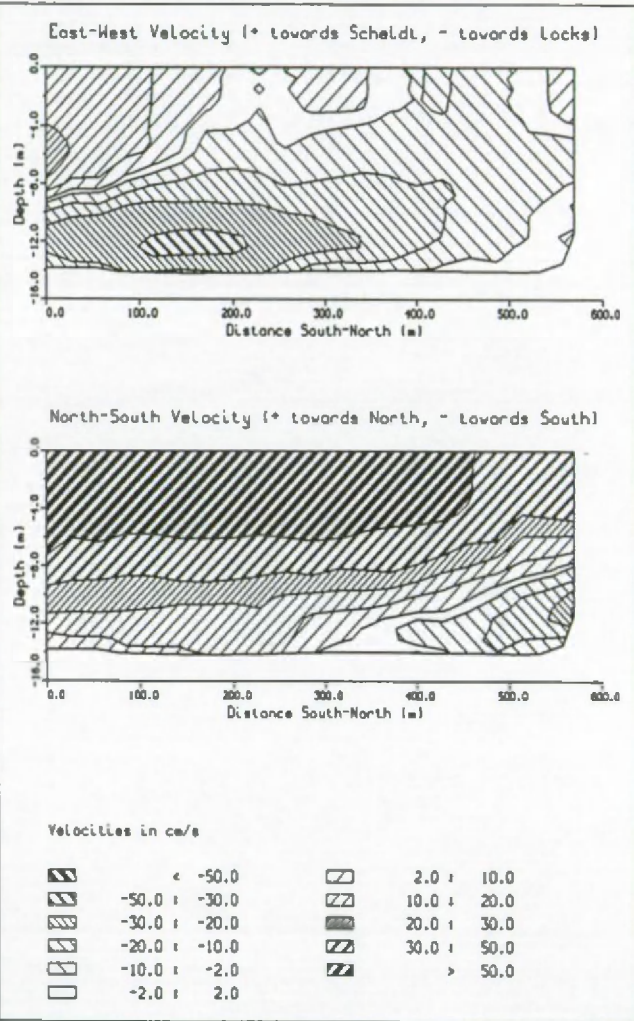


Figure 5.30: BBADCP measurements (29/04/93 - ebb), 13h02, 5h05 after HW, access channel Zandvliet-Berendrecht.

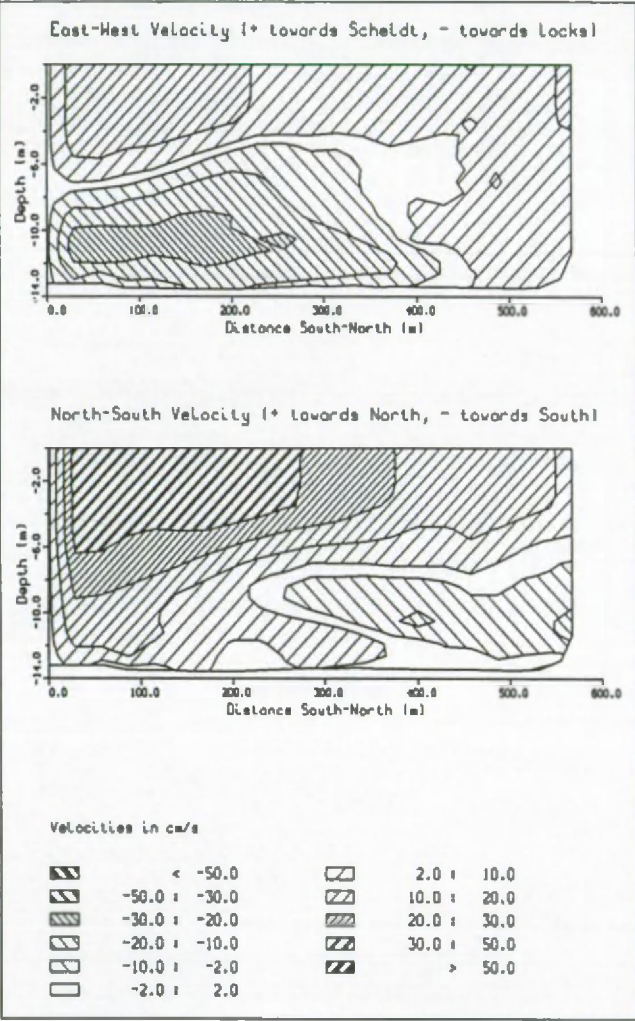


Figure 5.31: BBADCP measurements (29/04/93 - ebb), 15h03, 0h38 after LW, access channel Zandvliet-Berendrecht.

### **5.5.2.      *Salinity***

The two layered structure (inflow - outflow) of the currents in the measurement cross section of the access channel to the locks reflects the relatively strong vertical salinity gradients. Salinity profiles have been recorded in three points (North, Middle and South) over the cross section. The results are presented in Figures 5.32-33.

During flood a vertical salinity gradient is always present. The difference in salinity between bottom and surface lies between 1 and 3g/l. The salinity distribution during ebb is more complicated, revealing a difference between the northern part and the southern part of the cross section. In the northern part, the vertical salinity gradient decreases with time and is nearly absent at the end of the ebb period. In the rest of the cross section the gradient is always present. The maximum salinity differences between bottom and surface are about 3g/l. Due to the different tidal conditions a quantitative comparison between ebb and flood salinities has not been carried out. The fact that during flood a nearly homogeneous salinity distribution over the cross section is observed, corresponds with the pronounced two-layered flow during the same period. The weak salinity gradient in the northern part of the cross section is reflected in the almost uniformly directed currents in that part.

## **5.6.            Long Term Measurements At Prosperpolder**

### **5.6.1.      *Introduction***

The analysis of the two through tide measurements at the 'Drempel van Zandvliet' revealed the very dynamic behaviour of the cohesive suspended sediments. The mud concentration at a certain point is a function of local resuspension, turbulent diffusion, settling and non-local sources (transport). It was shown that the mud concentration varied as a function of time (i.e. during a single tidal cycle and between a neap and a spring tide), over the vertical and over the cross section. In order to investigate the variations of various quantities on a longer time scale continuous recordings of suspended mud concentration, salinity, temperature and water elevation have been undertaken at the tidal station of Prosperpolder (situated 55.975km from the mouth) during the period between September 1992 and December 1993, see Figure 5.4.



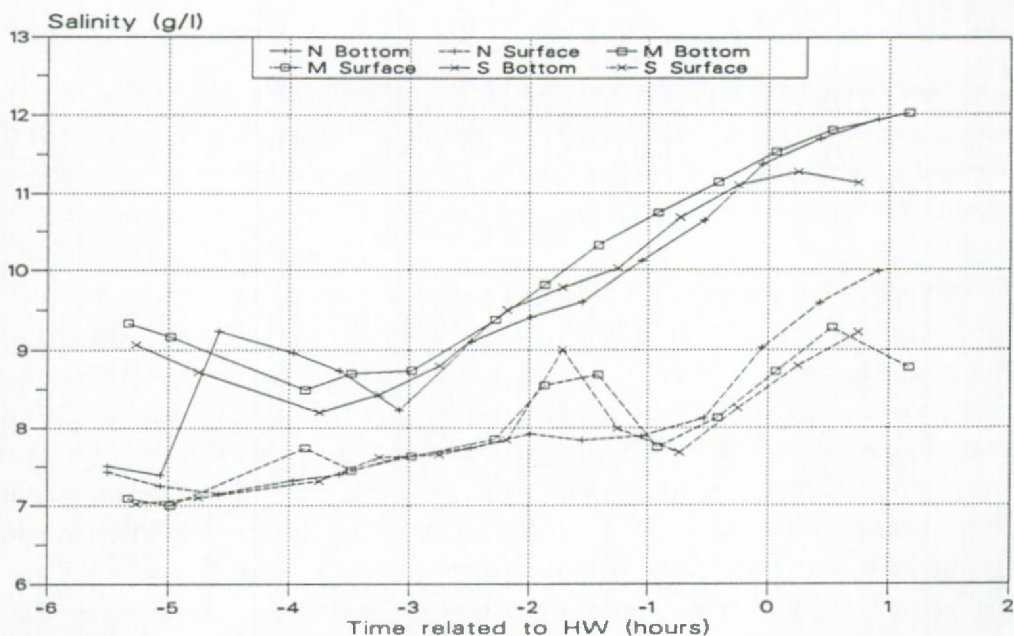


Figure 5.32: Salinity measurements during flood (19/04/93), access channel Zandvliet-Berendrecht (N = North, M = Middle, S = South).

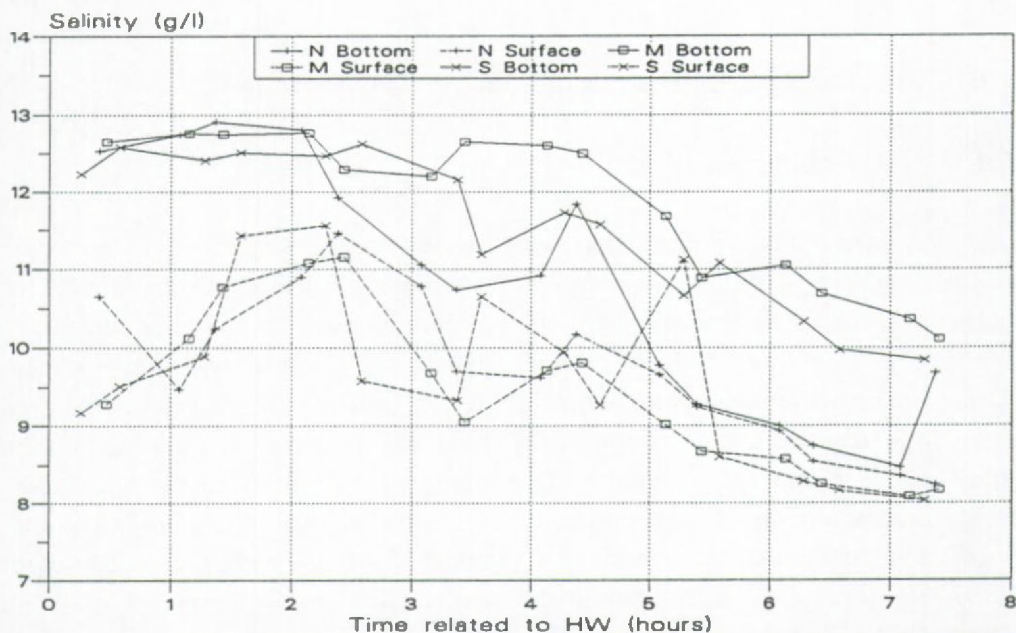


Figure 5.33: Salinity measurements during ebb (29/04/93), access channel Zandvliet-Berendrecht (N = North, M = Middle, S = South).

The suspended mud concentration has been measured using two Partech Twin-Gap sensors (see § 5.3.1.). The information obtained from the transducers was averaged over a 10 minute period and then stored in a data logger. The sensors were placed at 0.5m and 1.5m from the bottom. Calibration of the instrument was performed twice during the period. Every week the sensors have been put in water with a known concentration of 0mg/l and 500mg/l. These tests have shown that the zero concentration reading was nearly constant over the period but that for the 500mg/l reading variations occurred in course of time. These variations are probably due to a variations in quality of the 500mg/l solution. A description of the calibration can be found in I.M.D.C.-W.L.B. (1994).

The data set consists of about 70000 readings for every quantity (every 10 minutes). A detailed description of the salinity and mud concentration variations on a small time scale (but at a different location) is presented in § 5.3. Therefore we will focus here on the variations occurring on longer time scales (neap-spring tidal cycles and seasonal variations).

The division between neap, mean and spring tide which is used in the analysis is based on their average values during the period 1971-1980 (Claessens and Belmans, 1984) scaled by the ratio between mean tide during the period of observations and mean tide during 1971-1980. This scaling has been done because the mean tidal range during the observations is about 15cm higher than during 1971-1980. If  $\Delta h_{neap}$  stands for the average neap,  $\Delta h_{spring}$  for the average spring and  $\Delta h_{mean}$  for the average mean tidal range (scaled by the above mentioned ratio) then the definition of neap tide, spring tide and mean tide can be formulated as follows ( $\Delta h$  is the measured tidal range):

$$\text{Neap tide: } \Delta h < 0.5(\Delta h_{neap} + \Delta h_{mean})$$

$$\text{Spring tide: } \Delta h > 0.5(\Delta h_{spring} + \Delta h_{mean})$$

$$\text{Mean tide: } 0.5(\Delta h_{neap} + \Delta h_{mean}) \leq \Delta h \leq 0.5(\Delta h_{spring} + \Delta h_{mean})$$

A neap tide is thus a tide with an amplitude lower than the amplitude of the mean of an average neap and an average mean tide, a spring tide a tide with a higher amplitude than the mean of an average mean and spring tide. A mean tide is then situated between these two mean values. By doing so all the observations have been separated in three, approximately equally numbered, groups of amplitudes. A storm surge is defined as a tide with a high water level greater than 6.50m TAW.

In order to determine the relation between two signals (salinity vs. fresh water discharge and mud concentration tidal range) a cross correlation analysis has been performed. A cross correlation analysis permits to identify the time lag between two signals. The cross correlation of the averaged values will indicate a time lag of a multiple of one tide or one day.

The tidal variations of a quantity have been described by dividing all the values in groups of 10 minutes related to high water. For each group of data the mean and the standard deviation have been calculated. Because of the long term variations which are superposed on the tidal variations the measured quantities have been divided by their mean value during a tidal cycle.

### **5.6.2.        *Salinity***

#### **5.6.2.1.     *Seasonal variations***

The mean salinity value over a tidal cycle and the daily averaged fresh water discharge are displayed in Figure 5.34. The salinity value is a function of the fresh water discharge. During periods of high river run off the salinity is low, whereas during dry periods high salinity values are observed. Low salinity values occur in December and January. High salinity values are found at the end of the summer (September-October). The salinity during the measurement period at Prosperpolder varied between 1g/l and 19g/l. The salinity at the mouth does not show these big seasonal variations, the values are about 32g/l, with slightly higher values during summer than during winter (Otto et al., 1990).

The river Scheldt and its tributaries between Flushing and Ghent are tidal rivers and the exact fresh water discharge is almost impossible to determine. The discharge measurements carried out by the Antwerpse Zeehavendienst (A.Z., 1993a and 1994) are situated outside the tidal area and are extrapolated towards downstream. A daily fresh water discharge value (at Schelle) is not reported and only a discharge averaged over 10 days is given. In order to take into account the daily variations of discharge, the sum of all the discharge values at the measurement stations has been calculated using the data presented in the above mentioned A.Z. reports. This value is thus smaller than the discharge at Schelle. The magnitude of the discharge is here however of minor importance, since we are mainly interested in time shifts between salinity and discharge.

Ronday (1995) found, using an 1D numerical model forced with an idealized fresh



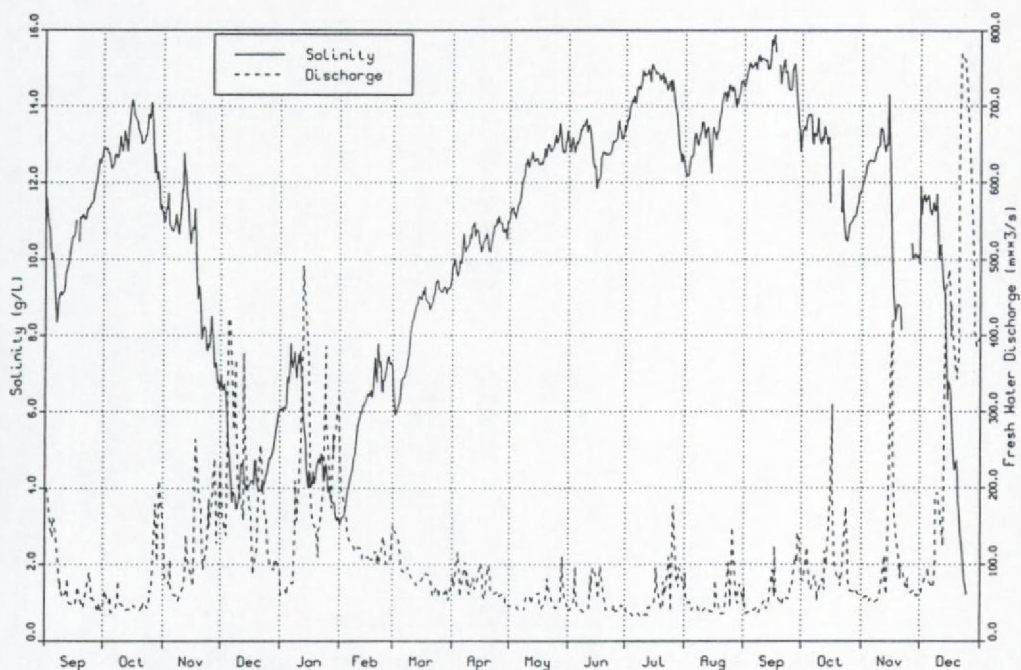


Figure 5.34: Tidal averaged salinity values and daily fresh water discharge, September '92 - December '93, Prosperpolder.

water discharge curve over a year, that salinity and fresh water discharge do not follow a simple exponential relationship: the same salinity value at a certain point in the estuary can occur during higher or lower fresh water discharges depending on whether the river run-off during the period previous to the recording was higher or lower than the current value. In Figures 5.35 the daily fresh water discharges are displayed as a function of salinity. The hysteresis of the salinity values as a function of fresh water discharge has been identified in the measurements at Prosperpolder, see Figure 5.36, in this figure the successive points in time are connected.

A cross correlation analysis between the daily fresh water discharge and the daily averaged salinity values indicates that the salinity minimum occurs 5 days after the maximum discharge. Because of the daily discharge values and the tides in the estuary an uncertainty of one tide in the cross correlation can be expected.



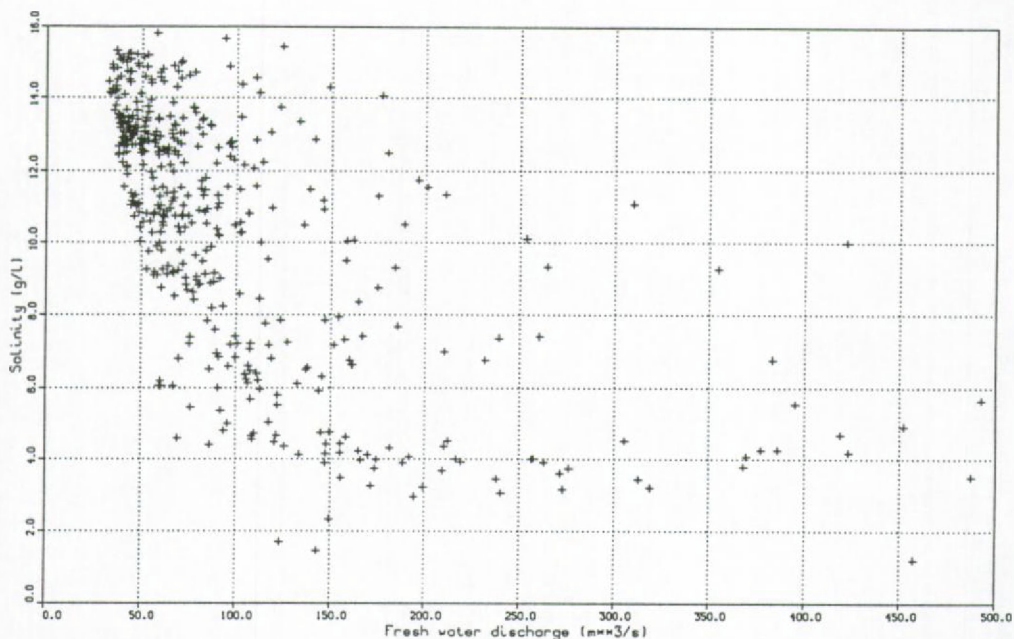


Figure 5.35: Salinity as a function of fresh water discharge, September '92 - December '93, Prosperpolder (daily averaged values).

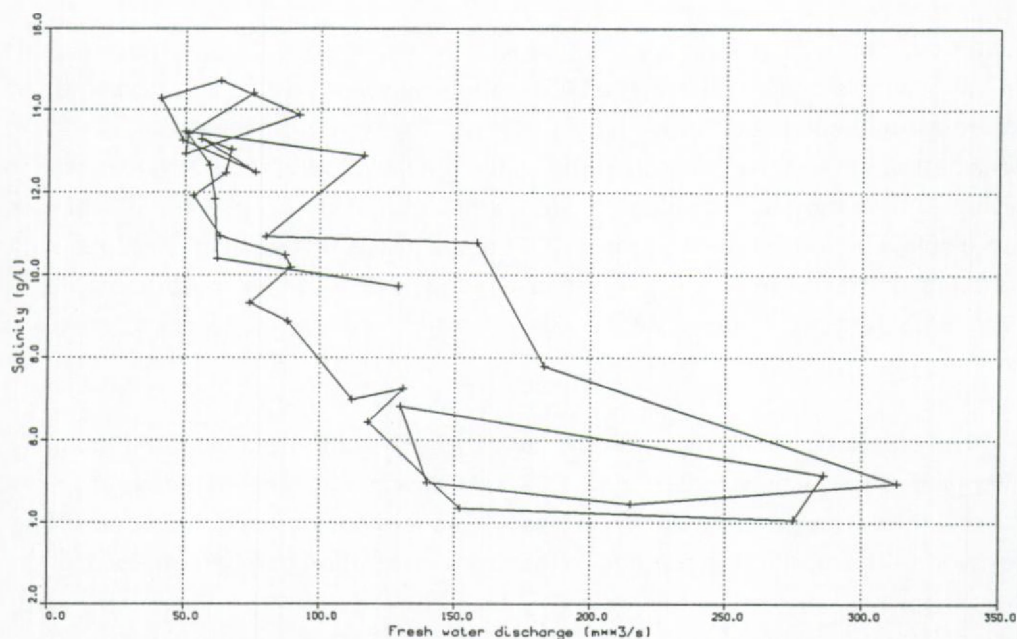


Figure 5.36: Hysteresis of fresh water discharge vs. salinity during September '92 - September '93, Prosperpolder (values are averaged over a decade).

#### 5.6.2.2. *Variations with tidal range*

Table 5.13 displays some averaged values of salinity differences (maximum - minimum during a tidal cycle) for different tidal ranges and over different periods.

The main factor influencing the salinity difference occurring during a tidal cycle is the tidal amplitude. This difference is, during a spring tide about 33% higher than during a neap tide. The seasons and thus the fresh water discharge have a minor influence on this value. During summer slightly higher salinity differences occur than during winter.

Table 5.13 Averaged salinity difference (max-min during tidal cycle) in g/l (mean  $\pm$  standard deviation) for different tidal conditions and over winter, summer and one year period.

	Neap Tide	Mean Tide	Spring Tide	All Tides
Year	3.7 $\pm$ 0.5	4.5 $\pm$ 0.6	5.1 $\pm$ 0.6	4.5 $\pm$ 0.8
Winter	3.6 $\pm$ 0.6	4.3 $\pm$ 0.7	4.8 $\pm$ 0.7	4.3 $\pm$ 0.8
Summer	3.9 $\pm$ 0.4	4.7 $\pm$ 0.3	5.3 $\pm$ 0.3	4.8 $\pm$ 0.6

#### 5.6.2.3. *Variations with tides*

The instantaneous values of salinity during a neap-spring-neap tidal cycle in October (low river run-off) and December (high river run-off) 1992 are shown in Figures 5.37-38. These figures show that during dry periods the tidal range correlates better with salinity than during wet periods.

The course of relative salinity (salinity divided by the mean salinity value over a tidal cycle) as a function of time related to HW is shown in Figure 5.39. A maximum in the curve is found at about 45 minutes after high water, the minimum salinity occurs at about 4.5 hours before high water.

#### 5.6.3. *Temperature*

Near bottom water temperature varied during the measurement period between 3°C in winter to about 23°C in summer. The tide-averaged value of temperature during the measurement period is shown in Figure 5.40.

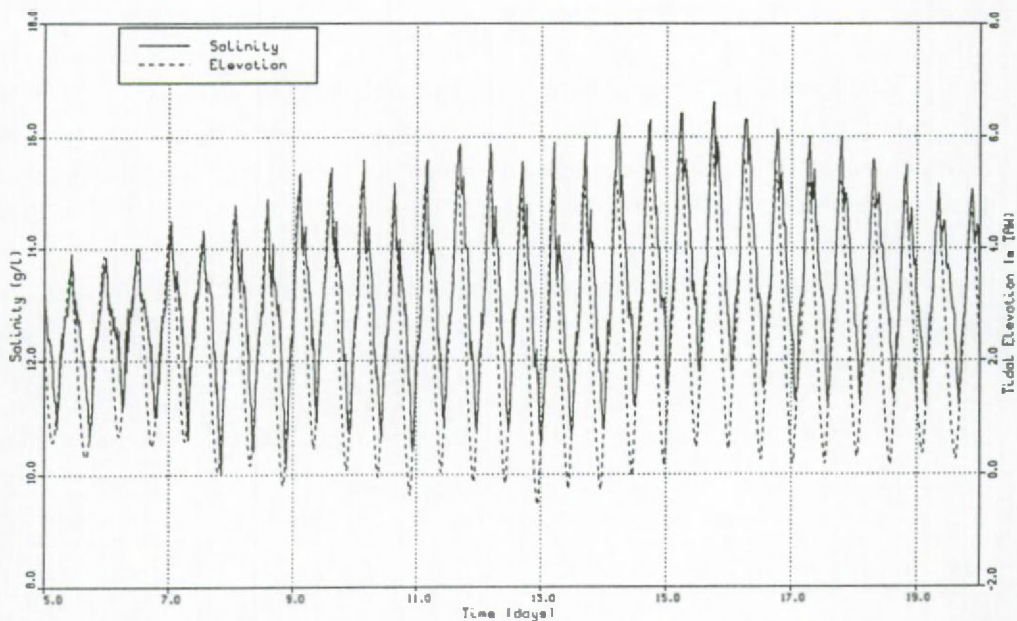


Figure 5.37: Salinity and tidal elevation, October '92, Prosperpolder.

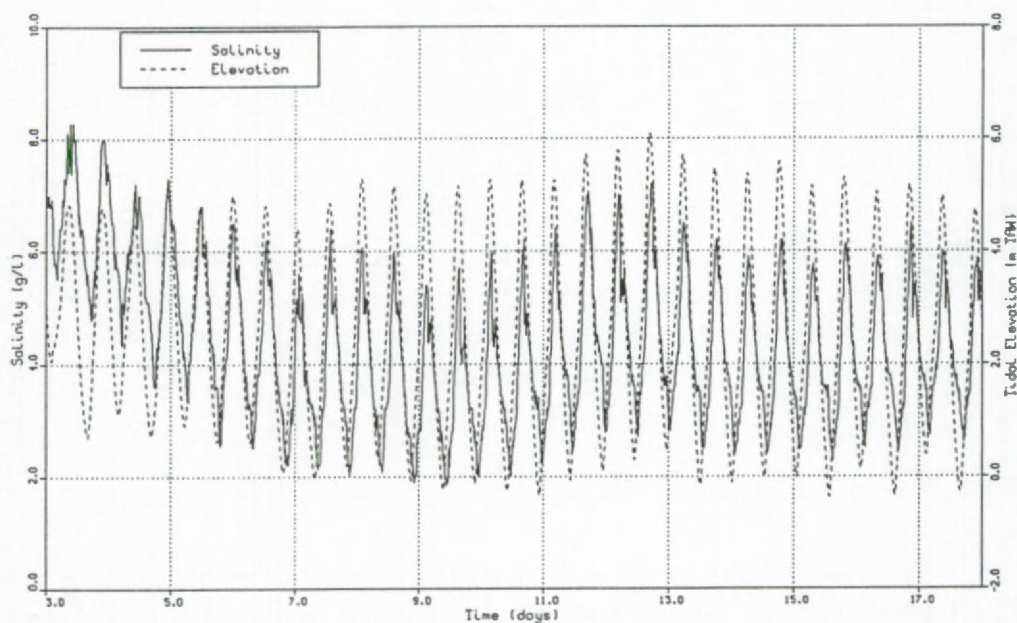


Figure 5.38: Salinity and tidal elevation, Days, December '92, Prosperpolder.



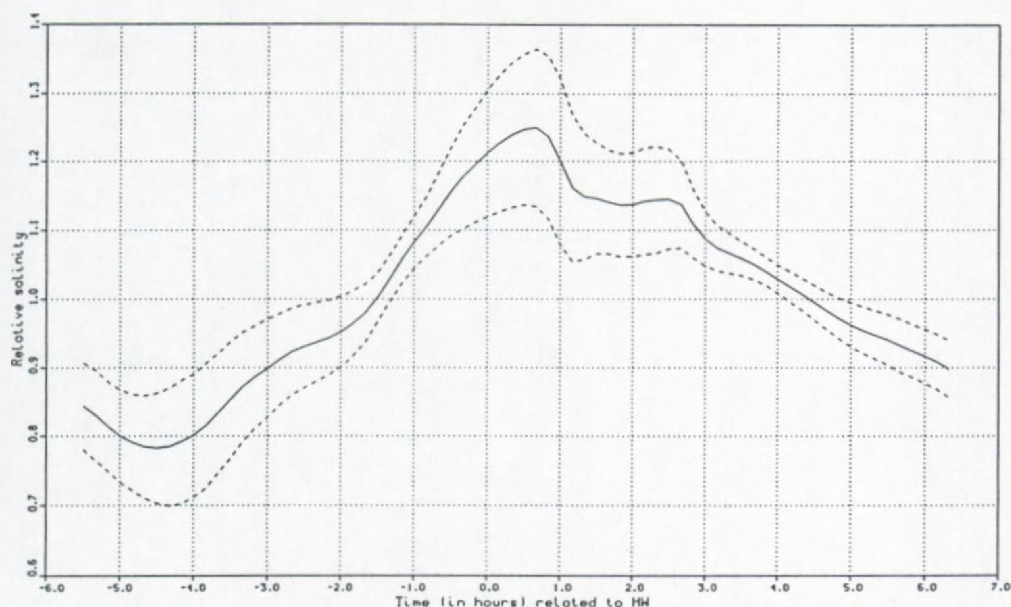


Figure 5.39: Relative salinity as a function of time related to HW, October '92 - September '93, Prosperpolder (dash:  $\pm$  standard deviation).

The differences between maximum and minimum temperature during a tidal cycle are presented in Table 5.14 for different tidal conditions and over different periods (see § 5.6.2.2.). The table shows that, in contrast with salinity differences, the main factor influencing the magnitude of the differences is the seasonal variation. The highest differences are found during winter ( $1.9^{\circ}\text{C}$ ), during summer the differences are a little lower ( $1.7^{\circ}\text{C}$ ). The influence of the tidal amplitude is of less importance. The mean sea surface temperature during February at the mouth of the Scheldt estuary is about  $4^{\circ}\text{C}$  and during August about  $18^{\circ}\text{C}$  (Otto et al., 1990).

Table 5.14 Averaged temperature difference (max-min during tidal cycle) in  $^{\circ}\text{C}$  (mean  $\pm$  standard deviation) for different tidal conditions and over winter, summer and one year period.

	Neap Tide	Mean Tide	Spring Tide	All Tides
Year	1.6 $\pm$ 0.5	1.7 $\pm$ 0.5	1.8 $\pm$ 0.4	1.7 $\pm$ 0.4
Winter	1.8 $\pm$ 0.5	1.9 $\pm$ 0.4	1.9 $\pm$ 0.4	1.9 $\pm$ 0.4
Summer	1.4 $\pm$ 0.3	1.5 $\pm$ 0.4	1.6 $\pm$ 0.3	1.5 $\pm$ 0.4



Figure 5.40: Tidal averaged temperature values, September '92 - December '93, Prosperpolder.

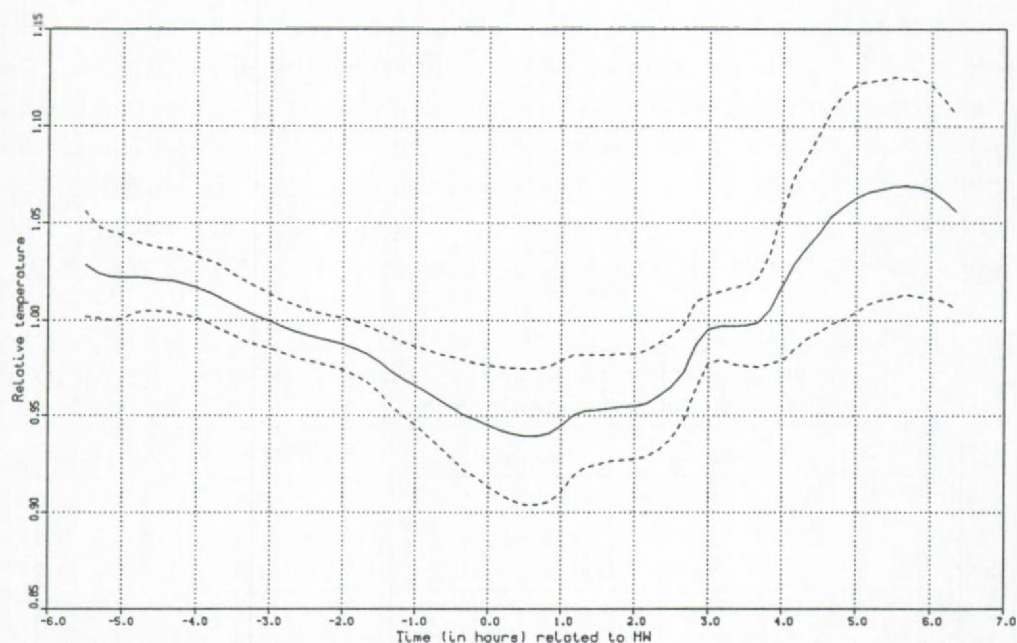


Figure 5.41: Relative temperature as a function of time related to HW, October '92 - September '93, Prosperpolder (dash:  $\pm$  standard deviation).

Figure 5.41 displays the relative temperature curve (temperature divided by mean temperature over tidal cycle) as a function of time related to high water. The maximum temperature occurs at 5.5 hours after high water, a minimum is found at the same moment as the salinity maximum, i.e. 45 minutes after high water. The minimum and the maximum occur at the same moment of the tide throughout the whole year. A reason for this somewhat unusual behaviour (one would expect that during winter the river water is colder than the sea water, whereas during summer the opposite holds) can be found in the fact that at about 6km upstream of Prosperpolder a nuclear power station is situated.

#### **5.6.4.        *Suspended mud***

##### **5.6.4.1.      *Variations of averaged quantities***

In order to investigate some of the long term variations of mud concentration, averaging of the data over a certain time has been carried out. It was found in (see § 5.3.) that mud in suspension has a different behaviour and thus different concentration values during flood and ebb, related to different velocity distributions in time and in the vertical plane. The averaged and the peak concentration during flood are generally higher than during ebb. The quantities were therefore averaged over respectively flood (LW slack to HW slack) and ebb (HW slack to LW slack). Since current velocities have not been recorded, the definition of high water and low water slack has been set at the moment of extreme salinity values.

The results after averaging are presented in Figures 5.42-43 (mud concentration at 0.5m from bottom) and Figures 5.44-45 (mud concentration at 1.5m from bottom). A first qualitative look at the figures shows that the (averaged) mud concentration is generally higher during flood than during ebb and that the concentration during flood corresponds better to variations in tidal range than the concentration during ebb, this has also been reported for the long term measurements at Liefkenshoek (I.M.D.C., 1989).

The averaged mud concentration during winter (October '92 - March '93), and summer (April '93 - September '93) and a whole year period (October '92 - September '93) for neap, mean and spring tides are shown in Table 5.15 and 5.16 (for the definition of neap, mean and spring tide see § 5.6.1.).



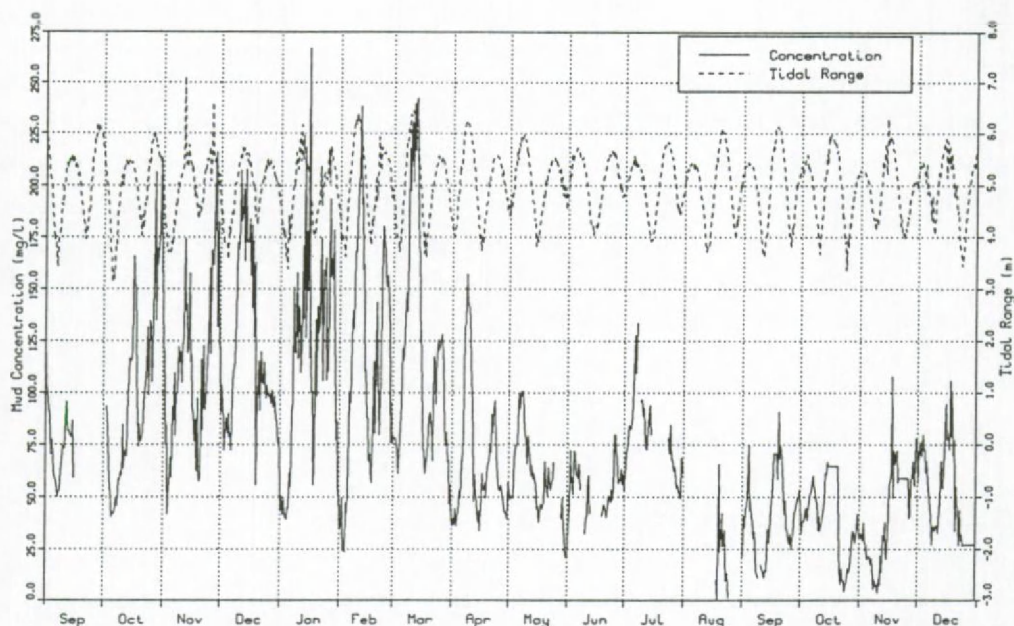


Figure 5.42: Flood-averaged mud concentration (0.5m above bottom) and tidal range, September '92 - December '93, Prosperpolder.

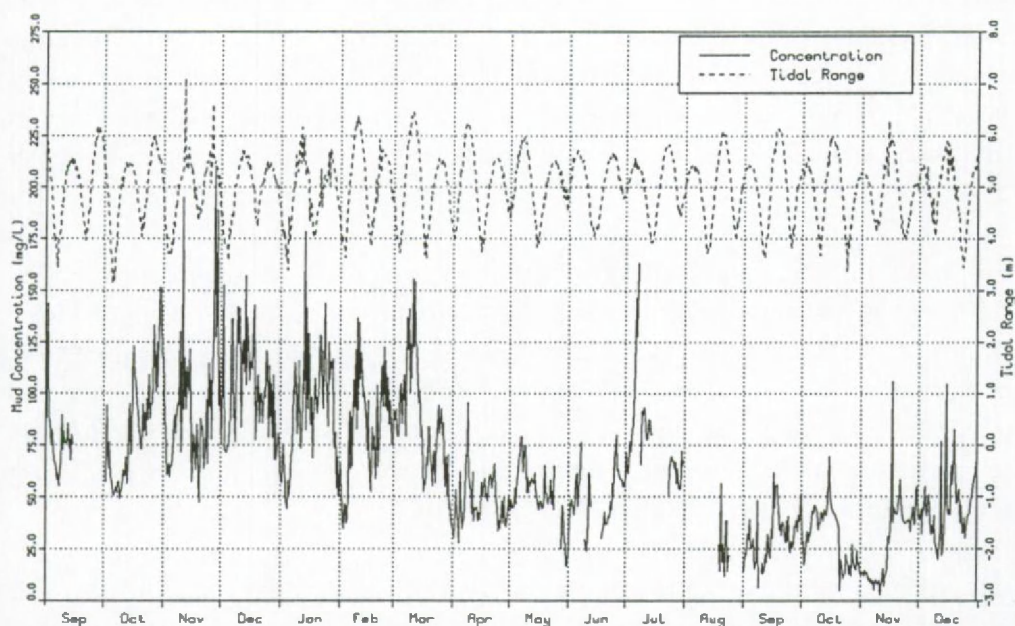


Figure 5.43: Ebb-averaged mud concentration (0.5m above bottom) and tidal range, September '92 - December '93, Prosperpolder.

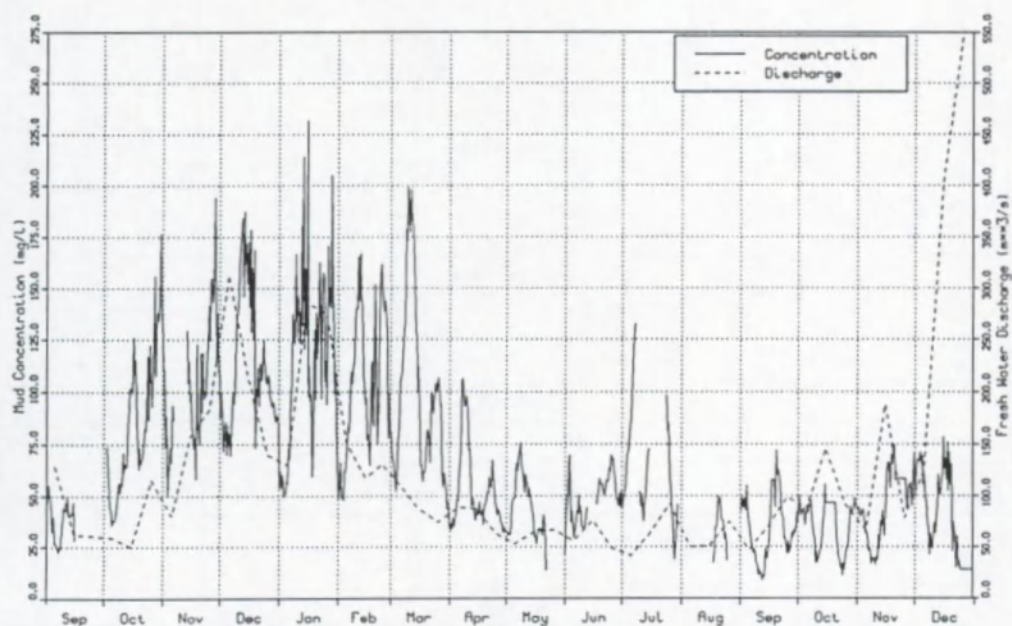


Figure 5.44: Flood-averaged mud concentration (1.5m above bottom) and fresh water discharge, September '92 - December '93, Prosperpolder.

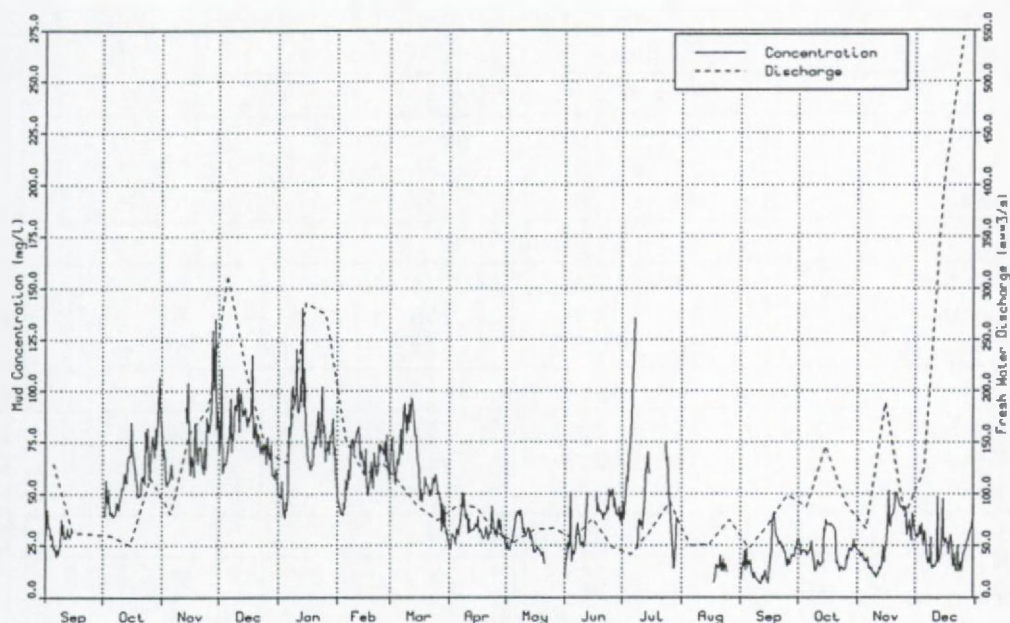


Figure 5.45: Ebb-averaged mud concentration (1.5m above bottom) and fresh water discharge, September '92 - December '93.

Table 5.15 Mud concentration (mg/l) 0.5m from bottom. Ebb, flood and tidal averaged data (Mean  $\pm$  standard deviation) for different tidal conditions and over winter, summer and one year period.

	Ebb	Flood	Tide
Neap Tide			
Winter	74 $\pm$ 50	71 $\pm$ 35	72 $\pm$ 44
Summer	46 $\pm$ 26	47 $\pm$ 24	46 $\pm$ 25
Year	64 $\pm$ 45	62 $\pm$ 34	63 $\pm$ 41
Mean Tide			
Winter	91 $\pm$ 62	112 $\pm$ 57	99 $\pm$ 61
Summer	49 $\pm$ 29	56 $\pm$ 28	52 $\pm$ 29
Year	73 $\pm$ 55	87 $\pm$ 54	72 $\pm$ 55
Spring Tide			
Winter	104 $\pm$ 35	151 $\pm$ 80	123 $\pm$ 78
Summer	54 $\pm$ 31	72 $\pm$ 43	62 $\pm$ 38
Year	82 $\pm$ 62	115 $\pm$ 77	96 $\pm$ 70
Storm Surges			
Year	117 $\pm$ 83	123 $\pm$ 56	120 $\pm$ 73
All Tides			
Winter	90 $\pm$ 63	114 $\pm$ 70	100 $\pm$ 67
Summer	50 $\pm$ 29	60 $\pm$ 35	55 $\pm$ 32
Year	74 $\pm$ 56	91 $\pm$ 63	81 $\pm$ 60

Table 5.16 idem Table 5.15 but now at 1.5m from the bottom.

	Ebb	Flood	Tide
Neap Tide			
Winter	57 $\pm$ 24	70 $\pm$ 28	63 $\pm$ 27
Summer	27 $\pm$ 16	34 $\pm$ 18	30 $\pm$ 17
Year	47 $\pm$ 26	57 $\pm$ 30	51 $\pm$ 29
Mean Tide			
Winter	71 $\pm$ 34	104 $\pm$ 46	84 $\pm$ 42
Summer	32 $\pm$ 19	45 $\pm$ 23	37 $\pm$ 22
Year	54 $\pm$ 35	77 $\pm$ 47	63 $\pm$ 42
Spring Tide			
Winter	76 $\pm$ 35	133 $\pm$ 63	100 $\pm$ 56
Summer	34 $\pm$ 21	57 $\pm$ 32	44 $\pm$ 29
Year	57 $\pm$ 37	97 $\pm$ 63	74 $\pm$ 53
Storm Surges			
Year	81 $\pm$ 26	122 $\pm$ 42	99 $\pm$ 39
All Tides			
Winter	69 $\pm$ 33	104 $\pm$ 55	83 $\pm$ 47
Summer	31 $\pm$ 19	48 $\pm$ 28	38 $\pm$ 25
Year	53 $\pm$ 34	79 $\pm$ 53	64 $\pm$ 45



The tables indicate that the concentration of mud during flood is generally higher than during ebb. An exception is given by the neap tide concentration values at 0.5m from the bottom. In the point situated higher above the bottom this is not observed. The general higher concentration during flood are related to the velocity differences between ebb and flood. As is shown in Figure 5.5 and 5.6 the distribution of the velocity over the cross section and the magnitude of ebb and flood peak currents are different between a spring tide and a neap tide. The ratio of peak ebb to peak flood currents is higher during spring than during neap tide. The course of velocity during flood, in contrast to the ebb course, is qualitatively different during neap tide compared to spring tide. At spring tide the flood velocity curve is more asymmetric and shows a pronounced double peak whereas during neap tide the flood velocity curve is more smooth. This means that during a neap-spring cycle the peak flood velocities increase relatively more than the peak ebb currents resulting thus in a relatively higher erosion of mud during a spring tide flood. It is reasonable to assume that a similar flow pattern is present at Prosperpolder. The similar mud concentration values at 0.5m from the bottom during ebb and flood at neap tide is then explained by the relative higher influence of local resuspension (and local velocity fields) than of transport of mud in suspension from more remote areas. In the point situated 1.5m from the bottom the influence of mud transported from elsewhere and distributed over the vertical is more important than the local resuspension.

The tide averaged mud concentration during a spring tide is 1.3 to 1.7 times greater than during a neap tide. This number is higher during flood (1.5 - 2) than during ebb (1.2 - 1.5). At spring tide the currents are higher and are thus able to erode and transport more sediment in suspension. The ratio flood to ebb concentration is higher in the point situated 1.5m above the bottom than in the point closer to the bottom.

The value of this ratio is not depending on the seasons but mainly on tidal amplitude. For the point at 1.5m from the bottom the ratio is for neap tide 1.2, for mean tide 1.4 and for spring tide 1.7. For the point closer to the bottom values calculated are respectively 1 (neap tide), 1.2 (mean tide) and 1.5 (spring tide). Meteorological factors (storm surges) seem not to have a significant influence on the mud concentration. The averaged concentration values during storm surges are in the same range of values as observed during 'winter' spring tides. The peak concentrations can however be higher.

In order to quantify the relation between mud concentration and tidal amplitude a cross correlation analysis has been performed. The correlation has been calculated between the tidal range and the tide averaged concentrations at (0.5m from bottom) for a whole year, a winter and a summer period. The calculations show a correlation with neap-spring cycles, the maximum tide averaged mud concentration occurs one tide later than the maximum tidal range. During winter a high cross correlation (0.8) exists whereas during summer the correlation is small (0.3). The cross correlation for the yearly averaged values is in between those for winter and summer. A possible reason why the 'summer coefficient' is lower than the 'winter coefficient' can be found in the fact that during winter more mud is available for deposition and resuspension (see next paragraph for a discussion of the seasonal variations). During summer less mud can be brought into suspension as is potentially possible by the currents (especially during spring tide), whereas during winter the currents can resuspend an amount of mud which is closer to the 'potential amount'.

#### 5.6.4.2. *Seasonal variations*

The above mentioned tables and figures show a clear coupling of the mud concentrations with seasons. High concentrations occur during winter (approximately October to March) and low concentrations during summer (approximately April to September). The seasonal influence is, however, as has been shown above, not influencing the variations occurring during one tidal cycle. The value of the ratio between winter to summer concentration increases with increasing tidal amplitude and is generally higher for flood than for ebb. The value is higher at 1.5m from the bottom than at 0.5m from the bottom and varies between 2 to 2.3 (1.5m from bottom) and 1.5 to 2 (0.5m from bottom).

The seasonal influence is due to a wide range of processes, which are very often interrelated, they can be grouped as follow:

- variations in fresh water discharge (shift of the position of the turbidity maximum, higher erosion of sediments in non-tidal part of the basin),
- variations in temperature (biological activity, weather),
- variations in land erosion (terrestrial input of fine sediments).

In the following we have tried to investigate whether these processes are or can be of importance in explaining the seasonal variations in mud concentration found in the measurements.

Wollast and Marijns (1981) have demonstrated that the turbidity maximum is situated at about 110km from the mouth during dry periods and at about 50km during wet periods, the latter is in the vicinity of Prosperpolder. Periods with high rainfall are more concentrated during winter. The correlation of fresh water discharge to mud concentration can be seen in Figures 5.44-45. The values of mud concentration at Prosperpolder during a wet (winter) and a dry period (summer) indicate that a shift in the turbidity maximum position towards downstream as a function of the fresh water discharge can explain the seasonal variations in concentration observed at Prosperpolder. The mud concentration in the turbidity maximum region can be 2 - 3 times higher than at the upstream border of it according to Wollast and Marijns (1981). In Figures 5.46-49 the course of mud concentration with time are displayed during a ten days period in January '93 and May '93. The figures show that the peak concentration values occur in general in January '93 during ebb and in May '93 during flood. This can especially be seen in the measurements taken at 1.5m from the bottom, see Figures 5.48-49. An explanation for this shift can be found in the variations of the position of the turbidity maximum in relation to the current velocities. Dyer (1986) mentioned that sediment concentrations at the extreme seaward end of the turbidity maximum are higher around low water (during ebb) whereas at the landward end of the turbidity maximum the highest concentration are observed at about high water (flood). The measurement station of Prosperpolder is either situated downstream (low fresh water flow) or at the seaward end (high fresh water flow) of the turbidity maximum (Wollast and Marijns, 1981). The higher peak concentration during ebb in January '93 can thus be explained by the nearby turbidity maximum. During May '93 the turbidity maximum is further up the estuary and the main influence on mud concentration variations are the currents, which are higher during flood than during ebb, resulting thus in higher peak concentration during flood. The measurements give an indication that the fresh water discharges have an influence on the mud concentration at Prosperpolder. The seasonal variations of mud concentration are observed in the whole estuary. Variations in position of the turbidity maximum have however only a local influence. This suggests that other processes are involved in creating seasonal variations, although in the turbidity maximum region variations in fresh water discharge can have an important or even dominant influence on the course of mud concentration with seasons.

Mud concentrations are correlated with temperature, since temperature is obviously related to seasons. The temperature variations during a year have an in-



fluence on biological activity. The biological activities have, besides a seasonal variation, a strong longitudinal variation, due to the strong salinity gradients (in term a function of the fresh water discharge) which influence the distribution of marine, brackish and fresh water organisms (van Leussen, 1994). Algae and other microorganism are increasing the erosion threshold of the mud on the bottom in the intertidal areas such that more mud is stored on the bottom and is thus taken out of the system resulting in a decrease of mud in suspension and a decrease of mud which can be brought in suspension due to erosion.

The comparison of the salinity variation (Figure 5.34) and the mud concentration as a function of time (Figures 5.42-45) shows that the high mud concentrations are coupled to low salinity values. The minimum tide-averaged salinity during winter varied between 2g/l and 6g/l. These salinity values are situated in the range of values reported in literature as 'point of flocculation', see Drake (1976), Whitehouse et al. (1960) and Einstein and Krone (1962) (from van Leussen, 1994). The high importance which is given to salinity as a mechanism for flocculation as presented in older literature is however more and more questioned as other mechanism (bioflocculation, organic aggregates, pelletization) have been identified. Eisma et al. (1991) concluded from field measurements that no evidence is found in the Rhine estuary for the occurrence of salt flocculation and that the large aggregates were almost all glued together by organic matter. The same authors found in the Gironde estuary that the floc size decreased in the direction of increasing salinity. Taking into account these different behaviours of flocculation found in other estuaries it is not possible yet to give an answer about the processes which are responsible for flocculation in the Scheldt estuary. If flocculation due to organic or biological processes is important than it is likely that seasons have an influence on the floc formation and on the floc forming processes. This would mean that during winter mud is more easily maintained in suspension since flocculation is less important than during summer.

Storm surges can increase the erosion of mud and thus the concentration. Their influence is partly due to the higher velocities and partly due to wave induced erosion in the shallow areas. Storm surges are generally occurring during winter. The peak concentrations of mud can be much higher during storm surges. As was found in the measurements, however, the averaged values of mud concentration are in the same range as during spring tides. Therefore it is believed that storm surges are not important in explaining seasonal variations.

Terrestrial erosion is higher during winter because of a less extended plant cover and because of the higher rain falls. Rainsplash is the most important detaching agent. Transport of the sediment particles is due to overland flow and due to water flow in small channels (rills) or in larger permanent gullies or rivers (Morgan, 1979). The sediment run off from land erosion enters only for a small part the river and can there or be transported further downstream or be deposited locally. The suspended sediment load of a river is a function of the river run-off and can be substantially higher during wet than during dry periods.

I.M.D.C. (1993a) has estimated the terrestrial input of fine grained sediments in the Scheldt estuary upstream of Rupelmonde as  $\pm 0.8 \times 10^6 \text{ t/yr}$ , from which  $\pm 80\%$  is from soil erosion in the catchment area of the basin. These are yearly averaged data. The measurement data on which this value is based are not mentioning how the suspended sediment load is varying with seasons. According to Sine and Agneesens (1978) the sediment load in the Meuse river (Hesbaye, Belgium) was approximately 7 times higher during a wet period (1973-1975) than during a dry period (1975-1977). Van Maldegem et al. (1993) estimated the net downstream transport of riverine mud at the Belgian/Dutch border (close to Prosperpolder) as  $0.4 \times 10^6 \text{ t/yr}$  and the net import (marine mud) as  $0.1 \times 10^6 \text{ t/yr}$ . If a seasonal variation in terrestrial input exists than it is likely that it has an influence on the yearly suspended sediment concentration in the estuary. Furthermore the influence will be strongly depending on the location in the estuary and decrease in downward direction.

It was shown that the above mentioned processes are all able to produce seasonal variations in mud concentration. It has also been shown that the relative importance of a certain process is depending on the position in the estuary. The question of to what extent the higher mud concentrations observed during winter at Prosperpolder are due to a downstream shift of the turbidity maximum area under influence of higher river run-offs or to an increase of the terrestrial sediment input or to a decrease in temperature of the water and its influence on biological and physical processes cannot be answered with the given observations. In order to do so, simultaneous recordings of mud concentration and biological factors at different points situated along the whole estuary would be required.

#### 5.6.4.3. *Tidal variations*

Instantaneous mud concentrations are presented in Figures 5.46-49 for a ten days period during January and May '93. The mud concentration varies clearly with tide and with tidal range. The signal is also superposed by some high frequency variations. Possible explanations are found in turbulent variations in current velocities, in the occurrence of peak velocities (flood), in inhomogeneities in the horizontal and vertical distribution and in the composition of the mud on the bottom, and in variations in transport of mud.

High frequency variations in current velocity recordings superposed on the tidal variation of velocity have been observed at Doel (some 5km upstream), see I.M.D.C. (1993b) and during the long term measurements at Liefkenshoek (some 8km upstream), see I.M.D.C. (1989).

Erosion and deposition of mud during a tidal cycle can explain some of the peaks which have been measured. During slack water mud is deposited on the bottom, this mud layer is very soft and is easily eroded once the velocities are increasing. This erosion results in a first peak in concentration. The critical shear stress for erosion of the currently exposed mud is higher and erosion occurs only when the velocity has increased sufficiently, resulting in a second concentration peak. The peak velocity during flood, which is more pronounced during spring tide than during neap tide, occurs at about 1 to 2 hours before high water. This moment can be related to the occurrence of another peak in concentration. During ebb the course of velocity is more uniform and only two peaks in concentration should be expected from the erodibility characteristics of the mud.

The figures show a great difference between maximum and minimum concentration which can occur during a tidal cycle. The ratio between maximum and minimum concentration can be up to 20 during spring tide. During neap tide the ratio is substantially smaller. Peak values of mud concentration during flood occur between 2 to 1 hour before high water and during ebb at about 3 hours after high water. The first peak corresponds to the moment of peak flood velocities as was shown in the through tide measurements at the 'Drempel van Zandvliet' (§ 5.3.). It has also been reported from the long term measurements at Liefkenshoek which have been carried out between 1/02/89 and 25/05/89 (I.M.D.C., 1989). The peak ebb mud concentration at 0.5m above the bottom is, in contrast with the point at 1.5m from the bottom, on the average higher than the peak flood concentration. The averaged mud concentration during a tidal cycle for the long term measurements at Liefkenshoek is about a factor



two higher than the values recorded at Prosperpolder. A reason for these differences which occur over a relative short distance (Liefkenshoek is situated about 7km upstream of Prosperpolder) cannot be identified clearly, but are maybe related to the position of the turbidity maximum, to the influence of lateral concentration variations, to the fact that the global mud contents in the estuary has changed in the course of the years or to differences in measurement instruments and calibration.

#### 5.6.4.4. *Conclusions*

The tables and figures indicate a correlation of the mud concentration with tides, neap-spring tidal cycles and seasons. The tidal and the neap-spring tidal cycle variations can be explained by the hydrodynamic conditions. The seasonal variation of mud concentration is due to various physical, chemical and biological properties of the water and the dissolved substances as well as the fresh water discharge and the terrestrial input of mud.

The distribution of suspended matter is influenced by a range of interrelated processes (e.g. temperature and biological activity, fresh water discharge and salinity, hydrodynamic conditions and turbulence, mineralogical composition, chemical conditions, aggregation and flocculation). The relative importance of each process is difficult to quantify, partly because of a lack of observations and partly because of the complex nature of the processes and the coupling between each other.

Ten Brinke (1992) mentioned the influence of dredging activities and navigation on the suspended mud concentration. Especially the use of the sweepbeam (a bulldozer blade) in the access channels to the harbour of Antwerp is thought to be responsible for periodical increases of suspended mud in the estuary. The sweepbeam pushes the mud from the access channels back to the river, the mud is thus not removed from the system, as is the case for conventional dredging methods. The effects of the sweepbeam as well as the spill of material during dredging and dumping on the mud concentration is not yet quantified.

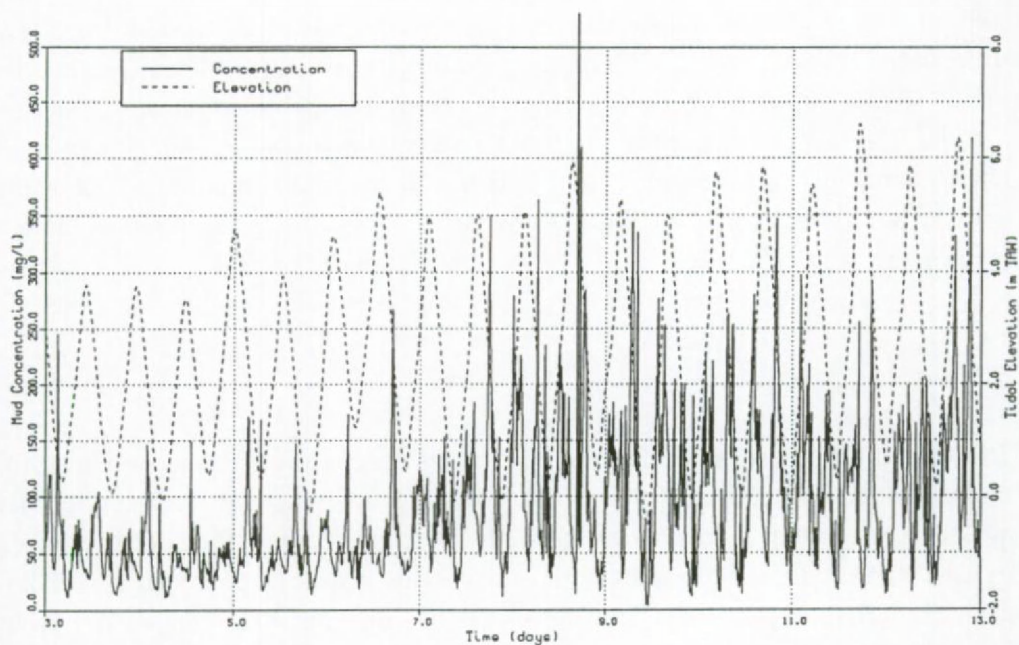


Figure 5.46: Mud concentration (0.5m above bottom) and tidal elevation, January '93, Prosperpolder.

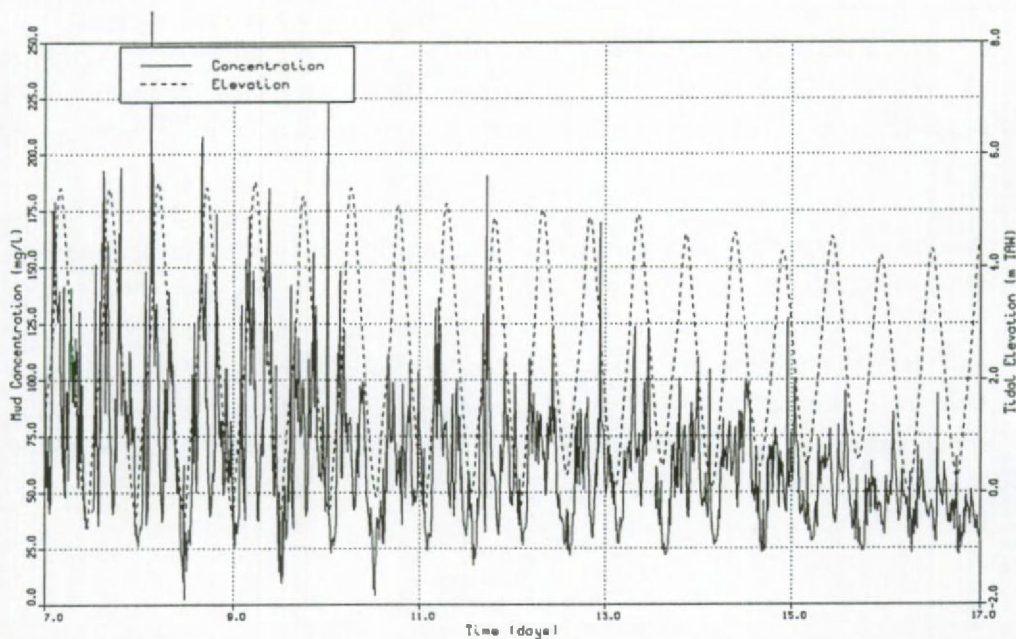


Figure 5.47: Mud concentration (0.5m above bottom) and tidal elevation, May '93, Prosperpolder.

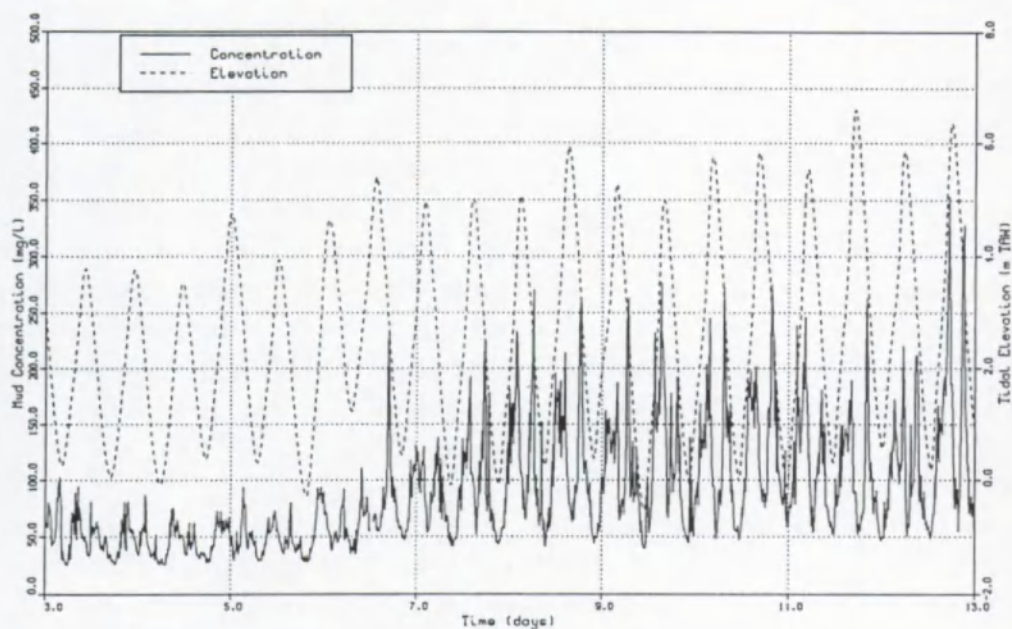


Figure 5.48: Mud concentration (1.5m above bottom) and tidal elevation, January '93, Prosperpolder.

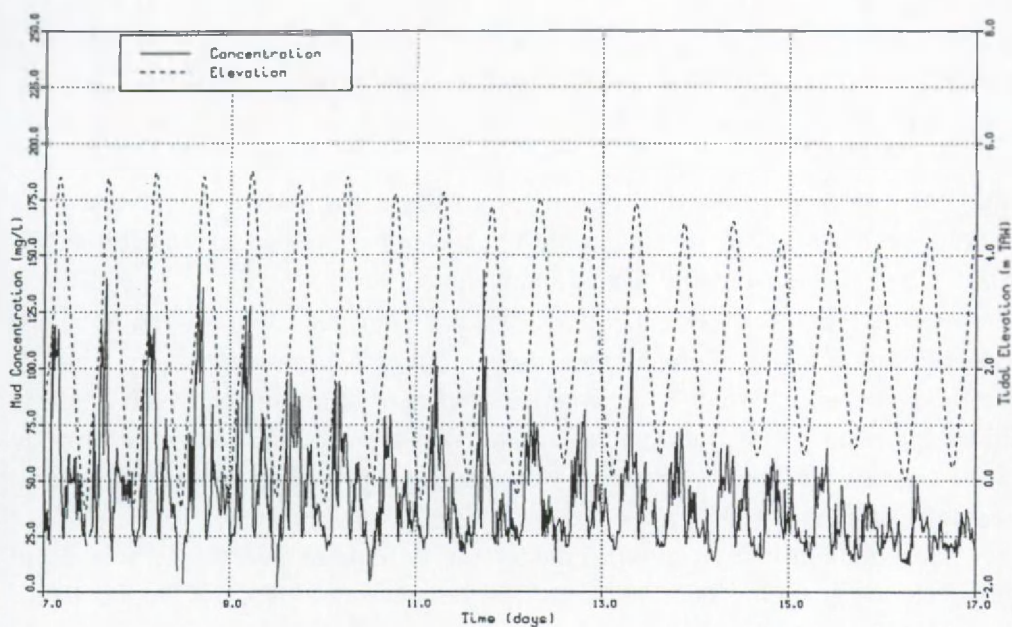


Figure 5.49: Mud concentration (1.5m above bottom) and tidal elevation, May '93, Prosperpolder.



## 5.7. Summary

In this chapter a review of the hydraulics and morphological characteristics of the Scheldt estuary has been presented. The Scheldt estuary is defined as a well-mixed to partially stratified estuary. The influence of stratification is highest in the Beneden Zeeschelde (between Antwerp and the Belgian-Dutch border). In this area measurements of velocity, salinity, mud concentration and temperature have been carried out. These measurements differed in duration, ranging from half a tide (ebb or flood) to more than one year and in 'intensity', from detailed vertical and horizontally distributed recordings of different quantities to single point measurements. The major conclusions can be summarized as follows:

### *'Drempel van Zandvliet'*

Two through tide measurements (one at neap and one at spring tide) in five points situated over the cross section at the 'Drempel van Zandvliet' has been described. The salinity stratification is highest at high water slack and reaches a maximum value of 2.8g/l during neap and 4g/l during spring tide. The influence of the stratification can be seen in the velocity profile. A downstream velocity component can be observed near the surface and an upstream one near the bottom. This results in a decrease of the velocity near the surface during flood and an increase of the velocity near the surface during ebb. The velocity near the bottom is increased during flood and decreased during ebb. The distorted velocity profile and the higher peak velocities during flood explain the higher re-suspension of mud during flood.

The lateral salinity gradient, which is due to the bathymetrical conditions (submerged dyke and shallow area) has a maximum at minimum salinity and is about 1.5g/l during neap and 2.5g/l during spring tide.

The maximum mud concentrations are higher during flood than during ebb. The concentration is lower during increasing than during decreasing velocity.

The ratio of depth averaged maximum to minimum mud concentration is about 2.5 during neap and 3.5 during spring tide. These vertical gradients are mainly due to transport of mud from up- or downstream and in a lesser extend to local erosion or settling.

The mud concentration is more homogenous distributed over the water depth during ebb than during flood. The surface concentration is small during flood. The vertical salinity gradient is higher during flood than during ebb, resulting in an inhibition of the vertical mixing due to a reduction of turbulence.

### *'Plaat van Lillo' and 'Vaarwater boven Bath'*

The vertical and lateral averaged mud concentration at two cross sections, calculated from two through tide measurements has been presented. The mud concentrations averaged over the vertical and the cross section are highest at the most upstream cross section ('Plaat van Lillo') and lowest at the most downstream cross section ('Vaarwater boven Bath'). At the 'Drempel van Zandvliet' the concentrations are in between the two above mentioned cross sections.

### *Access channel Zandvliet-Berendrecht*

At the entrance of the access channel two half-tide measurements, using a BBADCP, have been carried out. The flow entering or leaving the access channel is dominated by density differences which occur between the river and the entrance channel and in the vertical plane. As a consequence the flow is during almost all the tidal cycles divided in two vertical layers (in- and outgoing).

### *Prosperpolder*

The long term measurements at the tidal station of Prosperpolder have shown that a minimum in salinity is occurring 5 days after a maximum in fresh water discharge. The main factor influencing the difference between maximum and minimum salinity during a tidal cycle is the tidal range. The seasonal variations (fresh water discharge) have only a minor influence on this difference. The net values of salinity however are strongly affected by the fresh water discharge, varying between 16g/l at the end of summer to 1.5g/l in winter.

Temperature has a maximum at about low water and a minimum at about high water. The main factor influencing the difference between maximum and minimum temperature during a tidal cycle is the seasonal variation. This difference is highest during winter (1.9 °C) and lowest during summer (1.5 °C). Variations in tidal range have only a minor influence on the difference.

The long term mud concentration show variations on different time scales, i.e. tidal, neap-spring tidal and seasonal variations. Furthermore high frequency variations have been observed in the signals.

The mud concentration during flood is generally higher than during ebb. The ratio of flood to ebb concentration is not depending on the season but on the tidal amplitude. The ratio varies between 1 (neap tide) and 1.7 (spring tide). Peak concentrations are higher in winter during flood than during ebb. In summer the opposite is observed. An explanation for this phenomenon is found in the shift of the turbidity maximum under influence of the river run-off.

The concentration of mud averaged over a tidal cycle is 1.3 to 1.7 times greater during a spring tide than during a neap tide depending on the seasons. The ratio between spring to neap tide concentration is higher during winter than during summer.

The mud concentration during winter is about the double of the concentration during summer. Different explanations have been suggested, i.e. shift of the turbidity maximum as a function of the freshwater discharge, and a higher sediment load during winter due to a decreased biological activity and a higher erosion. With the given data set it was not possible to give an answer as to which of the processes is relatively more important.

Current velocity, sediment concentration, salinity and temperature are varying clearly as a function of tide. Mud concentration, salinity and of course temperature show furthermore a strong correlation with the seasons. The influence of the season is directly correlated to the climatological cycle, i.e. variations of the solar energy input. Their influence on mud concentration and salinity is however indirect through variations in biological activity, fresh water run off and land erosion. The quantification of these variations and the establishment of general rules and correlations remains the main goal of field measurements. This is a challenging task and will always be open to improvement as more observations and better measurement techniques become available.

'There is no substitute for long term monitoring if long term siltation prediction are required but much can be learned from detailed observations during a single tide' (Burt and Stevenson, 1986).



## CHAPTER 6

### 2D MODELLING OF COHESIVE SEDIMENT TRANSPORT

#### 6.1. Cohesive Sediment Processes

Transport of mud is determined by the settling of mud particles under influence of gravity and by erosion and sedimentation due to the local bottom shear stress. The complete process of erosion, transport, sedimentation and consolidation is a complex due to the cohesive characteristics of mud. A detailed description of these processes has been given by Mehta et al. (1989). These authors emphasize the basic processes (flocculation, deposition, resuspension, erosion and consolidation) and the practical implementation in numerical models. Teeter (1992) describes the parameters which characterise cohesive sediments, *i.e.* composition and amount of clay minerals, other anorganic and organic substances, density temperature and pH, and gives an overview of the laboratory experiments which allow the determination of these parameters.

In the following the basic processes are shortly described. § 6.2 and 6.3 are devoted to the description and the validation of the 2D horizontal mud transport model TRASIL. The validation has been carried out using laboratory experimental data. In § 6.4 the mud transport model of a part of the Scheldt estuary will be presented. This model makes use of the flow field, calculated with the 2D depth averaged hydrodynamic model FINEL. The hydrodynamic model and some of the results will be briefly presented. Finally, in § 6.5 some general conclusions are given.

### 6.1.1. *Bottom shear stress*

Currents and waves are exerting a friction force on the bottom. A general description of the velocity distribution over the depth is given by the von Karman-Prandtl relation (see e.g. van Rijn, 1989):

$$u = \frac{u_*}{\kappa} \ln \frac{z}{z_0} \quad (6.1)$$

where the friction velocity  $u_* = (\tau_b/\rho)^{0.5}$ ,  $\tau_b$  is the bottom friction,  $\kappa$  the von Karman constant,  $z_0$  the zero velocity level and  $\rho$  the density of the water. For rough walls  $z_0$  is given by  $k/30$  with  $k$  the bed roughness (given e.g. by the dimension of the sand grains). For smooth flow the roughness length  $z_0$  is equal to  $0.11(\nu/u_*) + k/30$ ,  $\nu$  is the viscosity of the fluid.

The bed shear stress is defined as:

$$\tau_b = \rho u_*^2 \quad (6.2)$$

The bottom shear stress in case of a depth averaged velocity can be written as:

$$\tau_b = \rho k U^2 \quad (6.3)$$

where  $k$  is the friction coefficient and  $U$  the depth averaged velocity.

The friction factor  $k$  can be written as

$$k = \frac{g}{C_h^2} = g \frac{n^2}{h^{1/3}} \quad (6.4)$$

with  $g$  the acceleration due to gravity,  $C_h$  the Chézy coefficient,  $n$  the Manning coefficient,  $f$  the Darcy-Weissbach coefficient and  $h$  the water depth.

### 6.1.2. *Settling of mud particles*

The settling of mud is described by the movements of a particle under influence of gravity, of viscous shear stresses (turbulence) and of interaction between particles. Fall or settling velocity is generally defined in case of quiescent water in laboratory measurements and with certain salinity concentrations (the formation of aggregates by other processes is thus not taken into account) and is represented by the median settling velocity  $w_{50}$ . The values are an order of magnitude smaller than in situ measurements. Marine as well as riverine mud can have a wide range of fall velocities (from order  $10^{-4}$  to some mm/s). These variations are a function of the

mud concentration, the mud composition, the physico-chemical properties of the water and the velocity field. Dyer (1986) has shown that fall velocities are varying strongly between different estuaries, which is the result of differences in mud and fluid composition. The mud particles are usually small ( $< 63 \mu\text{m}$ ) and the fall velocity of these particles is very low. The formation and break up of flocs is substantially influencing the magnitude of the fall velocity and is thus an important mechanism responsible for the distribution of cohesive sediments in suspension as well as on the bed.

Two conditions have to be fulfilled for the formation and the destruction of mud flocs or aggregates, *i.e.* collision between the particles and cohesive properties. Cohesion consist of the attraction between the clay particles. The cohesive forces are strong at small distances and decrease with increasing distance. Particles will form aggregates if the repulsive forces generated by the cation clouds on the clay particles are smaller than the cohesive forces. The strength of the repulsive forces are determined by the clay mineralogy and by the amount and the type of cations present in the water. Organic matter is a substantial constituent for flocculation (van Leussen, 1994). The formation of flocs or aggregates is only possible if collision of particles occur. Collision of particles are the result of the Brownian motion of the suspended particles, of the vertical shear of the water and of differential settling velocities of the particles (Delo and Burt, 1986). Krone (1962) found, under laboratory circumstances, that at low concentrations ( $< 0.3\text{g/l}$ ) particle interactions are very low and that the fall velocity can be defined as being independent of the concentration and thus constant. For concentration in the range of 5 to  $10\text{g/l}$ , the particles are undergoing interactions and one can generally say that the fall velocity is increasing with increasing concentration. Above this limit hindered settling occurs and the fall velocity is decreasing. Hindered settling is a consequence of the formation of a continuous structure in the sediment. Large aggregates can however also be formed at low concentrations. The effect of flocculation in nature may be expected at much lower suspended sediment concentration as in laboratory due to differences in time scale (van Leussen, 1994). This is probably the reason why in estuaries with low mud concentrations, such as the Scheldt estuary, significant deposition of mud is found. Measurements instruments are now available to determine the in situ settling velocities of mud particles (Eisma et al., 1994).

The size of the flocs formed by collision is limited by the size of the dissipating eddies in the turbulent flow, known as the Kolmogorov microscales of turbulence. Van Leussen (1994) showed that these microscales of turbulence are varying during a tidal cycle between  $200\mu\text{m}$  and  $1\text{mm}$  in the Ems estuary. Van Leussen



compared the turbulence microscales with the floc sizes and found that during high current velocities the floc sizes are in the range of the microscales. At slack tide the microscale as well as the floccsize strongly increases and the large aggregates settle down. The Kolmogorov microscales of turbulence are a good reference for the largest size of macroflocs.

### 6.1.3. *Deposition*

Deposition is the process by which sediment particles are attached to the bottom. Deposition will only occur if the bottom stress is lower than a certain critical shear stress value, known as the critical shear stress for deposition. A continuous settling of mud particles will thus not necessarily lead to sedimentation.

Krone (1962) showed that the probability of mud particles to be attached on the bottom varies linearly between 0 and 1 if the bottom stress reduces from a critical value to zero. He derived a general equation relating the suspended sediment concentration to the time from the start of the experiment:

$$D = \frac{dm}{dt} = wC(\tau_{cd} - \tau_b) / \tau_{cd} \quad (6.5)$$

where  $D$  is the source term for deposition [ $\text{kg}/\text{m}^2\text{s}$ ],  $C$  the mud concentration [ $\text{kg}/\text{m}^3$ ],  $w$  the fall velocity [ $\text{m}/\text{s}$ ],  $t$  time [ $\text{s}$ ],  $m$  the mass of suspended sediments per unit bed area over the depth of the flow [ $\text{kg}/\text{m}^2$ ] and  $\tau_{cd}$  the critical shear stress for deposition [ $\text{Pa}$ ]. When the bottom stress is lower than this critical value deposition will occur. The above mentioned equation essentially represents the rate of deposition in case of low suspended sediment concentration and thus no aggregation. Aggregation is very often indirectly considered as a function of concentration, see e.g. Mehta (1984). Recently relationships between settling velocity, concentration and bottom shear stress have been proposed by Le Hir et al. (1993) and van Leussen (1994). More complicated laws for deposition exist, however their use in tidal conditions did not show a significant improvement compared to the Krone formula (Teisson, 1994).

The value of  $\tau_{cd}$  is a function of the composition of the sediment under consideration and can be determined from e.g. a deposition test in an annular flume, see MAST (1993). Delo and Ockenden (1992) are giving an order of magnitude of 0.06Pa to 0.10Pa. For the Scheldt estuary values of 0.07Pa (HR, 1980) and 0.2Pa (Mulder and Udink, 1990) have been cited.

#### 6.1.4. Erosion

Erosion of mud is defined as the sum of the processes responsible for the resuspension and transport of particles attached to the bed (Teeter, 1992). Once brought into suspension, the mud particles can be transported during a long time and over a big distance due to their small fall velocities. The erosion of cohesive material is dependent on the cohesive links between the particles and on the alterations occurring in the sediment structures. Bottom stress is the main hydrodynamic factor which controls the resuspension of mud particles. The resistance of the particles to resuspension is a function of the sediment composition, the characteristics of the pore water (salinity, Sodium Adsorption Ratio, pH and temperature), the way the sediment has been deposited and the consolidation. Mehta et al. (1989) distinguishes in general between three types of erosion:

- Surface erosion, mud particle are successively brought in suspension.
- Mass erosion, big parts of the bottom are teared away due to high bottom stresses. This is a typical phenomenon of tidal areas with high current velocities.
- Re-entrainment of a stationary high density mud suspension, with quick resuspension of mud over the water column.

The rate at which mud is eroded is a function of the bottom stress and the critical bottom stress for erosion. Generally it is accepted that the rate of erosion is independent on the sediment concentration in the eroding current (Odd and Owen, 1972). The rate of erosion is defined as the mass of sediment eroded per unit area and per unit time. The erosion rate is zero until the bottom stress exceeds a certain threshold value, called the critical shear stress for erosion. Various formulations of the erosion rate have been proposed.

Partheniades (1962) and Ariathurai and Arulanandan (1978) used a formulation with a linear relation between the excess shear stress and the rate of erosion:

$$E = M(\tau_b - \tau_{ce}) / \tau_{ce} \quad (6.6)$$

where  $M$  is the erosion constant [ $\text{kg/m}^2\text{s}$ ],  $E$  the erosion rate ( $\text{kg/m}^2\text{s}$ ) and  $\tau_{ce}$  the critical shear stress for erosion, in the original model  $n = 1$ .

Later research indicated rather a formulation in which  $M/\tau_{ce}$  is a constant, see Mehta and Partheniades (1973) and Delo (1988):

$$E = M'(\tau_b - \tau_{ce}) \quad (6.7)$$

with  $M'$  the erosion constant ( $\text{kg/Ns}$ ). Both formulation are found to be adequate

for dense, consolidated beds.

Based on experiments Parchure and Mehta (1985) derived the following empirical relationship for the erosion rate  $E$  for soft, freshly deposited sediments:

$$E = \epsilon_0 \exp[\alpha(\tau_b - \tau_{ce})^{0.5}] \quad (6.8)$$

where  $\epsilon_0$  is an erosion constant ( $\text{kg/m}^2\text{s}$ ) and  $\alpha$  ( $\text{m/N}^{0.5}$ ).

Recently, research has been carried out to determine the erosive characteristics of non-homogenous sediment compositions (sand - mud mixtures), see Torfs (1994), Williamson (1994) and Chesher and Ockenden (1994). This work showed that sand content has a great effect on the erosion threshold, the rate of erosion and the bed consolidation. Biota are hindering the erosion of fine-grained cohesive sediments (Black, 1994). Paterson (1994) presents a review of a number of mechanisms of biogenic stabilisation, i.e. alteration of the flow field, network effects, animal burrow and extracellular polymeric substances. Alteration of the flow field occurs by a variety of processes such as reduction of the bed roughness due to covering with microbial mats and their secretions, increasing of the bed roughness due to bioturbation, elasticity of the bed and rheological changes due to microbiological secretions. At the microbial level organisms such as fungi, bacteria, cyanobacteria, algae and diatoms can form a dense network on the bed leading to an increase of the shear strength of the sediments. Animal burrows in the sediment can lead to a strengthening of the sediment bed. Extracellular polymeric substances play an important role in microbial ecology in a multitude of functions, among them the formation of a mucilage between diatoms. This increases the binding of the sediment and thus the erosive strength and results also in an enhanced deposition in intertidal mudflats.

#### 6.1.5. *Consolidation and bed structure*

Cohesive sediments can be considered to exist in four different states (Delo and Burt, 1986): suspended sediments, fluid mud, partially consolidated bed and settled bed. The processes responsible for the formation of and the processes acting on the suspended sediment state are deposition, erosion and flocculation and have been described in the previous paragraphs. Consolidation of a cohesive bed is defined as the gradual expulsion of the interstitial water resulting in an increase of the bed density and the bed strength with time. Consolidation is important because it changes the density structure of the sediments and thus also the erosive characteristics. It can be determined in the field by measuring the vertical



density profile at different time interval or under laboratory conditions (MAST, 1993).

#### **6.1.6. *Numerical modelling of cohesive sediment transport***

Most of the research efforts to determine erosion and deposition characteristics of cohesive sediments have been carried out under laboratory conditions. The advantage of laboratory experiments is that mutual interactions between the various factors affecting the processes can be eliminated or controlled. Most of the processes are complex and are depending on each other. The setting up of a numerical model for a real case (e.g. an estuary) would imply the incorporation and interactions of the hydrodynamic (current velocities, water levels, fresh water discharge, density induced currents, turbulence fields) as well as the morphological conditions (distribution and composition of the sediments, erosion and deposition as a function of sediment composition, transport, consolidation, biological processes). Up to know this has not been done. Reasons for this are due to the complexity and the limited knowledge of the physical background of the processes, the various time scales which apply (resulting in costly computer simulations) and also to the lack of field measurements. A review of the state of the art cohesive transport models has been given by Teisson (1994).

As a part of the MAST G8 Coastal Morphodynamics research programme an inter-comparison exercise involving four cohesive sediment transport models (among which the TRASIL model) versus a common database has been set up (Hamm et al. 1994). The TRASIL model results are described below. The dataset consists of measurements of velocity, suspended sediment concentration and bed structure. The mud used in the laboratory experiments was taken from the river Garonne and had been treated chemically in order to eliminate the organic matter. The measurements have been carried out in a racetrack flume (Viguier et al. 1994) under different hydrodynamic conditions (uniform flow, alternating flow) and with different consolidation grades of the mud bed. The conclusions of the study are that the available erosion and deposition laws seem to adequately model the basic processes in uniform and unsteady flows. Quantitative differences between the models indicate that the density structure of the bed and the resuspension of soft material having previously settled are the key parameters to be considered. The above mentioned intercomparison exercise underlined that modelling the transport of cohesive sediments using an extended set of laboratory data and a uniform bed sediment composition suffers from a good description of some aspects of the

physics. In an estuary the sediment composition is not uniform, varying from sand to mud (with different grain sizes, mineralogical compositions, organic contents etc.) and the bed structure of the cohesive (or the mixture of cohesive and non cohesive) sediments is in general poorly known. Modelling mud transport in an estuary can thus only be approximative since a lot of simplifications (due to the limited knowledge about the physics and the physical environment) have to be introduced. These models should therefore not be used as the ultimate tool to predict the behaviour of mud but rather as an instrument for a better understanding of some of the aspects of mud transport.

### 6.2. The 2D Particle Tracking Model TRASIL

The TRASIL model (Praagman, 1986; Sas, 1989) solves in a Lagrangian way the 2D depth averaged advection-diffusion equation in the following form:

$$\frac{dC}{dt} = K_h \frac{\partial^2 C}{\partial x^2} + K_h \frac{\partial^2 C}{\partial y^2} + \frac{E + D}{h} \tag{6.9}$$

where  $C$  is the concentration,  $x$  and  $y$  the horizontal space coordinates,  $h$  the water depth and  $D$  and  $E$  the sink and source terms for deposition and erosion respectively, they are described using equations (6.5) and (6.6)-(6.8). The advective part of the transport equation is the cause of many numerical problems. Lower order up-stream methods give rise to large numerical diffusion as has been briefly discussed in § 2.7. Lagrangian particle methods are free of numerical diffusion but have a disadvantage if the results are needed on an Eulerian grid. Several smoothing effects are present due to the fact that the concentrations are given at the squares and not at the nodal points of the grid.

It is assumed that the velocity vector ( $u$ ,  $v$ ) is given at nodal points of the domain of interest. The structure of the domain can either be a finite element or a finite difference type of grid. Using these discrete velocity nodal points, the velocity vector in each internal point is calculated by interpolation. An initial concentration field is created by covering the whole domain of interest with small volumes and by assigning to each the representative amount of species. Each square keeps its identity as long as it remains within the domain. Once the field of squares has been created, the transport of each of these volumes is computed by numerically solving the ordinary differential equations:

$$\frac{dx}{dt} = u(x, y, t), \quad x(t_0) = x_0 \tag{6.10}$$

$$\frac{dy}{dt} = v(x, y, t), \quad y(t_0) = y_0 \quad (6.11)$$

where  $(x_0, y_0)$  is the position of the centre of the square at time  $t = t_0$ . The numerical solution of equations (6.10) and (6.11) is obtained by using the classical fourth order Runge-Kutta method. During the computational process the right hand side functions  $u$  and  $v$  are being adjusted each sub step, using interpolation values of the velocity field. Since the fourth order Runge-Kutta method has very good amplification and phase error properties the advection of the squares will almost be optimal and positiveness and mass conservation are guaranteed. At the inflow boundary new particles with a well defined concentration and volume are entering the model. The particles which have been transported outside the domain are deleted. Erosion and sedimentation change the amount of mud in the particles.

In the original version of TRASIL, which we had at our disposal, diffusion was not taken into account. The intercomparison exercise, described in § 6.4.3. showed that this term cannot be neglected in the Scheldt estuary. A diffusion model has therefore been implemented. Turbulent diffusion is generally simulated by a so-called random-walk method, see e.g. Hunter (1987), Mead and Rodger (1988) and Wood et al. (1993). The random movement  $\Delta s$  of a particle during a time step  $\Delta t$  consists of components parallel and perpendicular to the mean tidal flow direction with an equal probability of stepping in each of the directions. In case of zero flow and with a sufficient number of particles this results in a mean displacement of all particles from the initial position of zero with a variance increasing linearly with the number of particles. The diffusion step can then be written as (Wood et al., 1993):

$$x_i(t+\Delta t) = 2(0.5 - R[0:1])\sqrt{6D_i\Delta t} \quad (6.12)$$

where  $D_i$  is the diffusive coefficient in each spatial direction,  $R[0:1]$  is a random number uniformly distributed between 0 and 1 and  $\Delta t$  is the time-step. The equation is scaled in such a way to yield a random number uniformly distributed between -1 and +1. The effective diffusivity  $D$  is defined as:

$$D = \Delta s^2 / (2 \Delta t) \quad (6.13)$$

In the model the diffusion coefficient is specified which is equivalent to specifying a turbulent displacement. If particles are hitting the coastline due to the computed turbulent displacement, then the diffusion step will not be taken into account. This results in a reduced diffusivity along the banks of the river.



The time-step has to be restricted in such a way that a particle cannot travel further than one grid spacing in a single time-step. The constraint on the time-step can thus be formulated as follows:

$$\Delta t \leq \Delta x / V \quad (6.14)$$

where  $\Delta t$  is the time-step,  $\Delta x$  the grid size and  $V$  the current velocity. This restriction is valid for rectangular grids, in case of triangular grids the time-step has to be taken smaller. Once the new position of the particles has been calculated, erosion and sedimentation are determined. If this restriction in time step is not accounted for, which is equivalent to a poor approximation of  $dx$  and  $dy$  in equations (6.10-11) then this can result in numerical diffusion.

## 6.3. Validation Of TRASIL Using Laboratory Data

### 6.3.1. *Introduction*

As a part of the validation of the TRASIL model the mud transport, erosion and deposition of a laboratory model test has been simulated. The data have been made available by SOGREAH in the framework of the EC MAST G8 Coastal Morphodynamic Research Project (Viguier et al., 1994). The aim of the laboratory model was to provide a data set for validation of numerical mud transport models. The experiments have been carried out in a racetrack flume of 1m width, 0.4m depth and 84m total length with two straight sections of 30m and two bends of 180° and 12m length. The water level remained constant during each of the experiments. The currents were generated by an Archimedean screw situated in the central part of one straight section. The measurements of velocity and turbidity have been done at the centre line of the flume at the other straight section. The mud used in the flume experiments has been taken from the river Garonne and has been treated chemically to eliminate organic matter. The coarser sediment particles ( $> 100\mu\text{m}$ ) have been filtered out by sieving. Two different series of experiments have been carried out by SOGREAH. The first one consist of erosion experiments under step-wise increasing uniform current. The currents are such that the critical shear stress for deposition is always lower than the bed shear stress. For the second set of experiments the current is alternating and mud can be eroded or deposited.

For the eight uniform flow tests an amount of roughly 800kg of mud was introduced into the flume and a deposited bed was build up by putting the mud into

suspension and then allowing it to consolidate naturally for a variable period ranging from 0.25 days to 7.6 days corresponding to a mean dry density of 98 to 309kg/m³ and a thickness of 97.2 to 32.4mm, see Tables 6.1 and 6.2. The current velocity was increased in successive stages from 25 to 85cm/s, with each stage lasting for at least 40 minutes.

The second series of experiments consisted of four tests with alternating current regimes and consolidation periods ranging from 0.7 to 7.8 days, mean dry densities from 193 to 310kg/m³ and thicknesses from 40 to 25mm, see Table 6.2.

This dataset has been used by various models (among which TRASIL) in an inter-comparison exercise. The results have been published (see Hamm et al., 1994). In the following only the results of the TRASIL model will be presented.

Table 6.1    Uniform flow tests: Initial properties of the mud layer (\* = interpolated value).

Test	2	3	4	5	6	7	A1	A2
Consolidation time (days)	4.9	4.0	1.75	0.8	7.6	0.25	2.9	2.9
Mean dry density (kg/m³)	291	280	238	200	309	98	259*	259*
Thickness of mud layer (mm)	32.7	34.0	40.0	47.6	32.4	97.2	36.8*	36.8*

Table 6.2    Alternating flow tests: Initial properties of the mud layer.

Test	1	2	3	4
Consolidation time (days)	4.6	2.6	0.75	7.8
Mean dry density (kg/m³)	287	259	193	310
Thickness of mud layer (mm)	29.0	30.5	40.0	25.0

### 6.3.2.        Numerical model setup

The model used for this study is the 2D horizontal mud transport model TRASIL. The model has been used without diffusion. The test reach of the racetrack flume (i.e. 30m) has been discretised. In order to simulate the circular nature of the flume the concentration at the outgoing boundary has been implemented as boundary condition for the ingoing open boundary. By doing so a small time lag will be introduced in the calculations. The bottom shear stress is calculated using the following formula:

$$\tau_b = \rho g (u/C_h)^2 \tag{6.15}$$

where  $C_h$  is the Chézy coefficient and  $u$  the current velocity.  
The critical shear stress for erosion  $\tau_{ce}$  has been set equal to the yield stress  $\tau_y$ .

This is only partly correct, a non-linear relationship between  $\tau_y$  and  $\tau_{ce}$  has been proposed by Toorman (1994). The yield stress has been expressed as a function of the concentration using a power law:

$$\tau_y = 7.9547 \cdot 10^{-10} \rho^{3.636} \tag{6.16}$$

where  $\rho$  is the dry density of the mud. Erosion was calculated using equations (6.6), (6.7) and (6.8). In the figures and the following text eq. (6.6) is referred as erosion model 1, eq. (6.7) as erosion model 2 and eq. (6.8) as erosion model 3. The deposition rate has been calculated using the formula of Krone (1962), see equation (6.5). The critical shear stress for deposition was set to 0.05Pa. The settling velocity has been taken as constant and equals 0.1mm/s. The description of the bed is a key parameter for the correct simulation of the mud transport. The measurements of the bed density have been carried out in settling columns, the bottom and the surface densities have however not been measured (Viguiet et al., 1994). The density profile was estimated from the results of settling columns tests. Based on the measured values the following relationship between  $\rho/\rho_{mean}$  and  $H/H_0$  ( $\rho$  is the dry density,  $\rho_{mean}$  is the mean dry density of the deposit,  $H_0$  is the initial and  $H$  the eroded bed thickness) is proposed:

$$H/H_0 = 0.355 \rho/\rho_{mean} + 1.125 \tag{6.17}$$

The mean dry density  $\rho_{mean}$  of the sediments has been given in the Viguiet et al. (1994), see Table 6.1 (uniform flow case) and Table 6.2 (alternating flow case). The thickness of the mud layer has been calculated based on the amount of mud in the flume (i.e. 800kg) and on the mean dry density  $\rho_{mean}$ .

Table 6.3      Uniform flow: Density profile of the mud bed for the different test cases. Depth (mm) and dry density (kg/m³), from Pathirana (1994).

Test 2	Test 3	Test 4	Test 5	Test 6	Test 7	A 1	A 2
0.0 174.6	0.0 172.0	0.0 142.8	0.0 100.0	0.0 185.4	0.0 95.0	0.0 160.0	0.0 162.0
3.5 230.0	3.7 252.0	4.0 200.0	4.0 110.0	3.0 247.2	4.5 100.0	4.0 230.0	3.5 232.0
7.0 280.0	7.4 280.0	8.0 238.0	8.0 145.0	6.0 296.6	9.0 120.0	8.0 258.0	7.0 270.0
10.5 320.0	11.1 300.0	12.0 251.3	12.0 175.0	9.0 324.4	13.5 140.0	12.0 298.0	10.5 318.6
14.0 442.3	14.8 380.0	16.0 331.7	16.0 205.0	12.0 432.6	18.0 150.0	16.0 380.0	14.0 410.4
17.5 506.3	18.5 487.2	18.0 414.1	20.0 225.0	15.0 537.6	22.5 175.0	20.0 435.0	17.5 469.8
			24.0 240.0		27.0 190.0		
			28.0 250.0		31.5 215.0		
			32.0 265.0		36.0 230.0		
			36.0 270.0		40.5 250.0		
			40.0 290.0		45.0 260.0		
			> 320.0		> 300.0		

Relationship (6.17) gave poor results for the uniform flow case, therefore the discrete density profile proposed by Pathirana (1994) have been used, Table 6.3. and 6.2. Equation (6.17) has been used for the alternating flow experiments.



6.3.3. Erosion tests under uniform currents

Numerical results of four tests (i.e. 2, 6, 7 and A1) are presented in Figure 6.1 and 6.4-6. These four tests are giving an overview of the experiments, as they cover the range from low consolidation (test 7, 0.25 days) to high consolidation time (test 6, 7.6 days). Test 2 has an intermediate consolidation time (4.9 days), see Table 6.1. The (standard) parameter values used for the simulations are given in Table 6.4. These values correspond with the ones proposed by Pathirana (1994), except that he used a Chézy coefficient of 69 instead of 80.

Table 6.4 Standard parameter values, uniform flow experiments.

Chézy	$\tau_{cs}$	erosion model 1 (eq. 6.6)	erosion model 2 (eq. 6.7)	erosion model 3 (eq. 6.8)
80	eq. 6.14	$M = 0.0025 \text{ kg/m}^2\text{s}$	$M' = 0.009 \text{ g/Ns}$	$\sigma = 14.0 \text{ mN}^{0.5}$ $\epsilon_0 = 0.01 \text{ g/m}^2\text{s}$

The figures indicate that the correspondence between measurements and numerical results is better in the experiments with low to medium consolidated mud beds (test 2, 7 and A1). The numerical results of test 6 show large discrepancies. This is due to the discretisation of the density structure of the bed. The measurements indicate that with increasing current velocity the sediment concentration in the flume is increasing exponentially, whereas in the simulation an almost linear increase is found. It seems that especially with 'old' mud layers the description of the bed is one of the important parameters.

The results of erosion models 2 and 3 are qualitatively similar, they give better results for beds with relative low density (test 7, Figure 6.5), whereas erosion model 1 scores a little better on more consolidated mud beds (Figures 6.2-3). These findings are not in complete agreement with Pathirana (1994), he found similar behaviour of models 1 and 2 which are more appropriate for dense beds. Reasons for these differences are not yet clear.

In order to investigate the sensitivity of some parameters of the model additional runs have been carried out with the uniform flow test 2. Variations of the erosion constant (M and M') have only a small influence on the results, see Figures 6.2 and 6.3. They determine the course of concentration with time but have no influence on the (final) asymptotic concentration. The knowledge of the bed roughness is important. A Chézy coefficient of 69 as used by Pathirana (1994) gives to large values of mud concentration.

6.3.4.            *Erosion and deposition tests under alternating currents*

The unsteady flow cases have been simulated using the bed density relationship (6.17). During the experiments erosion and deposition alternate. This results in a deposition of fresh mud at slack waters. These slack water deposits have a low critical shear stress for erosion and are quickly resuspended with increasing flow velocity. The erosion of fresh mud deposits is calculated using erosion model 3 (eq. 6.8), erosion model 1 (eq. 6.6) is used for the consolidated mud layers. The fresh mud depositions are not allowed to consolidate. The parameter values used for the simulation are presented in Table 6.5.

The results of test cases 1, 3 and 4 are presented in Figures 6.7 to 6.9. The mud in test case 1 has an intermediate (4.6 days), in test 3 a short (0.75 days) and in test 4 a long consolidation time (7.8 days). The comparison between observations and simulation results indicate that the discrepancies start to become larger from the third tide on ( $\pm 400$  minutes). This clearly shows that the discretisation of the bed is not appropriate. Nevertheless the differences which have been found between model results and measurements, one can say that the model results appear to represent the basic physics adequately.

Table 6.5      Standard parameter values, alternating flow experiments.

Chézy	$\tau_{ce}$	erosion model 1 (eq. 6.6)	erosion model 3 (eq. 6.8)	$\tau_{cd}$	fall velocity	bed model
80	eq. 6.14	$M = 0.003\text{kg/m}^2\text{s}$	$\sigma = 14.0\text{mN}^{-0.5}$ $\epsilon_0 = 0.01\text{g/m}^2\text{s}$	0.05Pa	0.3mm/s	eq. 6.17

6.3.5.            *Conclusions*

Two sets of simulations of laboratory experiments have been carried out using the 2D transport model TRASIL. In the first set of experiments the erosion of mud has been investigated under steady but step-wise increasing currents. The second set of experiments was under alternating currents, showing the effects of erosion, sedimentation and resuspension. From these applications the following general remarks can be formulated:

The bottom shear stress is the major acting force for deposition and erosion. A good knowledge of the bottom roughness is thus of primary importance. The critical shear stress for erosion is an important parameter. In the experiments this stress was calculated using the yield stress and the density of the bed.

Especially the description of the consolidated bed revealed to be a key parameter. The density values for the mud bed where obtained from column tests after 6 and 24 hours (Viguier et al, 1994). From these short consolidation tests extrapolations where done to longer time periods in order to obtain a bed density description. This is obviously not the good way to do it (see especially uniform test 6). In order to know how bed density varies as a function of time measurements after longer periods should be carried out. Another unknown is the density at the mud surface, Toorman (1994) proposed a value of 100g/l. From extrapolation much lower values are obtained.

The erosion constant and the erosion laws turned out to have only limited influence on the results. The erosion laws are so strong when the critical shear stress for erosion is far exceeded that the erosion reaches an asymptotic value for the erosion parameter values (uniform flow) and that the fresh deposits are completely eroded in all cases (alternating flow).

The fall velocity and the deposition flux appeared to be sensitive parameters.

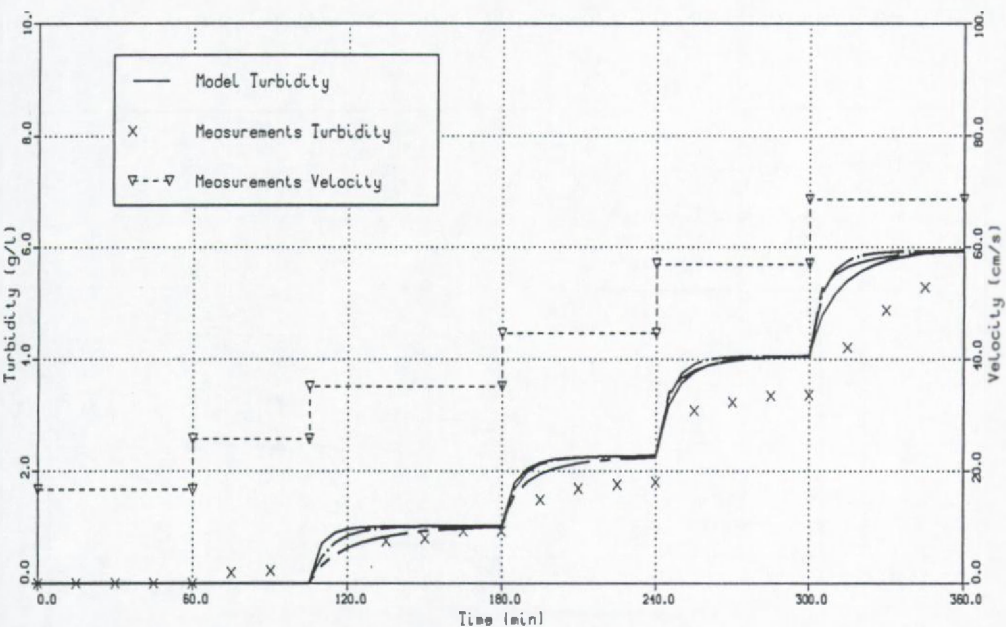


Figure 6.1: Uniform flow test 2, different erosion models (model 1: solid line, model 2: chain-dash, model 3: chain-dot).



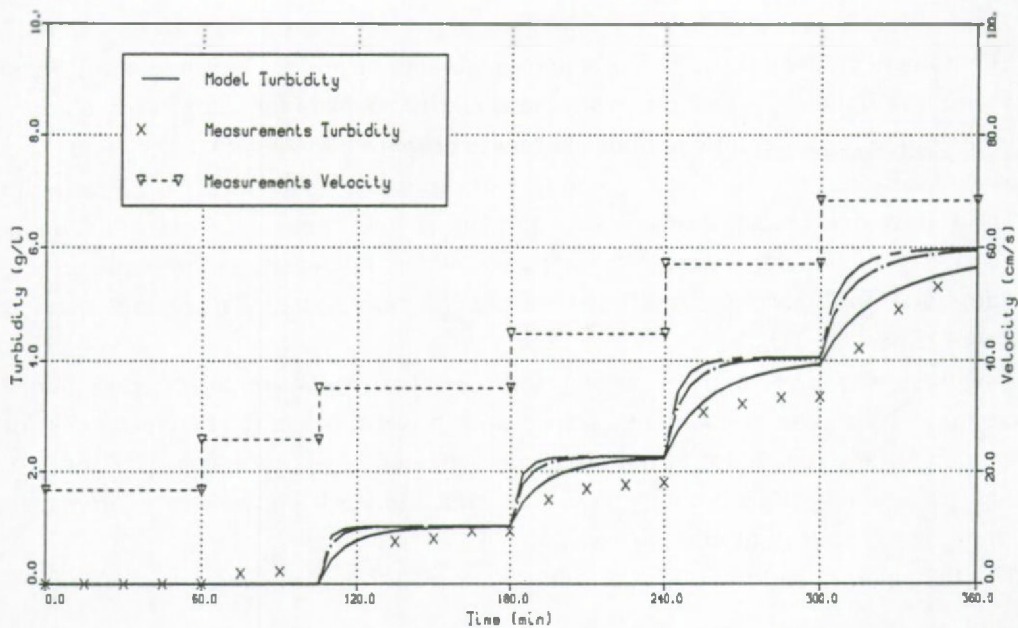


Figure 6.2: Uniform flow case 2, erosion model 1, different erosion rates  $M$  ( $0.0010 \text{ kg/m}^2\text{s}$ : solid line,  $0.0025 \text{ kg/m}^2\text{s}$ : chain-dot,  $0.0040 \text{ kg/m}^2\text{s}$ : chain-dash).

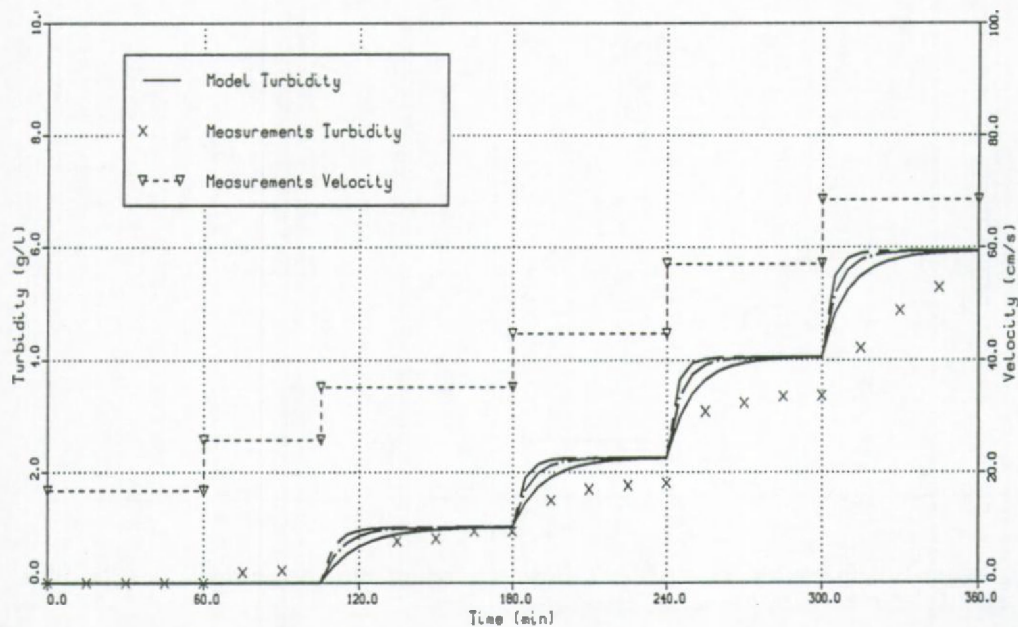


Figure 6.3: Uniform flow test 2, erosion model 2, different erosion rates  $M'$  ( $0.005 \text{ g/Ns}$ : solid line,  $0.009 \text{ g/Ns}$ : chain-dot,  $0.015 \text{ g/Ns}$ : chain-dash).

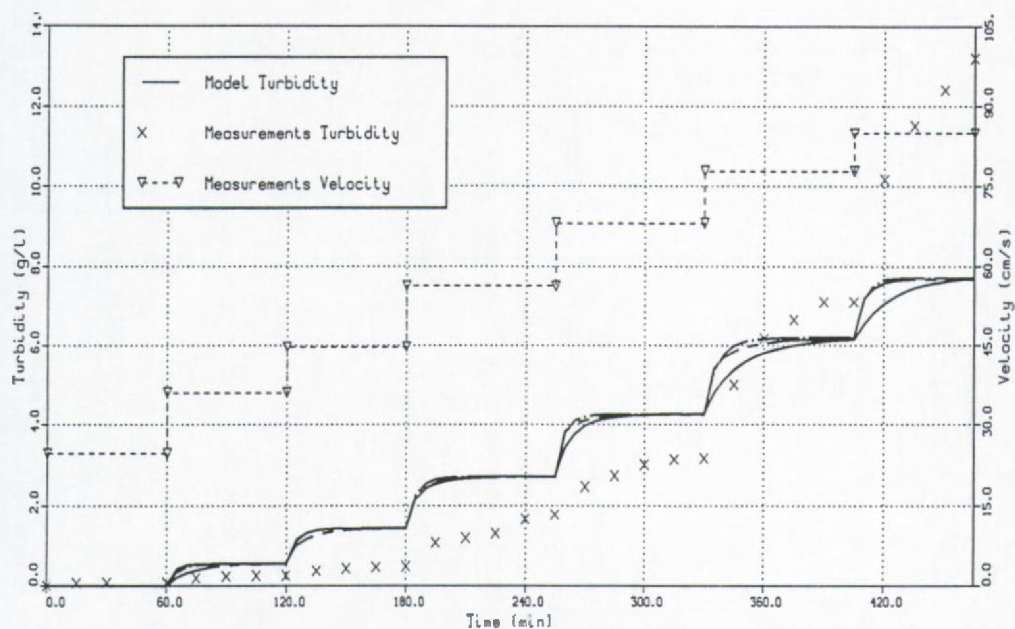


Figure 6.4: Uniform flow test 6, different erosion models (model 1: solid line, model 2: chain-dot, model 3: chain-dash).

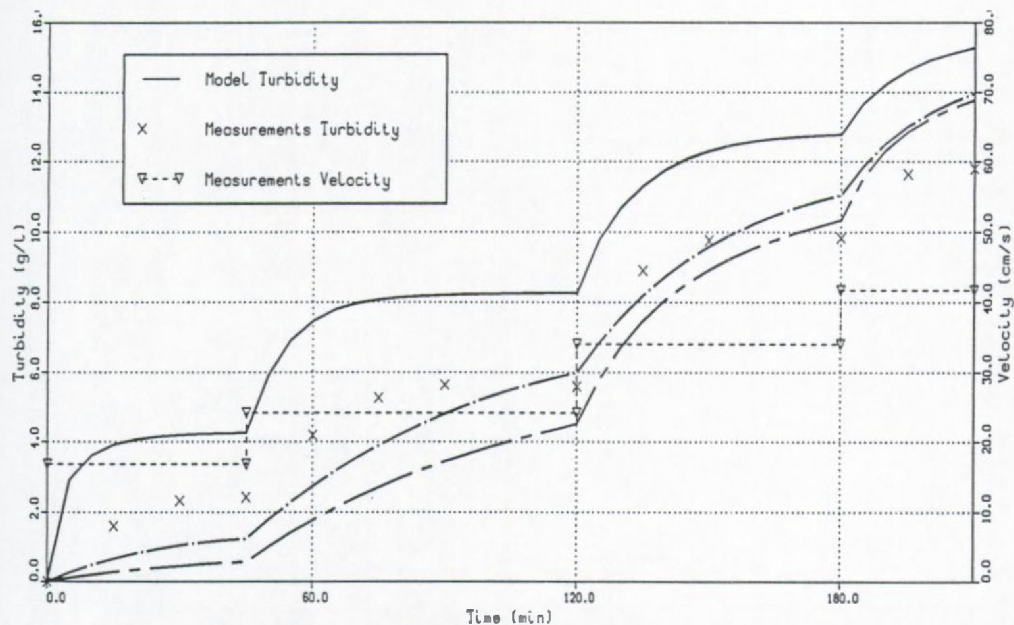


Figure 6.5: Uniform flow test 7, different erosion models (model 1: solid line, model 2: chain-dot, model 3: chain-dash).

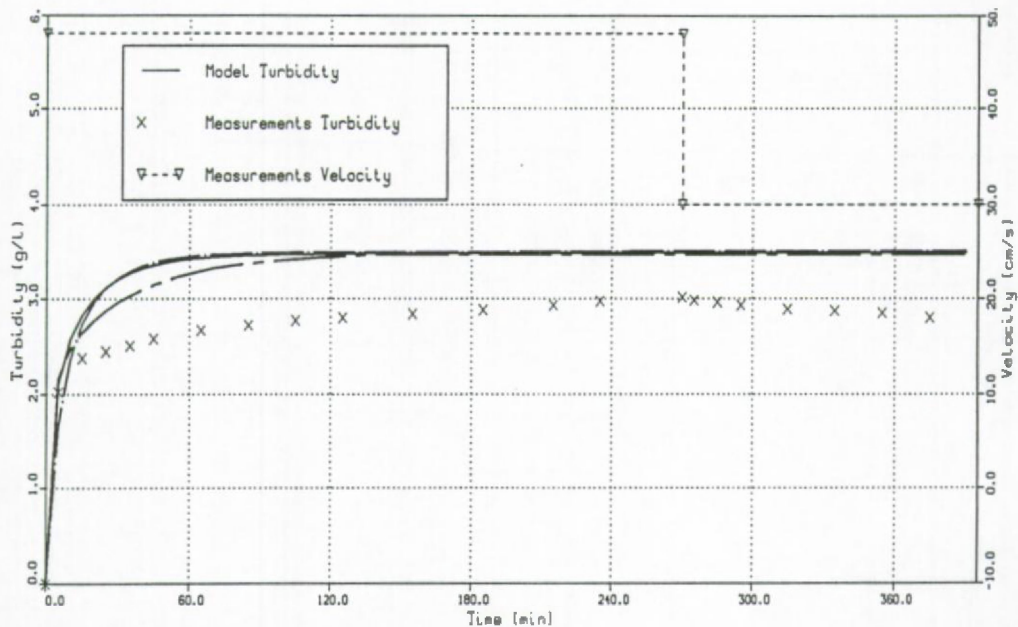


Figure 6.6: Uniform flow test A1, different erosion models (model 1: solid line, model 2: chain-dot, model 3: chain-dash).

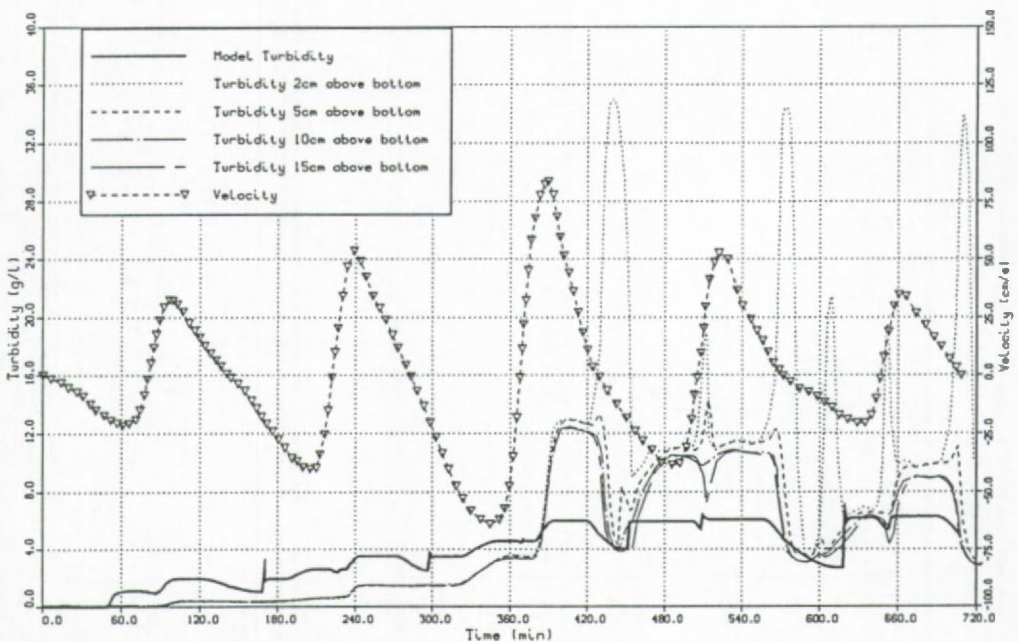


Figure 6.7: Alternating flow test 1.



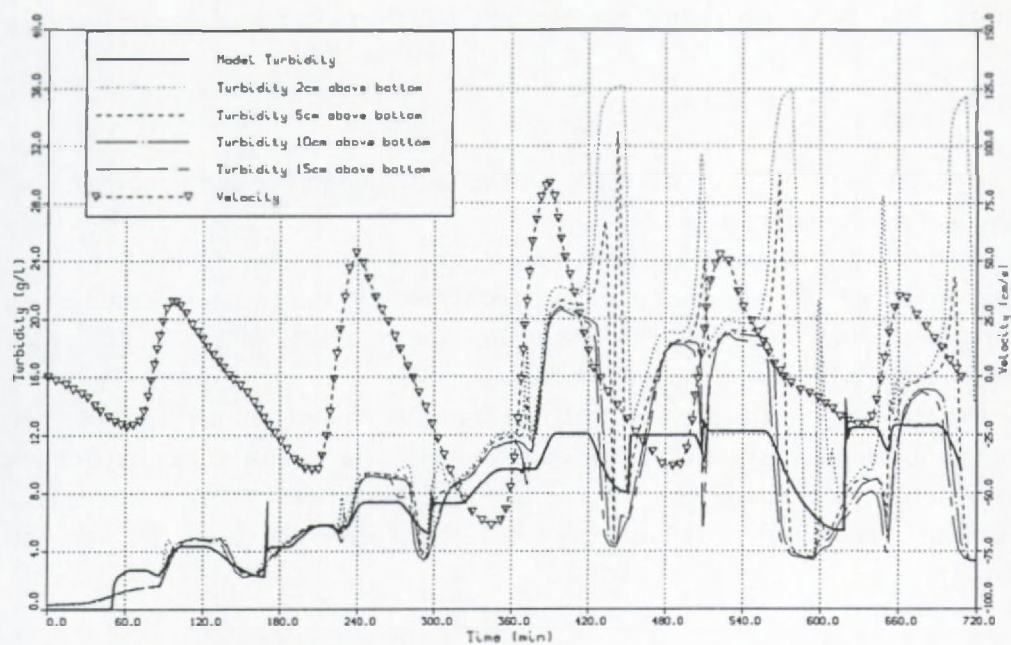


Figure 6.8: Alternating flow test 3.

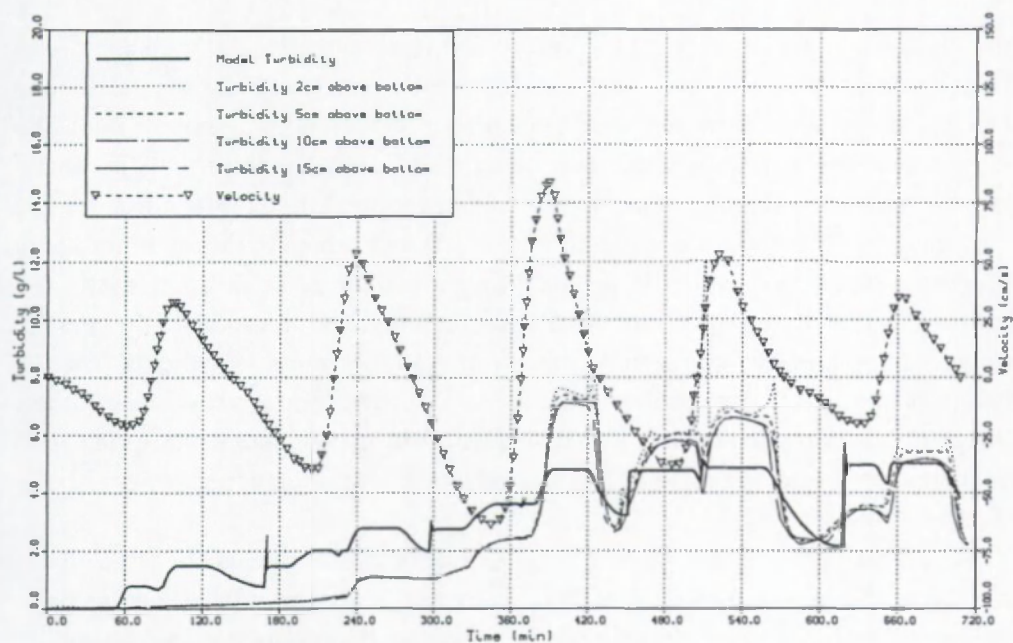


Figure 6.9: Alternate flow test 4.

## 6.4. 2D Mud Transport Model Of A Part Of The Scheldt Estuary

### 6.4.1. *The Scheldt model*

The model extends from Meestooft (upstream boundary) to Bath (downstream boundary), see Figure 6.10.

The bathymetry has been read from the appropriate maps edited by the Antwerpse Zeehavendienst. The geometry and the bathymetry of the two submerged dykes is based on the report of the Technische Scheldecommissie (1984). A picture of the bathymetry is presented in Figure 6.11.

In the framework of this thesis the mud transport model has participated in an intercomparison exercise with two other models. The results of this experiment have partly been reported in Fettweis et al. (1993b). Results of the simulations using the parameter set defined in § 6.4.1.2. are presented in the § 6.4.2. and 6.4.3.

#### 6.4.1.1. *The 2D hydrodynamic model FINEL*

The FINEL hydrodynamic model has been used to simulate the flow field in a part of the estuary. FINEL is a two-dimensional finite element model for the calculation of water levels and depth averaged velocities in estuaries and shallow sea. The model solves the well known 2D depth averaged Navier-Stokes equations, including the terms due to bottom friction (Manning formula), horizontal diffusion and Coriolis term. The long wave equations are transformed to a set of ordinary differential equations, which is solved using a semi-implicit Euler method. The advantage of using a finite element solution technique is that local bathymetrical or geometrical features can easily be incorporated in the numerical grid. The 2D model has been set up by Sas (see I.M.D.C.-W.L.B., 1991) and is therefore not the subject of this thesis. Because the hydrodynamic model results (flow field and water elevation) are the basis for the 2D mud transport calculations they are briefly presented here.

At the downstream open boundary a water elevation condition has been implemented. The tidal curve of 04/10/90 at Bath has been used. The tidal curve has been changed in such a way to obtain a cyclic signal. At the upstream open boundary a discharge boundary condition has been used. A discharge curve at the boundary has been extracted from the results of a previous model study (Van Dessel et al., 1993) and has been made cyclic and scaled with the appropriate tidal coefficient.

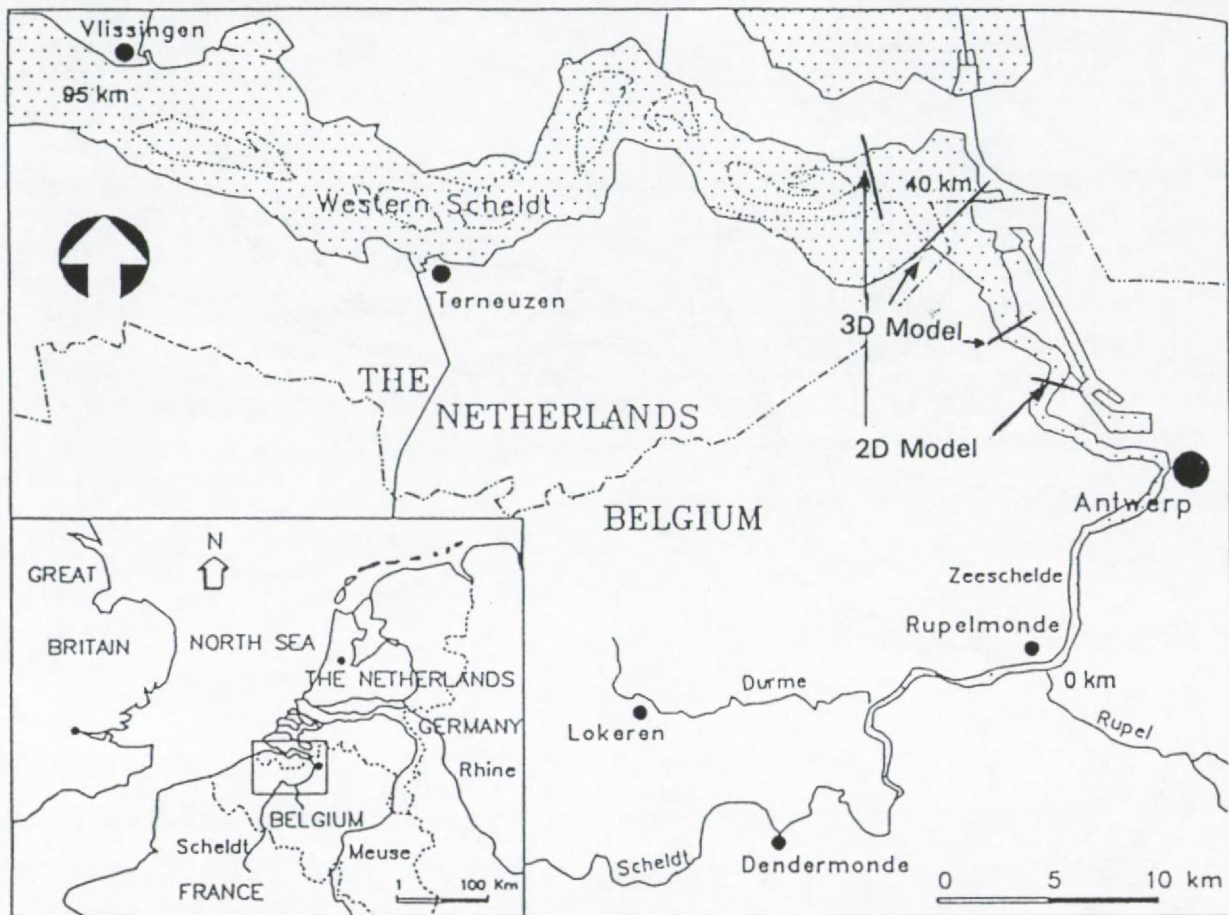


Figure 6.10: 2D hydrodynamic and mud transport model boundaries.



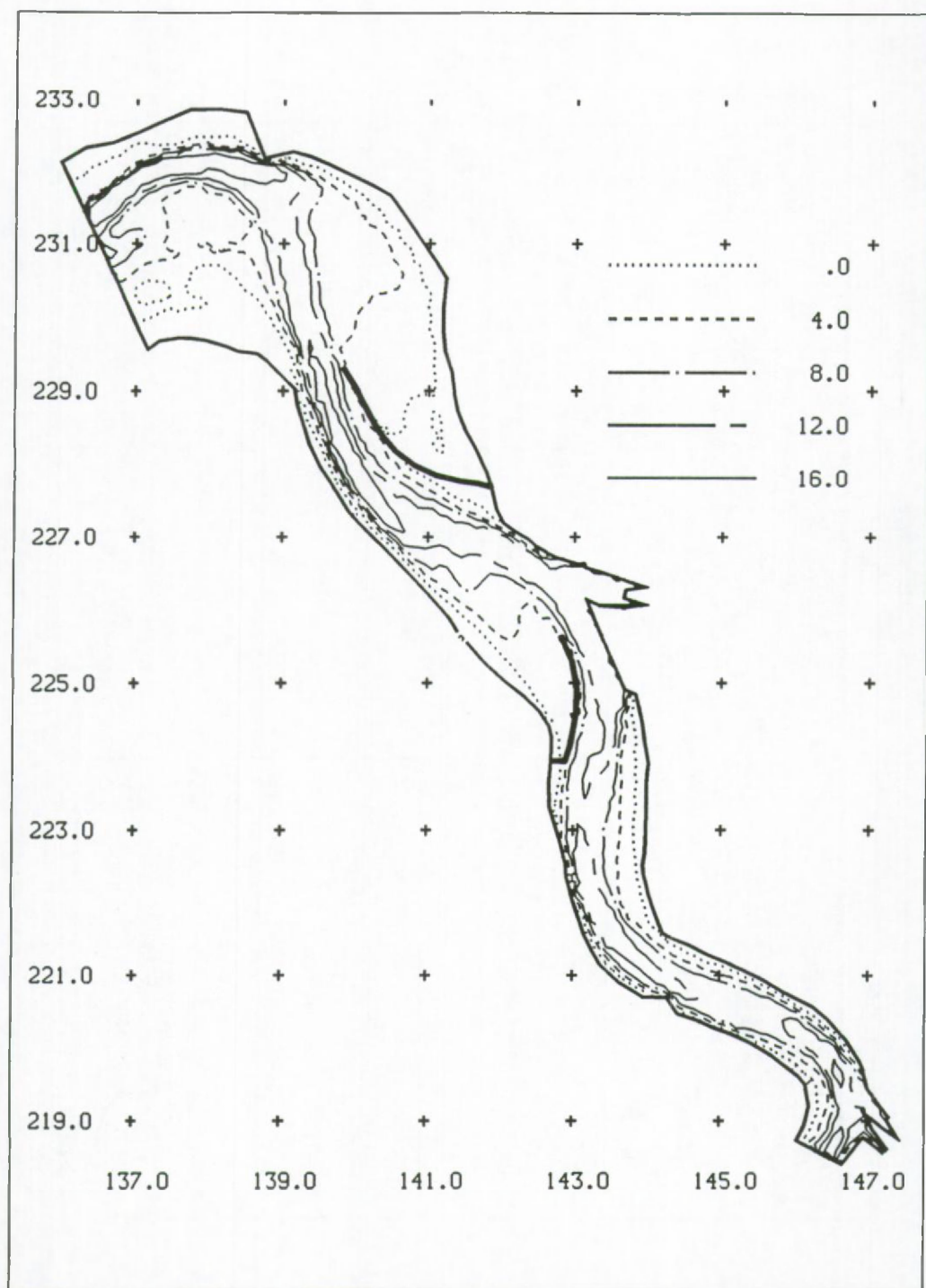


Figure 6.11: Bathymetry of the model area in m under TAW (coordinates are in km).

The  $u$  and  $v$  velocity components have been extracted from this discharge curve assuming that the vector velocity is perpendicular to the boundary, that the velocity is uniformly distributed over the cross section and that at the land boundaries (closed boundaries) the velocity is zero. The closed boundaries consist of a no-slip condition, except along the quay walls of the container terminal (south of the entrance channel to the Zandvliet and Berendrecht locks) and the entrance channel to the Zandvliet and Berendrecht locks, where a free slip condition (parallel with the wall) has been used.

The simulations have been started with an initial condition of zero velocity and a water level equals the tidal elevation at the starting time step. The Manning friction factor has been set to  $n = 0.02 \text{ s/m}^{1/3}$ , except in the nodes on the submerged dykes where  $n = 0.06 \text{ s/m}^{1/3}$ .

The model was calibrated by comparing the results with the observed velocities from 04/10/90 (see § 5.3.). Validation has been carried out with the same values of the parameters using the data set of the neap tide of 27/09/90 (see § 5.3.). The comparison has shown that the simulated flow pattern is generally in good agreement with the observations, except in point 1 where the ebb flow is underestimated by the model.

The hydrodynamic model has been set up to evaluate the morphological impact of a planned container terminal north of the locks of Zandvliet and Berendrecht (I.M.D.C.-W.L.B., 1991). The main goal of this study was to identify the changes in sedimentation and erosion pattern of cohesive sediments in the vicinity of the planned terminal as a function of the lay-out and placement of the quay walls, in order to evaluate and predict the changes in dredging activities which had to be expected. At the moment of the study it was not possible to run the model over a long course of time, due to insufficient computer capacity. Therefore it was decided to simulate a so-called morphological tide. As a consequence the simulated tidal curve had to be cyclic (see above) and had to be representative for the mean sediment transport in the Scheldt estuary. Conform the numerical simulations for the 'Liefkenshoek project' (Van Dessel et al., 1993) a morphological tide with a tidal amplitude of 1.06 times the mean tidal amplitude has been chosen. A morphological tide is defined as a tide which is representative for the mean sediment transport occurring during a spring-neap cycle. High bottom shear stresses are occurring during flood on the 'Plaat van Doel' and in the 'Schaar van Ouden Doel' (see § 5.3, measurement points 3 to 5). During ebb the maxima are situated in the main channel (measurement points 1 and 2). The bottom stress during ebb is in the shallower parts for a relative long period smaller than the critical shear stress for deposition of cohesive sediments (for neap tide:  $\pm 3.5$  hours, for spring tide:  $\pm 2$

hours, for a morphological tide this is a little longer than for a spring tide). In the main channel the bottom shear stress is only during a small time period (around slack waters) smaller than the critical value for deposition. As critical shear stress for deposition a value of 0.2Pa has been taken (see below).

#### 6.4.1.2. *The mud transport model*

The 2D model TRASIL has been used to simulate the transport of mud in a part of the Scheldt estuary. The area covered by the model is the same as for the 2D hydrodynamic model, see Figure 6.10. The numerical grid, the bathymetry, the flow field and the water depth has been extracted from the simulation results of the FINEL model. Calibration of a model is the process of determining parameter values in such a way that the results of the model corresponds with observations. The final chosen parameter values have to be so that the model can adequately simulate the phenomena for other data sets. Calibration of a model has also as goal to provide information about the sensitivity of the model to the various parameters. In order to calibrate a model, field data of the various characteristic features of mud, such as suspended mud concentration, distribution and composition of the sediments in the bed and the parameters describing fall velocity, erosion rate, erosion and deposition thresholds. For mud from the Scheldt estuary only limited information is available, especially with regard to erosion and deposition characteristics. Values of the erosion constant for the Scheldt river have been reported by Mulder and Udink (1990), they vary between 0.05g/m<sup>2</sup>s and 0.7g/m<sup>2</sup>s. For disposal of dredged mud in water a range of values for the erosion constant varying between 6 and 60g/m<sup>2</sup>s have been mentioned (Teeter, 1992). Dredging can however alter the sediment structure of the deposits, therefore the cited values are probably too high for undisturbed mud deposits. The critical shear stress for erosion gives the minimum value at which resuspension of mud particles begins. This value is during a major part of the tidal cycle lower than the bottom stress. Teeter (1992) mentioned for disposed mud values of 0.05 to 2.5Pa. Mulder and Udink (1990) proposed a value of 0.4Pa for the critical erosion stress for their Western Scheldt model. The critical shear stress for deposition has been determined in the laboratory as 0.07Pa (Hydraulic Research Station, 1980). Mulder and Udink (1990) used a value for the Scheldt of 0.2Pa. The fall velocity is restricted in the Scheldt river to 0.3mm/s as is reported by Manni (1986). This is in contrast with the in situ observations in the Kallo access channel, where fall velocities of 0.1 to 1.5mm/s have been measured with an Owen tube (I.M.D.C., 1988a). Be-



cause the mud aggregates are partially destroyed by this measurement device, we expect that the fall velocity can be even higher. The effective fall velocity has been calculated for the through tide measurements at the 'Drempel van Zandvliet' (see § 5.3.4.), the range of values was situated between 0 and 5mm/s. Due to the site specific character of the field data the final values of the parameters used in the model should be viewed as a good approximation of the real situation, the values are: fall velocity 2mm/s, critical shear stress for erosion 0.4Pa, critical shear stress for deposition 0.2Pa, erosion constant 0.05g/m<sup>2</sup>s.

Along the closed boundaries the condition is such that no particles can leave the domain. At the up- and downstream open boundary particles can enter or leave the domain depending on the current direction. During ebb new particles with a well defined concentration are entering the domain at the upstream boundary, whereas at the downstream boundary particles are leaving the domain. During flood this process is reversed. For this application we did not have at our disposal measurements of suspended sediments in the vicinity of the open boundaries. It was therefore decided to use a constant mud concentration as boundary condition for the ingoing particles. Based on the data in Van Eck et al. (1991) the concentration at the upstream boundary condition (active during ebb) was set to 200mg/l and at the downstream boundary (flood) to 100mg/l. The big difference in concentration condition at the two open boundary is also in agreement with the concentration gradient found between the different through tide measurements presented in § 5.4. (see Figure 5.32). As initial condition all the particle concentrations have been set to 0mg/l. The model calculations start with no mud depositions on the bed.

#### **6.4.3.      *Model intercomparison***

Modelling can lead to a better understanding of the erosion and deposition patterns in the estuary. However, as was already mentioned earlier, the mud model suffers from the fact that only little data are available on bed composition, suspended sediments, bed structure etc. for calibration and validation. Therefore, in order to illustrate the reliability of the model simulations, the TRASIL results were compared with two others transport models, i.e. SEDI-2D (Pathirana, 1994) and STUDH (Jabbari, 1994). These latter two models are both finite element models, the main difference between both models is that the domain is discretised by three and four in SEDI-2D and six and eight nodes elements in STUDH. These two models solve the equations in an Eulerian way, whereas TRASIL uses a Lagrangian technique. A brief presentation of the results has been given in Fettweis et al. (1993b). The neces-

sary input data on bathymetry, grid and sediment parameters are the same as the one presented in the previous paragraph. The velocity field has been generated by the 2D hydrodynamic model FINEL (see above) for a cyclic morphological tide. The results have been recorded after ten tidal cycles and a representative few of them are shown in Figures 6.12-13 (concentration field at one hour after and one hour before high water) and Figure 6.14 (deposition after one tidal cycle).

The results show that all the three models are qualitatively well predicting the distribution of suspended sediments over a tidal cycle. However, significant differences between the TRASIL model and the two other models can be identified, see Figures 6.12-13. The mud concentration in TRASIL is much higher than in the two other models. The mud concentration is, in addition, mainly restricted to the main channel. Such a result can be expected, since a particle tracking technique has been used in the TRASIL model and sediment particles are following the stream-lines. The TRASIL model has been used without diffusion terms, as a result little or no cross sectional spread of sediment concentrations occurs. In the SEDI-2D model a diffusion coefficient of 10 and in the STUDH model of  $100\text{m}^2/\text{s}$  has been chosen. The two Eulerian models predict similar concentration fields. The sharp gradients in concentration over a cross section as found in the TRASIL results are absent. The measurements at the 'Drempel van Zandvliet' gave also a smooth course of mud concentration over the cross section.

The deposition patterns are shown in Figure 6.14. The main areas of sedimentation are nearly the same. The main differences occur again between the TRASIL model and the two Eulerian models. TRASIL predicts higher siltation rates along the navigation channel, whereas the two Eulerian models show a higher sedimentation rate closer to the banks of the river. This is also illustrated in the access channel, where no mud is deposited in the TRASIL model results, in contrast with both Eulerian models. The Eulerian models and the Lagrangian model simulate different deposition patterns along the upstream submerged dyke. In TRASIL the dyke is a deposition area whereas in the other two models no mud is found on the bottom. The time history of sediment concentration in point 2 (§ 5.3.) is presented in Figure 6.15. As this point is located in the main navigation channel, the TRASIL model always predicted higher concentrations than the two other models. The results of the SEDI-2D and the STUDH model follow a similar trend. However, the concentration peaks in the SEDI-2D model are slightly earlier than the concentration peaks of the STUDH model. When compared with the measurements (as far as possible, different tidal conditions) the predicted concentration peaks are occurring earlier in both Eulerian models and later in the TRASIL model. The results of this intercomparison exercise reflected differences between the Lagrangian model and

the two Eulerian models. They are for a major part due to the value of the diffusion coefficient used in the simulation.

An interesting point is the sedimentation of mud in the entrance channel to the Zandvliet and Berendrecht locks. The access channel is a major catchment area of cohesive sediments. Both Eulerian models simulate sedimentation of mud in the channel, whereas in TRASIL no mud enters the channel. A first conclusion could be that the two Eulerian models are realistically predicting the deposition pattern. However, the high siltation rate in the channel is the consequence of the action of density differences between the river and the channel resulting in a complicated density induced velocity field in the channel, see chapters 5.5 and 7 for more detail. The flow is separated in two layers with opposite directions over the vertical. The separation in ingoing and outgoing flow is maintained by a salinity gradient which occurs in the horizontal (between the river and the access channel) and in the vertical plane. In case of no density induced currents the flow field changes drastically and the exchange of water between the channel and the river is reduced by a factor of two (see § 7.4.). The main driving force for the currents in the access channel is then formed by the flow passing along the access channel. This flow creates a large eddy with equal dimensions as the access channel. The exchange of suspended mud between the river and the access channel occurs in that case mainly through turbulent diffusion. The transport and the sedimentation of mud is governed by the flow field. A high sedimentation rate in the access channel can only occur if sufficient mud is transported into the channel. High transport rates are a consequence of the density differences between the channel and the river. The 2D hydrodynamic model FINEL cannot simulate this density induced velocity field in the channel. In case of no density gradients one would expect that the sedimentation is much smaller and concentrated at the entrance of the access channel, since the transport of mud is substantially reduced (see chapter 7.).

The results from the three different model show large differences in deposition pattern in the access channel, ranging from high sedimentation (STUDH) to no sedimentation (TRASIL). These differences in sedimentation pattern are due to the value of the diffusion coefficient (ranging from no diffusion to a high diffusion coefficient).

The conclusion of this exercise is that a good agreement with observations can be obtained (in the access channel) using high values for the diffusion coefficient. The 2D hydrodynamic model equations are however so that this result is not realistic under the assumptions made.



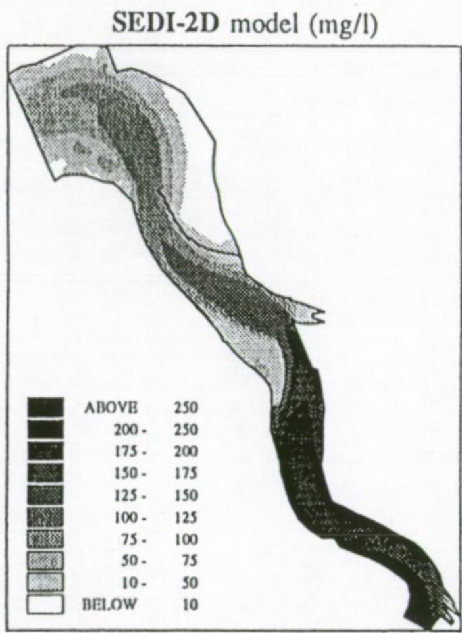
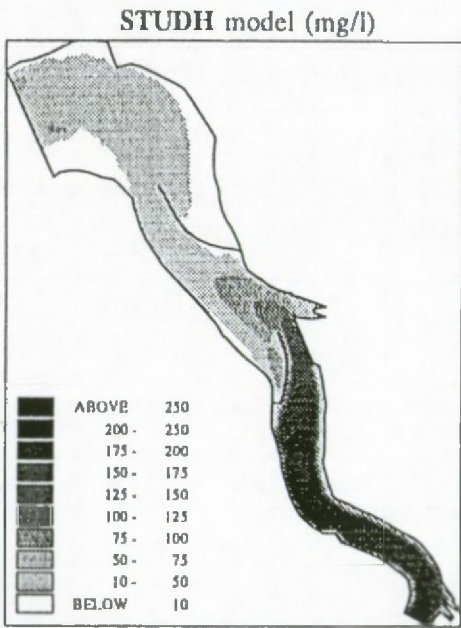
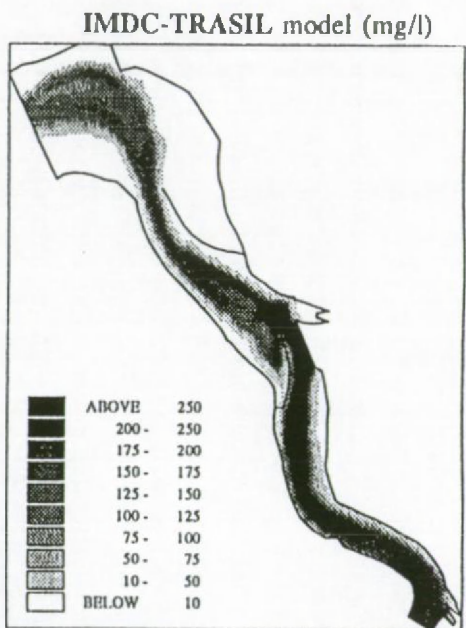


Figure 6.12: Concentration field 1 hour before low water.

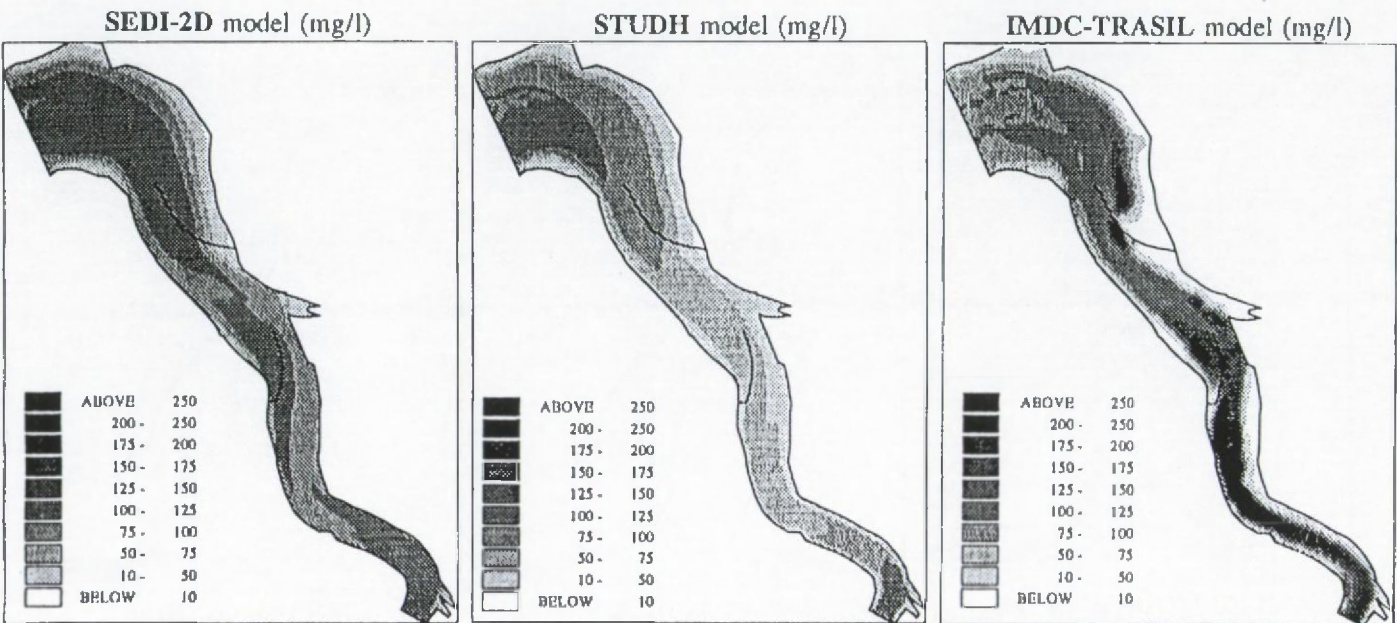
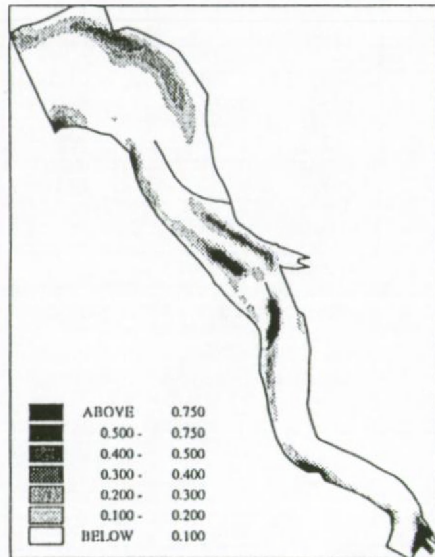
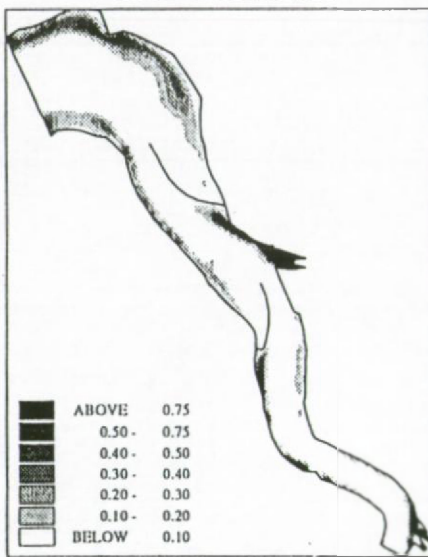


Figure 6.13: Concentration field 1 hour before high water.

IMDC-TRASIL model (cm)



STUDH model (cm)



SEDI-2D model (cm)

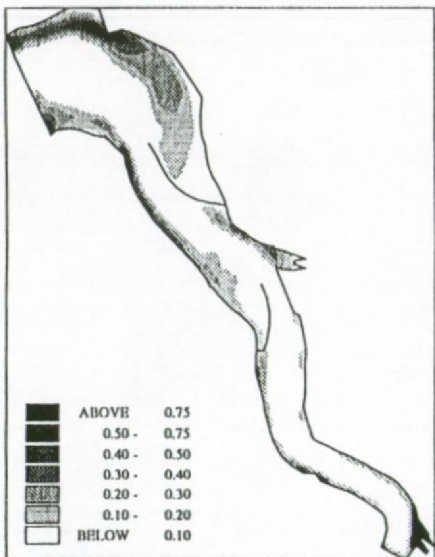


Figure 6.14: Deposition of mud after one tidal cycle.



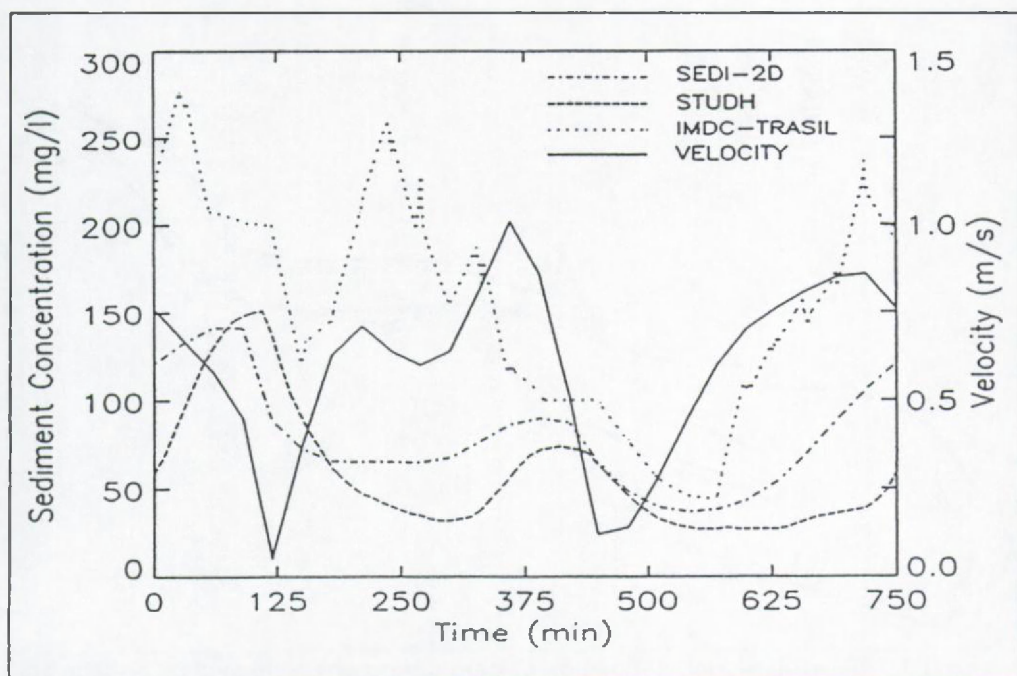


Figure 6.15: Mud concentration in function of time (measurement point 2).

#### 6.4.4. Diffusion sensitivity studies

An important part of model development is the validation of the model. In the previous sections this has been done by comparing the model results with laboratory experiments and by an intercomparison exercise of three different models for 'real' applications. The latter experiment showed that the TRASIL model results were different from the other two model results and that these differences were due to the absence of diffusion in the TRASIL model. In this paragraph some results will be shown with the implementation of diffusion using a random walk method (see § 6.2.).

The sensitivity of the model results to the diffusivity were examined by comparing the results of four simulations. These simulations differed only in the specified value of the diffusion coefficient ( $10\text{m}^2/\text{s}$  and  $100\text{m}^2/\text{s}$ ). The deposition pattern during one tidal cycle is shown in Figures 6.16-17. The differences between the simulations reflect the differences found between the three different model result as has been shown above. Increasing the diffusion coefficient results in a redistribution of the deposited mud towards the banks of the river.

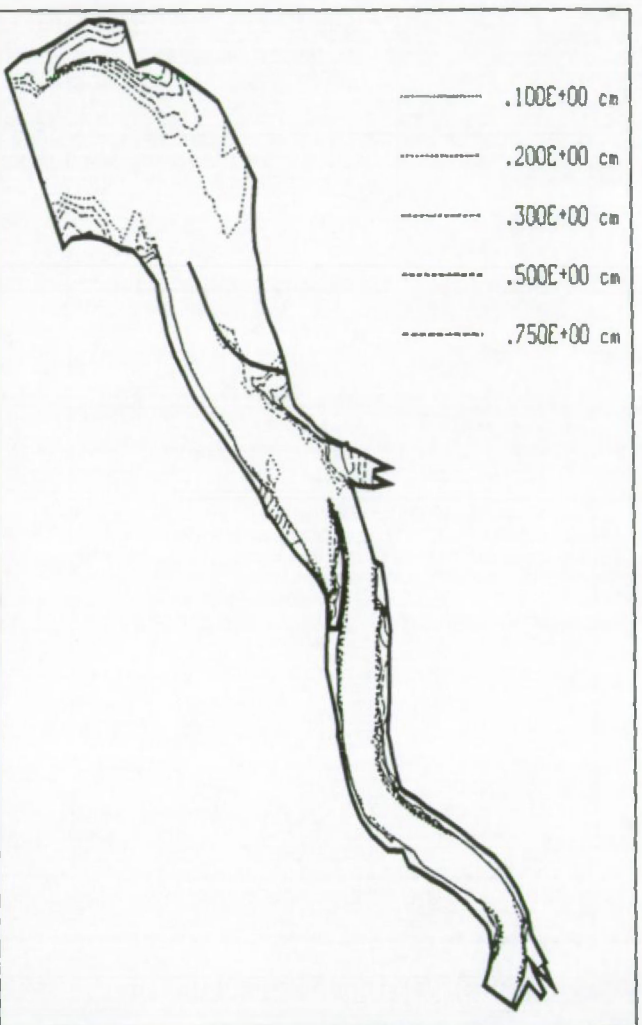


Figure 6.16: TRASIL model, deposition of mud during one tidal cycle ( $D = 10\text{m}^2/\text{s}$ ).

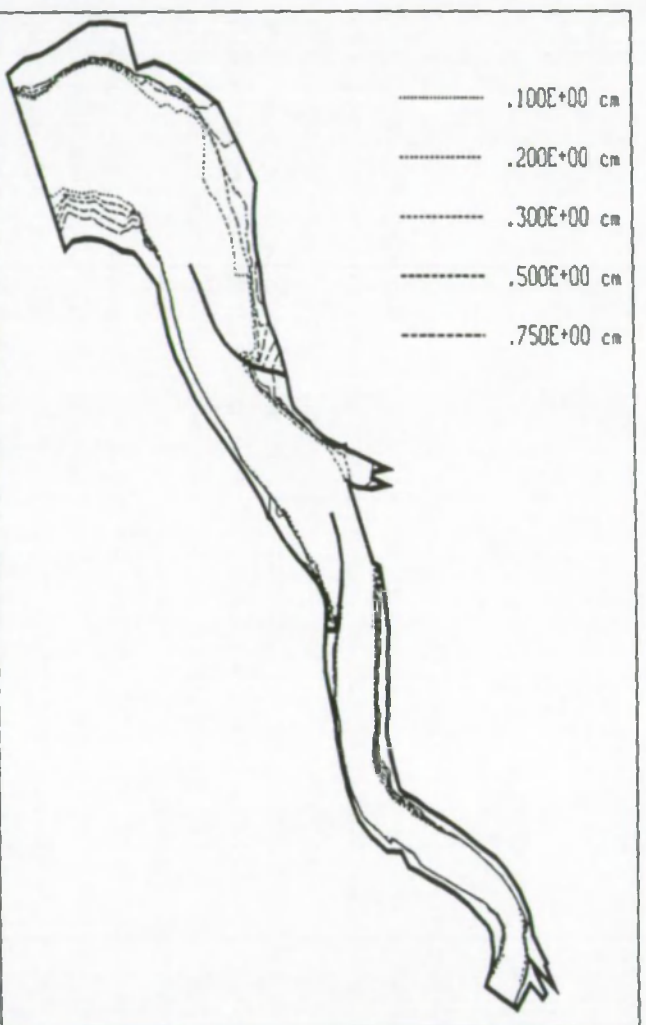


Figure 6.17: TRASIL model, deposition of mud during one tidal cycle ( $D = 100\text{m}^2/\text{s}$ ).

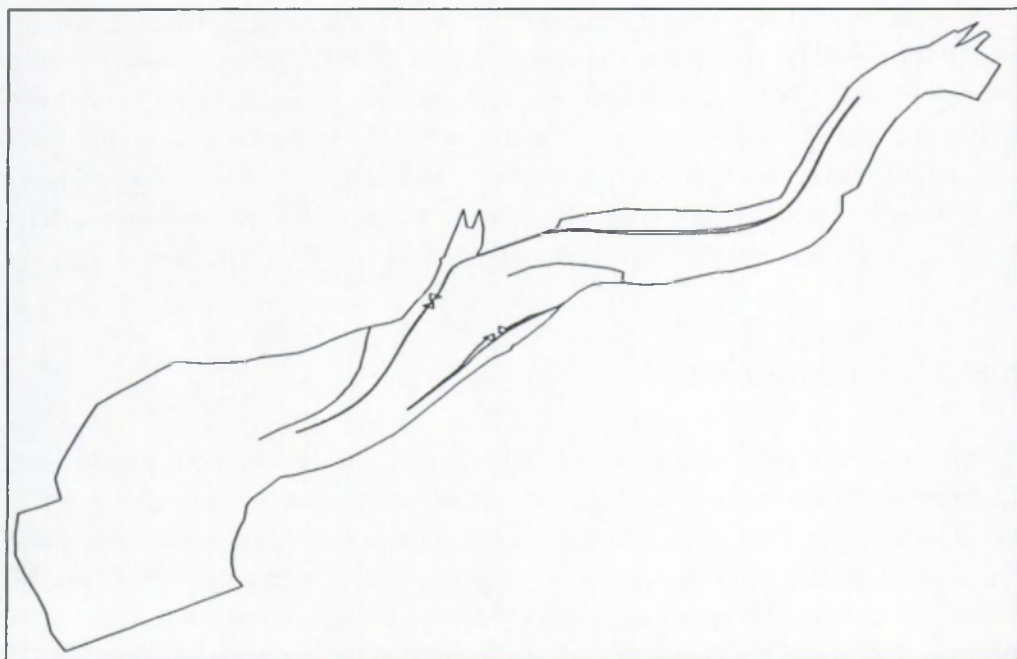


Figure 6.18: TRASIL model, particle tracking during one tidal cycle ( $D = 0\text{m}^2/\text{s}$ ).

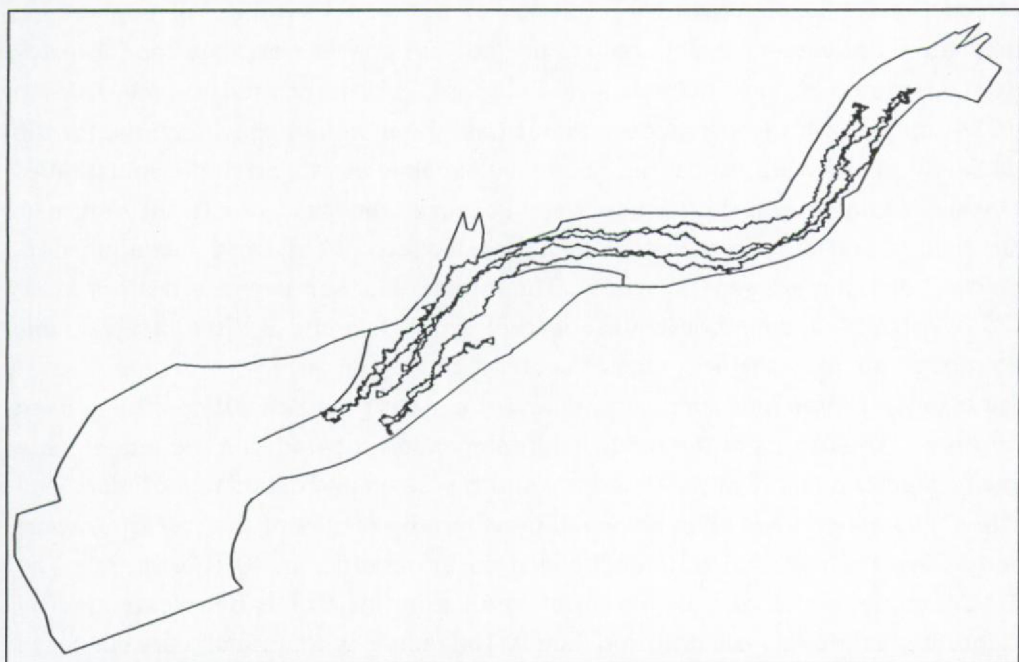


Figure 6.19: TRASIL model, particle tracking during one tidal cycle ( $D = 10\text{m}^2/\text{s}$ ).



The deposition patterns with a diffusion of  $10\text{m}^2/\text{s}$  are in good agreement with the results of the SEDI-2D model. The results of the  $100\text{m}^2/\text{s}$  diffusion value correspond well with the STUDH model results. A realistic value of the diffusion coefficient is probably situated between 1 and  $10\text{m}^2/\text{s}$ . The influence of a random walk step on the particle trajectories is shown in Figures 6.18 and 19 where two particles have been followed during a tidal cycle. The particles have been released in points 1 and 5 of the through tide measurement campaign on 04/10/90 (see § 5.3).

## 6.5. Conclusions

Calibration and validation are substantial steps in the development of a model. Calibration and validation of a real model application is a difficult task. The scarcity of field data of the various characteristics of cohesive sediments in an estuary and the predictive capabilities of the erosion and deposition laws are the main reason for this. A simple two step calibration-validation procedure does not necessarily increase the probability of having accurate results, as has already been pointed out by Mac Anally (1989). Validation of a transport model should lead to a quantification of the applicability and the accuracy of the model results. For engineering applications however, reliable results are not yet possible and the model use is often restricted to sensitivity analysis purposes. As is pointed out by Teisson (1994) cohesive transport models do not fulfil the standard specifications for the validation of software, since the 'predictive capabilities rely on the formulation of cohesive sediment transport processes, but these processes, due to their intrinsic variabilities, and site specificities, cannot be adequately treated in a validation step, which should have a general scope'. The intercomparison exercise (Hamm et al. 1994), which has been briefly described in § 6.1.6. and 6.3., is a first valuable attempt to quantify the accuracy of such models.

The results of three mud transport models of a part of the Scheldt river have been presented. The results of the model intercomparison showed that the models were able to predict qualitatively well the transport, erosion and deposition of mud. The differences which have been observed between the results of the three transport models are the result of differences in diffusion coefficient ( $0 - 100\text{m}^2/\text{s}$ ). The TRASIL model which had originally not included diffusion has been extended by integrating a random walk diffusion model. The results with diffusion are similar to those of the two other models.

The simulations have shown that the results of a cohesive transport model can only be as good as the accuracy of the hydrodynamic model. Some features, such

as the sedimentation in the access channel, which have been observed in nature, and which can be produced by the transport model are partially due to an 'over calibration' of the model and not to the good predictive capabilities of the model. It must be mentioned that these models, being limited in time and space scales, with only some basic cohesive sediment processes incorporated (erosion and deposition) and based on the input provided by a simplified hydrodynamic model (in the sense of 2D depth averaged, barotropic and a synthetic tide as boundary condition), cannot be used to simulate long term transport phenomena with a high reliability.

The data set used for calibration and validation consist of two through tide measurements in a cross section of the estuary (§ 5.3). This data set is, although well documented, too much site and time specific. In engineering applications a good intuitive feeling of the site and the model results is still an important part in the calibration and validation procedure. This procedure has however its limitation and has to be used with care.





## CHAPTER 7

### SEDIMENTATION OF MUD IN AN ACCESS CHANNEL

#### 7.1. Introduction

The locks of Zandvliet and Berendrecht are the major entrance to the Port of Antwerp. These locks are connected to the river Scheldt by an access channel. The flow field in this access channel is complex, it is driven by tides, horizontal eddies, density induced currents and boundary effects. Sedimentation is important in the access channel. In order to keep a constant depth frequent dredging activities have to be carried out. The main part of the bottom in the channel consists of fine cohesive sediments. The high sedimentation rates in the access channel are mainly explained by the presence of salinity differences between the channel and the river and by the fact that the access channel is situated in the area of the turbidity maximum. The salinity differences induce a horizontal pressure gradient resulting in density driven currents. This density current is maintained nearly during the whole tidal cycle, due to the very small velocities and the small turbulence (mixing) in the waters of the access channel. The exchange of water between the access channel and the river increases significantly due to the presence of the density gradients. Therefore more sediments are able to enter the channel and because of the extremely small velocities they will almost all settle down.

The flow field in the access channel is the result of 3D, unsteady processes with dynamic links between the flow and the buoyancy. Therefore a 3D flow and salt transport model has been used to model the flow structure, see Fettweis and Sas (1994). The results of the hydrodynamic model have been used as input for the mud transport model. Because the sedimentation in the access channel is caused by the flow a great part of this chapter will be dedicated to a detailed description of the currents and the salinity values in the entrance channel and in the river.

## 7.2. Flow In The Access Channel

### 7.2.1. The 3D hydrodynamic model

The 3D model (Cooper, 1983) solves the classical shallow water equations. These equations can be written as follows, assuming that (1) the pressure is hydrostatic, (2) the Boussinesq approximation is valid and (3) the horizontal and vertical turbulence terms can be approximated by eddy viscosities:

$$\frac{\partial u}{\partial t} + u \frac{\partial u}{\partial x} + v \frac{\partial u}{\partial y} + w \frac{\partial u}{\partial z} + \frac{1}{\rho} \frac{\partial p}{\partial x} = f_v + A_h \nabla^2 u + \frac{1}{\rho} \frac{\partial \tau_x}{\partial z} \quad (7.1)$$

$$\frac{\partial v}{\partial t} + u \frac{\partial v}{\partial x} + v \frac{\partial v}{\partial y} + w \frac{\partial v}{\partial z} + \frac{1}{\rho} \frac{\partial p}{\partial y} = -f_u + A_h \nabla^2 v + \frac{1}{\rho} \frac{\partial \tau_y}{\partial z} \quad (7.2)$$

The third momentum equation is simplified to the hydrostatic equation:

$$p = -g \int_z^{\eta} \rho dz \quad (7.3)$$

The mass continuity equation is written as:

$$\frac{\partial u}{\partial x} + \frac{\partial v}{\partial y} + \frac{\partial w}{\partial z} = 0 \quad (7.4)$$

and the continuity equation for salt as:

$$\frac{\partial s}{\partial t} + u \frac{\partial s}{\partial x} + v \frac{\partial s}{\partial y} + w \frac{\partial s}{\partial z} = K_h \nabla^2 s + \frac{\partial f_{sz}}{\partial z} \quad (7.5)$$

where  $x, y, z$  are the Cartesian coordinates,  $u, v, w$  the velocity components in  $x$ -,  $y$ - and  $z$ -direction,  $t$  time,  $\rho$  density,  $p$  pressure,  $f$  Coriolis parameter,  $\eta$   $z$  at the free surface,  $A_h$  horizontal eddy viscosity,  $\tau_x, \tau_y$  horizontal components of the vertical turbulent momentum transport,  $s$  salinity,  $K_h$  horizontal eddy diffusivity and  $f_{sz}$  vertical turbulent salt flux.

The density of the water is calculated using the following equation of state:

$$\rho = 1000 + 0.76s \quad (7.6)$$

At the bottom a quadratic friction formula is applied. The friction factor  $f$  is calculated using the rough channel law of Darcy-Weissbach:

$$f = \frac{1}{32} [\log_{10}(14.8z/k_n)]^{-2} \quad (7.7)$$

where  $k_n$  is the roughness following Nikuradse [m] and  $z$  the thickness of the bottom layer. The roughness length is a function of the size of the protuberances on the bed, either directly in the form of particle dimensions or indirectly in the form of ripple heights.

The equations are solved using a finite difference technique applied on a so-called Arakawa C grid. The equations are solved using explicit upstream finite differences horizontally and implicit finite differences in the vertical plane. The reduction of vertical mixing by density stratification is an essential element included in the model without which the salt would mix rapidly through the water column and the currents would form a uni-directional logarithmic profile unlike found in reality. The model uses a mixing length description of the turbulence which takes account of different size eddies dominating the turbulent diffusion at different levels in the water column. The vertical turbulent momentum transport is of the form:

$$\tau_{zx} = -\rho A_v \frac{\partial u}{\partial z}, \quad \text{with } A_v = l^2 \left( \left( \frac{\partial u}{\partial z} \right)^2 + \left( \frac{\partial v}{\partial z} \right)^2 \right)^{0.5} \quad (7.8)$$

with the form of the mixing length  $l_m$  from Odd and Rodger (1978):

$$l_m(z) = 0.4z(1-z/d)^{0.5} [1 + \beta Ri(z)]^{-n}, \quad \text{for } Ri(z) \leq 1.0 \quad (7.9)$$

where  $Ri$  is the Richardson number (if  $Ri > 1$  then  $Ri = 1$ ),  $d$  the depth, and  $\beta$  and  $n$  some dimensionless constants taken as 160 and 0.5 respectively. The solute mixing length  $l_c$  distribution in stratified flows (with  $Rf_c$  the flux Richardson number):

$$l_c(z) = l_m(z) \left[ 1 - \frac{l_c(z)}{l_m(z)} \frac{Ri(z)}{Rf_c} \right] / \left[ 1 - \frac{l_c(z)}{l_m(z)} Ri \right] \quad (7.10)$$

The model covers a part of the Scheldt estuary of nearly 8.5km, with the downstream boundary near the Belgian-Dutch border and the upstream boundary near Doel, see Figure 6.11. The bathymetry has been discretised on a rectangular equidistant grid with a grid distance of 50m. The orientation of the grid is such that the container terminal south of the entrance channel is parallel with the  $y$ -direction. The grid has therefore be rotated over  $22.8^\circ$  in counterclockwise direction. The four vertical layers have a minimum thickness of 3m. The lower layers are progressively removed as they become thinner than the specified thickness (= 3m) and the thickness of the new bottom layer is increased to compensate. The thickness



of the surface layer varies through tide to allow the incorporation of surface level variations. During spring tide the thickness of the surface layer is thus about 3m at low water and 9m at high water. This relatively coarse vertical resolution is usually suitable for the Scheldt estuary, because no sharply defined interface between fresh and saline water exist.

The model has closed and open boundaries. Along the closed boundaries a no slip condition has been implemented except along the container quay south of the entrance channel where a free slip condition has been used. At the downstream boundary a water elevation is imposed, whereas at the upstream boundary the model is forced with velocity. The boundary conditions have been extracted from the results of the 2D model presented before. The salinity boundary conditions results of a 1D model (Jabbari, 1994) were available for spring tide of 04/10/90. By scaling these salinity values a boundary condition for the neap tide of 27/09/90 has been constructed. The spring tide of 04/10/90 as well as the neap tide of 27/09/90 are typically for high salinity conditions. A third and fourth run have been carried out to simulate spring tide at low and no salinity conditions respectively.

#### *7.2.2. Flow field in the river*

The two data sets of the whole tide measurement at the 'Drempel van Zandvliet' have been used for calibration and validation, see § 5.3. In accordance with the 2D simulation (§ 6.4.1.1.), the spring tide of 04/10/90 has been simulated for calibration, validation has been carried out by simulating the neap tide of 27/09/90. Four simulations have been carried out:

- spring tide of 04/10/90 high salinity gradients,
- neap tide of 27/09/90 high salinity conditions,
- spring tide of 04/10/90 low salinity gradients,
- spring tide of 04/10/90 without salinity gradients.

The main factors influencing the salinity distribution are the tides and the fresh water discharge. High river run off occurs during the winter, the fresh water discharge is low during summer. High salinity values occur during fall and low values at the end of the winter. The salinity gradient between Prosperpolder and Liefkenshoek during fall was about 0.50g/l per km in 1977, during high fresh water discharge the gradient decreased down to 0.25g/l per km (A.Z., 1993b). From the measurements discussed in § 5.3., a horizontal salinity gradient of 0.42g/l per km during spring- and 0.35g/l per km during neap tide has been found at the 'Drempel

van Zandvliet'. These salinity gradients have been used for the calibration and validation simulations. A third and a fourth run have been carried out for a spring tide with a low horizontal salinity gradient (0.20g/l per km) and for a spring tide without salinity gradient. The calculations have been started at high water. As initial condition for salinity, velocity and water elevation a constant value throughout the whole domain has been taken.

The flow field at maximum flood and ebb flow during spring tide in the surface layer (calibration run, high salinity gradient) is presented in Figure 7.1. The flow field during flood is qualitatively equal to the 2D results. During maximum ebb differences between both model results can be seen. In the 3D model results an eddy in counterclockwise is present on the 'Plaat van Doel'. The velocities in this shallow area are very small (<10cm/s). In the 2D model results no eddy has been observed in this area at maximum ebb flow. The eddy on the 'Plaat van Doel' starts at the end of falling tide (about 5 hours after high water) at a time when the lateral salinity gradient reaches its maximum.

The velocity profile is typically distorted, see Figure 7.2: during flood a reduction of the velocity in the surface layer is observed whereas during ebb the velocity in the surface layer is increased. These distortions of the velocity profiles are an indication of stratification and correspond well with the observations.

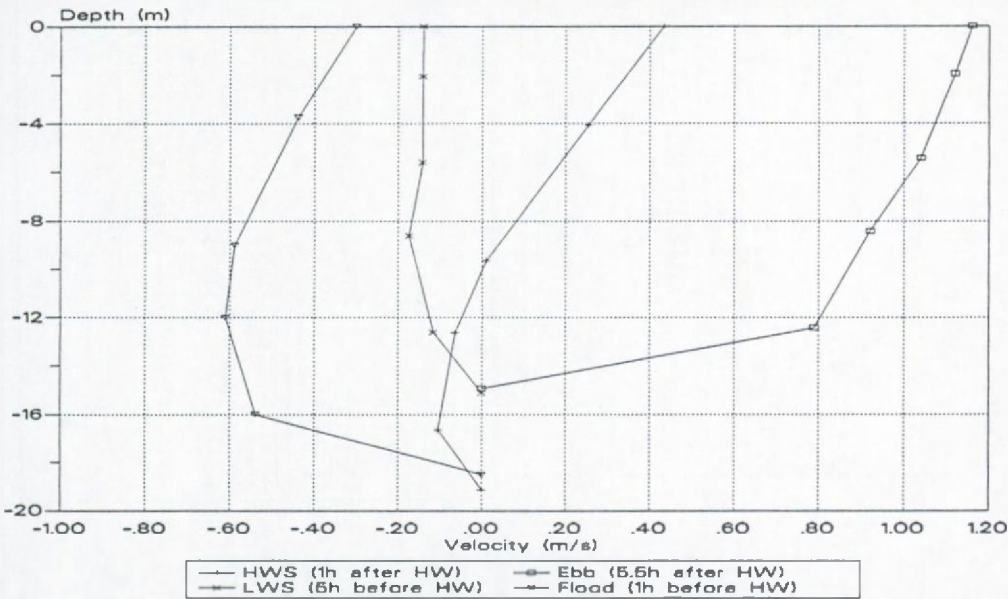


Figure 7.2: 3D model results, spring tide high salinity gradient. Velocity profiles during ebb, flood and at high water (HWS) and low water slack (LWS).

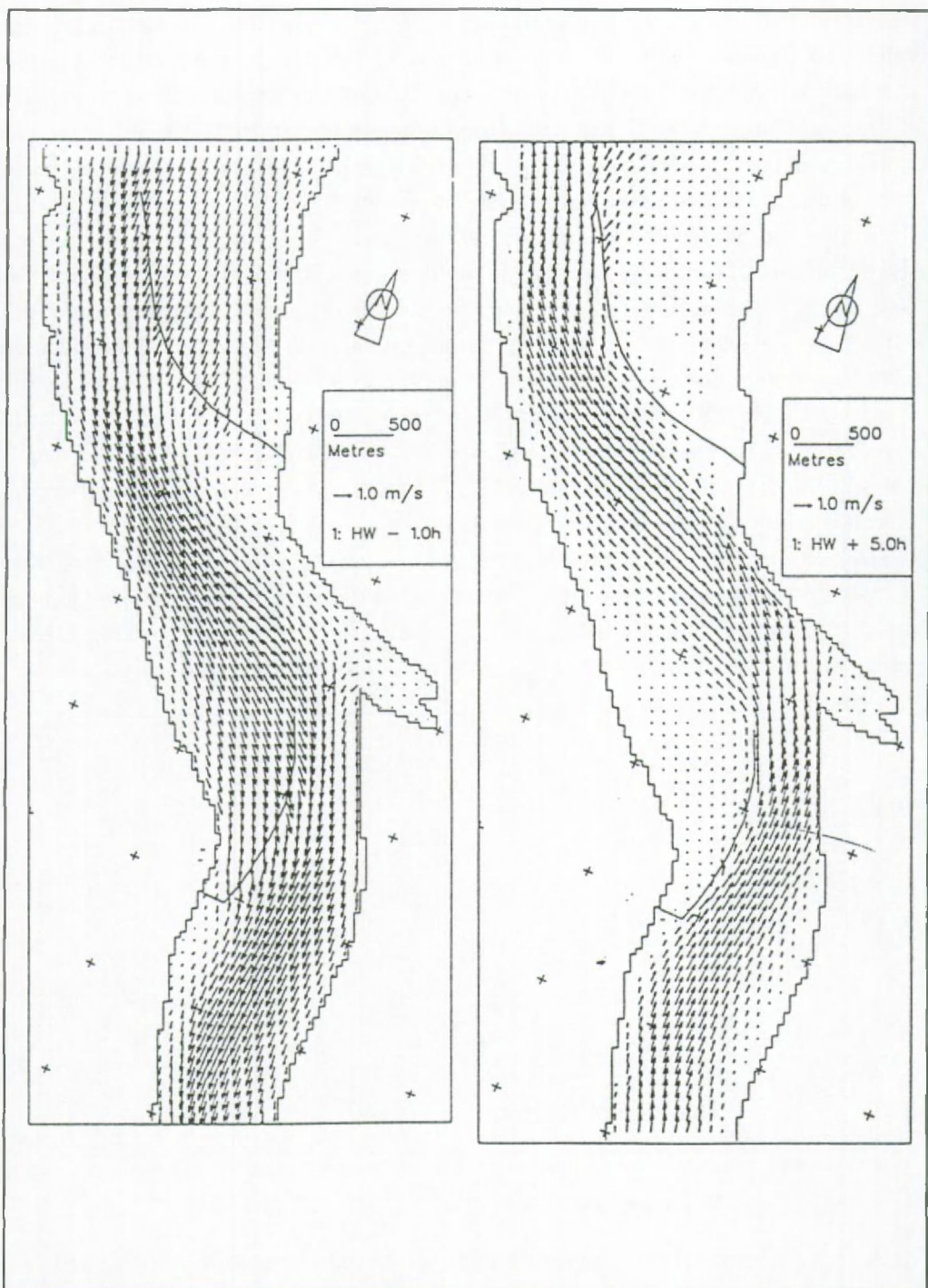


Figure 7.1: 3D model results. Spring tide high salinity gradient. (a) Maximum flood and (b) maximum ebb flow (surface layer).



### 7.2.3. *Flow field in the access channel*

The mathematical model makes it possible to incorporate the local information which has been collected during a measurement campaign in a global velocity distribution of the access channel. The velocity field in the access channel has been validated using the results of the ADCP measurement campaigns of 19/04/93 and 29/04/93, see § 5.5. A detailed comparison between these measurements and the results of the 3D model is not possible since the tidal and salinity conditions during the measurements are different from the one used in the 3D model (compare Tables 5.1 and 5.12). Furthermore the vertical resolution of the 3D model is much less (greater than or equal 3m) than the one of the ADCP profiles (0.5m). Nevertheless the comparison shows that the velocity is generally qualitatively and quantitatively well reproduced by the model.

The conformity is less good at about 2 to 3 hours after high water. In Figures 7.3 and 7.4 are shown the comparisons between measurements and calculations for a situation during ebb (5 hours before HW) and during flood (1 hour after HW). The first situation (Figure 7.3) is typical for the outflow of water towards the river in the bottom layer together with an inflow of water in the surface layer. The second situations (Figure 7.4) shows the inflow of saltier water towards the access channel in the bottom layer and the outflow of less saline water in the surface layer. The qualitative description of the velocity field in the access channel, based on the results of measurements and the mathematical model is summarized below:

#### *Beginning of flood (5-4 hours before HW)*

The less saline water enters the access channel in the surface layer, whereas the saltier water exits the access channel in the bottom layer. The salinity in the access channel is still low.

#### *Flood (3 hours before HW - HW)*

The salinity in the river is now higher than in the access channel. The saltier water from downstream has reached the access channel at about 3 hours before HW, due to this the currents are reversed. The saltier water enters the access channel in the bottom layer while the fresher waters leave the channel in the top layer in northern direction. As soon as the exiting water has reached the river it is carried away towards upstream.

#### *Beginning of ebb (1-2 hours after HW)*

The salinity has now reached its maximum in the river. The water in the access channel is however less saline. A clockwise eddy is formed over nearly whole the water column. The highest inflow occurs in the bottom layer. The water flows in a spiral towards the surface, where it leaves the access channel.

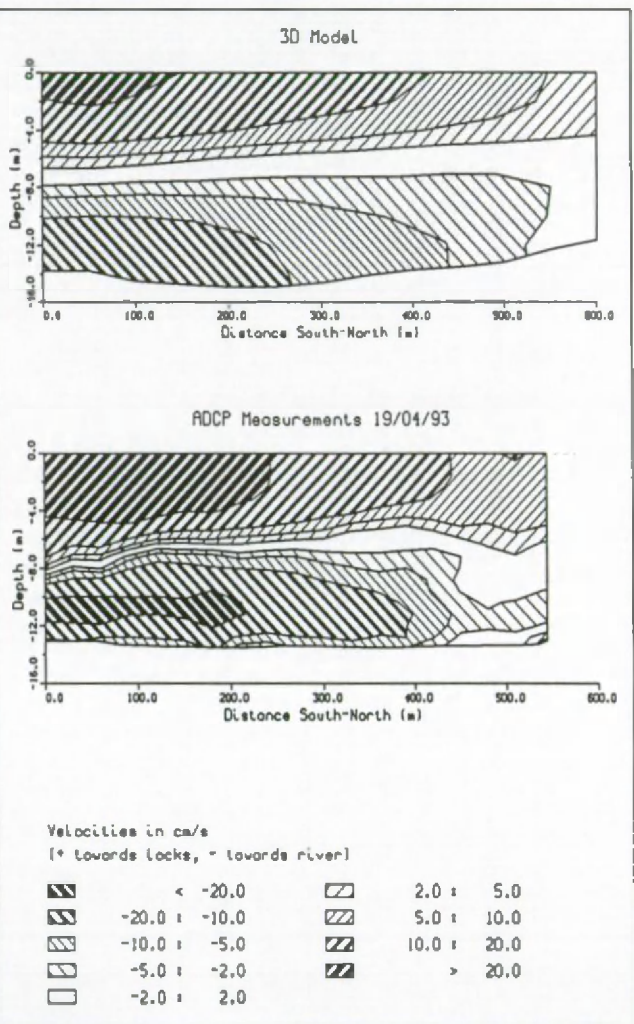


Figure 7.3: Access channel Zandvliet-Berendrecht. Comparison between 3D model results (spring tide with high salinity gradient) and ADCP measurements at about 5.5 hours before high water.

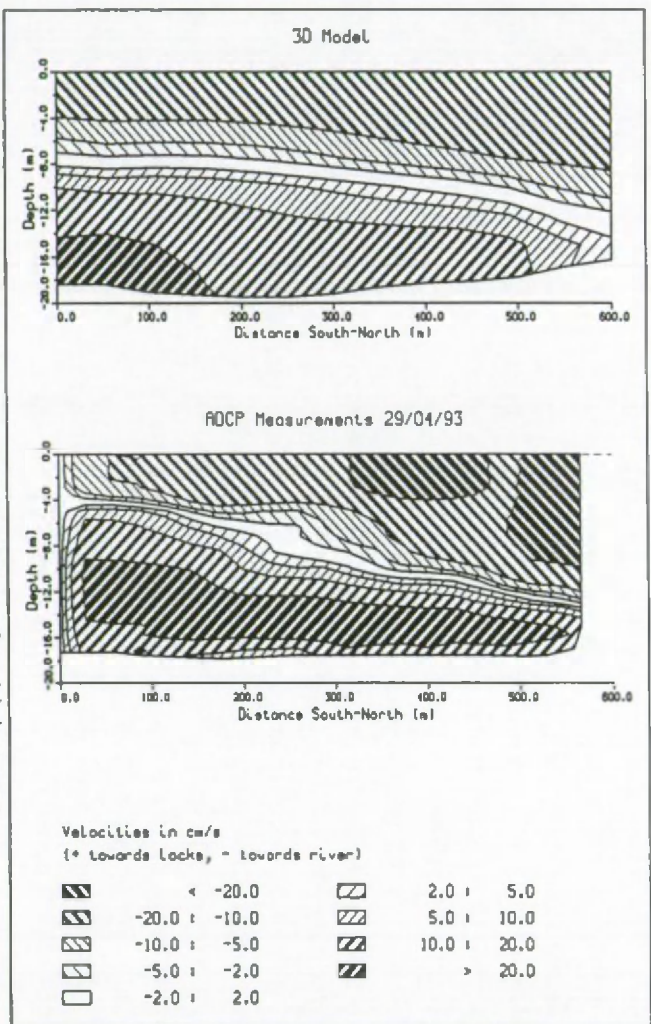


Figure 7.4: idem 7.3, but now at about 1 hour after high water.



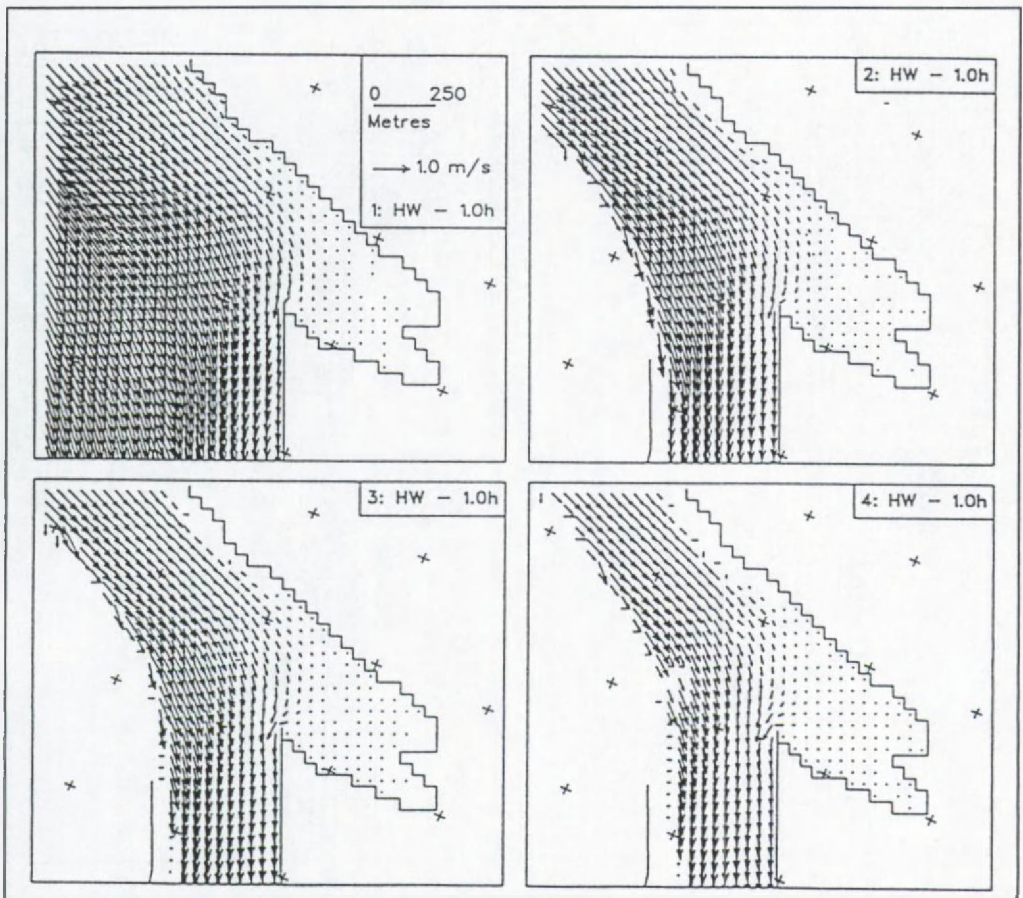


Figure 7.5: 3D model results. Spring tide without salinity gradients. Maximum flood flow (1 = surface layer, 4 = bottom layer).

#### *Ebb (3-6 hours after HW)*

The clockwise eddy still remains, but the spiral is now reversed. The less saline water is flowing downward to the bottom. The more saline water at the bottom leaves the access channel.

A detail of the flow field at spring tide and without salinity gradients is presented in Figure 7.5 (maximum flood flow) and 7.6 (maximum ebb flow). The corresponding results for the simulation with a high salinity gradient (calibration run) are presented in Figures 7.7 and 7.8. A comparison between these figures show that the main differences are found in the entrance channel. The current velocities are lower without density effects and the vertical structure is constant in the sense that no two layer flow occurs.



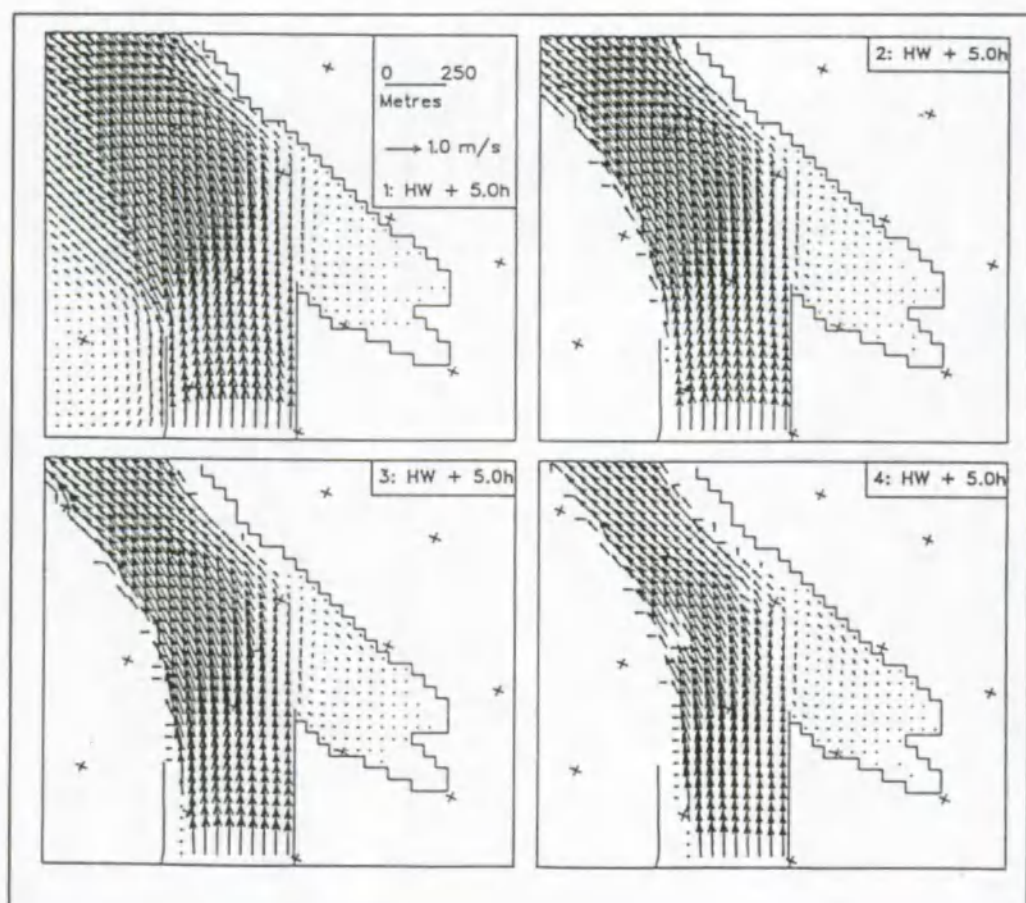


Figure 7.6: idem 7.5 but now for maximum ebb flow.

The current velocities in the access channel are for every tidal situation low: the velocities are restricted to 0.2m/s to 0.3m/s during spring tide as well as neap tide, at high or low salinity conditions. This means that the velocity in the access channel is favourable for the sedimentation of mud. The velocity during low salinity condition is 5% to 10% smaller than during high salinity values. The velocity is negligible during flood in the hypothetical case of no salinity gradient in the river. The velocities during ebb are higher due to the presence of an eddy in the access channel.

The structure of the velocity profile is complicated in the access channel. The presence of an eddy together with the water exchange due to density differences results in the fact that the current velocities in the surface and bottom layers are most of the time in opposite direction. The thickness of these layers is not constant, but varies in the course of the tide. The currents in case of no density

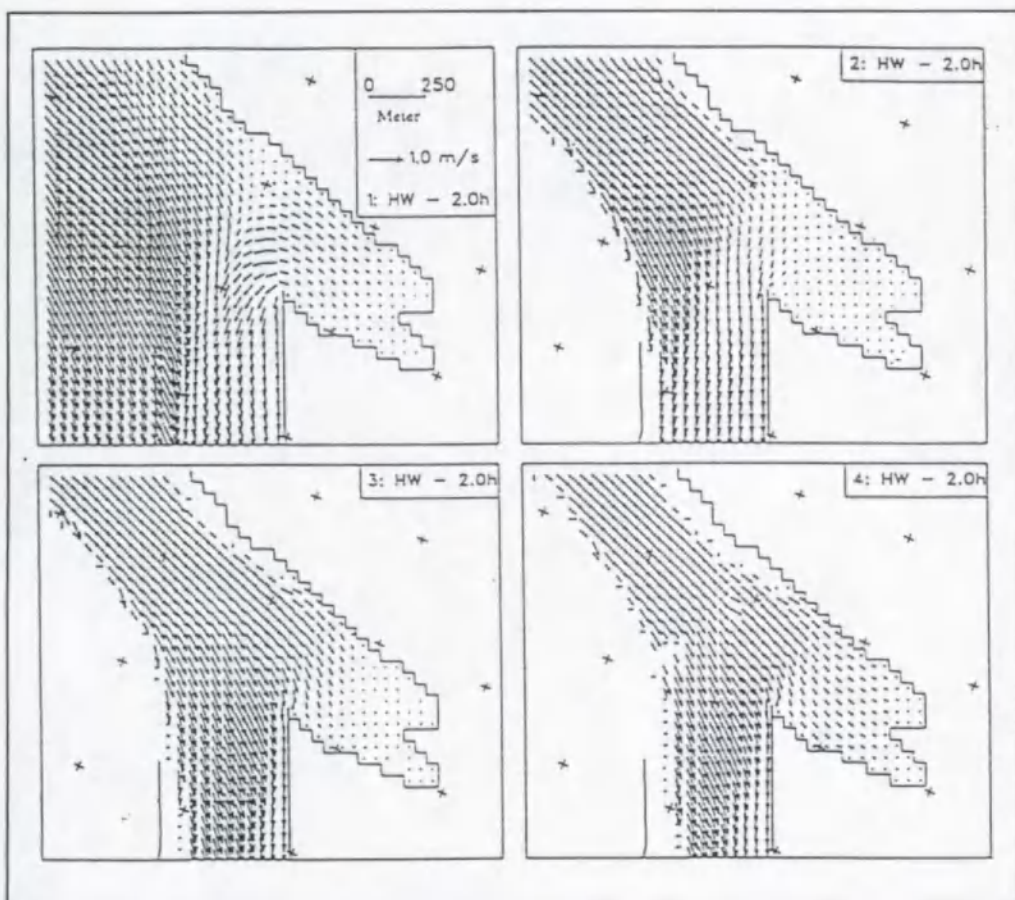


Figure 7.7: 3D model, spring tide high salinity gradient. Velocity field at 2 hours before high water (1 = surface, 4 = bottom layer).

forcing are nearly constant over the vertical and unidirectional.

### 7.3. Salinity In The Access Channel

#### 7.3.1. Salinity in the river

The spring tide of 04/10/90 is situated during high salinity values in the Scheldt river. The horizontal salinity gradient derived from the measurements of 1993 (A.Z., 1993b) is about 0.48g/l per km in the part of the Scheldt estuary where the measurements are situated. The salinity gradient implemented between the upstream and the downstream boundary is 0.45g/l per km. The salinity results are

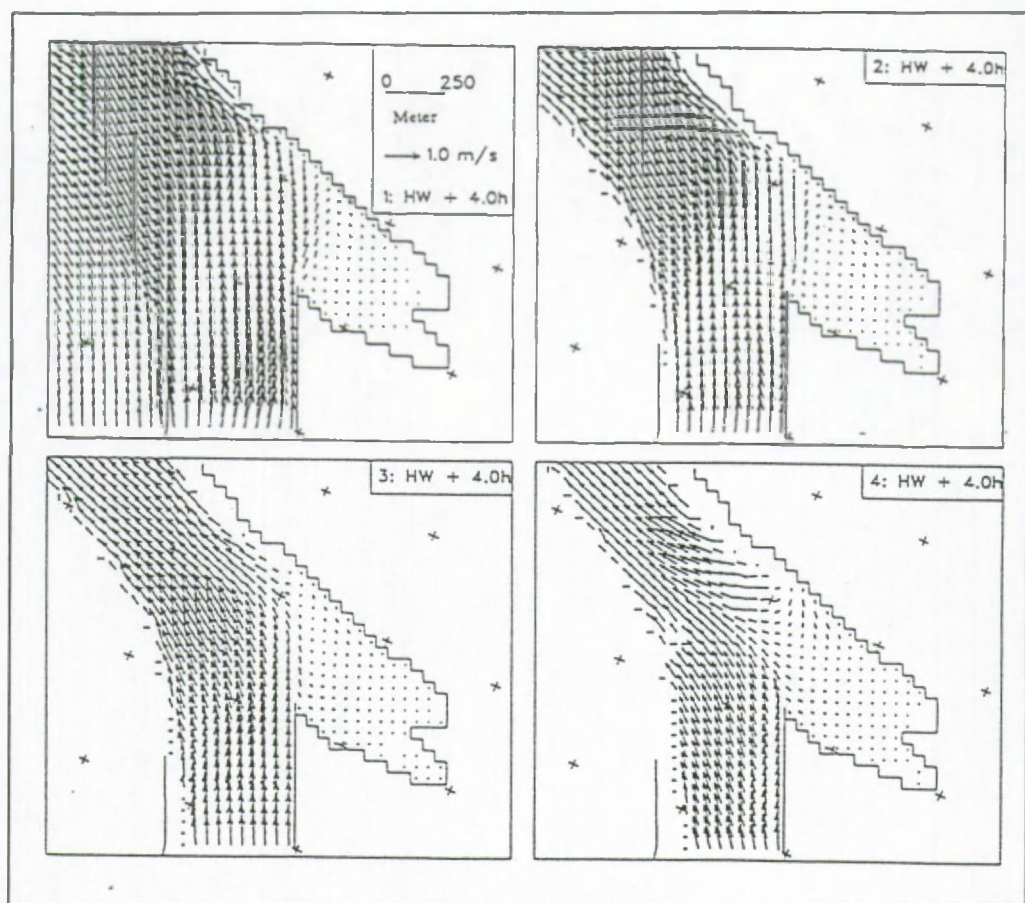


Figure 7.8: idem 7.7, but now at 4 hours after high water.

compared with the measurements of 04/10/90 in Figure 7.9. The calculated salinity values are systematically lower than the observed ones. This lower salinity value in the model has no influence on the density induced currents since the salinity gradients are well implemented and calculated by the model.

In Figures 7.10-11 are shown the salinity distribution in the surface and the bottom layers of the model at about salinity maximum and minimum for the spring tide simulation with high salinity gradient. The salinity is increasing towards downstream. At about maximum salinity (one hour after high water) a clear vertical salinity stratification is present in the water column. This gradient disappears gradually, at minimum salinity (one hour after low water) the river is well mixed. The magnitude of this vertical salinity gradient is depending on the location. The lateral gradient has, in contrast with the vertical one, a maximum at minimum salinity. In the entrance channel a lateral and vertical salinity gradient is observed.



# 3D Hydrodynamic Model - Spring Tide Comparison with observations Salinity in the measurement points of 04/10/90

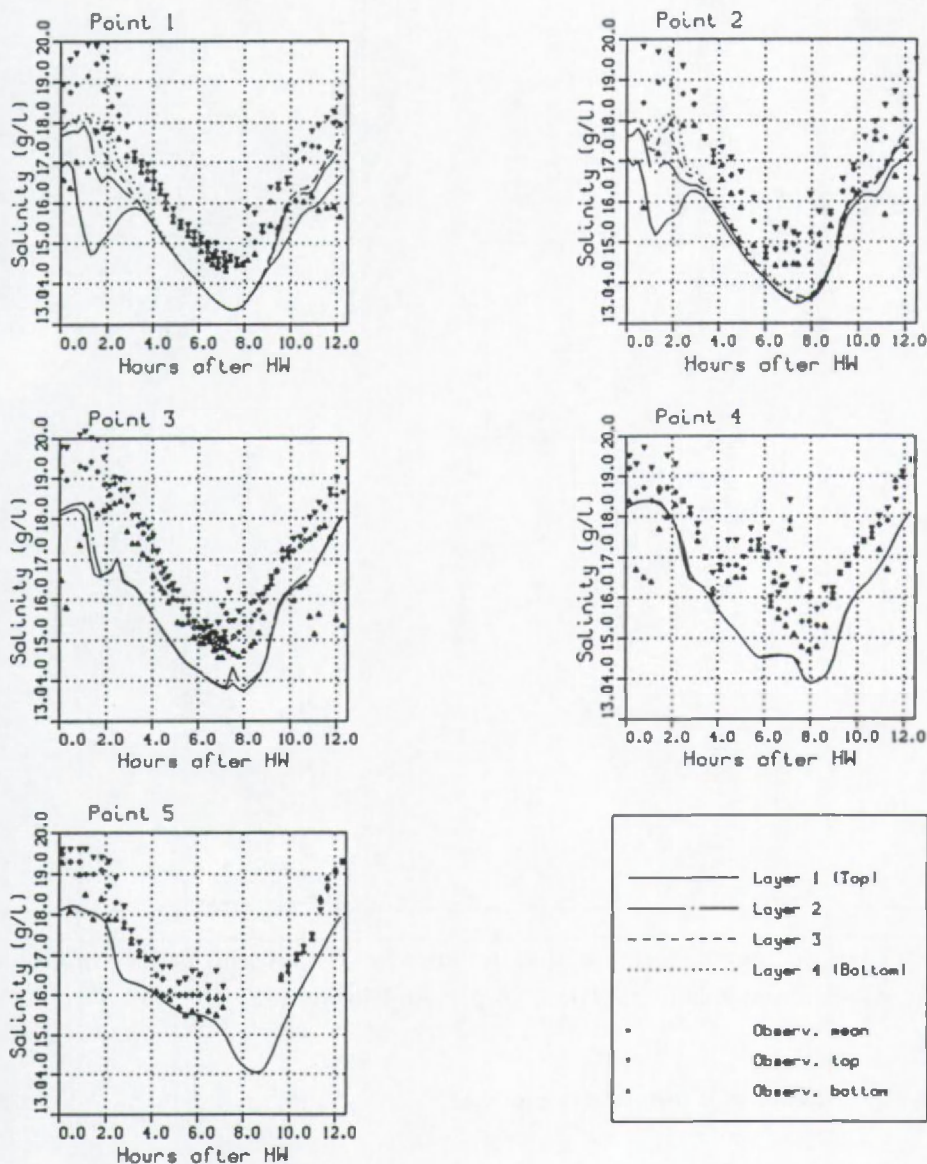


Figure 7.9: Spring tide simulation with high salinity gradient.

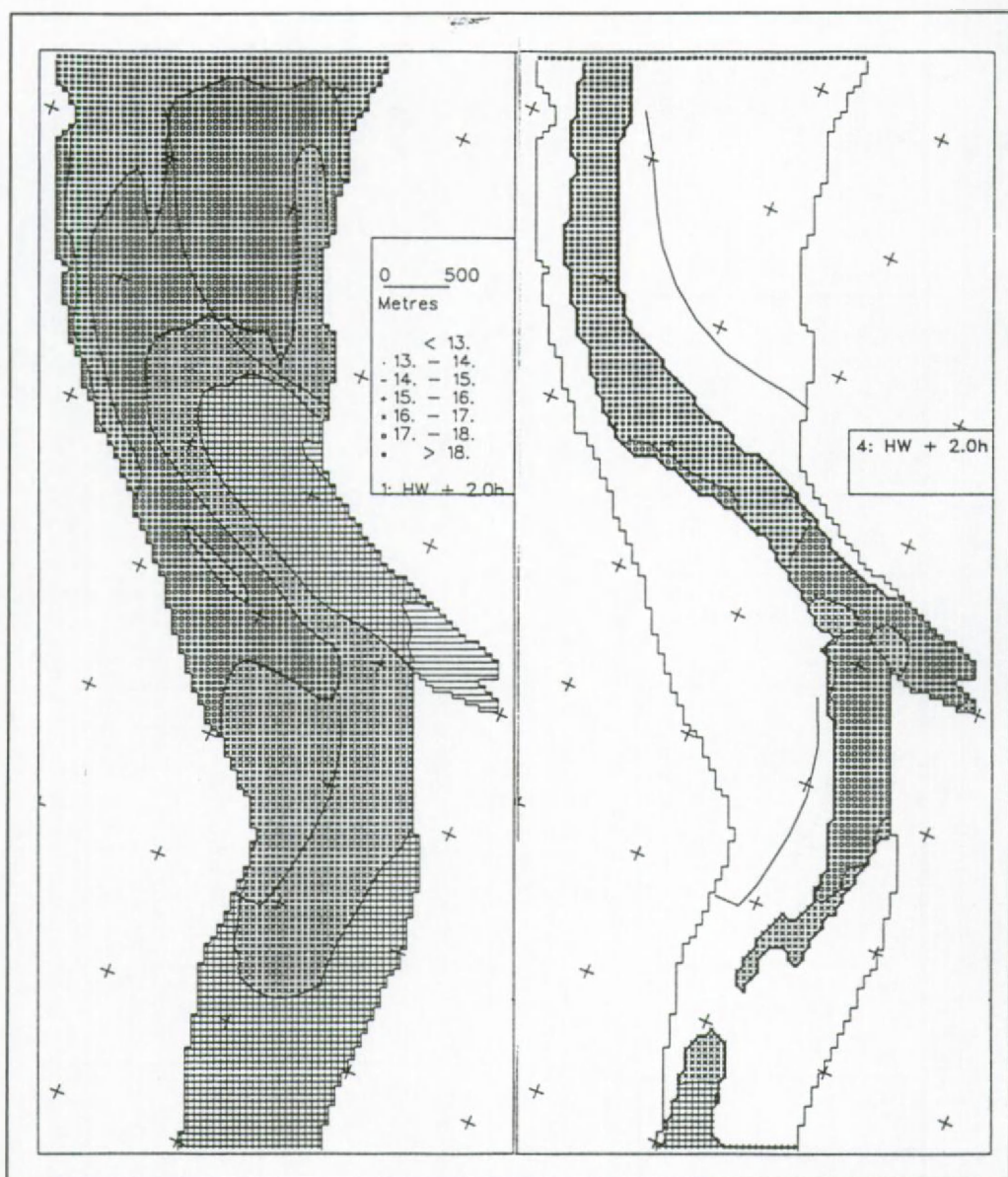


Figure 7.10: 3D model, spring tide with high salinity gradient. Salinity (g/l) distribution at maximum salinity, layers 1 (top) and 4 (bottom).

### 7.3.2. Salinity in the access channel

The vertical salinity gradient in the river is in general restricted to  $\pm 1$ g/l except during the salinity maximum (2 hours after high water slack), the values can then



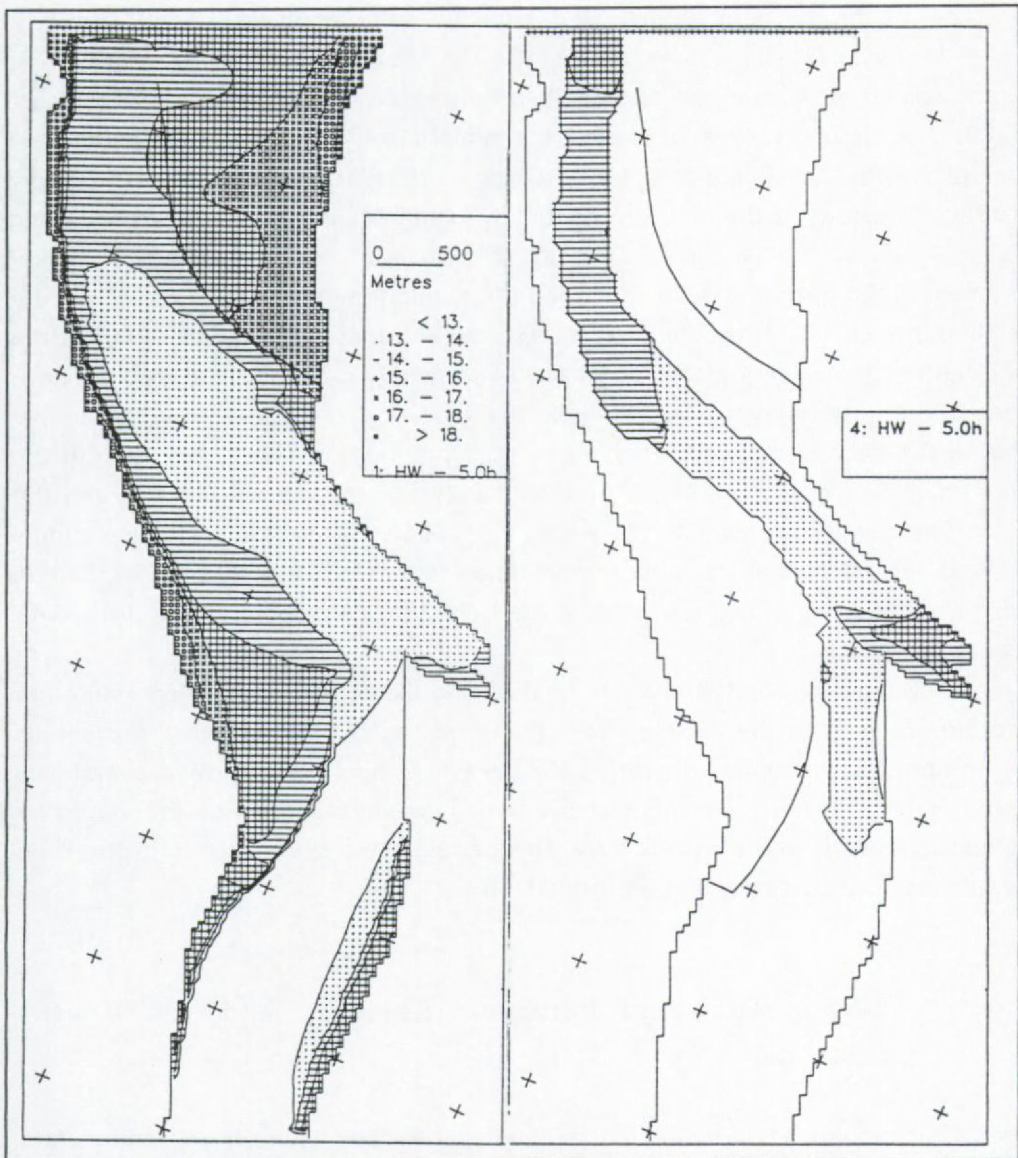


Figure 7.11: 3D model, spring tide with high salinity gradient. Salinity (g/l) distribution at minimum salinity, layers 1 (top) and 4 (bottom).

reach more than 3.0g/l depending on the location. In the access channel a clear vertical salinity gradient is found over whole the tidal cycle. The difference in salinity between surface and bottom is more or less constant, except during low water slack the difference is less, see (§ 5.5.2.). The vertical salinity difference is on the average about the double of that in the river. Near the southern side of the access channel the difference can reach up to 3g/l



whereas at the northern side of the channel the extreme value is about 2.5g/l.

Some salinity profiles in the access channel and the river are illustrated in Figure 7.12. The three points in the access channel correspond to the measurement points 'North, Middle and South' of the salinity measurements on 19 and 29 april 1993, the results of the measurements have been described in § 5.5. The strong vertical salinity gradient in the access channel is in contrast with the weaker gradient in the river. It can be seen that during ebb the vertical gradient of salinity is almost negligible at the northern side of the entrance channel, however, at the southern side a salinity gradient remains. The salinity in the surface layer is lower than in the bottom layer. The salinity in the surface layer is lower than in the river during the salinity maximum (near the 'Drempel van Zandvliet'), resulting in the formation of a horizontal salinity gradient between the access channel and the river. The salinity values over the whole vertical are higher in the access channel than in the river at about salinity minimum. The calculated salinity distribution corresponds qualitatively well with the observations (compare Figure 7.12 with Figures 5.32 and 5.33).

The differences in salinity between the river and the access channel are related to the current field in the access channel. As has been described in the previous paragraph, the water flows over nearly the whole tidal cycle in two layers. The water is replaced slower in the access channel than in the river due to the smaller velocities and due to the layered flow. This has as consequence that horizontal and vertical salinity gradients can be formed.

#### **7.4. Water Exchange Between The River And The Access Channel**

The water exchange between the river and the entrance channel is caused by vertical movements due to the tidal variations, by an eddy which is formed by the passing flow in the river, by density induced currents due to salinity differences between the river and the access channel and by wall effects (quay walls).

By integrating the ingoing and the outgoing discharge at the ADCP measurement cross section over the tide one obtains the total volume of water entering the access channel. A comparison with the tidal volume gives the possibility of determining the relative importance of the horizontal water exchange due to the combined effects of eddy formation and density induced currents.

The water exchange during spring tide due to the vertical water movements (sto-

# 3D Hydrodynamic Model - Calibration Salinity in the Access Channel and the River

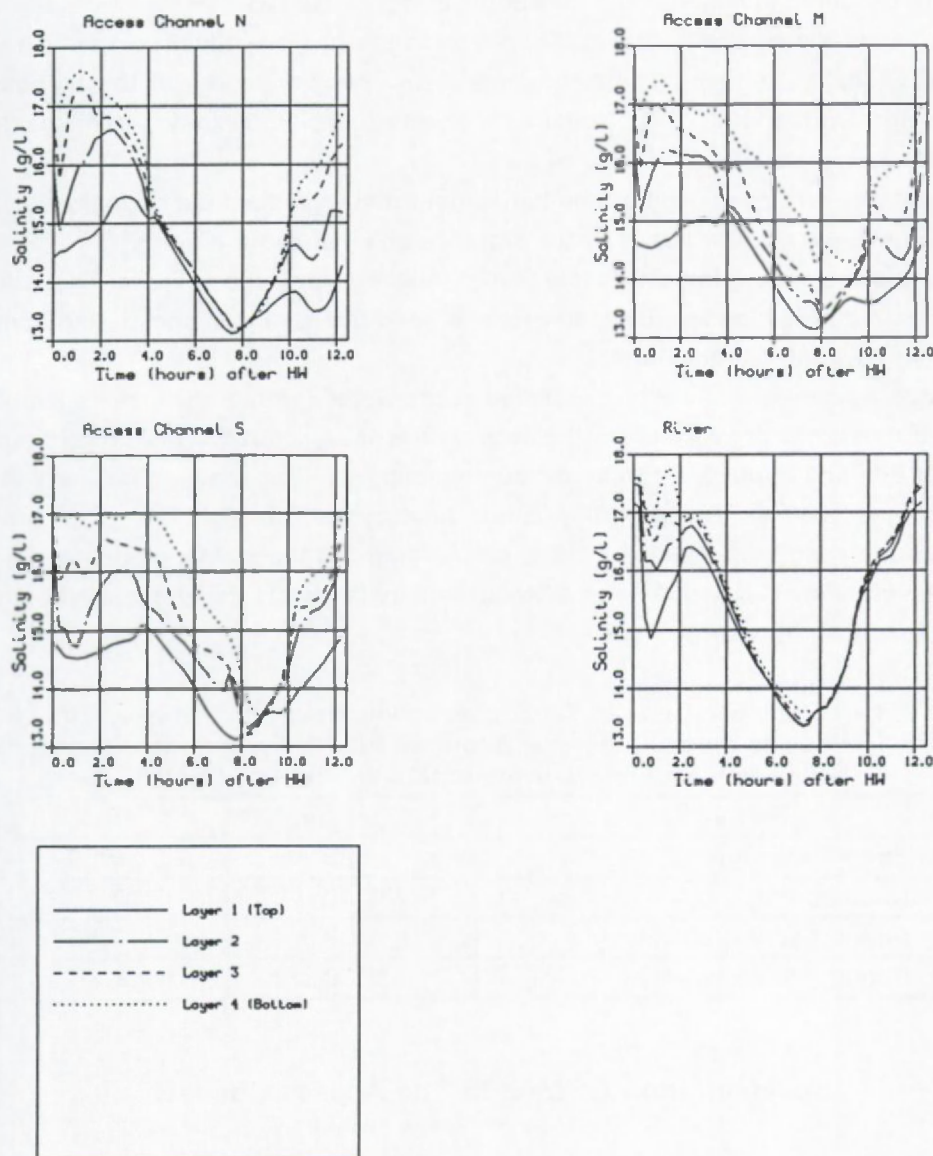


Figure 7.12: Spring tide simulation with high salinity gradient.

rage capacity) is  $1.88 \times 10^6 \text{ m}^3$  and during neap tide  $1.40 \times 10^6 \text{ m}^3$ , while the total water exchange (storage + horizontal effects) is nearly  $20 \times 10^6 \text{ m}^3$ . In Table 7.1 is given a summary of the volumes of water under different circumstances. From this the following conclusions can be drawn:

The total water exchange (eddy and density currents) is a 10 to 12 times bigger than the vertical (storage capacity). Earlier analysis for the former access channel of the Zandvliet lock resulted in a ratio of 20 to 25 (W.L.B., 1971).

The magnitude of the horizontal salinity gradient has an influence on the total water exchange. A lower salinity gradient ( $0.2 \text{ g/l}$  per km) decreases the exchange of water with about 16%. Without horizontal density (salinity) gradients the exchange is reduced by a factor of 2.

The density effects caused by the horizontal salinity gradient play a major role in the exchange of water between the entrance channel and the river.

Salinity plays a more important role than differences in tidal amplitude. The water exchange during high salinity gradients and neap tide is higher than during spring tide and low salinity gradients.

The average amount of water (calculated as the water depth + the water elevation at half tide times the surface) in the access channel is about 5.5 million  $\text{m}^3$  during spring tide and about 5.2 million  $\text{m}^3$  during neap tide. This means that the water is refreshed 3.6 times during one spring tidal cycle with high salinity, 3 times during one spring tidal cycle with low salinity and 3.3 times during one neap tide cycle with high salinity gradients. Without salinity gradients the water is refreshed only 1.7 times in case of a spring tide.

Table 7.1: Water exchange (in  $10^6 \text{ m}^3$ ) between the access channel and the river due to vertical (storage) and horizontal (eddy and density induced currents) water movements (total = vertical + horizontal).

Simulation	Storage	Total
Spring tide high salinity	1.88	19.89
Neap tide high salinity	1.40	17.15
Spring tide low salinity	1.88	16.65
Spring tide no salinity	1.88	9.35

7.5. Sedimentation Of Mud In The Access Channel

Sedimentation in the access channel is the result of the velocity field. The presence of a horizontal pressure gradient induced by salinity differences between the river and the access channel and the fact that the velocities in the channel are very low



and decrease towards the locks create an environment which is favourable for the sedimentation of fine grained material. Another important point is the availability of fine sediment materials in the river. The access channel is situated in the turbidity maximum zone, as was pointed out in Chapter 5.

### 7.5.1. *The 3D mud transport model*

The 3D mud transport model of HR Wallingford has been used to calculate the mud transport in a part of the Scheldt river. The extension of the 2D equations (6.7) to 3D can readily be seen by analogy with the equation of conservation of salt in the 3D hydrodynamic model with addition of a settling flux between the layers and a erosion and deposition source term:

$$\frac{\partial C_i}{\partial t} + u \frac{\partial C_i}{\partial x} + v \frac{\partial C_i}{\partial y} + w \frac{\partial C_i}{\partial z} = D_l \nabla^2 C_i + \frac{\partial}{\partial z} (D_v \frac{\partial C_i}{\partial z}) + D + E \quad (7.11)$$

where  $C_i = C \cdot d$  and  $d$  a vertical distance,  $C$  the mud concentration,  $D_l$  is the longitudinal (shear flow) dispersion coefficient or the lateral (turbulent) diffusion coefficient and  $D_v$  the vertical turbulent diffusion coefficient. Deposition ( $D$ ) is modelled using equation (6.5) and erosion ( $E$ ) using equation (6.6). An explicit upstream finite difference technique is used to solve the advection-diffusion equation.

The model uses the same grid and bathymetry as the 3D hydrodynamic model. The flow field calculated by the 3D hydrodynamic model is used as input.

The grid is such that it is completely situated in the grid of the 2D model TRASIL. The boundary conditions of mud concentration for spring- and neap tide have been extracted from the results of this 2D model.

### 7.5.2. *Observations of sedimentation in the access channel*

During a measurement campaign over a whole tide on 4/4/89 (I.M.D.C., 1990a) in two points situated on the southern side of the entrance channel it was found that the highest values of mud concentration occurred at the river side of the entrance channel. The concentration of mud reached peak values of 1000mg/l during flood and 400mg/l during ebb. More inside the channel the peak concentrations were lower, *i.e.* 600mg/l during flood and 150mg/l during ebb. These differences show that the mud in suspension is falling out during its travel towards the

inside of the channel.

The busy navigation to and from the locks has resulted in the use of alternative dredging techniques such as the sweepbeam, see Smits et al. (1994). The sweepbeam can be considered as a huge bulldozer blade which can push the settled mud back into the river for further natural transport. Data on sedimentation rates in the entrance channel are therefore difficult to obtain. Nevertheless the following data from the entrance channel of the Kallo lock and the Zandvliet and Berendrecht locks are available.

The daily sedimentation in the entrance channel to the Kallo lock is about 1.4cm or nearly 4000m<sup>3</sup> (1.5 million m<sup>3</sup> yearly), see W.L.B. (1983), Claessens and Marain (1988) and Sas and Claessens (1988). Because the surface of the entrance channel to the Zandvliet and Berendrecht locks is about the same size we expect that the sedimentation is of the same order of magnitude. Calculations based on turbidity and velocity measurements in the entrance channel to the Zandvliet lock resulted in an estimation of the sedimentation speed of 5 to 10kg/m<sup>2</sup> per day (2 to 4cm/day), see Wollast (1973). During the dredging works for the southern part of the entrance channel (construction of the Berendrecht lock) a mud catchment area had been dredged up to 21.5m below TAW. The averaged sedimentation speed in the mud catchment area was 4 to 7cm/day whereas a sedimentation speed of 1 to 2cm/day in the (shallower) rest of the entrance channel had been measured, see I.M.D.C. (1990a). If we assume that the mean sedimentation speed is equal to the mean measured sedimentation speed outside the mud catchment area then we obtain a daily sedimentation of about 3500 to 7000m<sup>3</sup> of mud in the entrance channel (1.3 tot 2.6 million m<sup>3</sup> yearly). The daily sedimentation is thus equal to 2.4 to 4.9kg/m<sup>2</sup> in case of a mean density of the mud of 1.15g/l.

### **7.5.3.      *Model Results***

Four different simulations have been carried out (see also above):

- spring tide of 04/10/90 with a high salinity gradient,
- neap tide of 27/09/90 with a high salinity gradient,
- spring tide of 04/10/90 with a low salinity gradient,
- spring tide of 04/10/90 without salinity gradients.

The sedimentation of mud for one tidal cycle is shown in Figure 7.13a (spring tide high salinity gradient) and 7.13b (spring tide no salinity gradient).

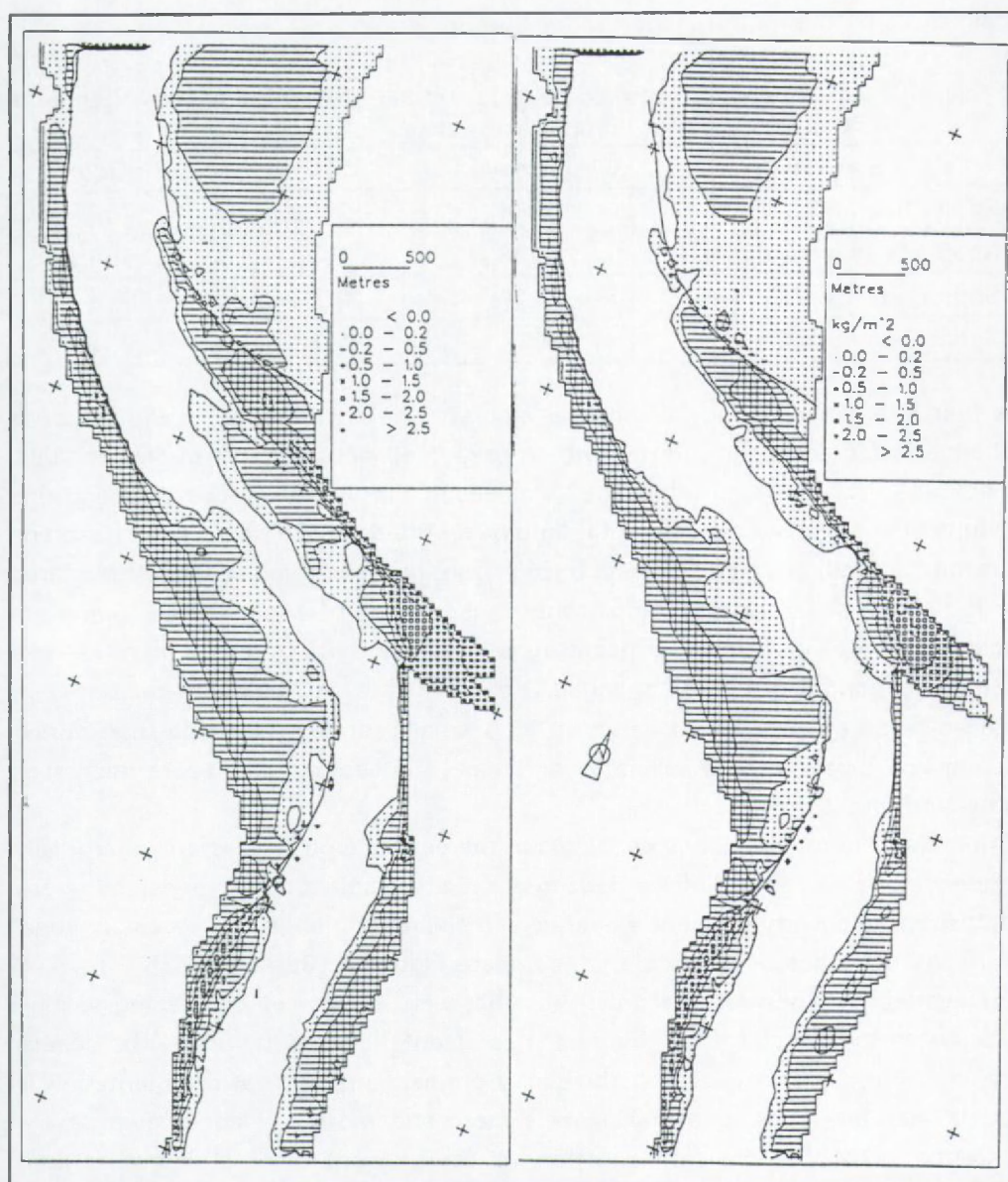


Figure 7.13: 3D model, mud deposition after one tidal cycle. (a) spring tide high salinity gradient and (b) spring tide without salinity gradient.

The sedimentation speed in the entrance channel as calculated by the model is about  $4.6 \text{ kg/m}^2$  per day ( $1.8 \text{ cm/day}$ ), in case of a spring tide simulation with high salinity gradient. The yearly amount of mud sedimentation in the entrance channel is between 1.1 and 2.3 million  $\text{m}^3$ . This corresponds with the above mentioned values. In Table 7.2 the amounts of mud deposited in the entrance channel as



calculated by the mud transport model are presented.

Table 7.2: Sedimentation of mud per tide and per year in the access channel to the Zandvliet and Berendrecht locks.

Simulation	m <sup>3</sup> /day	10 <sup>6</sup> m <sup>3</sup> /yr	t/tide
Spring tide high salinity	6384	2.33	799
Neap tide high salinity	4438	1.62	564
Spring tide low salinity	6274	2.29	813
Spring tide no salinity	3014	1.10	385

A first interesting remark is that the amount of sedimentation in the entrance channel is decreasing (in contrast with the expected increase) with decreasing tidal amplitude (spring - neap tide). The velocities in the river decrease then and this results in an increase of sedimentation outside the entrance channel (at neap tide the model calculates an increase of 50% in front of the entrance channel compared to the spring tide situation). This has as consequence that the water entering the access channel has a lower concentration of suspended sediments and thus less sediments can fall out in the channel. The total water volume exchange between the entrance channel and the river is 16% smaller during neap tide than during spring tide (both for high salinity conditions). The sedimentation rate decreases however with 30%.

The amount of mud which is deposited in the entrance channel is only marginally influenced by a decrease of the horizontal salinity gradient in the model. Whereas in case of no salinity gradient a decrease in sedimentation in the access channel of nearly 50% has been calculated, compare Figure 7.13a and 7.13b. There is, however, a common feature which can be seen in case of decreasing salinity gradient in the Scheldt river: the mud is sedimentating less far inside the access channel. For the case with a high salinity gradient the highest sedimentation is found near the locks, this maximum is more and more displaced towards the entrance of the channel. In case of no salinity gradient there is almost no mud deposited near the locks. The sedimentation pattern is reflected by the flow field, which is, in the access channel, mainly driven by density induced currents. In case of decreasing density currents in the channel, the flow velocity and thus the amount of mud entering the channel is also decreasing.

## 7.6. Conclusions

The measurements and the numerical modelling study have lead to a description of the different processes which are responsible for the sedimentation of fine grained material in the access channel. It was shown that the pressure differences between the river and the channel, formed by salinity gradients, are the main driving forces of the flow in the channel. This phenomena is known in the literature, (e.g. Wollast (1973)), a detailed numerical and in situ measurement campaign (ADCP) had however not been carried out up to know. The main conclusions are:

A horizontal salinity gradient is present between the access channel and the river. The flow in the access channel has a pronounced two layered structure, with inflow in the surface layer and outflow in the bottom layer or vice versa.

A strong vertical salinity gradient can be found in the access channel during almost the whole tide. During ebb the vertical gradient is weaker and almost absent in the northern part of the channel.

The flow changes fundamentally in case of no salinity gradients. Sedimentation of mud decreases then with a factor of two.

The high sedimentation rates found in the channel are due to the density induced currents. The major part of the suspended sediments are entering the channel in the bottom layer. Inflow of water near the bottom occurs from roughly 3 hours before high water to 2 hours after high water.





## CHAPTER 8

### CONCLUSIONS AND RECOMMENDATIONS

#### 8.1. General Conclusions

At the end of each chapter conclusions have been formulated. In what follows we will give an overview of the thesis and will present the main conclusions.

The main goal of the thesis is the simulation of hydrodynamic and transport phenomena in shelf sea and estuaries using mathematical models. The numerical models which have been developed or used have been presented and some applications have been worked out. An important part of the thesis has been spent on validating the numerical models. Validation has been carried out by comparing the model results with the results of other models, of analytical solutions and of measurements. Validation is important because it leads to a quantification of the accuracy and applicability of the numerical model results.

In chapters 2 to 4 the attention is focused on the development and the application of numerical models for wind induced flows in high latitudes. In chapters 5 to 7 cohesive sediment transport in the Scheldt estuary is described using measurements and numerical models. In chapter 1 the introduction and the scope of the work is presented, chapter 8 is devoted to the conclusions.

In *chapter 2* an ice-ocean model is presented. The ocean model enters the class of the so-called 2.5D models. These models are calculating the 3D velocity field in a vertical plane, assuming that the gradients perpendicular to this plane are zero. The assumption on which the model equations have been developed are: hydrostatic pressure distribution, rigid-lid approximation, Boussinesq approximation, eddy

viscosity and diffusivity concepts. The governing equations are solved using an explicit scheme. The ice model only takes into account the dynamics of ice. Thermodynamic processes have been ignored, because we are only interested in mesoscale phenomena.

Open boundary conditions are necessary when the domain of integration is smaller than the geographical dimensions of the basin. The most appropriate open boundary conditions are those which allow disturbances generated in the interior of the domain to leave the domain without disturbing the interior solution. Open boundary condition based on the Sommerfeld condition have been most widely used. Two different implementation of this condition, i.e. Orlanski's and Camerlengo and O'Brien's have been implemented in an existing 2D depth averaged model (Moelans and De Bruyn, 1986). The performance of these open boundary conditions has been tested in some numerical experiments. It was found that the Camerlengo and O'Brien implementation is giving equal or better results than the Orlanski implementation. The Camerlengo and O'Brien open boundary condition has then been implemented in a 2D horizontal flow model. The model has been developed to calculate the flow at a backward facing step and to investigate the accuracy of some advection schemes together with an open boundary condition. It has been shown that the discretisation of the advection terms determines the accuracy of the solution. Higher order upstream schemes, such as the QUICK scheme, give better results than lower order schemes. In order to get a similar accuracy with a lower order scheme than with a higher order one, the grid size has to be decreased. The Camerlengo and O'Brien open boundary condition gave good results even when the open boundary was placed at the eddy.

The circulation induced by katabatic winds in the Antarctic coastal zone has been presented in *chapter 3*. The flow due to katabatic winds in the Adélie land has been chosen as test case to perform an intercomparison exercise between two 2.5D coastal ocean models and an analytical solution. The two ocean circulation models used in the exercise are both 2.5D models. The density has been taken as constant and the vertical turbulent flux of momentum has been parameterized by means of a constant eddy viscosity coefficient. While the governing equations are the same for the two models, the numerical procedures to solve them is different. In a first stage, a set of simulations have been carried out using the models in their original configuration. In these simulations, the forcing was the same but the bottom topography was different (either constant or variable). The results of those first model runs show that an overall agreement exists between the model solutions and especially that both models predict a seaward flow at the surface close

to the continental margin. This seaward flow indicates that coastal polynyas can be formed by katabatic winds. The discrepancies which have been found between both model results, have to be ascribed to differences in numerical procedures. Therefore a set of additional simulations has been realized as an attempt to identify where the differences came from. These simulations dealt with the simplest bottom topography (flat bottom) for which the Ekman solution can be taken as the reference outside the lateral boundary layer. The differences between the finite difference analogues of the horizontal advection and diffusion terms did not contribute significantly to the discrepancies found between the model results. For a given vertical resolution, the differences between the model solutions and the Ekman solution are partially due to the value of the horizontal diffusion coefficient. If this latter is reduced, both model results converge towards the Ekman solution. It appeared clearly that the crux of the difficulties encountered came from the numerical procedures used along the vertical. An improvement of the results of the KUL model has been obtained by introducing a second order accurate analogue of the vertical diffusion term at the surface and at the bottom. A significant improvement of the two model results (compared to the analytical solution) is obtained by reducing the vertical grid size.

In a second part of chapter 3 a brief presentation of the 3D model results of a katabatic wind forcing off the Terra Nova was given. Interesting to notice is that in the 2.5D as well as the 3D models a seaward flux exist near the coast. This results is supporting the idea of coastal polynya formation by a combination of wind and surface flow.

*Chapter 4* deals with wind induced upwelling along an ice edge at the shelf break. The basin for this experiment has the same dimension as those used in the inter-comparison exercise of chapter 3. The 2.5D baroclinic model developed in chapter 2 has been used. The wind is blowing parallel to the ice edge/coast in direction favourable for up- or downwelling. A flow perpendicular to the ice edge/coast is generated due to the Coriolis force. The upwelling is carrying denser water upward, a horizontal density gradient is formed and the resulting density current decreases the upward flow. The initial density stratification is sufficiently high to decrease the magnitude of the upward flow and to enlarge the upwelling zone. At the ice edge the up- or downwelling is reversed when the ice is allowed to move, compared to the stationary ice cover case. The coastal up- or downwelling is, however, qualitatively equal as in the ice free case. The reverse of the up- or downwelling is explained by the fact that the water under the ice is flowing faster than the water in the ice free part of the sea. The up- or downwelling at the ice edge is not as



effective as the one found at a coastal boundary, because the currents extend under the ice. Upwelling along the shelf slope is strongly influenced by the presence of an ice cover. The shelf slope upwelling is reduced substantially with a stationary ice cover and is enhanced in case the ice is allowed to move. The initially vertical density stratification is reducing the upwelling flow. The denser water which is upwelling at the break is deviated and increasing the bottom flow over the shelf when compared to the constant density case. The ice edge in the experiments moved about 16km to 24km away from its initial position in case the wind induces an off-shore current. The magnitude of the horizontal displacements of the ice edge are in the same order as reported from literature. At the coast a polynya is formed. Although the ice and the ocean is simulated in a simplified way, the model is able to reproduce the main features occurring at an ice edge and at a continental slope.

A characteristic feature of marginal ice edges is the development of an along ice edge jet. The jet is attributed to Coriolis force, turning the along ice flow at the ice edge less than further away from the edge. After about 12 hours the jet has been diffused away due to horizontal diffusion. The occurrence of an along ice jet in case of non moving ice cover has already been described. Interesting to notice is the formation of a coastal jet in case of an ocean with a moving ice layer forced by an off coastal current favourable wind. This coastal current is present as long as the coastal polynya has not been formed. The coastal jet is a consequence of the Coriolis force and the stress exerted on the water by the ice and the wind forcing. As the ocean becomes more and more ice free along the coast, the ice stress on the water decreases and the wind is directly acting on the water. Since the ice/ocean stress is higher than the air/water stress, the alongshore current decrease in magnitude in course of time.

Chapters 5 to 7 describe the cohesive suspended sediment transport in a part of the Scheldt estuary (Antwerp to Belgian/Dutch border) by means of measurements and numerical models. In *chapter 5* a review of the hydraulics, morphological and sedimentological characteristics of the Scheldt estuary has been presented. The Scheldt estuary is well-mixed to partially stratified. The influence of stratification is highest in the Beneden Zeeschelde (between Antwerp and the Belgian-Dutch border). In this area measurements of velocity, salinity, mud concentration and temperature have been carried out. These measurements differed in duration, ranging from half a tide (ebb or flood) to more than one year and in 'intensity', from detailed vertical and horizontally distributed recordings of different quantities to single point measurements. The main conclusions are:

Current velocity, sediment concentration, salinity and temperature are varying clearly as a function of tide and neap-spring cycle. Mud concentration, salinity and of course temperature show furthermore a strong correlation with the seasons. The influence of the season is directly correlated to the climatological cycle, i.e. variations of the solar energy input. Their influence on mud concentration and salinity is however indirect through variations in biological activity, fresh water run off and land erosion. The turbidity maximum is situated between Antwerp and the Belgian/Dutch border. The exact location is a function of the fresh water discharge. At the 'Drempel van Zandvliet' the maximum mud concentrations are higher during flood than during ebb. The concentration is lower during increasing than during decreasing velocity. The ratio of depth averaged maximum to minimum mud concentration is about 2.5 during neap and 3.5 during spring tide. These vertical gradients are due to local erosion, settling, and transport of mud from up- or downstream. The mud concentration is more homogenous distributed over the water depth during ebb than during flood. The surface concentration is small during flood, the vertical salinity gradient, which is higher at flood, reduces vertical mixing due to a reduction of turbulence.

The long term measurements at Prosperpolder have shown that the ratio of flood to ebb concentration is not depending on the season but on the tidal amplitude. The ratio varies between 1 (neap tide) and 1.7 (spring tide). Peak concentration are higher in winter during flood than during ebb. In summer the opposite is observed. An explanation for this phenomenon is found in the shift of the turbidity maximum under influence of the river run-off. The concentration of mud averaged over a tidal cycle is 1.3 to 1.7 times greater during a spring tide than during a neap tide depending on the seasons. The ratio between spring to neap tide concentration is higher during winter than during summer. The mud concentration during winter is about the double of the concentration during summer. Different explanations have been suggested, i.e. shift of the turbidity maximum as a function of the freshwater discharge, and a higher sediment load during winter due to a decreased biological activity and a higher erosion. With the given data set it was not possible to give an answer of which processes is relatively more important.

*Chapter 6* deals with the mathematical description of the various cohesive sediment processes and presents a 2D depth averaged particle tracking mud transport model. Calibration and validation of a real cohesive transport model application is a difficult task. The scarcity of field data of the various characteristics of cohesive sediments in an estuary and the predictive capabilities of the erosion and deposition laws are the main reason for this. A simple two step calibration-validation

procedure does not necessarily increase the probability of having accurate results. Validation of a transport model should lead to a quantification of the applicability and the accuracy of the model results. To obtain accurate and reliable results is very often not possible and the model is then restricted to sensitivity purposes. As is pointed out by Teisson (1994) cohesive transport models do not fulfil the standard specifications for the validation of software. The intercomparison exercise (Hamm et al. 1994), which has been briefly described in § 6.1.6. and § 6.3., is a first valuable attempt to quantify the accuracy of such models. The exercise underlines that modelling the transport of cohesive sediments using an extended set of laboratory data and a uniform bed sediment composition suffers from a good description of some aspects of the physics. In an estuary the sediment composition is not uniform, varying from sand to mud (with different grain sizes, mineralogical compositions, organic contents etc.) and the bed structure of the cohesive (or the mixture of cohesive and non cohesive) sediments is generally poorly known. Modelling mud transport in an estuary can thus only be approximative since a lot of simplifications have to be introduced. These models should therefore not be used as the ultimate tool to predict the behaviour of mud but rather as a mean for a better understanding of some of the aspects of mud transport.

The results of three mud transport models of a part of the Scheldt river have been presented. The results of the model intercomparison showed that the model were able to predict the transport, erosion and deposition of mud qualitatively well. The differences which have been observed between the results of the three transport models are the result of differences in diffusion coefficient. The TRASIL model which had originally not included diffusion has been extended by integrating a random walk diffusion model. The results with diffusion are approaching those of the two other models. The simulations have shown that the results of a cohesive transport model can only be as good as the accuracy of the hydrodynamic model. Some features, such as the sedimentation in the access channel, which have been observed in nature, and which can be produced by the transport model are due to an 'over calibration' of the model. It must be mentioned that these models, being limited in time and space scales, with only some basic cohesive sediment processes incorporated (erosion and deposition) and based on the input provided by a simplified hydrodynamic model (in the sense of 2D depth averaged, barotropic and a synthetic tide as boundary condition), cannot be used to simulate long term transport phenomena with a high reliability. The data set used for calibration and validation consist of two through tide measurements in a cross section of the estuary (§ 5.3).



The measurements (chapter 5) have lead to a description of the different processes which are responsible for the sedimentation of fine grained material in the access channel. It was shown that the pressure differences between the river and the channel, formed by salinity gradients, are the main driving forces of the flow in the channel. This phenomena is known in the literature, a detailed numerical and in situ measurement campaign has however not been carried out up to now and is presented in *chapter 7*. The main conclusions are:

A horizontal salinity gradient is present between the access channel and the river. The flow in the access channel has a pronounced two layered structure, with inflow in the surface layer and outflow in the bottom layer or vice versa. A strong vertical salinity gradient can be found in the access channel during almost whole the tide. During ebb the vertical gradient is weaker and almost absent in the northern part of the channel. The flow changes fundamentally in case of no salinity gradients. Sedimentation of mud decreases then by a factor of two. The high sedimentation rates found in the channel are due to the density induced currents. The major part of the suspended sediments are entering the channel in the bottom layer. Inflow of water near the bottom occurs from roughly 3 hours before high water to 2 hours after high water.

## **8.2. Recommendation For Further Research**

The following recommendations are made as an extension of the present work:

The 2.5D and the 3D hydrodynamic models make use of a simplified description for the turbulence closure. Further research is necessary to incorporate more complex turbulence closure models, e.g. mixing length or  $k-\epsilon$  models.

The 3D model is barotropic and should be extended to incorporate density effects.

The density in the 2.5D model is considered to be only a function of salinity and has to be extended to consider temperature effects. The influence of air temperature and freezing or melting processes can then be taken into account.

The 1.5D ice model only takes into account dynamic processes. Dynamic ice processes can explain partially the formation of coastal polynyas. In order to simulate coastal polynya formation thermodynamic processes have to be incorporated.

In the present study, ice effects are only simulated in the 2.5D model. The ice model should be extended to a fully 2D thermodynamic-dynamic model and coupled to the 3D hydrodynamic model.

Measurements of wind, flow, salinity, temperature and ice concentration in time and space will be most useful to apply and validate the models to real situations.

The sedimentation, erosion, consolidation and flocculation processes of cohesive sediments in the 'Beneden Zeeschelde' are not well known. In order to decrease the uncertainties with respect to mud processes in the estuary it is necessary to carry out further measurements.

In the intertidal areas it is possible to carry out measurements which will lead to a quantification of the accumulation or erosion of mud in course of time. These measurements can easily be carried out by regularly measuring the bed level. In parallel, the biota in and on top of the sediments should be determined and quantified as to study the seasonal influence.

The amount of sedimentation and erosion is a function of tides, tidal amplitude and seasons. Measurements of bed level, near bottom velocity, salinity, temperature and mud concentration during a neap-spring cycle and during winter and summer will give detailed information of the cohesive sediment dynamics.

The erosion sensitivity of muddy beds is depending on the consolidation, the biota and the seasons. In order to determine the erosion threshold in situ or laboratory measurements are necessary. The advantage of in situ measurements is that the sediment structure will not be altered, they can, however, only be carried out in the intertidal areas.

Mud concentration measurements together with salinity, temperature and velocity are essential to determine the mud fluxes in the estuary and to investigate the effects of location, tides, tidal amplitude, discharge and seasons. The measurements should be carried out in some stations along the estuary over a long time span (> 1 year). Detailed through tide observations at the long term measurement locations are necessary to investigate the mud concentration variations over a cross section and will allow to calculate the cross sectional averaged mud concentration. These values can then be correlated to the long term measurements and will form the basis of calculating mud fluxes.

The main factor restricting measurements is the cost price. Research to use cheaper measurement instruments or procedures (BBADCP for sediment concentration measurements) is therefore needed.

The results of the measurements will make possible the better quantification of the various model parameters and will give a data base for validating numerical models.





## REFERENCES

- A.G.U. (1994). Quantitative skill assessment for coastal ocean models, *Coastal Estuarine Series*, (eds. D.R. Lynch and A.M. Davies), American Geophysical Union.
- Allen J.R.L. (1985). Principles of physical sedimentology. *Chapman & Hall*, 272p.
- Allen J.S. (1980). Models of wind-driven currents on the continental shelf. *Ann. Rev. Fluid Mech.*, 12, 389-433.
- Ariathurai R. and K. Arulanandan (1978). Erosion rate of cohesive soils. *J. Hydr. Div., ASCE*, 104(HY2), 279-283.
- Aubrey D.G. and P.E. Speer (1985). A study of non-linear tidal propagation in shallow inlet/estuarine systems. Part I: Observations. *Estuarine, Coastal and Shelf Science*, 21, 185-205.
- A.Z. (1987). Zeeschelde, temperatuur en zoutgehalte 1981-1985. *Ministerie van Openbare Werken, Antwerpse Zeehavendienst*, Report Nr. AZ.87/2.
- A.Z. (1991). Maand en decade gemiddelde debieten van het Scheldebekken 1990. *Ministerie van de Vlaamse Gemeenschap, Antwerpse Zeehavendienst*.
- A.Z. (1993a). De afvoer van de Schelde in 1992. *Ministerie van de Vlaamse Gemeenschap, Antwerpse Zeehavendienst*, Report Nr. AZ. 93/04.
- A.Z. (1993b). Zeeschelde, temperatuur en zoutgehalte 1986-1990. *Ministerie van de Vlaamse Gemeenschap, Antwerpse Zeehavendienst*, Report Nr. AZ. 93/05.
- A.Z. (1993c). ADCP meting toegangsgeul Zandvliet - Berendrecht op 19/04/93 en 29/04/93. *Ministerie van de Vlaamse Gemeenschap, Antwerpse Zeehavendienst*.
- A.Z. (1994). De afvoer van de Schelde in 1993. *Ministerie van de Vlaamse Gemeenschap, Antwerpse Zeehavendienst*, Report Nr. AZ. 94/01.
- Bastin A. (1988). Schelde, lithologische kaart 1986-1987. *Ministerie van Openbare Werken, Antwerpse Zeehavendienst*.
- Bastin A. en H. Belmans (1988). A new bottom composition map of the river Scheldt and the general use of a fast method to chart the composition of sea and river bottoms for the study of siltation problems. *9th Int. Harbour Congress, Antwerp*.
- Bella D.A. and W.J. Grenney (1970). Finite-difference convection errors. *J. San. Eng., ASCE*, 96.
- Belmans H. (1991). Debieten van het Scheldebekken. Maand- en jaargemiddelden 1981-1990. *Ministerie van de Vlaamse Gemeenschap, Antwerpse Zeehavendienst*.
- B.G. (1993). Verslag over de resultaten van de boringen te water met bijhorend laboratoriumonderzoek uitgevoerd in verband met de bouw van de Containerkaai Noord langs de Schelde in de haven van Antwerpen. *Ministerie van de Vlaamse Gemeenschap, Bestuur Geotechniek, Report Nr. 9709-92/94*.

- Bills P. and J. Noye** (1987). An investigation of open boundary conditions for tidal models of shallow seas. In: *Numerical Modelling: Applications to Marine Systems*, (ed. J. Noye), Elsevier Science Publishers B.V. (North Holland), 159-194.
- Black K.S.** (1994). Bio-physical factors contributing to erosion resistance in natural cohesive sediments. *Proc. 4th Nearshore and Estuarine Cohesive Sediment Transport Conf.* (INTERCOH '94, July 1994), Paper 18.
- Blumberg A.F. and L.H. Kantha** (1985). Open boundary conditions for tidal models of shallow seas. *J. Hydr. Eng. ASCE*, 111(2), 237-255.
- Brink K.H.** (1991). Coastal-trapped waves and wind-driven currents over the continental shelf. *Ann. Rev. Fluid Mech.*, 23, 389-412.
- Buckley J.R., T. Gammelsrød, J.A. Johannessen, O.M. Johannessen and L.P. Røed** (1979). Upwelling: oceanic structure at the edge of the arctic ice pack in winter. *Science*, 203, 165-167.
- Burt T.N. and J.R. Stevenson** (1986). Monitoring cohesive sediment transport in estuaries. *Int. Conf. on Measuring Techniques of Hydraulic Phenomena in Offshore, Coastal and Inland Waters*, BHRA, London, 325-335.
- Camerlengo A.L. and J.J. O'Brien** (1980). Open boundary condition in rotating fluids. *J. Comp. Phys.*, 35, 12-35.
- Chapman D.C.** (1985). Numerical treatment of cross-shelf open-boundaries in a barotropic coastal ocean model. *J. Phys. Oceanography*, 15, 1060-1074.
- Chen J.H.** (1973). Numerical boundary conditions and computational modes. *J. Comp. Phys.*, 13, 522-535.
- Chesher T.J. and M.C. Ockenden** (1994). Numerical Modelling of Mud and Sand Mixtures. *Proc. 4th Nearshore and Estuarine Cohesive Sediment Transport Conf.* (INTERCOH '94, July 1994), Paper 38.
- Chieh S.H., A. Wake and R.R. Rumer** (1983). Ice forecasting model for Lake Erie. *J. of Waterway, Port, Coastal & Ocean Engineering ASCE*, 109(4), 392-415.
- Claessens J. and H. Belmans** (1984). Overzicht van de getijwaarnemingen in het Zeescheldebekken gedurende het decennium 1971-1980. *Tijdschrift de Openbare Werken van België*, Nr. 3.
- Claessens J. and J. Marain** (1988). Access channel to the Kallo lock, research of alternative dredging methods. *KVIV, 9<sup>th</sup> Int. Harbour Congress*, 4.189-4.200.
- Claessens J., J. Van Hoof and J.H.M. De Ruig** (1991). Interactie morfologie en baggerwerken. *Water*, 60, 182-189.
- Cooper A.J.** (1983). Formulation and development of a 3D numerical model of estuaries. *HR Wallingford*, Report IT 254.
- Darbyshire E.J. and J.R. West** (1993). The turbidity maximum in the Tamar estuary. *Neth. J. of Aquatic Ecology*, 27(2-4), 121-133.



- D.D.K. and A.Z. (1993). Getijtafels 1993. *Ministerie van de Vlaamse Gemeenschap, Dienst Der Kusthavens en Antwerpse Zeehavendienst.*
- Dee D.P. (1994). A pragmatic approach to model validation. In: *Quantitative skill assessment for coastal ocean models*, (eds. D.R. Lynch and A.M. Davies), American Geophysical Union.
- Delo E.A. and T.N. Burt (1986). The hydraulic engineering characteristics of estuarine muds. *Hydraulics Research, Report No SR 77.*
- Delo E.A. and M.C. Ockenden (1992). Estuarine muds manual. *Report HR Wallingford*, SR 309, 23p. + app.
- Dobereiner C. and J. McManus (1983). Turbidity maximum migration and harbour siltation in the Tay estuary. *Amer. J. Fish. Aquatic Sci.*, Suppl. 40, 117-129.
- Drake D.E. (1976). Suspended sediment transport and mud deposition on continental shelves. In: *Marine Sediment Transport and Environmental Management*, (Eds. D.J. Standley and D.J.P. Swift), John Wiley & Sons, New York, London, 127-158.
- Dronkers J. (1986). Tidal asymmetry and estuarine morphology. *Neth. J. of Sea Research*, 20(2-3), 117-131.
- Dyer K.R. (1986). Coastal and Estuarine Sediment Dynamics. *Wiley Interscience Publication*, J. Wiley & Sons, 342p.
- Einstein H.A. and H.B. Krone (1962). Experiments to determine modes of suspended sediment transport in salt water. *J. Geoph. Res.*, 67, 1451-1464.
- Eisma D., P. Bernard, G.C. Cadee, V. Ittekkot, J.Kalf, R. Laane, J.M. Martin, W.G. Mook, A. Van Put and T. Schumacher (1991). Suspended-matter particles size in some West-European estuaries; Part I: Particle size distribution. *Neth. J. of Sea Research*, 28(3), 193-214.
- Eisma D., K.R. Dyer and W. van Leussen (1994). The in situ determination of the settling velocities of fine-grained sediment - A review. *Proc. 4th Nearshore and Estuarine Cohesive Sediment Transport Conf.*, (INTERCOH '94, July 1994), Paper 2.
- Ekman V.W. (1905). On the influence of the earth's rotation on ocean currents. *Ark. Mat. Astron. Fys.* 2(11).
- Falconer R.A. and S. Liu (1988). Modelling solute transport using QUICK scheme. *J. Env. Eng., ASCE*, 114(1), 3-20.
- Fettweis M., C.S. YU and J. Berlamont (1989). Flow simulation in the Weddell sea. In: *Belgian Scientific Research Programme on Antarctica Phase 1*, Vol. III (ed. S. Caschetto), Prime Minister's Services - Science Policy Office, 69p.
- Fettweis M. and C.S. Yu (1990a). Numerical experiments of convection-diffusion dominated flow problems and open boundary conditions in finite difference models. In: *Ocean Wave Mechanics, Computational Fluid Dynamics and Mathematical Modelling*, Comp. Mech. Publ., Southampton, 409-416.

- Fettweis M. and C.S. Yu (1990b). Solving the Navier-Stokes equations by using the artificial compressibility method, description of a computer program. *Internal Report, Lab. Hydraulics, K.U.Leuven, Leuven*, 37p.
- Fettweis M., C.S. Yu, J. Berlamont and M. Rosso (1990c). A 2.5D numerical model for wind driven flows in a partially ice covered shelf sea. *Interim Report, ANTAR 02/II project, Science Policy Office*, 48p.
- Fettweis M., C.S. Yu and J. Berlamont (1991a). Modelling upwelling along a shelf break in high latitudes. *Computer Modelling in Ocean Engineering 91* (Eds. A.S.-Arcilla et al.). A.A. Balkema, Rotterdam, 21-31.
- Fettweis M., C.S. Yu, B. Petit, J. Ozer, Cl. Demuth and H. Gallée (1991b). Comparison of two 2.5D ocean models forced by a katabatic wind. *Belgian Scientific Program on Antarctic. Services of the Prime Minister - Science Policy Office*. 52p.
- Fettweis M., C.S. Yu and J. Berlamont (1993a). Numerical simulation of wind-driven flows in the Antarctic coastal zones. In: *Belgian Scientific Research Programme on Antarctica Phase 2*, Vol. III (ed. S. Caschetto), Prime Minister's Services - Science Policy Office, 54p.
- Fettweis M., M. Sas, K.P.P. Pathirana, E. Jabbari and C.S. Yu (1993b). Suspended sediment transport modelling in the Scheldt estuary: Comparison of different models. *Advances in Hydro-Science and -Engineering*, (Ed. S.S.Y. Wang), I, 1705-1710.
- Fettweis M., M. Sas and L. Meyvis (1994). Analyse van stroom- en sedimentmetingen ter hoogte van de Drempel van Zandvliet (Schelde). *Water*, 76, 88-99.
- Fettweis M. and M. Sas (1994). De complexe stroming in de toegangsgeul van de Zandvliet- en Berendrechtsluis: Inzicht via metingen en modellering. *Water*, 77, 109-116.
- Friederichs C.T. and D.G. Aubrey (1988). Non-linear tidal distortion in shallow well-mixed estuaries: A synthesis. *Estuarine, Coastal and Shelf Science*, 24.
- Gallée H., A. Berger, G. Schayes, T. Fichefet, I. Marsiat, C. Tricot and J.-P. van Ypersele (1989). Numerical study of the air sea interactions in the Antarctic coastal zone and their implications on deep sea formation in the case of katabatic winds. In: *Belgian Scientific Research Program on Antarctica Phase 1*, Vol. III (ed. S. Caschetto), Prime Minister's Services - Science Policy Office, 40p.
- Gallée H., G. Schayes and A. Berger (1993). Development of a 3D meso- $\gamma$  primitive equations model: Katabatic winds simulation in the area of Terra Nova bay, Antarctica. In: *Belgian Scientific Research Programme on Antarctica Phase 2*, Vol. III (ed. S. Caschetto), Prime Minister's Services - Science Policy Office, 36p.
- Golub G.H. and C.F. Van Loan. (1989). Matrix computations. *The Johns Hopkins University Press*, Baltimore and Londen.

Gresho P. and R. Sani (1988). Test problems for the 10 July 1989 outflow boundary condition minisymposium in Wales.

Hackett B., L.P. Røed, B. Gjevik, E.A. Martinsen and L.I. Eide (1994). A review of Metocean modeling project (MOMOP), Part 2: Model validation study, In: *Quantitative skill assessment for coastal ocean models*, (eds. D.R. Lynch and A.M. Davies), American Geophysical Union.

Hamm L., T. Cheshier, M. Fettweis, K.P.P. Pathirana and E. Peltier (1994). An inter-comparison exercise of cohesive sediment transport models. *Proc. 4th Nearshore and Estuarine Cohesive Sediment Transport Conf.*, (INTERCOH '94, July 1994), Paper 43.

Helsloot I.C.M., C. Storm and P. Hoekstra (1988). Ruimtelijke en temporele variabiliteit van slibtransporten in de Westerschelde. *Westerschelde Studies, Studierapport No. 16*.

Hunter J.R. (1987). The application of Lagrangian particle-tracking techniques to modelling of dispersion in the sea. In: *Numerical Modelling: Applications to Marine Systems*. (ed. J. Noye). Elsevier Science Publishers. 257-269.

Hydraulics Research Station (1980). River Scheldt surge barrier - Study of estuary sediments. *HR Wallingford, Ex 928*.

I.M.D.C. (1988a). Optimalisatie van de baggerwerken in de toegangsgeul naar de Kallosluis - Mathematisch model SLIBTRANS. *IMDC Report Nr. 908-88.01.02*.

I.M.D.C. (1988b). Tunnel Liefkenshoek. Onderzoek betreffende de morfologische factoren. *Eindrapport. IMDC Nr. 130-88.09.03*.

I.M.D.C. (1989). Tunnel Liefkenshoek. Onderzoek betreffende de morfologische factoren. Langdurigestroom- en sedimentmeting. *Rapport IMDC Nr. 138-89.11.06*.

I.M.D.C. (1990a). Toegangsgeul Zandvliet - Berendrecht. Meetcampagne t.b.v. de baggerwerken. *Final report*.

I.M.D.C. (1990b). Tunnel Liefkenshoek. Onderzoek betreffende de morfologische factoren. Analyse stroom- en sedimentmetingen. *Rapport IMDC Nr. 138-90.11.05*.

I.M.D.C. (1990c). Toegangsgeul Zandvliet - Berendrecht. Meetcampagne t.b.v. de baggerwerken. *Eindrapport*.

I.M.D.C. (1993a). Gedrag van particulier materiaal in het Schelde-estuarium. *Final report by order of the MUMM* (Ministry of Public Health and Environment).

I.M.D.C. (1993b). Diepte- en stroommeting watervang kerncentrale Doel, 24-25 november 1993. *Report IMDC*.

I.M.D.C.-W.L.B. (1991). Containerkaai noord - Hydraulisch onderzoek. *Final Report IMDC, Nr. 1146-91.12.08*.



- I.M.D.C.-W.L.B. (1992a). Containerkaai Noord - hydraulisch en sedimentologisch onderzoek. Deelrapport 1: Stroom- en sedimentmeting 27/09/90. *Report IMDC Nr. 1166-92.01.02-03*.
- I.M.D.C.-W.L.B. (1992b). Containerkaai Noord - hydraulisch en sedimentologisch onderzoek. Deelrapport 2: Stroom- en sedimentmeting 04/10/90. *Report IMDC Nr. 1166-92.01.04-05*.
- I.M.D.C.-W.L.B. (1993). Containerkaai Noord - hydraulisch en sedimentologisch onderzoek, Deelrapport 9: Stroom- en sedimentmeting 13/06/91. *Report IMDC*.
- I.M.D.C.-W.L.B. (1994). Containerkaai Noord - hydraulisch en sedimentologisch onderzoek. Langdurige turbiditeitsmeting, Augustus 92 - December 93. *Report IMDC*.
- Israeli M. and S.A. Orszag (1981). Approximation of radiation boundary conditions. *J. Comp. Phys.*, 41, 115-135.
- Jabbari E. (1994). Modelling estuarine circulation. *PhD Thesis, Katholieke Universiteit te Leuven*, 241p.
- Jamart B.M., R. Miliff, W. Lick and J. Paul (1982). Numerical studies of the wind-driven circulation in the Santa-Barbara channel. *Final report to Exxon Production Research Company*, 126p.
- Jamart B.M. and J. Ozer (1986). Numerical boundary layers and spurious residual flows. *J. Geoph. Res.*, 91(C9), 10621-10681.
- Johnson J.A. and N. Rockliff (1986). Shelf break circulation processes. In: Baroclinic Processes on Continental Shelves (ed. C.N.K. Mooers). *Coastal and Estuarine Sciences 3*, A.G.U., Washington, 33-62.
- Kollé J.J. and R.S. Pritchard (1983). A comparison of two sea ice trajectory models with AIDJEX observations. *Trans. of ASME*, 105, 346-351.
- Kreiss H.-O. (1970). Initial boundary value problem for hyperbolic systems. *Communications on Pure and Applied Mathematics*, XXIII. 277-298.
- Krone R.B. (1962). Flume studies of the transport of sediment in estuarial shoaling processes. *Final report, Hydraulic Eng. Lab. & samitary Eng. Res. Lab*, University of California, Berkeley.
- Lang G., R. Schubert, M. Markofsky, H.-U. Fanger, I. Grabemann, H.L. Krasemann, L.J.R. Neumann and R. Riethmüller (1989). Data interpretation and numerical modelling of the mud and suspended sediment experiment 1985. *J. Geoph. Res.*, 94(C10), 14381-14393.
- Le Hir P., P. Bassoulet and J. L'Yavanac (1993). Application of a multivariate transport model for understanding cohesive dynamics. In: *Near-Shore and Estuarine Cohesive Sediment Transport*. (Ed. A.J. Mehta). Coastal and Estuarine Studies No. 42, AGU. 148-166.

- Lemke P.** (1986). Stochastic description of atmosphere - sea ice - ocean interactions. In: *The geophysics of sea ice* (ed. N. Untersteiner). Proc. NATO Adv. Study Inst. on Air-Sea-Ice Interactions. Plenum Press, New York. 785-823.
- Mac Anally W.H.** (1989). Lessons from ten years experience in 2D sediment modelling. *Proc. Int. Symp. on Sediment Transport Modelling*. New Orleans, 350-355.
- Manni R.J.** (1986). Slibtransport en slibbalans in de Westerschelde. *Studierapport Nr. 4, Westerschelde Studies*, Rijkswaterstaat, Vlissingen.
- MAST** (1993). On the methodology and accuracy of measuring physico-chemical properties to characterize cohesive sediments. 183p. + app.
- Markofsky M., G. Lang and R. Schubert** (1986). Numerische Simulation des Schwebstofftransportes auf der Basis der Messkampagne MASEX '83. *Die Küste*, 44, 171-189.
- Mead C.T. and J.G. Rodger** (1988). Random walk dispersion modelling. Application to effluent discharges from sea outfalls. *HR Wallingford Report*, No. IT 324.
- Mehta A.J. and E. Partheniades** (1973). Depositional behaviour of cohesive sediments. *Technical Report No. 16, Coastal and Engineering Laboratory*, University of Florida.
- Mehta A.J.** (1984). Characterization of cohesive sediment properties and transport processes in estuaries. In: *Estuarine Cohesive Sediment Dynamics*, (Ed. A.J. Mehta). Lecture Notes on Coastal and Estuarine Studies 14, Springer Verlag, 290-325.
- Mehta A.J., E.J. Hayter, W.R. Parker, R.B. Krone and A.M. Teeter** (1989). Cohesive sediment transport. I Process description and II Application. *ASCE J. Hydr. Eng.*, 115(8), 1076-1112.
- Miller M.J. and A.J. Thorpe** (1981). Radiation condition for the lateral boundaries of limited-area numerical models. *Quart. J. Roy. Met. Soc.*, 107, 615-628.
- Moelans D. and R. De Bryun** (1986). Tweedimensionaal numeriek stromingsmodel van het continentaal plat van de Noordzee. *Internal Report 28-HY-10, Lab. Hydraulics, K.U.Leuven*, Leuven, 62p.
- Morgan R.P.C.** (1979). Soil erosion. *Topics in Applied Geography*, Longman, London & New York, 113p.
- Mulder H.P.J. and C. Udink** (1990). Modelling of cohesive sediment transport. A case study: The western Scheldt estuary. *Int. Conf. on Coastal Eng.*
- Nichols M.M.** (1984). Effects of fine sediment resuspension in estuaries. In: *Estuarine Cohesive Sediment Dynamics* (Ed. A.J. Mehta). Lecture Notes on Coastal and Estuarine Studies, 14, Springer-Verlag.
- Niebauer H.J.** (1982). Wind and melt driven circulation in a marginal sea ice edge frontal system: A numerical model. *Cont. Shelf Res.* 1(1). 49-98.

- Niebauer H.J. and W.O. Smith, Jr. (1989). A numerical model of mesoscale physical-biological interactions in the Fram Strait Marginal ice zone. *J. Geoph. Res.*, 94(C11), 16151-16175.
- Nihoul J.C.J., F. Ronday, J.J. Peters and A. Sterling (1978). Hydrodynamics of the Scheldt estuary. In: *Hydrodynamics of Estuaries and Fjords*. (Ed. J.C.J. Nihoul). Elsevier, Amsterdam.
- Nihoul J.C.J. and S. Djenidi (1987). Perspective in three-dimensional modelling of the marine system. In: *Three-Dimensional Models of Marine and Estuarine Dynamics*, (eds. J.C.J. Nihoul and B.M. Jamart), Elsevier Oceanography Series 45, 1-34.
- O'Brien J.J., R.M. Clancy, A.J. Clarke, M. Crepon, R. Elsberry, T. Gammelsrød, M. MacVean, L.P. Røed and J.D. Thompson (1977). Upelling in the ocean: two- and three-dimensional models of upper ocean dynamics and variability. In: *Modelling and Prediction of the Upper Layer of the Ocean*. (Ed. E.B. Krauss). Pergamon Press, Oxford and New York.
- Odd N. and M. Owen (1972). A two-layer model of mud in the Thames estuary. *Proc. of the Institution of Civil Eng.*, Paper 7517S.
- Odd N.V.M. en J.G. Rodger (1978). Vertical mixing in stratified flows. *J. Hydr. Div.*, ASCE, 104(HY3).
- Orlanski J. (1976). A simple radiation boundary condition. *J. Comp. Phys.*, 21, 251-269.
- Otto L., J.T.F. Zimmerman, G.K. Furnes, M. Mork, R. Saetre and G. Becker (1990). Review of the physical oceanography of the North Sea. *Neth. J. of Sea Research*, 26(2-4), 161-238.
- Ou H.W. (1988). A time-dependent model of a coastal polynya. *J. Phys. Oceanogr.*, 18, 584-590.
- Paul J.F. and W.J. Lick (1981). A numerical model for the three-dimensional variable-density, rigid-lid hydrodynamic flows, Vol. 1: Details of the numerical model. *U.S. Environmental Protection Agency Report*, 150p.
- Partheniades E. (1962). A study of erosion and deposition of cohesive soils in salt water. *PhD Thesis, University of California*.
- Parchure T.M. and A.J. Mehta (1985). Erosion of soft sediment deposits. *J. Hydr. Eng.*, ASCE, 111(10), 1308-1326.
- Paterson D.M. (1994). Biological mediation of sediment erodibility: Ecology and physical dynamics. *Proc. 4th Nearshore and Estuarine Cohesive Sediment Transport Conf.* (INTERCOH '94, July 1994), Paper 17.
- Pathirana K.P.P. (1994). Modelling cohesive sediment transport in estuaries and coastal waters. *PhD Thesis, Katholieke Universiteit te Leuven*, 207p.



- Peters J.J. (1972). Transport de sédiments dans l'estuaire de l'Escaut. *Programme National sur l'Environnement Physique et Biologique, Projet Mer Rapport II*.
- Peters J.J. (1975). Les mécanismes de mélange des eaux dans l'estuaire de l'Escaut. *Annales des Travaux Publics de Belgique*, No.2.
- Peters J.J. and A. Sterling (1976). Hydrodynamique et transport de sédiments de l'estuaire de l'Escaut. In: *Projekt Zee, Eindverslag, Boekdeel 10: Het Schelde estuarium*, (Eds. J.C.J. Nihoul and R. Wollast), 1-70.
- Petit B. (1991). Programme de recherche sur l'Antarctique. *Rapport d'Activité de l'UGMM du 1 aout au 31 janvier 1991*.
- Peyret R. and T.D. Taylor (1983). Computational methods for fluid flow. *Springer Verlag*, New York, 358p.
- Pond S. and G.L. Pickard. (1986). Introductory dynamical oceanography. *Pergamon Press*, 329p.
- Praagman N. (1986). TRASIL: A numerical simulation model for the transport of silt. *Internal Report Svasek B.V.*, Rotterdam.
- Pritchard D.W. (1967). Estuaries. *AAAS Publ.*, USA.
- RDInstrument (1989). Principles of operation: A practical primer. *Hydrotech*, 35p.
- Rodi W. (1987). Examples of calculation methods for flow and mixing in stratified fluids. *J. Geoph. Res.*, 92(C5), 5305-5328.
- Røed L.P. and J.J. O'Brien (1983). A coupled ice-ocean model of upwelling in the marginal ice zone. *J. Geoph. Res.*, 88(C5), 2863-2872.
- Røed L.P. (1983). Sensitivity studies with a coupled ice-ocean model of the marginal ice edge. *J. Geoph. Res.*, 88(C10), 6039-6042.
- Røed L.P. and O.M. Smedstad (1984). Open boundary conditions for forced waves in a rotating fluid. *SIAM J. Sci. Stat. Comp.*, 5, 414-426.
- Røed L.P. and C.K. Cooper (1986). Open boundary condition in numerical ocean models. In: *Advanced Physical Oceanographic Numerical Modelling*, (ed. O'Brien J.J.), D. Reidel Publishing Company, Dordrecht, 411-436.
- Ronday F. (1995). Personal communication.
- Rothrock D.A. (1975). The mechanical behaviour of pack ice. *Ann. Rev. of Earth and Planetary Science*, 3, 317-342.
- R.W.S (1991). Meetresultaten debiet- en sedimentmeting vaarwater boven Bath. *Rijkswaterstaat, Meetdienst Zeeland*, ZLMD-91.N.061.
- Sas M. and J. Claessens (1988). The impact of flow pattern and sediment transport on maintenance dredging in the Kallo access channel. *KVIV 9<sup>th</sup> Int. Harbour Congress*, 4.111-4.120.

- Sas M. (1989). The recognition and simulation of silt transport in the Kallo access channel. In: *Progress in Belgian Oceanographic Research*. (Ed. G. Pichot). Prime Minister Services, Science Policy Office.
- Schneider W. and G. Budéus (1995). On the generation of the Northeast water polynya. *J. Geoph. Res.*, 100(C3), 4269-4286.
- Shyy W. (1983). Study of finite difference approximations to steady-state, convection-dominated flow problems, *General Electric Report No. 83CRD189*, Schenectady, N.Y.
- Shutler R., D. Ryder and C. Johnson (1993). Quality of laboratory calibrations. In: *Calibration of Hydrographic Instrumentation*, *The Hydrographic Society*, Special Publication No. 31, 7-12.
- Sine L. and J.P. Agneessens (1978). Etude de débits solides et du phénomène de migration dans une rivière drainant un bassin agricole. *Pédologie*, XXVIII(2), 183-191.
- Smedstad O.M. and L.P. Røed (1985). A coupled ice-ocean model of ice breakup and banding in the marginal ice zone. *J. Geoph. Res.*, 90(C1), 876-882.
- Smith R.L. (1980). A comparison of the structure and variability of the flow field in three coastal upwelling regions: Oregon, Northwest Africa and Peru. In: *Coastal Upwelling* (ed. F.A. Richards), Coastal and Estuarine Sciences 1. AGU, Washington, 107-118.
- Smits J., L. Meyvis and F. Wens (1994). Maintenance dredging in the river Scheldt, an environmental approach. *ASCE Dredging* 94, 499-508.
- Spitz Y., J. Ozer and B. Jamart (1987). Numerical experiments with a vertical plane 2.5D hydrodynamic model. *MUMM's Contribution to BSEX, Technical Report No. TR05*.
- Swart J.P. (1982). Onderzoek oppervlaktebemonstering slib in de Westerschelde, periode '69 - '80. *Rijkswaterstaat, Directie Waterhuishouding en Waterbeweging*, Nota WWKZ-82.V003. 21p. + app.
- Swart J.P. (1987). Onderzoek verhouding marien/fluviaal slib in de Westerschelde. *Rijkswaterstaat, Directie Zeeland*, Nota NXL-97.015. 14p.
- Technische Scheldecmissie (1984). Verdieping Westerschelde 48'/43'. *Studierapport, Middelburg, Antwerpen*.
- Teeter A.M. (1992). Erosion of cohesive dredged material in open-water disposal sites. *US Army Engineering Waterways Experiment Station, DRP-1-07*, Vicksburg.
- Teisson C. (1994). A review of cohesive sediment transport models. *Proc. 4th Nearshore and Estuarine Cohesive Sediment Transport Conf.*, (INTERCOH '94, July 1994), Paper 36.

- ten Brinke W.B.M. (1992). Slib in het estuarium van de Schelde: Paden en lotgevallen. *Instituut voor Marien en Atmosferisch Onderzoek Utrecht*, Report R92-9 (RUU-IMAU), GWAO-92.841x (RWS-DGW).
- ten Brinke W.B.M. (1994). De menging van marien en fluviatiel slib in het estuarium van de Schelde. *ESTUCON*, 14p.
- Thevenot M.M. and N.C. Kraus (1993). Comparison of acoustical and optical measurements of suspended material in the Chesapeake estuary. *J. Marine Env. Engg.*, 1, 65-79.
- Toorman E.A. (1994). A study of erosion and deposition of cohesive sediments with a 1D point transport model. *KULeuven, Hydraulics Laboratory Report*, 16p.
- Torfs H. (1994) Erosion of mixed cohesive/ non-cohesive sediments in uniform flow, *Proc. 4th Nearshore and Estuarine Cohesive Sediment Transport Conf.*, (INTERCOH '94, July 1994), Paper 20.
- Ukita J. and R.E. Moritz (1995). Yield curves and flow rules of pack ice. *J. Geoph. Res.*, 100(C3), 4545-4557.
- Van Dessel I., F. Wens and M. Sas (1993). The Liefkenshoek tunnel: An important river crossing. *Terra et Aqua*, 52, 20-27.
- Van Eck G.T., N. De Pauw, M. Van Langenbergh, G. Verreet (1991). Emissies, gehalten, gedrag en effecten van (micro)verontreinigingen in het stroomgebied van de Schelde en het Schelde-estuarium. *Water*, 60.
- van Leussen W. (1994). Estuarine macroflocs and their role in fine-grained sediment transport. *PhD thesis, University of Utrecht*. 488p.
- van Maldegem D.C. (1987). Eerste benadering slibbalans Westerschelde. *Rijkswaterstaat, Dienst Getijdewateren*. Nota GWAO-87.101. 68p. + app.
- van Maldegem D.C. (1993). De slibbalans van het Schelde-estuarium. *Rijkswaterstaat, Dienst Getijdewateren, Algemeen Onderzoek Fysica*, Nota GWA-91.081, SAWES-Nota 91.08, 87p. + app.
- van Maldegem D.C., H.P.J. Mulder and A. Langerak (1993). A cohesive sediment balance for the Scheldt estuary. *Neth. J. of Aquatic Ecology*, 27(2-4), 247-256.
- van Maldegem D.C. (1995). Slibscanning Schelde-estuarium in 1993 en 1994. *Rijkswaterstaat, Rijksinstituut voor Kust en Zee*, RIKZ/AB/95.820x. 17p. + app.
- Van Rijn L.C. (1989). Handbook sediment transport by currents and waves. *Delft Hydraulics Report H 461*.
- van Ypersele J.-P. (1989). Coupled ocean and sea-ice models: Review and perspectives. In: *Climate and geo-sciences. A challenge for science and society in the 21st century* (eds. A. Berger, S. Schneider and J.Cl. Duplessy). Kluwer Academic Publishers, Dordrecht, Boston & London, 253-277.



- Van Zoest R. and G.T.M. Van Eck (1990). Behaviour of particulate polychlorinated biphenyls and polycyclic aromatic hydrocarbons in the Scheldt estuary. *Neth. J. of Sea Research*. 26(1), 89-96.
- Vereeke S.J.P. (1994). Geactualiseerde slibbalans Schelde-estuarium, *Rijkswaterstaat, Rijksinstituut voor Kust en Zee*, Nota AX 94.065. 13p.
- Viguié J., J.M. Gallissaires and L. Hamm (1994). Flume measurements of mud transport on a flat bottom under uniform and alternating currents. *Internal Report MAST-G8M Project 4, Topic E*. SOGREAH 52184R1, Grenoble, France.
- Wake A. and R.R. Rumer (1983). Great Lakes ice dynamic simulations. *J. of Waterway, Port, Coastal and Ocean Engineering ASCE*, 109(1), 86-102.
- Wartel S. (1977). Composition, transport and origin of sediments in the Schelde estuary. *Geologie en Mijnbouw*, 56(3), 219-233.
- Wartel S., E. Keppens, P. Nielsen, F. Dehairs, P. Van Den Winkel and L. Cornand (1993). Bepaling van de verhouding marien en fluviatiel slib in de Beneden Zeeschelde, *KBIN and VUB, report to Ministerie van de Vlaamse Gemeenschap, Antwerpse Zeehavendienst*. 16p. + app.
- Washington W.W. and C.L. Parkinson (1986). An introduction to three-dimensional climate modelling. *Oxford University Press*.
- Whitehouse U.G., L.M. Jeffrey and J.D. Debbrecht (1960). Differential settling tendencies of clay minerals in saline waters. In: *Clays and Clay Minerals*, (Ed. A. Swineford), Pergamon Press, New-York, 1-79.
- Williamson H.J. (1994). Recent field measurements of erosion shear stress using ISIS, *Proc. 4th Nearshore and Estuarine Cohesive Sediment Transport Conf.*, (INTERCOH '94, July 1994), Paper 30.
- W.L. (1975). Voorkomen en gedrag van zware metalen in slib uit de Westerschelde. *Waterloopkundig Laboratorium, Instituut voor Bodemvruchtbaarheid*, Report No. R994.
- W.L.B. (1971). De aanslibbing en de aanzanding van de toegangsgeul tot de zeesluis van Zandvliet, model 277. *Ministerie van Openbare Werken, Waterbouwkundig Laboratorium Borgerhout*.
- W.L.B. (1983). Toegangsgeul zeesluis Kallo, evolutie van het bodempeil periode 1/6/82 - 1/8/83, model 302/3-1. *Ministerie van Openbare Werken, Waterbouwkundig Laboratorium Borgerhout*.
- Wollast R. (1973). Origines et mécanisme de l'envasement de l'estuaire de l'Escaut. *Service d'Océanographie Chimique, Institut de Chimie Industrielle - U.L.B.*, 140p.

- Wollast R. and J.J. Peters (1979).** Biochemical properties of an estuarine system: The river Scheldt. In: *Biogeochemistry of Estuarine Sediments*. (Ed. E.D. Goldberg). Unesco, Paris, 279-293.
- Wollast R. and A. Marijns (1981).** Evaluation des contributions de différentes sources de matières en suspension à l'envasement de l'Escaut. *Final report to the Ministry of Public Health and Environment*, 152p.
- Wood I.R., R.G. Bell and D.L. Wilkinson (1993).** Ocean disposal of wastewater. *Advanced Series on Ocean Engineering*, 8, World Scientific, 425p.
- Wooster W.S. (1981).** An upwelling mythology. In: *Coastal Upwelling*, (ed. F.A. Richards), Coastal and Estuarine Sciences 1. AGU, Washington, 1-3.
- Yu C.S., M. Fettweis and J. Berlamont (1988a).** A 2D model for tidal flow computations. *Computational Methods in Water Resources* (eds. Celia M.A. et al.), Comp. Mech. Publ. and Elsevier, 1, 281-288.
- Yu C.S., M. Fettweis, J. Berlamont, D. Decroo and E. Blomme (1988b).** Tidal currents along the West-Belgian coast. *Computer Modelling in Ocean Engineering* (eds. Schrefler and Zienkiewicz), Balkema, Rotterdam, 245-250.
- Yu C.S., M. Fettweis, I. Hermans and J. Berlamont (1989).** Tidal flow simulation in the English Channel and the Southern North Sea. *Adv. Water Resources*, 12, 194-203.
- Yu C.S. (1993).** Modelling shelf sea dynamics and estuarine circulation. *Ph.D. Thesis, Katholieke Universiteit te Leuven*, 206p.





## APPENDIX 1

### POSITION OF SOME LOCATIONS IN THE SCHELDT ESTUARY

Name	Distance (km) from mouth
Breskens	2.0
Vlissingen (Flushing)	2.0
Hoofdplaat	9.0
Terneuzen	20.5
Hansweert	35.8
Walsoorden	39.0
Bath	51.8
Ballastplaat	54.5
Prosperpolder	56.0
Zandvliet	57.5
Plaat van Doel	58.0
Fort Frederich	59.5
Doel	61.5
Lillo	62.5
Liefkenshoek	63.1
Meestoof	66.5
Fort de Parel	68.5
Fort Filip	68.8
St. Marie	69.6
Oosterweel	74.7
Antwerp	77.6
Hemiksem	89.1
Schelle	91.2
Rupelmonde	92.0
Temse	98.3
St. Amands	108.8
Dendermonde	121.8
Schoonaarde	132.6
Uitbergen	138.2
Wetteren	144.7
Melle	150.8
Gentbrugge	159.6



## LIST OF PUBLICATIONS

The following publications and reports are related to this study:

- Fettweis M., J. Berlamont and I. Hermans (1987). 2D simulation of Weddell Sea Circulation. *Proc. Belgian National Colloquium on Antarctic Research*, Brussels, October 20, 1987, Prime Minister's Services - Science Policy Office.
- Yu C.S., M. Fettweis, R. De Bruyn and J. Berlamont (1988). A 2D model for steady and unsteady flows. *Computer Methods and Water Resources, Vol. 2 Computational Hydraulics* (Eds. D. Ouazar et al.), Computational Mechanics Publications and Springer-Verlag, 402-414.
- Yu C.S., M. Fettweis and J. Berlamont (1988). A 2D model for tidal flow computations. *Computational Methods in Water Resources* (eds. Celia M.A. et al.), Comp. Mech. Publ. and Elsevier, 1, 281-288.
- Yu C.S., M. Fettweis, J. Berlamont, D. Decroo and E. Blomme (1988). Tidal currents along the West-Belgian coast. *Computer Modelling in Ocean Engineering* (eds. Schrefler and Zinkiewicz), Balkema, Rotterdam, 245-250.
- Yu C.S., M. Fettweis and J. Berlamont (1989). Hydrodynamic modelling of the North Sea. *Progress in Belgian Oceanographic Research 1989* (ed. G. Pichot), Prime Minister Services - Science Policy Office and MUMM, Brussels, 17-30.
- Fettweis M., C.S. Yu and J. Berlamont (1989). Flow simulation in the Weddell sea. In: *Belgian Scientific Research Programme on Antarctica Phase 1*, Vol. III (ed. S. Caschetto), Prime Minister's Services - Science Policy Office, 69p.
- Yu C.S., M. Fettweis, I. Hermans and J. Berlamont (1989). Tidal flow simulation in the English Channel and the Southern North Sea. *Adv. Water Resources*, 12, 194-203.
- Fettweis M. and C.S. Yu (1990). Numerical experiments of convection-diffusion dominated flow problems and open boundary conditions in finite difference models. In: *Ocean Wave Mechanics, Computational Fluid Dynamics and Mathematical Modelling*, Comp. Mech. Publ., Southampton, 409-416.
- Fettweis M. and C.S. Yu (1990). Solving the Navier-Stokes equations by using the artificial compressibility method, description of a computer program. *Internal Report, Lab. Hydraulics, K.U. Leuven*, Leuven, 37p.
- Fettweis M, C.S. Yu, J. Berlamont and M. Rosso (1990). A 2.5D numerical model for wind driven flows in a partially ice covered shelf sea. *Interim Report, ANTAR 02/II project*, Science Policy Office, 48p.
- Yu C.S., M. Fettweis, M. Rosso and J. Berlamont (1990). A 2D Model with Changing Land- Water Boundaries. *Computational Methods in Surface Hydrology* (Eds. G. Gambolati et al.). Computational Mechanics Publications and Springer-Verlag, 101-106.



- Rosso M., M. Fettweis and C.S. Yu (1991). Tidal flow simulation in the Lagoon of Venice. *Proc. 2nd. Int. Conf. on Computer Methods and Water Resources*, Marrakesh, Morocco, 18-22 feb. 1991.
- Yu C.S. and M. Fettweis (1991). 2D and 3D Numerical Models of Ocean and Shelf Dynamics. *Proc. of the IX Annual Convention of Chinese Academics and Professionals in Europe*, July 5-8, 1991, Brussels, Belgium, 108-123.
- Fettweis M., C.S. Yu and J. Berlamont (1991). Modelling upwelling along a shelf break in high latitudes. *Computer Modelling in Ocean Engineering 91* (Eds. A.S.-Arcilla et al.). A.A. Balkema, Rotterdam, 21-31.
- Fettweis M., C.S. Yu, B. Petit, J. Ozer, Cl. Demuth and H. Gallée (1991). Comparison of two 2.5D ocean models forced by a katabatic wind. *Belgian Scientific Program on Antarctic. Services of the Prime Minister - Science Policy Office*. 52p.
- Fettweis M., C.S. Yu and J. Berlamont (1993). Numerical simulation of wind-driven flows in the Antarctic coastal zones. In: *Belgian Scientific Research Programme on Antarctica Phase 2*, Vol. III (ed. S. Caschetto), Prime Minister's Services - Science Policy Office, 54p.
- Fettweis M., M. Sas, K.P.P. Pathirana, E. Jabbari and C.S. Yu (1993). Suspended sediment transport modelling in the Scheldt estuary: Comparison of different models. *Advances in Hydro-Science and -Engineering*, (Ed. S.S.Y. Wang), I, 1705-1710.
- Fettweis M., M. Sas and L. Meyvis (1994). Analyse van stroom- en sediment-metingen ter hoogte van de Drempel van Zandvliet (Schelde). *Water*, 76, 88-99.
- Fettweis M. and M. Sas (1994). De complexe stroming in de toegangsgeul van de Zandvliet- en Berendrechtshuis: Inzicht via metingen en modellering. *Water*, 77, 109-116.
- Hamm L., T. Cheshier, M. Fettweis, K.P.P. Pathirana and E. Peltier (1994). An inter-comparison exercise of cohesive sediment transport models. *Proc. 4th Nearshore and Estuarine Cohesive Sediment Transport Conf.*, (INTERCOH '94, July 1994), Paper 43.

## **CURRICULUM VITAE**

*Michael Fettweis was born on the 24th of September 1962 in Geel. He went to the European School in Mol (german section) and completed high school in july 1980. He studied Geology at the KULeuven and graduated in 1984. The licentiate thesis was carried out at the Laboratory of Petrology and is entitled 'Study of magmatic rocks in Tamazzarra, Anti Atlas, Morocco'. From 1984 to 1986 he followed courses in informatics at the KULeuven.*

*From October 1986 till September 1991 he worked as a researcher at the Laboratory for Hydraulics of the KULeuven in the framework of the Belgian Scientific Programme on Antarctica (Services of the Prime Minister - Science Policy Office). He collaborated in several studies concerning the numerical simulation of tides and currents in the southern North Sea, the North-West European continental shelf (HAECON, MUMM) and the Lagoon of Venice.*

*In October 1991 he joined IMDC. In November 1991 he was author and lecturer of a ABOS course on mathematical modelling in coastal engineering in Bandung, Indonesia. From the end of 1991 till September 1994 he was involved in various engineering projects related to harbour extensions and dredging problems. As such he was a project geologist for the study of the morphological consequences of the construction of a new container terminal along the Scheldt estuary using mathematical models and in situ measurements.*

*In september 1994, with a study leave from IMDC, he joined again the Laboratory for Hydraulics of the KULeuven. During his stay in Leuven he received a scholarship of the Belgian National Fund for Scientific Research (NFWO).*

*From September 1995 on he restarted working at IMDC.*